

UNIVERSITY OF BIRMINGHAM

Effect of inlet turbulence generation methods on Large-eddy Simulation results

Yi Wang

Ph.D. Dissertation

in Wind Engineering

Supervisors:

Dr Hassan Hemida

Dr Bruno Fraga

Dr Jianchun Wang

School of Engineering

Department of Civil Engineering

University of Birmingham

United Kingdom

UNIVERSITY OF
BIRMINGHAM

University of Birmingham Research Archive

e-theses repository

This unpublished thesis/dissertation is copyright of the author and/or third parties. The intellectual property rights of the author or third parties in respect of this work are as defined by The Copyright Designs and Patents Act 1988 or as modified by any successor legislation.

Any use made of information contained in this thesis/dissertation must be in accordance with that legislation and must be properly acknowledged. Further distribution or reproduction in any format is prohibited without the permission of the copyright holder.

Acknowledgments

When I begin to write this part, I even cannot help crying. I have so much difficult time during these four years, and I never imagine that I can finish my thesis until now. I really want to appreciate the people who helped me during this tough period here. Even if I lost my confidence, you still encourage me and help me, thank you very much. Let me start now.

I want to show my special thanks to my supervisors at the beginning. Firstly, I want to thank my chief supervisor Dr Hassan Hemida. His guidance and encouragement are very helpful when I am in the tough period. And I really like my PhD topic since it is very useful even though it is hard for me, and I believe that my research will be instructive for many peers in the future. Then, I want to thank my second supervisor Dr Bruno Fraga. His encouragement and assistance for me is very important. I also thank my Chinese supervisor Dr Jianchun Wang, he gave me so much support and comfort when I was in the Southern University of Science and Technology (SUStech), and he set a good researcher example for me. Dr Giulio Vita is not my supervisor, but he gave me lots of useful suggestions and helped me with the research. He told me not to be stubborn and gave me some advice, which saved me a lot of time. He is a very interesting person, and it is my honour to recognize him in the UK. I want to thank Dr Yin Luo, without his help, I cannot finish the simulation with the Lund method. He is a very diligent and positive person that is also a good example for me. Dr Jiawei Wan, another person I want to thank, I would not finish the simulation based on the Digital filter methods without his assistance.

Now I want to convey a huge thank to the person who made me warm during this period. I want to thank Dr Ting Yang, my undergraduate classmate. She gave me great strength when I felt desperate about the thesis. Without her encouragement and support, I cannot complete this complex work. I want to speak to her that you are a light in my life, I hope that you can enjoy your life in the future, and I always believe that you can achieve your dream. Next, I want to thank my research group fellow and "the real family member" in the SUStech: Chenghao Lyu, Yuandong Chen, Lishu Duan, Tengfei Luo, Qinmin Zheng, Jian Teng, Zelong Yuan, Dehao Xu, Wenjin Zhao, Xiaoning Wang and Zhijie Li. They gave me a lot of useful suggestions during each group meeting, which is very helpful for my research. We are also good friends of each other and hope that everyone in our group will have a good future.

Then I want to thank the very good friends that I recognized in Birmingham: Danhua Wang, Yang Ma, Jing Song, Anam, Seyma, Simon, Richeal, Ryan, Zhengwei Chen, Junlin Heng, Cong Wu, Min Zhao, Jingwen Kuai, Yueyue Tao, Yuanye Zhou etc. I want to speak to them "I cannot imagine that how I can spend my time in the UK without you guys, you are so nice. I still remember the very warm moment that we stay together, such as cooking food, swimming, hiking and even running half-marathon. I miss you guys and hope that we will have a reunion after the COVID-19 epidemic. Simultaneously, I want to thank my friends in the SUStech: Peijiang Qin, Xiaotian Zhang, Yang Yu, Xiangjun Wang, Yuhan Huang, Tianyi Li, Kangcheng Zhou, Jiashun Zhou etc. I have the fortune to experience the joy and gratitude on a daily basis because of these friends.

I also want to convey my gratitude to the SUStech and the University of Birmingham (UoB), I am fortunate to be a joint program student and enjoy two kinds of education and campus culture on both sides. I love the Y3 building in the UoB where I begin my PhD student life, it is a beginning of a tremendous journey in my life. I also thank the support given by the SUStech. The facility here is awesome and the mental service here is warm and comforting, I received much assistance here when I felt anxious and even desperate. I also want to thank the Chinese government to supply the funding and care for me to finish my education in the UK and China.

Finally, I want to express my best gratitude to my parents and other relatives who gave me great love. I am a full-time student over 20 years hitherto. My parents nearly poured everything they own into myself. It is a very tough journey for them to cultivate me from a small kid to a PhD student. I often made them nervous and anxious. I still remember that my mother phoned all people who might stay with me in the UK when I did not reply to her phone call for a long time. I think there is not enough space for me to express my gratitude and love to them. I want to tell them, "I love you forever, you always protect me and support me, now I want to be a person that can protect you in the future".

At the end of this part, I want to speak something about myself. Honestly, I cannot speak that I fulfilled my PhD life, indeed I wasted a lot of time might be due to the bad emotion, wrong direction and just procrastination. But I still want to thank myself in that I finish this journey finally. No matter how much burden on myself I still did not give up, and this is what I really obtained from my PhD life.

Abstract

For large eddy simulation, it is critical to choose the suitable turbulent inlet boundary condition as it significantly affects the calculated flow field. In the thesis, the effect of different inlet boundary conditions including random method (RAND), Lund method and divergence-free synthetic eddies method (DFSEM) on the flow in a channel with a hump are investigated through large-eddy simulation. The simulation results are further compared with experimental data. It has been found that turbulence is nearly fully developed in the case based on Lund method, not fully developed in the case based on DFSEM and not developed in the case based on RAND method. In the flow region before the hump, mean velocity profiles in the case applying Lund method gradually fit the law of the wall as main flow moves towards the hump, but the simulation results based on RAND and DFSEM methods cannot fit the wall function. In the flow region after the hump, cases applying Lund and DFSEM methods could relative precisely predict the size of turbulent bubble and turbulent statistics profiles. While the case based on RAND method cannot capture the positions of flow separation and re-attachment point and overestimates the turbulent bubble size. From this part, it could be found that different turbulent inflow generation methods have a manifested impact on the flow separation and re-attachment after the hump. If the coherent turbulence is maintained in the approach flow, even though turbulent intensity is not large enough, the simulation can still predict the flow separation and turbulent bubble size relative precisely. From the results, even if the simulation based on the Lund method and DFSEM have a better performance than the simulation based on the RAND method, the results still cannot agree well with the experimental data. There are some possible reasons that result in the big difference. Firstly, the spanwise width of the simulation domain is relatively small. Additionally, the LES sub-grid scale model has a slight impact on the results according to the previous research. Finally, the DFSEM is sensitive to the surface normal gradient schemes.

Beside the choice of the turbulent inlet boundary condition (IBC) methods, the settings of each turbulent IBC method are critical as well. In this thesis, the effect of setting different IBC methods in LES using the Lund method, the divergence-free synthetic eddies method (DFSEM) and the digital filter method (DFM) on the simulation of the boundary layer over a flat plate is investigated. This research also fully explained the influences of different IBC methods on the results of turbulent kinetic energy budget terms, and it is found that the DFM and the DFSEM both have good performance. In addition, for the DFM and DFSEM, the input parameter such as turbulent length scales are hard to set generally without prior knowledge of the flow field. It is found that the simulation results based on these two methods with constant turbulent length scales of 0.4-1.0 times of the value of boundary layer thickness could agree well with the DNS results to a great extent after about 10 boundary layer thickness along the streamwise direction. Overall, it could be recommended that the DFM and the DFSEM can be used in this case with the constant input turbulent length scale about 0.4-1.0 times of the value of boundary thickness.

Contents

Acknowledgments....3

Abstract....5

Contents....7

List of figures....9

Nomenclature....12

Chapter 1 Introduction....20

1.1. Motivation for research....20

1.2. Aim of research and objectives....24

1.3. The Scope of thesis....25

1.4. Thesis Outline....27

Chapter 2 Literature review....29

2.1. Precursor Methods....29

2.2. Synthetic turbulence generation methods....31

2.3. Research gap....36

Chapter 3 Turbulent inlet boundary condition methods....38

3.1. The Lund method....38

3.2. The divergence-free synthetic eddies method (DFSEM)....41

3.3. The digital filter method (DFM)....46

3.4. The random method (RAND)....46

Chapter 4 Numerical method and platform in the simulation....50

4.1. Governing Equations....50

4.2. Introduction of the OpenFOAM platform....53

Chapter 5 Hump channel flow....57

5.1. Numerical setup of the hump channel flow....57

5.2. Mesh sensitivity analysis....61

5.3. Flow properties analysis 65
5.3.1. Velocity field analysis 65
5.3.2. Flow separation and reattachment 68
5.3.3. Turbulent properties before the hump 73
5.3.4. Turbulent properties over the hump 77
5.4. Conclusion of this chapter 83
Chapter 6 Flat plate boundary layer 86
6.1. Computational domain and mesh configuration 86
6.2. Length sensitivity analysis 94
6.2.1. The Digital Filter Method (DFM)) 95
6.2.2. The Divergence Free Synthetic Eddies Method (DFSEM) 104
6.2.3. The Lund method 112
6.3. Flow properties analysis 116
6.3.1. Analysis of velocity field 116
6.3.2. Analysis of Turbulent Budget terms 120
6.3.3. Analysis of Turbulent Reynolds stresses 124
6.4. Conclusion of this chapter 129
Chapter 7 Conclusion 133
7.1. Original Research Contribution 133
7.2. Further steps of the research 134
References 136
Appendices 142
A1. The grid independency analysis after the hump 142
A2. The grid independency analysis for the flat plate boundary layer 145
A3. Simulations based on DFSEM with different turbulent length scales and SGS models 150
A4. The code implemented in this work 160

List of figures

Figure 1.1 The tree diagram of the outline of the thesis in which objectives are covered 27
Figure 3.1 Simulation of the recycling and rescaling method 39
Figure 3.2 Simulation of the recycling and rescaling method 39
Figure 3.3 Flow chart of the application of Divergence Free Synthetic Eddies Method (Jarrin et al., 2006) 42
Figure 3.4 Lumley triangle on the plane of the invariants ξ and η of the Reynolds stress anisotropy tensor. The triangle is mapped with the DFSEM where $6\eta 2 = bii2, 6\xi 3 = bii3 \; and \; bij = ui'ui'uk'uk' - 13\delta ij$, the mapped region can be referred to the research of Poletto. et al. (2013) 46
Figure 5.1 (a) Experimental model of the wall-mounted hump given by ERCOFTAC. (b) the simulation domain for hump case: $Lx = 6.14c; Lx = 6.14c; Lz = 0.2c$. 58
Figure 5.2 Side view of the computational domain with main dimensions expressed in chord unit length. Inlet is located at x/c = −2.14, while hump profile extends from x/c = 0 and x/c = 1. Outflow is at x/c = 4. Channel height is 0.909c. Chanel extends for 0.2c in z direction. 58
Figure 5.3 Input for the simulation based on DFSEM at the inlet (a) Nondimensional time-averaged velocity profiles at the inlet (b) Distribution of Reynolds stresses components $u'u', v'v'$ and $u'v'$ at the inlet of simulation based on Lund method and experimental data ($u'u'$). (c) Profile of the turbulent length scale 59
Figure 5.4 Effect of mesh resolution on streamwise mean velocity based on Lund method at (a) 4 positions before the hump (b) x/c = −2 (c) x/c = −1.5 (d) x/c = −1.0 (e) x/c = −0.5. 62
Figure 5.5 Effect of mesh resolution on streamwise mean velocity based on DFSEM at (a) 4 positions before the hump (b) x/c = −2 (c) x/c = −1.5 (d) x/c = −1.0 (e) x/c = −0.5. 63
Figure 5.6 Effect of mesh resolution on streamwise mean velocity based on RAND method at (a) 4 positions before the hump (b) x/c = −2 (c) x/c = −1.5 (d) x/c = −1.0 (e) x/c = −0.5. 65
Figure 5.8 Instantaneous velocity field (a–c) at T = 3TA and the corresponding iso-surface at the inlet by using the (a) Lund, (b) RAND, and (c) DFSEM. 66
*Figure 5.9 Streamline distribution around the lump plotted from (**a**) Lund method, (**b**) Random method and (**c**) DFSEM method. 68*
Figure 5.10 Distribution of pressure coefficient for three IBCs 70
Figure 5.11 Distribution of friction coefficient for three IBCs 73
Figure 5.12 Time-averaged streamwise velocity U+ profiles (a) at four stations before the hump: (b) x = -2c, (c) x = -1.5c, (d) x = -1c, (e) x = -0.5c. 75
Figure 5.13 Time-averaged streamwise Reynolds stress $u'u'/Uinf2$ profiles at: (a) four stations before the hump (b) x/c = −2 (c) x/c = −1.5 (d) x/c = −1 (e) x/c = −0.5. 76
Figure 5.14 Time-averaged streamwise velocity U+ profiles (a) at four stations over the hump (b) x = 0.65c (c) x = 0.8c (d) x = 1.0c (e) x = 1.2c. 78
Figure 5.15 Time-averaged streamwise velocity $u'u'$ profiles (a) at four stations over the hump (b) x = 0.65c (c) x = 0.8c (d) x = 1.0c (e) x = 1.2c. 80
Figure 5.16 Time-averaged Reynolds stress component $v'v'/Uinf2$ profiles (a) at four stations over the hump (b) x = 0.65c (c) x = 0.8c (d) x = 1.0c (e) x = 1.2c. 81
Figure 5.17 Time-averaged Reynolds stress component $u'v'/Uinf2$ profiles (a) at four stations over the hump (b) x = 0.65c (c) x = 0.8c (d) x = 1.0c (e) x = 1.2c. 83

Figure 6.1 Schematic of the computational domains used for the different simulations: (a) Simulation based on Lund method (precursor domain), (b) Simulation based on all methods Lund, DFSEM and DFM (main domain). *87*
Figure 6.2 The profiles of the turbulent kinetic energy spectrum of the simulation based on DFM with different input turbulent length scales at the same vertical position where $y = 0.5\delta$ $y+= 300$ *and distinctive horizontal positions where (a)* $x = 10\delta$ *(b)* $x = 20\delta$ *(c)* $x = 30\delta$ *(d)* $x = 40\delta$ *(e)* $x = 50\delta$ *96*
Figure 6.3 The profiles of friction velocity along the streamwise direction based on DFM with different input turbulent length scale *97*
Figure 6.4 Distribution of the mean velocity profiles of simulations based on DFM with different input turbulent length scales at different positions: (a) x=inlet (b) $x/\delta = 10$ *(c)* $x/\delta = 20$ *(d)* $x/\delta = 30$ *(e)* $x/\delta = 40$ *(f)* $x/\delta = 50$ *99*
Figure 6.5 Distribution of the streamwise fluctuating velocity profiles of simulations based on DFM with different input turbulent length scales at different positions: (a) x=inlet (b) $x/\delta = 10$ *(c)* $x/\delta = 20$ *(d)* $x/\delta = 30$ *(e)* $x/\delta = 40$ *(f)* $x/\delta = 50$ *101*
Figure 6.6 Distribution of the vertical fluctuating velocity profiles of simulations based on DFM with different input turbulent length scales at different positions: (a) x=inlet (b) $x/\delta = 10$ *(c)* $x/\delta = 20$ *(d)* $x/\delta = 30$ *(e)* $x/\delta = 40$ *(f)* $x/\delta = 50$ *101*
Figure 6.7 Distribution of the Reynolds shear stresses profiles of simulations based on DFM with different input turbulent length scales at different positions: (a) x=inlet (b) $x/\delta = 10$ *(c)* $x/\delta = 20$ *(d)* $x/\delta = 30$ *(e)* $x/\delta = 40$ *(f)* $x/\delta = 50$ *102*
Figure 6.8 Distribution of the profiles of the production rate in simulations based on DFM with different input turbulent length scales at different positions: (a) x=inlet (b) $x/\delta = 10$ *(c)* $x/\delta = 20$ *(d)* $x/\delta = 30$ *(e)* $x/\delta = 40$ *(f)* $x/\delta = 50$ *103*
Figure 6.9 Distribution of the profiles of the dissipation in simulations based on DFM with different input turbulent length scales at different positions: (a) x=inlet (b) $x/\delta = 10$ *(c)* $x/\delta = 20$ *(d)* $x/\delta = 30$ *(e)* $x/\delta = 40$ *(f)* $x/\delta = 50$ *104*
Figure 6.10 The profiles of the turbulent kinetic energy spectrum of the simulation based on DFSEM with different input turbulent length scales at the same vertical position where $y = 0.5\delta$ $y+= 300$ *and distinctive horizontal positions where (a)* $x = 10\delta$ *(b)* $x = 20\delta$ *(c)* $x = 30\delta$ *(d)* $x = 40\delta$ *(e)* $x = 50\delta$ *105*
Figure 6.11 The profiles of friction velocity along the streamwise direction based on DFSEM with different input turbulent length scale *106*
Figure 6.12 Distribution of the mean velocity profiles of simulations based on DFSEM with different input turbulent length scales at different positions: (a) x=inlet (b) $x/\delta = 10$ *(c)* $x/\delta = 20$ *(d)* $x/\delta = 30$ *(e)* $x/\delta = 40$ *(f)* $x/\delta = 50$ *107*
Figure 6.13 Distribution of the streamwise fluctuating velocity profiles of simulations based on DFSEM with different input turbulent length scales at different positions: (a) x=inlet (b) $x/\delta = 10$ *(c)* $x/\delta = 20$ *(d)* $x/\delta = 30$ *(e)* $x/\delta = 40$ *(f)* $x/\delta = 50$ *109*
Figure 6.14 Distribution of the vertical fluctuating velocity profiles of simulations based on DFSEM with different input turbulent length scales at different positions: (a) x=inlet (b) $x/\delta = 10$ *(c)* $x/\delta = 20$ *(d)* $x/\delta = 30$ *(e)* $x/\delta = 40$ *(f)* $x/\delta = 50$ *109*
Figure 6.15 Distribution of the spanwise fluctuating velocity profiles of simulations based on DFSEM with different input turbulent length scales at different positions: (a) x=inlet (b) $x/\delta = 10$ *(c)* $x/\delta = 20$ *(d)* $x/\delta = 30$ *(e)* $x/\delta = 40$ *(f)* $x/\delta = 50$ *110*

Figure 6.16 Distribution of the turbulent shear stresses profiles of simulations based on DFSEM with different input turbulent length scales at different positions: (a) x=inlet (b) $x/\delta = 10$ (c) $x/\delta = 20$ (d) $x/\delta = 30$ (e) $x/\delta = 40$ (f) $x/\delta = 50$ 110

Figure 6.17 Distribution of the profiles of the production rate in simulations based on DFSEM with different input turbulent length scales at different positions: (a) x=inlet (b) $x/\delta = 10$ (c) $x/\delta = 20$ (d) $x/\delta = 30$ (e) $x/\delta = 40$ (f) $x/\delta = 50$ 111

Figure 6.18 Distribution of the profiles of the turbulent dissipation in simulations based on DFSEM with different input turbulent length scales at different positions: (a) x=inlet (b) $x/\delta = 10$ (c) $x/\delta = 20$ (d) $x/\delta = 30$ (e) $x/\delta = 40$ (f) $x/\delta = 50$ 112

Figure 6.19 Instantaneous turbulent boundary layer thickness, momentum thickness and the friction velocity at the inlet plane at different time step with different average time applied for the simulation based on the Lund method 113

Figure 6.20 Distribution of the mean velocity profiles of simulations based on Lund with different length of the precursor domain: (a) x=inlet (b) $x/\delta = 10$ (c) $x/\delta = 20$ (d) $x/\delta = 30$ (e) $x/\delta = 40$ (f) $x/\delta = 50$ 114

Figure 6.21 Distribution of the turbulent Reynolds stresses profiles of simulations based on Lund with different length of the precursor domain at: (a) x=inlet (b) $x/\delta = 10$ (c) $x/\delta = 20$ (d) $x/\delta = 30$ (e) $x/\delta = 40$ (f) $x/\delta = 50$ 115

Figure 6.22 Distribution of the TKE budget terms profiles of simulations based on Lund with different length of the precursor domain at: (a) x=inlet (b) $x/\delta = 10$ (c) $x/\delta = 20$ (d) $x/\delta = 30$ (e) $x/\delta = 40$ (f) $x/\delta = 50$ 116

Figure 6.23 Instantaneous velocity field (a-c) and the corresponding iso-surface of $Q = 20$ in the x-y plane of different cases using the (a) DFSEM, (b) DFM, and (c) Lund method. Instantaneous velocity field (d-f) and the corresponding iso-surface of $Q = 20$ in the y-z plane (at the inlet) of different cases using the (d) DFSEM, (e) DFM, and (f) Lund method. 117

Figure 6.24 Distribution of the mean velocity profiles of simulations based on different IBC methods at different positions: (a) at x=inlet (b) at $x/\delta = 10$ (c) $x/\delta = 20$ (d) $x/\delta = 30$ (e) $x/\delta = 40$ (f) $x/\delta = 50$ 118

Figure 6.25 The profiles of friction velocity along the streamwise direction based on DFM with different input turbulent length scale 119

Figure 6.26 The profiles of the production of simulations based on different IBC methods at different downstream positions: (a) at x=inlet (b) at $x/\delta = 10$ (c) $x/\delta = 20$ (d) $x/\delta = 30$ (e) $x/\delta = 40$ (f) $x/\delta = 50$ 120

Figure 6.27 The profiles of the turbulent convection of simulations based on different IBC methods at different downstream positions: (a) at x=inlet (b) at $x/\delta = 10$ (c) $x/\delta = 20$ (d) $x/\delta = 30$ (e) $x/\delta = 40$ (f) $x/\delta = 50$ 121

Figure 6.28 The profiles of the pressure of simulations based on different IBC methods at different downstream positions: (a) at x=inlet (b) at $x/\delta = 10$ (c) $x/\delta = 20$ (d) $x/\delta = 30$ (e) $x/\delta = 40$ (f) $x/\delta = 50$ 122

Figure 6.29 The profiles of the viscous diffusion of simulations based on different IBC methods at different downstream positions: (a) at x=inlet (b) at $x/\delta = 10$ (c) $x/\delta = 20$ (d) $x/\delta = 30$ (e) $x/\delta = 40$ (f) $x/\delta = 50$ 123

Figure 6.30 The profiles of the dissipation of simulations based on different IBC methods at different downstream positions: (a) at x=inlet (b) at $x/\delta = 10$ (c) $x/\delta = 20$ (d) $x/\delta = 30$ (e) $x/\delta = 40$ (f) $x/\delta = 50$ 124

Figure 6.31 Distribution of the streamwise velocity fluctuation of simulations based on different IBC methods at different positions: (a) at x=inlet (b) at $x/\delta = 10$ (c) $x/\delta = 20$ (d) $x/\delta = 30$ (e) $x/\delta = 40$ (f) $x/\delta = 50$..... 125

Figure 6.32 Distribution of the streamwise velocity fluctuation of simulations based on different IBC methods at different positions: (a) at x=inlet (b) at $x/\delta = 10$ (c) $x/\delta = 20$ (d) $x/\delta = 30$ (e) $x/\delta = 40$ (f) $x/\delta = 50$..... 126

Figure 6.33 Distribution of the spanwise velocity fluctuation of simulations based on different IBC methods at different positions: (a) at x=inlet (b) at $x/\delta = 10$ (c) $x/\delta = 20$ (d) $x/\delta = 30$ (e) $x/\delta = 40$ (f) $x/\delta = 50$..... 128

Figure 6.34 Distribution of the turbulent shear stresses $u'v'$ of simulations based on different IBC methods at different positions: (a) at x=inlet (b) at $x/\delta = 10$ (c) $x/\delta = 20$ (d) $x/\delta = 30$ (e) $x/\delta = 40$ (f) $x/\delta = 50$..... 129

Figure A1. Grid independency analysis after the hump for the simulation based on Lund method: (a) Mean velocity profiles (b) profiles of Reynolds stresses component $u'u'$ (c) profiles of Reynolds stresses component $v'v'$ (d) profiles of Reynolds stresses component $u'v'$ 142

Figure A2. Grid independency analysis after the hump for the simulation based on DFSEM: (a) Mean velocity profiles (b) profiles of Reynolds stresses component $u'u'$ (c) profiles of Reynolds stresses component $v'v'$ (d) profiles of Reynolds stresses component $u'v'$..... 143

Figure A3. Grid independency analysis after the hump for the simulation based on RAND method: (a) Mean velocity profiles (b) profiles of Reynolds stresses component $u'u'$ (c) profiles of Reynolds stresses component $v'v'$ (d) profiles of Reynolds stresses component $u'v'$ 144

Figure A8. Distribution of the mean velocity profiles of simulations based on DFSEM with different mesh size at different positions: (a) at x=inlet (b) at $x/\delta = 10$ (c) $x/\delta = 20$ (d) $x/\delta = 30$ (e) $x/\delta = 40$ (f) $x/\delta = 50$..... 145

Figure A9. Distribution of the profiles of Reynolds stresses component $u'u'$ in simulations based on DFSEM with different mesh size at different positions: (a) at x=inlet (b) at $x/\delta = 10$ (c) $x/\delta = 20$ (d) $x/\delta = 30$ (e) $x/\delta = 40$ (f) $x/\delta = 50$ 145

Figure A10. Distribution of the profiles of Reynolds stresses component $v'v'$ in simulations based on DFSEM with different mesh size at different positions: (a) at x=inlet (b) at $x/\delta = 10$ (c) $x/\delta = 20$ (d) $x/\delta = 30$ (e) $x/\delta = 40$ (f) $x/\delta = 50$ 146

Figure A11. Distribution of the profiles of Reynolds stresses component $w'w'$ in simulations based on DFSEM with different mesh size at different positions: (a) at x=inlet (b) at $x/\delta = 10$ (c) $x/\delta = 20$ (d) $x/\delta = 30$ (e) $x/\delta = 40$ (f) $x/\delta = 50$ 146

Figure A12. Distribution of the profiles of Reynolds stresses component $u'v'$ in simulations based on DFSEM with different mesh size at different positions: (a) at x=inlet (b) at $x/\delta = 10$ (c) $x/\delta = 20$ (d) $x/\delta = 30$ (e) $x/\delta = 40$ (f) $x/\delta = 50$ 147

Figure A13. Distribution of the profiles of Reynolds stresses component $u'u'$ in simulations based on DFSEM with different mesh size at different positions: (a) at x=inlet (b) at $x/\delta = 10$ (c) $x/\delta = 20$ (d) $x/\delta = 30$ (e) $x/\delta = 40$ (f) $x/\delta = 50$ 147

Figure A14. Distribution of the profiles of Reynolds stresses component $v'v'$ in simulations based on DFM with different mesh size at different positions: (a) at x=inlet (b) at $x/\delta = 10$ (c) $x/\delta = 20$ (d) $x/\delta = 30$ (e) $x/\delta = 40$ (f) $x/\delta = 50$..... 148

Figure A15. Distribution of the profiles of Reynolds stresses component $w'w'$ in simulations based on DFM with different mesh size at different positions: (a) at x=inlet (b) at $x/\delta = 10$ (c) $x/\delta = 20$ (d) $x/\delta = 30$ (e) $x/\delta = 40$ (f) $x/\delta = 50$..... 148

Figure A16. Distribution of the profiles of Reynolds stresses component $u'v'$ in simulations based on DFM with different mesh size at different positions: (a) at x=inlet (b) at $x/\delta = 10$ (c) $x/\delta = 20$ (d) $x/\delta = 30$ (e) $x/\delta = 40$ (f) $x/\delta = 50$..... 149

Figure A19. Distribution of the mean velocity profiles of simulations based on DFSEM where the turbulent length scale is 0.2δ with different sub-grid scale models at different positions: (a) at x=inlet (b) at $x/\delta = 10$ (c) $x/\delta = 20$ (d) $x/\delta = 30$ (e) $x/\delta = 40$ (f) $x/\delta = 50$..... 151

Figure A20. Distribution of the profiles of Reynolds stresses component $u'u'$ in simulations based on DFSEM where the turbulent length scale is 0.2δ with different sub-grid scale models at different positions: (a) at x=inlet (b) at $x/\delta = 10$ (c) $x/\delta = 20$ (d) $x/\delta = 30$ (e) $x/\delta = 40$ (f) $x/\delta = 50$ 151

Figure A21. Distribution of the profiles of Reynolds stresses component $v'v'$ in simulations based on DFSEM where the turbulent length scale is 0.2δ with different sub-grid scale models at different positions: (a) at x=inlet (b) at $x/\delta = 10$ (c) $x/\delta = 20$ (d) $x/\delta = 30$ (e) $x/\delta = 40$ (f) $x/\delta = 50$ 152

Figure A22. Distribution of the profiles of Reynolds stresses component $w'w'$ in simulations based on DFSEM where the turbulent length scale is 0.2δ with different sub-grid scale models at different positions: (a) at x=inlet (b) at $x/\delta = 10$ (c) $x/\delta = 20$ (d) $x/\delta = 30$ (e) $x/\delta = 40$ (f) $x/\delta = 50$ 152

Figure A23. Distribution of profiles of Reynolds stresses component $u'v'$ in simulations based on DFSEM where the turbulent length scale is 0.2δ with different sub-grid scale models at different positions: (a) at x=inlet (b) at $x/\delta = 10$ (c) $x/\delta = 20$ (d) $x/\delta = 30$ (e) $x/\delta = 40$ (f) $x/\delta = 50$ 153

Figure A24. Distribution of the TKE budget terms profiles in simulations based on DFSEM where the turbulent length scale is 0.2δ with different sub-grid scale models at different positions: (a) at x=inlet (b) at $x/\delta = 10$ (c) $x/\delta = 20$ (d) $x/\delta = 30$ (e) $x/\delta = 40$ (f) $x/\delta = 50$..... 153

Figure A25. Distribution of the mean velocity profiles of simulations based on DFSEM where the turbulent length scale is 0.6δ with different sub-grid scale models at different positions: (a) at x=inlet (b) at $x/\delta = 10$ (c) $x/\delta = 20$ (d) $x/\delta = 30$ (e) $x/\delta = 40$ (f) $x/\delta = 50$..... 154

Figure A26. Distribution of the profiles of Reynolds stresses component $u'u'$ in simulations based on DFSEM where the turbulent length scale is 0.6δ with different sub-grid scale models at different positions: (a) at x=inlet (b) at $x/\delta = 10$ (c) $x/\delta = 20$ (d) $x/\delta = 30$ (e) $x/\delta = 40$ (f) $x/\delta = 50$ 154

Figure A27. Distribution of the profiles of Reynolds stresses component $v'v'$ in simulations based on DFSEM where the turbulent length scale is 0.6δ with different sub-grid scale models at different positions: (a) at x=inlet (b) at $x/\delta = 10$ (c) $x/\delta = 20$ (d) $x/\delta = 30$ (e) $x/\delta = 40$ (f) $x/\delta = 50$ 155

Figure A28. Distribution of the profiles of Reynolds stresses component $w'w'$ in simulations based on DFSEM where the turbulent length scale is 0.6δ with different sub-grid scale models at different positions: (a) at x=inlet (b) at $x/\delta = 10$ (c) $x/\delta = 20$ (d) $x/\delta = 30$ (e) $x/\delta = 40$ (f) $x/\delta = 50$ 155

Figure A29. Distribution of the profiles of Reynolds stresses component $u'v'$ in simulations based on DFSEM where the turbulent length scale is 0.6δ with different sub-grid scale models at different positions: (a) at x=inlet (b) at $x/\delta = 10$ (c) $x/\delta = 20$ (d) $x/\delta = 30$ (e) $x/\delta = 40$ (f) $x/\delta = 50$ 156

Figure A30. Distribution of the TKE budget terms profiles in simulations based on DFSEM where the turbulent length scale is 0.6δ *with different sub-grid scale models at different positions: (a) at x=inlet (b) at* $x/\delta = 10$ *(c)* $x/\delta = 20$ *(d)* $x/\delta = 30$ *(e)* $x/\delta = 40$ *(f)* $x/\delta = 50$ *156*
Figure A31. Distribution of the mean velocity profiles of simulations based on DFSEM where the turbulent length scale is 1.0δ *with different sub-grid scale models at different positions: (a) at x=inlet (b) at* $x/\delta = 10$ *(c)* $x/\delta = 20$ *(d)* $x/\delta = 30$ *(e)* $x/\delta = 40$ *(f)* $x/\delta = 50$ *157*
Figure A32. Distribution of the profiles of Reynolds stresses component $u'u'$ *in simulations based on DFSEM where the turbulent length scale is* 1.0δ *with different sub-grid scale models at different positions: (a) at x=inlet (b) at* $x/\delta = 10$ *(c)* $x/\delta = 20$ *(d)* $x/\delta = 30$ *(e)* $x/\delta = 40$ *(f)* $x/\delta = 50$ *157*
Figure A33. Distribution of the profiles of Reynolds stresses component $v'v'$ *in simulations based on DFSEM where the turbulent length scale is* 1.0δ *with different sub-grid scale models at different positions: (a) at x=inlet (b) at* $x/\delta = 10$ *(c)* $x/\delta = 20$ *(d)* $x/\delta = 30$ *(e)* $x/\delta = 40$ *(f)* $x/\delta = 50$ *158*
Figure A34. Distribution of the profiles of Reynolds stresses component $w'w'$ *in simulations based on DFSEM where the turbulent length scale is* 1.0δ *with different sub-grid scale models at different positions: (a) at x=inlet (b) at* $x/\delta = 10$ *(c)* $x/\delta = 20$ *(d)* $x/\delta = 30$ *(e)* $x/\delta = 40$ *(f)* $x/\delta = 50$ *158*
Figure A35. Distribution of the profiles of Reynolds stresses component $u'v'$ *in simulations based on DFSEM where the turbulent length scale is* 1.0δ *with different sub-grid scale models at different positions: (a) at x=inlet (b) at* $x/\delta = 10$ *(c)* $x/\delta = 20$ *(d)* $x/\delta = 30$ *(e)* $x/\delta = 40$ *(f)* $x/\delta = 50$ *159*
Figure A36. Distribution of the TKE budget terms profiles in simulations based on DFSEM where the turbulent length scale is 1.0δ *with different sub-grid scale models at different positions: (a) at x=inlet (b) at* $x/\delta = 10$ *(c)* $x/\delta = 20$ *(d)* $x/\delta = 30$ *(e)* $x/\delta = 40$ *(f)* $x/\delta = 50$ *159*
Figure A31. Distribution of the mean velocity profiles of simulations based on DFM where the turbulent length scale is 0.2δ *with different sub-grid scale models at different positions: (a) at x=inlet (b) at* $x/\delta = 10$ *(c)* $x/\delta = 20$ *(d)* $x/\delta = 30$ *(e)* $x/\delta = 40$ *(f)* $x/\delta = 50$ *160*
Figure A32. Distribution of the Reynolds stresses component $u'u'$ *of simulations based on DFM where the turbulent length scale is* 0.2δ *with different sub-grid scale models at different positions: (a) at x=inlet (b) at* $x/\delta = 10$ *(c)* $x/\delta = 20$ *(d)* $x/\delta = 30$ *(e)* $x/\delta = 40$ *(f)* $x/\delta = 50$ *161*
Figure A33. Distribution of the Reynolds stresses component $v'v'$ *of simulations based on DFM where the turbulent length scale is* 0.2δ *with different sub-grid scale models at different positions: (a) at x=inlet (b) at* $x/\delta = 10$ *(c)* $x/\delta = 20$ *(d)* $x/\delta = 30$ *(e)* $x/\delta = 40$ *(f)* $x/\delta = 50$ *161*
Figure A34. Distribution of the Reynolds stresses component $w'w'$ *of simulations based on DFM where the turbulent length scale is* 0.2δ *with different sub-grid scale models at different positions: (a) at x=inlet (b) at* $x/\delta = 10$ *(c)* $x/\delta = 20$ *(d)* $x/\delta = 30$ *(e)* $x/\delta = 40$ *(f)* $x/\delta = 50$ *161*
Figure A35. Distribution of the Reynolds stresses component $u'v'$ *of simulations based on DFM where the turbulent length scale is* 0.2δ *with different sub-grid scale models at different positions: (a) at x=inlet (b) at* $x/\delta = 10$ *(c)* $x/\delta = 20$ *(d)* $x/\delta = 30$ *(e)* $x/\delta = 40$ *(f)* $x/\delta = 50$ *162*
Figure A36. Distribution of the TKE budget terms profiles in simulations based on DFM where the turbulent length scale is 0.2δ *with different sub-grid scale models at different positions: (a) at x=inlet (b) at* $x/\delta = 10$ *(c)* $x/\delta = 20$ *(d)* $x/\delta = 30$ *(e)* $x/\delta = 40$ *(f)* $x/\delta = 50$ *162*

Figure A37. Distribution of the mean velocity profiles of simulations based on DFM where the turbulent length scale is 0.6δ *with different sub-grid scale models at different positions: (a) at x=inlet (b) at* $x/\delta = 10$ *(c)* $x/\delta = 20$ *(d)* $x/\delta = 30$ *(e)* $x/\delta = 40$ *(f)* $x/\delta = 50$ *163*
Figure A38. Distribution of the Reynolds stresses component $u'u'$ *of simulations based on DFM where the turbulent length scale is* 0.6δ *with different sub-grid scale models at different positions: (a) at x=inlet (b) at* $x/\delta = 10$ *(c)* $x/\delta = 20$ *(d)* $x/\delta = 30$ *(e)* $x/\delta = 40$ *(f)* $x/\delta = 50$ *163*
Figure A39. Distribution of the Reynolds stresses component $v'v'$ *of simulations based on DFM where the turbulent length scale is* 0.6δ *with different sub-grid scale models at different positions: (a) at x=inlet (b) at* $x/\delta = 10$ *(c)* $x/\delta = 20$ *(d)* $x/\delta = 30$ *(e)* $x/\delta = 40$ *(f)* $x/\delta = 50$ *164*
Figure A40. Distribution of the Reynolds stresses component $w'w'$ *of simulations based on DFM where the turbulent length scale is* 0.6δ *with different sub-grid scale models at different positions: (a) at x=inlet (b) at* $x/\delta = 10$ *(c)* $x/\delta = 20$ *(d)* $x/\delta = 30$ *(e)* $x/\delta = 40$ *(f)* $x/\delta = 50$ *164*
Figure A41. Distribution of the Reynolds stresses component $u'v'$ *of simulations based on DFM where the turbulent length scale is* 0.6δ *with different sub-grid scale models at different positions: (a) at x=inlet (b) at* $x/\delta = 10$ *(c)* $x/\delta = 20$ *(d)* $x/\delta = 30$ *(e)* $x/\delta = 40$ *(f)* $x/\delta = 50$ *165*
Figure A42. Distribution of the TKE budget terms profiles in simulations based on DFM where the turbulent length scale is 0.6δ *with different sub-grid scale models at different positions: (a) at x=inlet (b) at* $x/\delta = 10$ *(c)* $x/\delta = 20$ *(d)* $x/\delta = 30$ *(e)* $x/\delta = 40$ *(f)* $x/\delta = 50$ *165*
Figure A43. Distribution of the mean velocity profiles of simulations based on DFM where the turbulent length scale is 1.0δ *with different sub-grid scale models at different positions: (a) at x=inlet (b) at* $x/\delta = 10$ *(c)* $x/\delta = 20$ *(d)* $x/\delta = 30$ *(e)* $x/\delta = 40$ *(f)* $x/\delta = 50$ *166*
Figure A44. Distribution of the Reynolds stresses component $u'u'$ *of simulations based on DFM where the turbulent length scale is* 1.0δ *with different sub-grid scale models at different positions: (a) at x=inlet (b) at* $x/\delta = 10$ *(c)* $x/\delta = 20$ *(d)* $x/\delta = 30$ *(e)* $x/\delta = 40$ *(f)* $x/\delta = 50$ *166*
Figure A45. Distribution of the Reynolds stresses component $v'v'$ *of simulations based on DFM where the turbulent length scale is* 1.0δ *with different sub-grid scale models at different positions: (a) at x=inlet (b) at* $x/\delta = 10$ *(c)* $x/\delta = 20$ *(d)* $x/\delta = 30$ *(e)* $x/\delta = 40$ *(f)* $x/\delta = 50$ *167*
Figure A46. Distribution of the Reynolds stresses component $w'w'$ *of simulations based on DFM where the turbulent length scale is* 1.0δ *with different sub-grid scale models at different positions: (a) at x=inlet (b) at* $x/\delta = 10$ *(c)* $x/\delta = 20$ *(d)* $x/\delta = 30$ *(e)* $x/\delta = 40$ *(f)* $x/\delta = 50$ *167*
Figure A47. Distribution of the Reynolds stresses component $u'v'$ *of simulations based on DFM where the turbulent length scale is* 1.0δ *with different sub-grid scale models at different positions: (a) at x=inlet (b) at* $x/\delta = 10$ *(c)* $x/\delta = 20$ *(d)* $x/\delta = 30$ *(e)* $x/\delta = 40$ *(f)* $x/\delta = 50$ *168*
Figure A48. Distribution of the TKE budget terms profiles in simulations based on DFM where the turbulent length scale is 1.0δ *with different sub-grid scale models at different positions: (a) at x=inlet (b) at* $x/\delta = 10$ *(c)* $x/\delta = 20$ *(d)* $x/\delta = 30$ *(e)* $x/\delta = 40$ *(f)* $x/\delta = 50$ *168*

Nomenclature

P	=	Pressure
U	=	İnstantaneous velocity
u_i	=	instantaneous velocity along the i direction
$\bar{u}$	=	filtered velocity
τ_{ij}	=	stress tensor
$\overline{S}_{ij}$	=	filtered rate-of-strain tensor
ν_T	=	turbulent viscosity
C_s	=	Smagorinsky coefficient
Δ	=	sub-grid length
y^+	=	non-dimensional near wall distance defined by $y^+ = u_\tau y/\upsilon$
k_{sgs}	=	the production rate
U	=	Mean velocity
U_i	=	mean velocity along the i direction
U^∞	=	free stream velocity
u_i'	=	fluctuating velocity along the i direction
u'	=	x component of fluctuating velocity
v'	=	y component of fluctuating velocity
w'	=	z component of fluctuating velocity
u_τ	=	Wall friction velocity
$W(\eta)$	=	The weighting function with respect to η
t_0	=	The time when the running average was initiated
T_0	=	The value of the averaging interval used prior to t_0
γ	=	the ratio of friction velocity at the inlet plane to the friction velocity at the recycle plane

δ	=	boundary layer thickness
δ^*	=	displacement thickness
η	=	non-dimensional wall distance defined by $\eta = y/\delta$
$W(\eta)$	=	weighting function
θ	=	momentum thickness
Re_θ	=	Reynolds number based on momentum thickness
Δt	=	computational time step
T	=	characteristic time scale of the averaging interval
α	=	weighting average factor
R_{ij}	=	Reynolds stress tensor
$f_\sigma(x)$	=	suitable shape function
ε_j	=	random numbers with zero average
L	=	turbulent length scale
σ	=	turbulent length scale of eddies
σ_i^k	=	turbulent length-scale of the kth eddy
x^k	=	the location of the centre of the kth eddy
ε_j^k	=	random numbers with zero average
a_{ij}	=	Lund coefficients
R_{ij}	=	Reynolds stress tensor
ω'	=	vorticity of fluctuating velocity
r_j^k	=	non-dimensional distance to the centre of the kth eddy
q_i	=	a suitable shape function based with respect to x_j, x_j^k and σ^k
α_l^k	=	random numbers with zero average
$R_{im}^{P\to G}$	=	rotation transformation matrix
$u_m'^P$	=	velocity fluctuation in the principal axis

$u_m'^G$ = velocity fluctuation in the global system

C_1 = normaliztion coefficient

V_0 = Eddy box volume

Γ = The length-scale ratio

λ_j = Normal stresses in the principal reference system

u_m = Filtered fluctuating velocity

b_k = Filter coefficients in the digital filter method

r_m = Random signal with $\overline{r_m} = 0, \overline{r_m r_m} = 1$

Ψ_β = A two-dimensional slice of fluctuating velocity

u_i^n = Current instantaneous velocity

u_i^{n-1} = Previous instantaneous velocity

R = Random value subject to standard normal distribution

α_R = Weighting averaging factor in the random method

s = Fluctuating scale

v_{sgs} = Sub-grid viscosity

τ_{ij} = The residual stress based on the single filter operation

T_{ij} = The residual stress based on the double filter operation

S_{ij} = Rate-of-strain tensor

$\overline{S_{ij}}$ = Filtered rate-of-strain tensor

s_{ij} = Fluctuating rate-of-strain tensor

κ = Von Karman constant

L_i^j = The i component of the integral length scale along the j direction

L_u = Streamwise integral length scale

T_u = Integral time scale

R = Space lag

τ = Time lag

K = Turbulent kinetic energy

ε = Rate of dissipation of turbulnet kinetic energy

P = Production rate of production of turbulnet kinetic energy in equation (53) and equation (55)

T = Transfer rate of energy from large eddies to small eddies in equation (53) and equation (55)

Subscripts

Q_{inlt} = Quantity evaluated at the inlet plane

Q_{recy} = Quantity evaluated at the recycle plane

Superscripts

Q^{inlt} = Quantity evaluated at the inlet plane

Q^{recy} = Quantity evaluated at the recycle plane

Q^{inner} = Quantity evalutated in the inner region

Q^{outer} = Quantity evalutated in the outer region

Chapter 1

Introduction

1.1. Motivation for research

Atmospheric wind is almost always turbulent and has a strong impact on the aerodynamic loads for objects in the atmospheric boundary layer (ABL) such as wind turbines referred above, ground transportation, high-rise buildings, and many other engineering applications. In complex terrain, local wind phenomena can be expected to greatly affect the aerodynamic loads on these applications (Bechmann et al., 2007).

The wind loads on buildings and other structures, dispersion of pollutants and agricultural production are dependent upon accurate wind predictions including both statistics and turbulent fluctuations (Yan and Li, 2015). This accurate prediction of the wind information is crucial for the wind engineers, experimental aero-dynamists and numerical engineers who are interested in aerodynamic loading, dispersion of pollutions, flow in urban environment and wind energy production. It is well known that topographic features such as hills, ridges and escarpments can greatly influence the wind characteristics, and hence it is important to investigate the flow separation and behaviour in and after these sites before designing, installing and investing in any structure in these sites. There are different methods of obtaining the wind behaviour around there structures, including cite measurements, physical modelling in wind tunnels and computer simulations. For physical and numerical simulations, only a small domain of interest from the universe is simulated and thus the inherent unsteady features of the flow must be simulated accurately both in physical and numerical simulations to provide reliable predictions of the wind within the domain. As almost all of the engineering applications are in the bottom part of the atmospheric boundary layer. It is significant to calculate the properties of atmospheric wind close to the ground in order to accurately predict the effects of turbulent flow

on the performance, loads and reliability of such applications (Quon et al., 2018). The atmospheric boundary layer has been investigated through experiments (Druilhet and Durand, 1997) and computational fluid dynamics (CFD) simulations. Measurements obtained from field experiments are a result of many simultaneous effects and processes being superimposed and it can be difficult to isolate or focus on a specific process. Besides, conducting field measurements is time-consuming and expensive. CFD simulations are often a great supplement to field experiments and the effect of changing a single parameter can be easily investigated. Accurate and efficient predictions of turbulent flow separation and re-attachment at high Reynolds numbers can produce significant performance enhancements for many technological applications as well. However, accurate predictions of unsteady separation remain a very challenging task through the CFD simulation (Fagbade and Heinz, 2022). The challenge includes using CFD models, e.g., Large Eddy Simulation (LES) and the representation of inlet boundary conditions (Cao, 2019).

CFD can be conducted through different simulation methods, including direct numerical simulation (DNS), large-eddy simulation (LES) and Reynolds Averaged Navier-Stokes (RANS). The nonlinear terms in the N-S equations transfer energy between different length scales (Moin and Mahesh, 1998). DNS is capable of resolving all the scales of motion with initial and boundary conditions (S. Pope, 2001). However, DNS cannot be applied to high Reynolds number atmospheric flows since the associated computational cost increase with the Reynolds number as Re^3 (Immer, 2016). The RANS is applied to describe the evolution of the mean quantities. The effect of turbulent fluctuations appears in a Reynolds stress term is modelled to close the system. A very wide range of models for the Reynolds stress is available, ranging from simple, algebraic models to $K-\varepsilon$ models, to full of algebraic Reynolds stress closures (Piomelli, 1999). Most predictions for engineering applications are obtained from solution of the RANS equations. The RANS model can predict the attached flows and some

shallow separation flows (Fröhlich et al., 2005). For instance, RANS can be used to investigate the average quantities of ABL. This approach, however, suffers from one principal shortcoming that the model must represent a wide range of scales. The small scales are dependent upon viscosity and may be somewhat universal, while the large scales are strongly affected by the boundary conditions. Thus, it does not model the large scales of turbulence accurately (Piomelli, 1999). Aerodynamic features of road vehicles are strongly related to some complex interactions between flow separations and strong trailing vortices. However, such structures are not observed in RANS studies (Minguez et al., 2008). More recently, large eddy simulation (LES) of the simulation method becomes an alternative to predict the flow field (Krishna et al., 2004).

In LES, the larger three-dimensional unsteady turbulent motions are directly resolved, whereas the effects of the smaller-scale motions are modelled. In computational expense, LES lies between RANS and DNS and it is motivated by the limitations of each of these approaches (S. Pope, 2001). At an inlet, turbulent fluctuations are present on the grid scale, some methods must be found for generating stochastic fluctuations in the grid scale quantities that 'look' like turbulence. Although in some problems (such as bluff body flows), turbulence at the inlet is not a significant contribution to the turbulence within the domain, in many cases the inlet conditions will have a significant impact on the flow dynamics and the correct of implementation of inlet conditions is important (Tabor and Baba-Ahmadi, 2010). A proper turbulent flow field at the inlet as an inflow boundary condition is required to calculate pressure coefficient accurately in LES. The behaviour of the turbulent field in the interior domain is highly dependent on the physical quality of inflow field (Mansouri et al., 2022). According to the work of It has been considered that the quality of specification of LES inlet condition can exert a critical effect on the simulation accuracy (Tyacke and Tucker, 2015; Lund et al., 1998; Xiao et al., 2013; McMullan et al., 2009). It has been found that the influence of the inlet boundary conditions on the downstream flow not only depends on the accuracy of the inflow

data, but also on the flow consideration (Li et al., 2000). The detailed reviews of different approaches for inlet turbulence generation can be found in papers of Tabor (Tabor and Baba-Ahmadi, 2010), Wu (2016) and most recently of Nitin (Dhamankar et al., 2018). A critical property named development length is highly emphasised by these studies. The development length indicates the distance downstream of the inlet boundary where the specified fluctuations imposed at the inlet becomes completely and consistently correlated (Fukami et al., 2019). To obtain fully developed turbulent flow without significantly increasing computation, it is necessary to implement reliable turbulence inlet boundary condition (IBC) (Castro et al., 2011). The importance of using the proper inflow turbulent boundary condition with LES was extensively discussed by several researchers (Sagaut et al., 2003; Tominaga and Stathopoulos, 2011).

In the thesis, the effects of using different IBCs in LES on the flow over two kinds of flow regimes, one complex and one simpler are investigated. The complex flow regime is the hump channel flow that is a commonly used test case for sake of the analysis of the flow separation and reattachment in many works (Krishna et al., 2004; Uzun and Malik, 2018; Fagbade and Heinz, 2022) with open-source experimental data (Greenblatt et al., 2006). The simpler flow regime is a zero pressure gradient boundary layer flow. The flow properties such as mean velocity profiles, Reynolds stresses profiles and pressure coefficients distribution in the approach flow and the flow downstream were calculated through applying different IBCs. Applicability of different methods in LES for various parameters is discussed and the results of these methods are compared with the data obtained experimentally. The work provides potential strategies for implementation of IBC methods on the flat plate boundary layer, complex terrain problems and then the ABL when using LES as the simulation method (Vasaturo et al., 2018).

1.2. Aim of research and objectives

The aim of the research is to investigate the characteristics and applications of different existing turbulent inflow generation methods in large eddy simulations. Emphasis is given to the integral length scale of turbulence found in the inflow and its relationship with the boundary layer thickness.

To fulfil this aim, four objectives are identified as follows:

(O1.) To investigate the effect of three different types of commonly used inlet boundary conditions within large eddy simulation including the Lund method, the random method and the divergence-free synthetic eddies method on the flow around a hump. The case represents a complex flow regime with different types of flow separation and reattachment.

(O2.) To investigate the effects of three different types of commonly used turbulent inlet boundary conditions including the Lund method, the digital filter method and the divergence-free synthetic eddies method on the large eddy simulation of flow over a flat plate. This study focuses on the impact of such approached on the generation of coherent structures and the turbulent kinetic energy budget term.

(O3.) To develop a methodology to simplify the application of turbulent inlet boundary conditions through the use of constant turbulent length scales.

(O4.) To investigate the computational cost of commonly used IBC methods and produce recommendations for future lines of enhancement of turbulent inlet boundary condition methods.

1.3. The Scope of thesis

The scope of the thesis includes the investigations of the effects of the different turbulent inlet boundary conditions on Large-Eddy Simulations when applied for the flow in two different cases: one complex, and one simple. The complex flow has been represented by a channel flow with a hump and the simple flow has been represented by a simple channel flow without any obstacles. The latter represents flat plate boundary layer. The application of these includes the simulations of a controlled flow in a wind tunnel (simple flow) or the flow in complex terrain such as the flow of the atmospheric boundary layer.

Five different turbulent inlet boundary condition methods including Lund method, divergence-free synthetic eddies method (DFSEM), digital filter method (DFM) and random method (RAND) are discussed here. The details of the definition and implementation of each method is explicitly introduced.

For the complex flow, the simulation results are described by the profiles of mean velocity, turbulent Reynolds stresses, wall shear stresses, pressure coefficient and the size of the separation bubble. For the simple flow, the simulation results are interpreted by the profiles of mean velocity, Reynolds stresses, friction velocity and turbulent kinetic energy budget terms. The comparison between the simulation results and the DNS or experimental data can evaluate the effects of different inlet boundary condition methods on the simulation.

After the investigation of the hump channel flow, it is found that the application of 2 kinds of synthetic turbulence methods is not convenient since the turbulent length scale should be pre-defined. The much simpler flow regime, a flat plate boundary layer is simulated to resolve this problem. It is found that the constant value can be used as the input turbulent length scale. The thesis emphasizes the application of each method, the limitations of each inlet boundary condition result are considered. However, the deep analysis of the physical mechanism of turbulence in these two cases is out of the scope of the thesis. Meanwhile, the thesis applies a

kind of wall function in the hump channel flow as the wall boundary condition according to the previous researches about the hump channel flow. While the interaction between the wall function and the turbulent inlet boundary conditions is out of the scope of the thesis. The comparison of the different algorithms is out of the scope of the thesis as well.

1.4. Thesis Outline

The thesis is structured as a collection of original and stand-alone research papers resembling the objectives given in Section 1.2. When applicable, a disclaimer is present at the beginning of each chapter, if the work or part of it has been published elsewhere by the author himself and other co-authors and reproduced with permission, as requested by the University of Birmingham Plagiarism Guidelines. The thesis outline is illustrated by Figure 1.1.

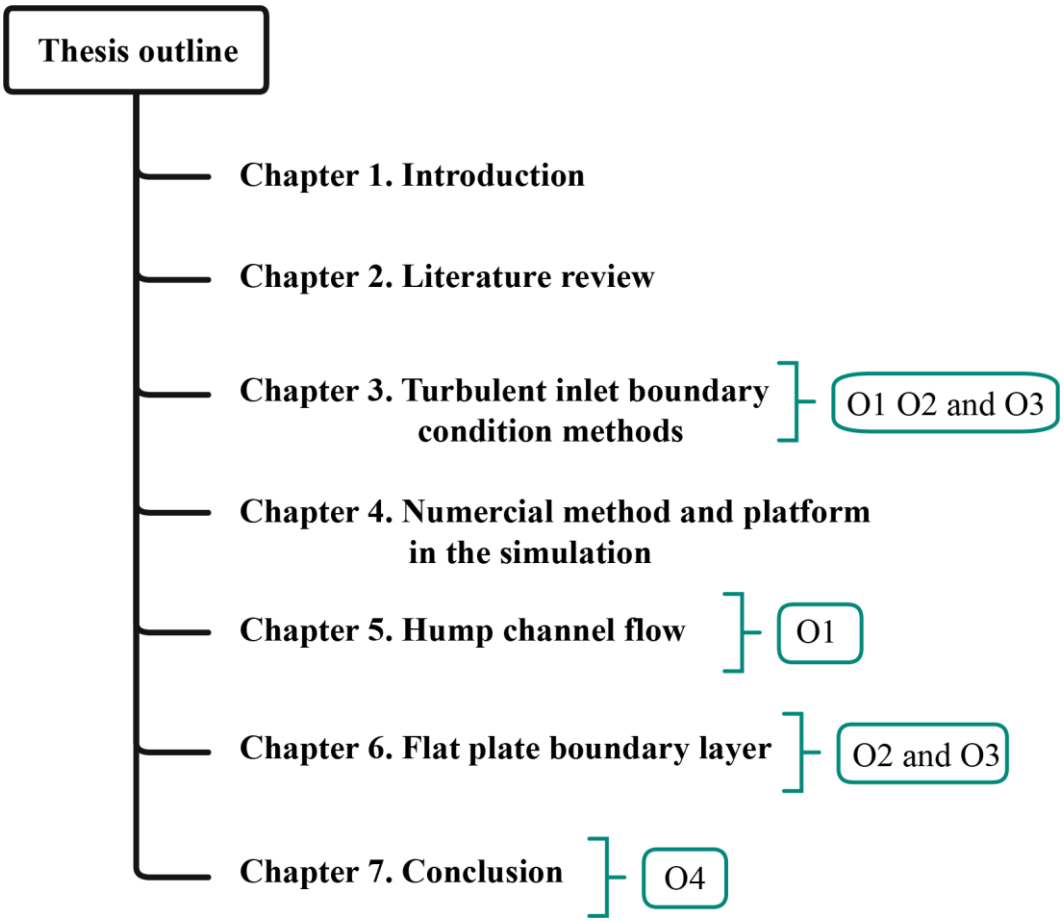


Figure 1.1 The tree diagram of the outline of the thesis in which objectives are covered

In Chapter 2, a detailed literature review of different inlet boundary condition methods is given. The history and development of each IBC method is elaborated. Additionally, the chapter explain the strengths and limitations of each inlet boundary condition method in detail, incorporating some typical results and conclusions of the previous work. At the end of this chapter, compared with the properties and the applications of different inlet boundary

conditions, the research gap is put forward that is corresponding to the aim of research written in the chapter 1.

In Chapter 3, the IBC methods used in this thesis are shown mathematically with schematic diagram and flow chart. In addition, the LES is elaborated including the filter size and the sub-grid scale models. At the end of this chapter, the simulation tool, OpenFOAM is introduced.

In Chapter 4, the governing equations are introduced. This chapter states the LES sub-grid scale models applied in the thesis. The OpenFOAM platform with some application details is elaborated in this chapter.

In Chapter 5, the cases with LES based on different IBC methods applied in the hump channel flow are introduced. There are three IBC methods applied in this chapter. The profiles of mean velocity and turbulent Reynolds stresses are investigated. In addition, the effects of the IBC methods on the flow separation are explored in this chapter. The objective 2 is covered in this chapter.

In Chapter 6, the cases with LES based on different IBC methods and the same IBC method with different input parameters are investigated in the flat plate boundary layer flow. Besides the profiles of the mean velocity and turbulent Reynolds stresses, the distribution of the power spectrum and the turbulent kinetic energy budget terms is considered and the objective 3 is covered in this chapter.

In Chapter 7, the conclusion of this thesis is given, which consists of the original research contribution and the further steps of the research. Besides, the objective 4 is covered in this chapter.

Chapter 2

Literature review

2.1. Precursor Methods

The most straightforward method is to simulate the natural transition, starting from the laminar velocity profile with superimposed random fluctuations, as was examined by Rai and Moin (1993) and also used in a recent direct numerical simulation (DNS) of turbulent boundary layer by Wu and Moin (2009).This method seems to be ideal, however, high computational cost is required due to the requirement of a sufficiently long computational domain for laminar-turbulent transition. There is another method that is direct and natural to generate inflow turbulence named Wind Tunnel Replication Method (WTRM). It contains the driving domain of passive simulation devices such as roughness elements and spires. The WTRM generates turbulence in the same way as the traditional natural transition method. The numerical simulation results can agree well with the wind tunnel test results. However, the method requires fine computational grids to generate a fully developed boundary layer (Ji et al., 2022).

There is another popular method using an auxiliary turbulence simulation with a periodic computational domain. Spalart (1988) proposed a multiple-scale procedure to approximate the local effects of the streamwise growth of the flow (e.g., boundary layer thickness and momentum thickness). The method transforms the system of equations into a self-similar coordinate frame, where the flow was periodic. From the streamwise periodicity, Spalart performed DNS of flat-plate boundary layers providing valuable data at Re_θ up to 1410. However, there are some disadvantages in this method. Firstly, it needs to evaluate the growth terms (Spalart, 1988) that are numerous and complicated in form. Besides, the similarity does not always occur, the modification was made by adding the fringe region downstream of the physical domain where the boundary layer thickness is decreased and re-introduced as the

inflow. The key assumption is that the nonphysical phenomena occurring in the fringe region do not invalidate the solution in the other.

To consider the spatial development in the periodic driver domain, Lund et al. (1998) proposed a rescaling and recycling approach to generate the instantaneous velocity, which is illustrated in the Chapter 3. The velocity fluctuation is based on the law of the wall, which is the development of the Spalart method (1988). Here, the growth-terms are eliminated and substituted by a simpler and flexible rescaling technique. The inflow velocity is generated in a first simulation and used on the second one. The inflow condition is generated by rescaling the instantaneous velocity data of a downstream recycling plane, which are then reintroduced at the inlet. It rescales the inner and outer layers of the velocity profiles separately to account for the different similarity laws observed. This method has been successfully used in LES on a spatially developing boundary layer of $Re_\theta = 1530$ to 2150. The development of turbulent boundary layer is successfully reproduced by this process. However, there are still some problems in this method, Liu and Pletcher (2006) addressed that the rescaling method is difficult to rapidly generate correct downstream turbulence to use for recycling if the initial inflow conditions are not accurate. A dynamic procedure was proposed where the recycling plane was initially placed close to the inlet and then it moves downstream gradually until becomes equilibrium in their study. Araya et al. (2011) put forward an alternative dynamic approach using three planes and modified scaling scales. There are several studies where precursor methods were successfully employed and evaluated (Khosronejad et al., 2020; Kanchi et al., 2013; Mukha and Liefvendahl, 2017). These two dynamic methods shorten the adjustment length, however, there are two major drawbacks in these methods, the first one is its additional computational cost. The second one, more crucial, is the spurious periodicity issue arising from the streamwise periodicity in the precursor simulation as discussed by Wu (2016).

2.2. Synthetic turbulence generation methods

There is another option often named synthetic turbulent inflow generator to generate the inflow turbulence by imposing artificial fluctuations to the mean velocity profile of the turbulent flow (Smirnov et al., 2001). As discussed by Keating et al. (2004), the inflow velocity vector is a function of time and two spatial directions, with given first and second moments, an assigned spectrum and the appropriate phase information between modes. It is possible to match the moments and the spectra using stochastic methods, while the specification of the phase information is more difficult since it relates to the structure and shape of the turbulent eddies that are strongly dependent on the type of the flow (mixing layer vs boundary layer) and the location in the flow (quasi-streamwise vortices are present near a wall while horseshoes vortices and arches farther away). Despite the structural information, inflow conditions cannot be regarded as accurate, and the flow must undergo an adjustment that the turbulent eddies are generated and evolve until the correct phase information is established. the synthesized velocity fluctuations should have the similar spectral contents as those of actual turbulent flows for purpose of the maintain of turbulence. Several attempts have been made to generate random fluctuations having spatial and temporal correlations. The spectrum of the wind velocity fluctuations is used to build a trigonometric series with Gaussian random coefficients. However, the spatial correlations are hard to control since the field cannot be generated independently at each point (Kondo et al., 1997).

In the work proposed by Kraichnan, several harmonics with random amplitude vectors are used to reproduce the spectrum at a given wavenumber (Kraichnan, 1970). This approach named random flow generators (RFG) is well adapted for the generation of isotropic turbulence. The approach was subsequently applied by Drummond et al. (1984) and Maxey (1987) in their passive particle studies. Smirnov et al. (2001) proposed a rescaling procedure on basis of Kraichnan RFG to generate anisotropic turbulence. However, the method is not capable of

providing full control over the synthesized spectra. Huang et al. (2010) modified this process, then revised by Castro and Rodrigo to synthesize random fluctuating fields characterized by arbitrary prescribed spectra for each velocity component (Castro et al., 2011). It has been remarked that the DSRFG technique shows some coherency and spectra discrepancies compared with the target flow statistics, for purpose of enhancing the ability of DSRFG, a consistent discrete RFG (CDRFG) is proposed by Aboshosha et al (2015). However, this method is not capable of fully controlling integral length scales when anisotropic turbulence is considered. To guarantee the method can synthesize solenoidal fields by arbitrary spectra and preserve the proportionality between space and time scales, the prescribed RFG method (PRFG) is presented (Patruno and Ricci, 2017). Through the analysis of the experimental conclusions, it is found that compared with the CDRFG method, the PRFG method ensures the divergence-free flow field. Nevertheless, a shortcoming of PRFG is that turbulent structures generated by this method have non-physical restraint, which makes this technique strongly dependent on the application. Yu et al. (2018) proposes an improved inflow turbulence generator for LES, the narrowband synthesis random flow generator (NSRFG). This approach yields a more concise expression that could strictly maintain a divergence-free condition, coherency function, and the turbulent spectra of the atmospheric boundary layer flow theoretically.

The inhomogeneous non-solenoidal synthetic turbulence generation method called turbulent spots method (TSM) is proposed, in which turbulence is simulated by a series of stochastically distributed vortex structures (Kornev and Hassel, 2003). The Synthetic Eddies Method (SEM) proposed by Jarrin is theoretically identified to the TSM (Jarrin et al., 2006). This approach applies a three-dimensional correlation of fluctuations with a pre-defined shape function. Pamis et al (Pamiès et al., 2009) improved the original SEM by incorporating a new definition of the eddy shape-function that is more detailed. However, the approach is case-dependent even if the benefits are clear. In addition, one common shortcoming of these

schemes is that velocity fields they generate are not divergence-free. If the velocity field at the inlet is not divergence-free, a large pressure fluctuation will occur with rapid velocity changes. Poletto et al (2013) proposed a divergence-free SEM (DFSEM) that can generate divergence-free velocity field at the inlet and reproduce almost all possible states of Reynolds stress anisotropy. While, the turbulence velocity field simulated with SEM and DFSEM can hardly meet the spectrum of velocity fluctuation, Luo et al. (2017) proposed a developed method named multi-scale SEM (MSSEM). This method introduces multi-scale eddies with spectrum energies on different frequency ranges and then synthesize eddies with different scales and energy to match the target spectrum. Nevertheless, in nearly all different advanced SEMs, the Reynolds stresses are determined by incorporating primary fluctuations with a unit amplitude and applying a Lund transformation (Lund et al., 1998). The continuity of the primary field is destroyed, and length scales are modified after the Lund transformation. Hannes et al (Kröger and Kornev, 2018) proposed a method that focuses on fulfilment of the continuity constraint by preserving arbitrary anisotropy form in the Reynolds stresses without the Lund transform. Davidson et al. (2022) proposed a methodology to integrate the synthetic turbulent generator based on the SEM into the lattice Boltzmann framework.

Druault et al. (2004) and Perret et al. (2008) reconstructed inflow turbulence from measured experimental data using proper orthogonal decomposition and linear stochastic estimation. The method takes advantage of the good temporal resolution of hot-wire measurements. However, it suffers from a low spatial resolution due to the limited number of probes that can be implemented simultaneously. The first POD modes representing the large-scale organization of the flow but is still unphysical and it needs an adaption region. The developed PODFS (proper orthogonal decomposition Fourier series) method uses POD to compress the large set into a handful of modes that are optimally chosen to represent the high energy turbulent structures while a Fourier series representation of the temporal components

of the POD modes means that the data becomes continuous, periodic and flexible in terms of time step (Treleaven et al., 2020). But this method can only compress and interpolate the data generated by the digital filter process rather than extrapolate it. It means that the PODFS could only generate the turbulent inlet in a specific time series and it is hard to change the time series.

Klein et al. (2003), diMare et al. (2006), and Hepffner et al. (2011) used digital filter method (DFM) to generate correlated field out of random noise. The technique takes a Gaussian form correlation function and a three-dimensional digital. Xie and Castro et al. (2008) developed the DFM on basis of the Klein's work, the modified method allows spatially varying turbulence scales on non-uniform grids to be imposed on the inlet based on exponential velocity correlation functions and this method is capable of generating the spatially correlated two-dimensional slices of data with two-dimensional filter. While divergence-free velocity field cannot be generated by this method. As the above instrument concludes, a large pressure fluctuation occurs due to this condition. A divergence-free inflow generation method based on DFM is proposed by Kim et al. (2013) to overcome this shortcoming. However, the DFM allows for specification of length scales in all spatial direction for all velocity components (Allegrini and Carmeliet, 2017). There is no formal rule of determination of turbulent length scales on the generated turbulence. Zhong et al (2019) and Xie et al (2008) investigates that the numerical results are not significantly sensitive in a certain range of the 0.6-1.4 of the streamwise integral length scale. To reproduce the desired turbulent statistics at the downstream location of interest, Giacomo proposed a modified DFM incorporating a gradient-based optimization procedure (Lamberti et al., 2018a). Mansouri et al (2022) investigated the performance of different synthetic turbulence generator methods in wind engineering applications. They found that the SEM with Gaussian shape function is a suitable method for peak pressure prediction with upmost 30% error.

Recently, it was reported that the unsupervised learning of turbulence generation is feasible. The generated data can be statistically the same as the training data without the initial input field. The generative adversarial network (GAN) proposed by Goodfellow et al (Mahdizadehaghdam et al., 2019) as an unsupervised learning method that have been improved steadily (Karras et al., 2018; Karras et al., 2021; Roth et al., 2017; Benedicto et al., 2014; Radford et al., 2016). The advanced machine learning inflow turbulence generator combines the unsupervised learning method GAN with a recurrent neural network (RNN) to generate the time-varying fully developed flow at various Reynolds numbers. However, the DNS data of a fully developed turbulent flow is required for training, besides, the generator could not generate a statistically perfect field at a Reynolds number beyond the trained one. Therefore, this method cannot be extensively used due to these limitations (Kim and Lee, 2020).

Although these different kinds of inflow generation methods have undertaken a great development independently. There are still many limitations in these approaches. In precursor methods, two major drawbacks exist. The first one is its additional computational cost. The second one, more crucial, is the spurious periodicity issue arising from the streamwise periodicity in the precursor simulation as discussed by Wu (2016). For the synthetic turbulence methods, turbulent structures generated by the PRFG method have non-physical restraint, which makes this technique strongly dependent on the application (Patruno and Ricci, 2017). The POD based method suffers from a low spatial resolution due to the limited number of probes that can be implemented simultaneously. The first POD modes representing the large-scale organization of the flow but is still unphysical and it needs an adaption region. For the advanced DFM and SEM, it needs external input parameters such as turbulent integral length scale. This parameter is hard to obtain generally, Taylor's hypothesis is used by Giacomo (Lamberti et al., 2018a) to compute the streamwise integral length scales due to the

insufficiency of the resolution of the hot-wire measurements. Additionally, they give an approximation of the vertical and spanwise length scales based on the streamwise length scales.

2.3. Research gap

According to the previous statements, there is not a 'perfect' method within LES to generate the inflow turbulence in different cases. For the complex flow regime represented by the NASA wall-mounted hump geometry, i.e. hump channel flow, there are many researches applied this case as the research objective to investigate the flow separation and reattachment. It is reported that flow separation and reattachment phenomena are accompanied by a substantial loss of energy, affecting the performance of the fluid machine, and severely limiting the design and operation of many of the fluid flow devices (Šarić et al., 2005). For this case, the effects of the domain span on the solutions are considered in the work of Uzun and Malik (2018). The effects of the SGS models on the simulation results are considered by You et al. (2006) and Mart ńez (2015). The wall model within LES in this case is investigated by I.Park (2015). The application of the detached eddies simulation (DES) in this case is discussed by Krishna et al. (2004). However, it is hard to find some work considering about the effects of the application of different IBC methods on the simulation results in this case. The work of Montorfano et al. (2013) investigated the influence of three IBCs on the LES results. Nonetheless, they merely quantitatively discussed the flow characteristics upstream the hump, the critically important part that is the flow separation after the hump is not analysed explicitly. In this thesis, different IBC methods are applied in the hump channel flow. The flow properties, such as mean velocity profiles, Reynolds stresses profiles, and pressure and friction coefficients distribution in the approach flow as well as the flow downstream especially in the separation region were calculated and quantitatively analysed to evaluate the effects of each turbulent IBC method.

Generally, the synthetic turbulence generator method can directly provide turbulent inlet conditions without additional domains, while the fluctuating velocity generated by computer program is different from the real turbulent inflow. The turbulence characteristics probably change during the development of flow (Ji et al., 2022). Therefore, it is important to shorten the development length that the flow is transformed from non-developed turbulent flow to fully-developed turbulent flow is important for synthetic turbulent methods.

For the simple flow regime represented by flow over a flat plate, there are many studies investigated the effect of different IBC methods on LES results (Aliabadi et al., 2018; Fröhlich et al., 2005; Lamberti et al., 2018b; Yang et al., 2020). Nevertheless, many studies as referred to previously have drawn a comparison of different IBC methods considering about mean velocity profiles and Reynolds stresses profiles of the simulation results, while there are less studies concentrating on the profiles of turbulent kinetic energy budget that is important to reflect the transportation of the turbulent kinetic energy (Blackman et al., 2017). Moreover, for DFM and DFSEM, there is no simple and reliable rule of determination of turbulent length scales on the generated turbulence when the values of turbulent length scales are hard to obtain (Allegrini and Carmeliet, 2017). Hence, these problems are exploited in this thesis. This work investigates the effect of using different IBCs in LES on the prediction of the flow over a flat plate of interest. Then, the determination of the input turbulent length scales is discussed. The flow properties such as mean velocity, Reynolds stresses and turbulent kinetic energy budget terms are calculated and then compared with the Direct Numerical Simulation (DNS) results (Philipp, 2011). The post-processing code is implemented in OpenFOAM, which is displayed in the appendix. The present work provides potential strategies for the implementation of IBC methods to predict the boundary layer over a flat plate, and can also be transposed to atmospheric Boundary Layer (ABL) flows, providing a valuable strategy to implement LES if chosen as simulation method (Vasaturo et al., 2018).

Chapter 3

Turbulent inlet boundary condition methods

3.1. The Lund method

Lund method is an approach to extract instantaneous velocity data at a fixed plane in an auxiliary simulation. The auxiliary simulation is spatially developing but generates its own inflow conditions through a sequence of operations where the velocity field at a downstream station is rescaled and re-introduced at the inlet. The rescaling factors are determined by the parameters of turbulent boundary layer thickness, displacement thickness and the momentum thickness at the beginning (Inoue, 2012). The velocity field with random noise is generated firstly, and the mean velocity profile is derived from the value of the displacement thickness (OpenFOAM-v2006, n.d.). To arrive at the rescaling procedure, the velocity is decomposed into a mean and fluctuating part and then applied the appropriate scaling laws to each component separately. The decomposition is achieved by defining the mean as an average in time. The velocity fluctuations are defined as:

$$u_i'(x,y,z,t) = u_i(x,y,z,t) - U_i(x,y) \tag{1}$$

The mean flow is rescaled according to the law of wall in the inner region and the defect law in the outer region. U_{recy} denotes the mean velocity at the downstream to be recycled and U_{inlt} denotes the mean velocity at the inlet. The law of wall and the defect law written above indicate that there is a relationship between U_{recy} and U_{inlt}, which can be expresses as:

$$U_{inlt}^{inner} = \gamma U_{recy}(y_{inlt}^{+}) \tag{2}$$

$$U_{\text{inlt}}^{\text{outer}} = \gamma U_{\text{recy}}(\eta_{\text{inlt}}) + (1-\gamma)U_{\infty} \tag{3}$$

where $\gamma = (u_{\tau,inlt}/u_{\tau,recy})$. The independent varaibles y^+_{inlt} and η_{inlt} are the inner and outer coordinates of the grid nodes at the inlet station. Therefore, $U_{recy}(y^+_{inlt})$ is the mean velocity at the recycle station, expressed as a function of y^+ and evaluated at the inner coordinate of the mesh at the inlet (Lund et al., 1998).

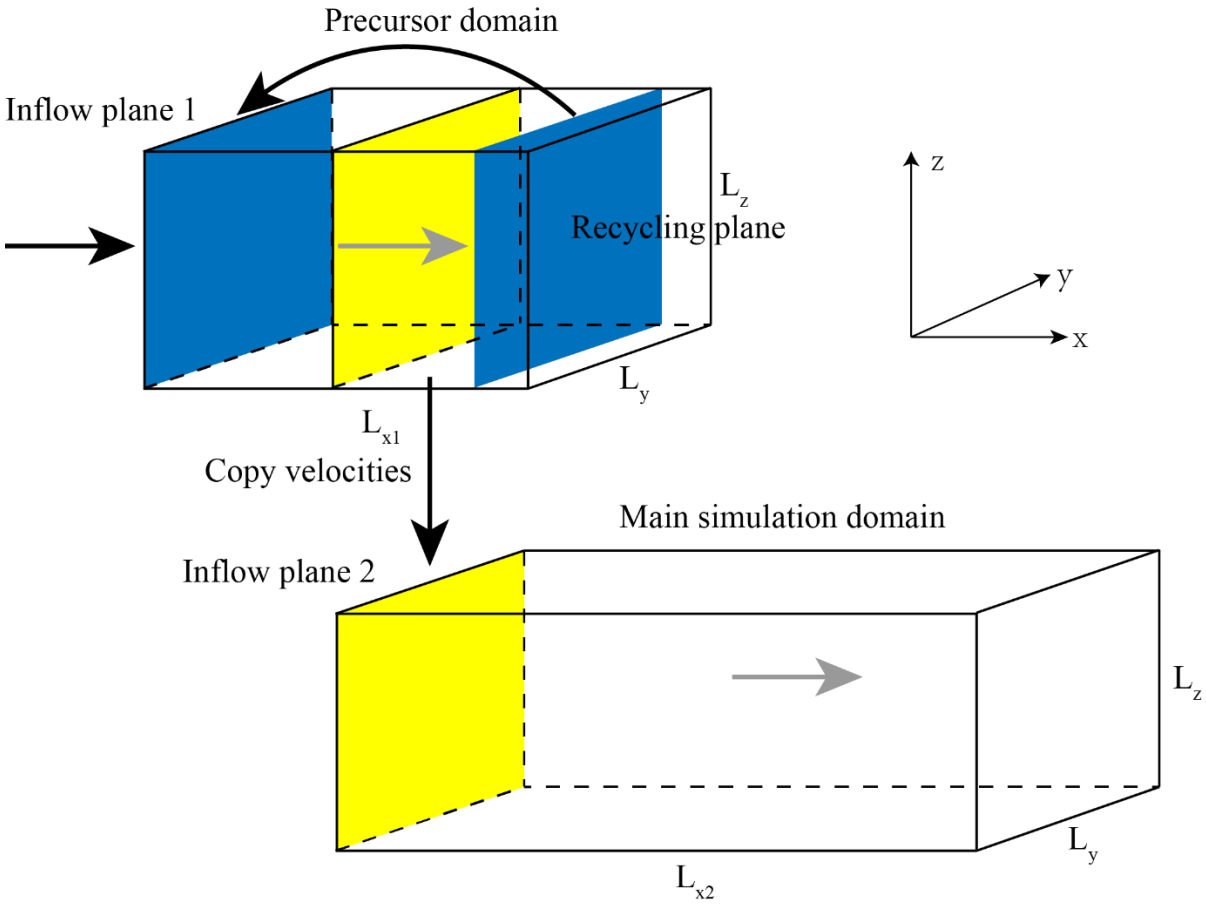


Figure 3.1 Simulation of the recycling and rescaling method

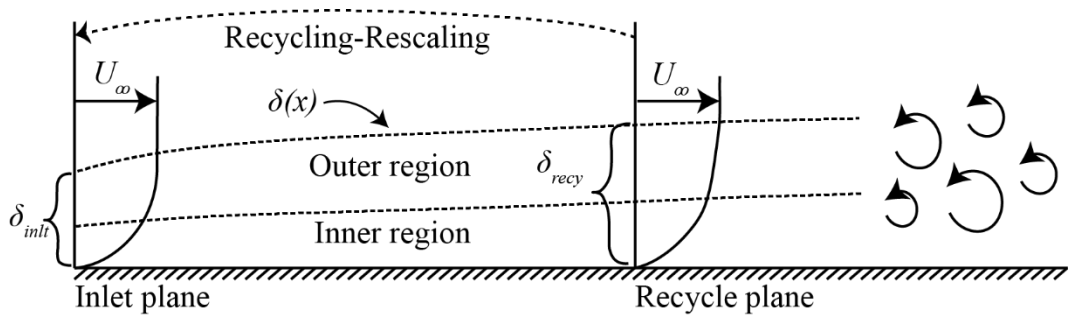


Figure 3.2 Simulation of the recycling and rescaling method

The mean vertical velocity in the inner and outer regions is expressed as:

For the inlet plane and the recycled plane, the mean velocity meets that

$$U_{inlt}^{inner}/U_{recy}^{inner}(y^+) = (U^\infty - U_{inlt}^{outer})/(U^\infty - U_{recy}^{outer}(\eta)) = u_\tau^{inlt}/u_\tau^{recy} = \gamma \tag{4}$$

and the fluctuating velocity is

$$(u_i')_{inlt}^{inner}/(u_i')_{recy}(y^+) = (u_i')_{inlt}^{outer}/(u_i')_{recy}(\eta) = u_\tau^{inlt}/u_\tau^{recy} = \gamma \tag{5}$$

where y^+ and η are defined at the inlet, and $y^+ = {u_\tau y}/{\upsilon}, \eta = {y}/{\delta}$, where δ is the boundary layer thickness determined at the inlet plane. The velocity profiles in the inner and the outer region can be combined with a weight function,

$$(u_i)_{inlt} = [(U_i)_{inlt}^{inner} + (u_i')_{inlt}^{inner}][1 - W(\eta)] + [(U_i)_{inlt}^{outer} + (u_i')_{inlt}^{outer}]W(\eta) \tag{6}$$

the weighting function $W(\eta)$ is defined as:

$$W(\eta) = \frac{1}{2}\{1 + tanh[\frac{\alpha(\eta - b)}{(1-2b)\eta + b}]/tanh(\alpha)\} \tag{7}$$

where $\alpha = 0.4$ and $b = 0.2$. For $\alpha \longrightarrow \infty$, $W(\eta)$ becomes a step function centred at $\eta = b$. As $\alpha \longrightarrow 0$, the transition is spread across the entire boundary layer. The values of α and b are determined from the analysis of the independent spatially evolving boundary layer. The rescaling operation requires the scaling parameters u_τ and δ at the recycle station at the inlet. There is a suitable relation where:

$$\frac{\mathrm{u}_\tau^{\mathrm{inlt}}}{\mathrm{u}_\tau^{recy}} = (\frac{\theta_{recy}}{\theta_{inlt}})^{1/[2(n-1)]} = \gamma \tag{8}$$

where θ_{inlt} is the momentum thickness at the inlet and θ_{recy} is the momentum thickness at the recycling plane.

The time average used to compute the mean velocity field is a simple running average when the flow is fully developed, but it should be modified to eliminate the starting transients if the solution is initialized with a crude guess. A convenient way to realize this process by using the equation,

$$U^{n+1} = \frac{\Delta t}{T}\langle u^{n+1}\rangle_z + (1 - \frac{\Delta t}{T})U^n \quad (9)$$

where Δt is the computational time step, T is the characteristic time scale of the averaging interval, and $\langle\rangle_z$ denotes an average in the spanwise direction. To eliminate the transients, the averaging interval should be modified 3 times. At the beginning, $T = 10\delta/U_\infty$. When the flow equilibrates, the averaging interval should be increased to $T = 100\delta/U_\infty$ to stabilize the statistics. After these two stages, the simple running average is used as $T = T_0 + t - t_0$, t_0 is the time when the running averaging was initiated, T_0 is the value of the averaging interval used prior to t_0 and t is the current time in the simulation.

3.2. The divergence-free synthetic eddies method (DFSEM)

The DFSEM is based on the methodology described in Jarrin (Jarrin et al., 2006), where synthetic eddies represent a series of velocity fluctuations that are transferred through a box that surrounds the inlet plane on which a turbulent velocity field is required. These eddies defined by their centres and a formulation for the velocity fluctuation distribution around it are convected at each time step by the locally imposed mean velocity. Once they have traversed and exited the box, they are regenerated at a random position on the inlet plane of the box. Generally, the steps of the DFSEM algorithm can be summarized by the flow chart:

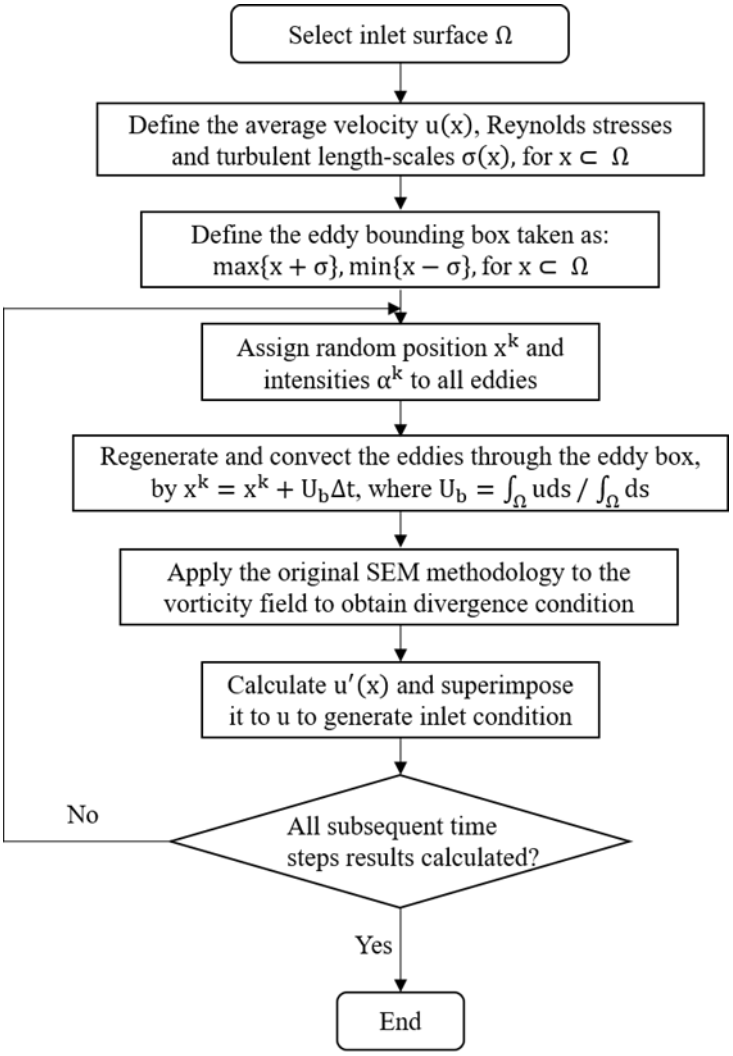


Figure 3.3 Flow chart of the application of Divergence Free Synthetic Eddies Method (Jarrin et al., 2006)

The following steps improved the original SEM by incorporating a divergence free fluctuating velocity field. The SEM proposed defines velocity fluctuations according to the following:

$$u'_x(x) = \frac{1}{\sqrt{N}} \sum_{k=1}^{N} a_{ij} \varepsilon_j^k f_\sigma^k \left(\frac{x - x^k}{\sigma^k} \right) \tag{10}$$

where N is the number of eddies introduced into the SEM domain; x^k is the location of the centre of the kth eddy; σ^k is the turbulence length-scale of eddies; $f_\sigma(x)$ is a suitable shape function; ε_j^k are random numbers with zero average and $\langle \varepsilon_j^k \varepsilon_j^k \rangle = 1$. a_{ij} represents the eddy intensities, and written as:

$$a_{ij} = \begin{bmatrix} \sqrt{R_{11}} & 0 & 0 \\ \frac{R_{21}}{a_{11}} & \sqrt{R_{22} - a_{21}^2} & 0 \\ \frac{R_{31}}{a_{11}} & \frac{R_{32} - a_{22}a_{31}}{a_{22}} & \sqrt{R_{33} - a_{31}^2 - a_{32}^2} \end{bmatrix} \tag{11}$$

R_{ij} are the elements of the Reynolds stress tensor. The amplitude tensor a_{ij} named Lund coefficients is proposed by Lund et al. (1998). This formulation allows any desired Reynolds stress field to be prescribed through the a_{ij} coefficients, the velocity field is hard to be divergence-free (Kornev and Hassel, 2003).

There is an approach to get a divergence-free field by imposing the original SEM method on the vorticity field, then the velocity field can be obtained by taking the curl of the vorticity field as following:

$$\nabla \times \omega' = \nabla\left(\nabla \cdot u^{'}\right) - \nabla^2 u^{'} \tag{12}$$

According to the continuity equation of impressible flow, the first term on the right-hand side equals zero, this equation can be regarded as a Poisson equation for the velocity. The Biot-Savart kernel is used to deal with this equation, the fluctuating velocity field can be expressed as:

$$u_i'(x) = \sqrt{\frac{1}{N}} \sum_{k=1}^{N} \frac{q_\sigma\left(\left|r_j^k\right|\right)}{\left|r_j^k\right|^3} \varepsilon_{ijl} r_j^k \alpha_l^k \tag{13}$$

where $r_j^k = \frac{x_j - x_j^k}{\sigma_j^k}$, $q_\sigma\left(\left|r_j^k\right|\right)$ is a suitable shape function and α_l^k are random numbers with zero average which represents the eddy intensities.

It is worth noticing the similarities between (10) and (13). A random level eddy intensity and a user defined shape function and are incorporated by these equations. However, the Lund coefficients are not observed in the equation (13). According to the previous analysis, the Lund coefficients are crucial to reconstruct the given turbulence state. Nevertheless, they are hardly re-introduced if the divergence free condition is not satisfied. To obtain a physical artificial

turbulent velocity field at the inlet, it is critical to increase the turbulence anisotropy reproduction capabilities. However, the implementation results in the equation hardly satisfies the divergence-free condition, therefore more constraints need to be considered on the shape functions. There is a convenient way to redefine the shape functions as the form $q_\sigma = q_i\left|r_j^k\right|^3$ where q_i is a function dependent upon the positions x_j, x_j^k and r_j^k and it considers the length-scale anisotropy. The updated velocity fluctuations can be expressed by:

$$u_i'(x) = \sqrt{\frac{1}{N}}\sum_{k=1}^{N} q_i\left(x_j, x_j^k, \sigma_i^k\right)\varepsilon_{ijl}r_j^k\alpha_l^k \tag{14}$$

Equation (13) can be rewritten as (14) by using the index notation, where $\varepsilon_{\beta jl}$ means Levi-Civita symbol. The redefined shape functions cannot automatically satisfy the divergence-free condition. To ensure a divergence-free condition, the velocity is substituted into the condition that $\nabla \cdot u' = 0$.

$$r_2^k\frac{\partial q_1}{\partial x_1} = r_1^k\frac{\partial q_2}{\partial x_2}, \quad r_3^k\frac{\partial q_2}{\partial x_2} = r_2^k\frac{\partial q_3}{\partial x_3}, \quad r_3^k\frac{\partial q_1}{\partial x_1} = r_1^k\frac{\partial q_3}{\partial x_3} \tag{15}$$

There is a simple analytical function that can satisfy the conditions for q_i:

$$q_i = \begin{cases} \sigma_i^k[1-(d^k)^2], & \text{if } d^k < 1 \\ 0, & \text{elsewhere} \end{cases} \tag{16}$$

where $d^k = \sqrt{\left(r_j^k\right)^2}$

The above formulation satisfies divergence-free at the eddy surface and the formal omission cannot result in serious problems. After the Substitution of the shape function into (14), the fluctuating velocity can be written as:

$$u_i'(x) = \sqrt{\frac{1}{N}}\sum_{k=1}^{N} \sigma_i^k[1-(d^k)^2]\varepsilon_{ijl}r_j^k\alpha_l^k \tag{17}$$

Time-averaging the product of equation (17) represents the Reynolds stresses:

$$\langle u'_\beta u'_\gamma \rangle = \frac{1}{N}\sum_{k=1}^{N} \sigma_\beta^k \sigma_\gamma^k \varepsilon_{\beta jl}\varepsilon_{\gamma mn}\langle\{[1-(d^k)^2]^2 r_j^k r_m^k\}\rangle\langle(\alpha_l^k)(\alpha_n^k) \tag{18}$$

It is obvious that the eddies are independent due to their uncorrelated intensities ($so\ \langle \alpha_l^k \alpha_m^k \rangle = 0$ for $l \neq m$); the predicted shear stresses ($\langle u'_\beta u'_\gamma \rangle$ for $\beta \neq \gamma$) will be zero. To resolve this problem, fluctuations in the global coordinate system are computed by a standard rotation transformation of the eddies:

$$u_i'^G(x) = C_1 R_{im}^{P\to G} u_m'^P \tag{19}$$

In equation (19), $R_{im}^{P\to G}$ is the rotation transformation matrix, $u_m'^P$ and $u_i'^G$ are the velocity fluctuations in the principal axis and global systems respectively. C_1 is a normalization coefficient used to determine $\langle u_i'^2 \rangle = 1$ when $\left\langle \left(\alpha_l^k\right)^2 \right\rangle = 1$:

$$C_1 = \frac{\sqrt{10V_0}\sum_{i=1}^{3}\frac{\sigma_i}{3}}{\sqrt{N}\prod_{i=1}^{3}\sigma_i} min\{\sigma_i\} \tag{20}$$

V_0 is the eddy box volume. For the normal stresses, the contribution of the kth eddy presents:

$$\langle u'_\beta u'_\beta \rangle = 2C_2\sigma_\beta^2 \varepsilon_{\beta ln}\left\langle \left(\alpha_l^k\right)^2 \right\rangle \langle (\alpha_n^k)^2 \rangle \tag{21}$$

The terms not reported in equation (21) are written as C_2. The remaining problem is to use appropriate length-scales and eddy intensities to ensure the desired Reynolds stress statistics can be reproduced. For different length-scale ratios (σ_x/σ_y and σ_x/σ_z), the change of the intensity α_l^k results in possible turbulence anisotropy values distributed over a particular region of the Lumley triangle. The length-scale ratios is defined by $\Gamma = \frac{\sigma_x}{\sigma_y} = \frac{\sigma_x}{\sigma_z}$ and each ratio allows one of the regions of the triangle mapped. For any Γ, the Reynolds stresses are reproduced by the following equation:

$$\langle \left(\alpha_\beta^k\right)^2 \rangle = \frac{\lambda_j/\sigma_j^2 - 2\lambda_\beta/\sigma_\beta^2}{2C_2} \tag{22}$$

In equation (22), λ_j represent the normal streses in the principal reference system. Besides, equation (22) must be positive for any value of Γ.

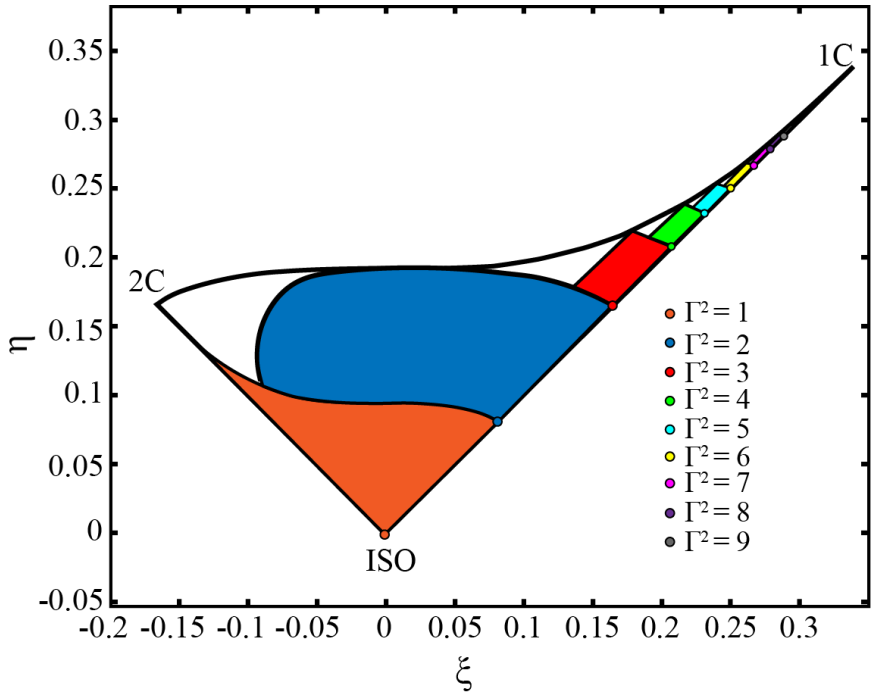


Figure 3.4 Lumley triangle on the plane of the invariants ξ and η of the Reynolds stress anisotropy tensor. The triangle is mapped with the DFSEM where $6\eta^2 = b_{ii}^2, 6\xi^3 = b_{ii}^3$ and $b_{ij} = \frac{\langle u_i' u_i' \rangle}{\langle u_k' u_k' \rangle} - \frac{1}{3}\delta_{ij}$, the mapped region can be referred to the research of Poletto. et al. (2013)

The mapped regions determined by the Γ are displayed in Figure 3.4. When different values of Γ are chosen in the Table 3-1, nearly the whole Lumley triangle can be covered.

Table 3-1 Constant C_2 values in this work accoring to the research of Poletto. et al. (2013)

Γ^2	1	$\sqrt{2}$	$\sqrt{3}$	$\sqrt{4}$	$\sqrt{5}$	$\sqrt{6}$	$\sqrt{7}$	$\sqrt{8}$
C_2	2	1.875	1.737	1.75	0.91	0.825	0.806	1.5

3.1. The digital filter method (DFM)

The digital filter method was proposed by Klein et al (2003), they applied a filter to random Gaussian white noise. Then velocity field with prescribed autocorrelations is generated. At each time step of the simulation, the random velocity signal is filtered on a 2D slice. Then the filtered fluctuating velocity data is superimposed with the desired mean velocity profile and applied to the inlet boundary (Immer, 2016).

The filtered instantaneous velocity is generated according to the equation (23)

$$u_m = \sum_{j=-N}^{N} b_k r_{m+k} \tag{23}$$

where r_m is a series of random signal with $\overline{r_m} = 0, \overline{r_m r_m} = 1$, the b_j are the filter coefficients and N is related to the length scale of the filter. The mean value of u_m satisfies $\overline{u_m} = 0$, due to $\overline{r_m r_n} = 0$ for $m \neq n$, The relationship between the fluctuating velocity and the filter is obtained:

$$\overline{u_m u_{m+k}} = \sum_{k=-N+j}^{N} b_k b_{k-j} \tag{24}$$

For any correlation function $\overline{u_m u_{m+k}}$, it is not simple to solve this equation directly. However, if the correlation function has the similar form of a Gaussian or an exponential function, it will be accessible to obtain an approximate solution. The correlation functions for a fully developed turbulent flow in the gap between two counter-rotating disks with $Re_\lambda = 740$ are closer to exponential than Gaussian (Mordant et al., 2001). The correlation function can be written as:

$$R(r, 0,0) = exp\left(-\frac{\pi r}{2L}\right) \tag{25}$$

where L represents the length scale. Based on this correlation function, the exponential correlation function is used to design a filter and applied on random data. For one dimensional data, with $L = n\Delta x$, Δx is the grid size, the correlation function is written as:

$$\frac{\overline{u_m u_{m+k}}}{\overline{u_m u_m}} = R_{uu}(k\Delta x) = exp\left(-\frac{\pi|k|}{2n}\right) \tag{26}$$

According to the correlation function, the filter coefficient b_k is guessed as:

$$b_k = exp(-\frac{\xi\pi|k|}{n})/\zeta \tag{27}$$

where ξ is a normalizing factor and it can constraint $\overline{u_m u_m} = 1$. The b_k is then re-written to satisfy $\overline{u_m u_m} = 1$,

$$b_k = \widetilde{b_k} / \left(\sum_{j=-N}^{N} \widetilde{b_j^2} \right)^{1/2} \tag{28}$$

where

$$\widetilde{b_k} = exp\left(-\frac{\xi \pi |k|}{n} \right) \tag{29}$$

To obtain a suitable value of ξ, the following expression should be minimised,

$$\sigma \left[\sum_{j=-N+k}^{N} b_j b_{j-k} / \left(\sum_{j=-N}^{N} \widetilde{b_j^2} \right) - exp\left(-\frac{\pi |k|}{2n} \right) \right] \text{for } N \geq 2n \text{ and } n = 2, \ldots, 20 \tag{30}$$

σ is the standard deviation of the terms in the square brackets. It could be found that $\xi \approx 1.14$ obtained a minimum σ. Dataset with mean value $\overline{u_m} = 0$, $\overline{u_m u_m} = 1$ and prescribed length scale L is obtained after this process. A two-dimensional filter is obtained as: $b_{jk} = b_j b_k$. The filter is applied in a two-dimensional slice of random data of dimensions $[-N_y + 1 : M_y + N_y, -N_z + 1 : M_z + N_z]$, where $M_y \times M_z$ are the dimensions of the grid in the inflow plane, $N_\alpha \geq 2n_\alpha, \alpha = y, z$. At the first-time step, a two-dimensional slice of data $\Psi_\beta(t, y, z), \beta = 1,2,3$ with prescribed length scale $L_\alpha = n_\alpha \Delta\alpha$ is obtained. Constant length scales are used as input parameters at the inlet. For the next time step,

$$\Psi_\beta(t + \Delta t, y, z) = \Psi_\beta(t, y, z) exp(-\frac{\pi \Delta t}{2T}) + \psi_\beta(t, y, z)[1 - exp(-\frac{\pi \Delta t}{T})]^{0.5} \tag{31}$$

where $\psi_\beta(t, y, z)$ is obtained in the same way as $\Psi_\beta(t, y, z)$ but a new set of random data is used. T is the Lagrangian time scale, calculated from measurements or previously computed data. $\psi_\beta(t, y, z)$ is fully random in time and the variance of it is unity. In the final step, the transformation proposed by Lund (1998) is simplified and performed as:

$$u_i = \overline{u_\iota} + a_{ij} \Psi_j \tag{32}$$

The term a_{ij} is prescribed by the Reynolds stress tensor at the inlet, and it has the same form as the equation (11). The Reynolds stresses tensor applied here generally obtained from a

previous numerical simulation with periodic inlet-outlet condition or experimental data. For a boundary layer flow, a_{31}, a_{32} vanish due to the homogeneity in the spanwise direction. According to the description, it is assumed that a uniform mesh is required at the inlet. However, the digital filter process can also work in a non-uniform mesh. There is a simple approach to implement the digital filter method for a non-uniform mesh. At the beginning, a duplicate of the inlet is discretized and imported into a uniform mesh. Then, the filter process is performed in the mesh to obtain three velocity components. After these two steps, the velocity components of the uniform mesh are interpolated onto the non-uniform mesh at the inlet.

3.2. The random method (RAND)

In the end of this chapter, the most straightforward method named random method (RAND) is introduced. The method generates the random noise on basis of the mean velocity,

$$u_i^n = (1 - \alpha_R)u_i^{n-1} + \alpha_R(U + sRU) \tag{33}$$

In Equation (33), u_i^n is the current instantaneous velocity, and u_i^{n-1} is the previous instantaneous velocity. U is spatial and temporal average velocity. R is the random value subject to standard normal distribution. α_R is the weighting average factor and s is the fluctuation scale (OpenFOAM-v2006, n.d.). The application of this method is fully discussed in the Chapter 5.

Chapter 4
Numerical method and platform in the simulation

4.1. Governing Equations

For the flat plate turbulent boundary layer and the turbulent flow in the atmospheric boundary layer, the flow velocity is much less than the speed of sound (Elghorab and Ahmed, 2020). In the flow field, the density does not change significantly, so the flat plate turbulent boundary layer and the turbulent flow within the atmospheric boundary layer can be viewed as an incompressible fluid. The continuity equation and the momentum equation can be written as:

$$\frac{\partial u_i}{\partial x_i} = 0$$
$$\frac{\partial u_i}{\partial t} + \frac{\partial}{\partial x_j}(u_i u_j) = -\frac{1}{\rho}\frac{\partial p}{\partial x_i} + v\frac{\partial^2 u_i}{\partial x_j \partial x_j} \tag{34}$$

In equation (34), ρ is the fluid density, v is the kinematic viscosity, p is the pressure and u_i is the velocity component along each direction. This equation can also be named as the N-S equation (Leonard, 1975). The equation can only obtain a relatively accurate theoretical solution under some simple flow field conditions. For most of the turbulent motion, the numerical methods are used to solve the governing equations of the fluid. According to the previous analysis, the LES is adopted.

The basic equations for LES were first proposed by Smagorinsky (1963). On basis of the theory of Kolmogorov, the smallest scales of motion are uniform and could be approximated and represented by a model. The large scales of motion, which contain most of the energy, are calculated directly. To separate the large scales of motion from the small, the filter is used. By applying a filter kernel through a convolution, the filtered velocity field is obtained. When the filter is imposed on the equation (34), the filtered incompressible governing equations are shown as:

$$\frac{\partial \bar{u}_i}{\partial t} + \frac{\partial}{\partial x_j}\left(\overline{u}_i \overline{u}_j\right) = -\frac{1}{\rho}\frac{\partial \bar{p}}{\partial x_i} + v\frac{\partial^2 \bar{u}_i}{\partial x_j\, \partial x_j} - \frac{\partial \tau_{ij}}{\partial x_j} \tag{35}$$

$$\frac{\partial \bar{u}_i}{\partial x_i} = 0 \tag{36}$$

in equation (35) and (36), $\bar{*}$ represents the spatial filter, which decomposes physical quantities into the resolved scale components and the sub-grid scale components. The tensor

$$\tau_{ij} = \overline{u_i u_j} - \bar{u}_i \bar{u}_j \tag{37}$$

is the residual stress tensor or the sub-grid stress (SGS) tensor. The SGS tensor arises through the filtering of the convection term $\partial\left(u_i u_j\right)/\partial x_j$. The residual stress poses a closure-problem and has to be modelled by an appropriate sub-grid model. A commonly used class of SGS models are based on the eddy viscosity hypothesis, where the residual stress tensor is related to the resolved strain rate tensor S_{ij} through the sub-grid viscosity ν_{sgs}.

$$\tau_{ij} - \frac{1}{3}\delta_{ij}\tau_{kk} = -\nu_{sgs}\left(\frac{\partial \bar{u}_i}{\partial x_j} + \frac{\partial \bar{u}_j}{\partial x_i}\right) = -2\nu_{sgs}\overline{S}_{ij} \tag{38}$$

where, δ_{ij} is the Kronecker function, when $i = j, \delta_{ij} = 1$, when $i = j, \delta_{ij} = 0$. $\bar{S}_{ij}$ is the filtered strain rate tensor, i.e., the resolved strain rate, where $\overline{S}_{ij} = 1/2(\partial\overline{u}_i/\partial x_j + \partial\overline{u}_j/\partial x_i)$,$\bar{S} = \left(2\overline{S}_{ij}\overline{S}_{ij}\right)^{1/2}$. The values for ν_{sgs} can be algebraically computed as with the Smagorinsky model, which can be represented as:

$$\nu_{sgs} = (C_s \Delta)^2 \sqrt{2\bar{S}_{ij}\, \bar{S}_{ij}} \tag{39}$$

where C_S is the Smagorinsky constant, the range of C_S generally is 0.1~0.2 and Δ is filter width which is related to the size of the mesh cell (Lilly, 1992; Sagaut, 2006). This model is stable and robust because it yields enough diffusion and dissipation to the numerical computations. However, there is a problem in the Smagorsinsky model that the appropriate value of the coefficient C_s is different for different flow regimes. In general, the value is zero in laminar flow, and the value decreases in the near wall region compared with that ($C_s \approx 0.15$) in high-

Reynolds-number free turbulent flows. The Dynamic model provides a methodology for determining an appropriate local value of the Smagorinsky coefficient. Both of two models are used as the SGS models in the present study. The value of C_s is redefined and determined by the dynamic procedure proposed by Germano et al. (1992) . Where L_{ij} is the resolved Lenard stress tensor and T_{ij} is the SGS stress at a test filter scale $\tilde{\Delta}$ (typically $\tilde{\Delta}= 2\Delta$). As stated above, Δ is the grid scale, which equals $(\Delta_1\Delta_2\Delta_3)^{1/3}$ (Kim and Menon, 1995). The residual stresses based on the double-filtering operations are defined by

$$T_{ij} = \widetilde{\overline{u_i}\overline{u_j}} - \tilde{\overline{u}}_i\tilde{\overline{u}}_j \tag{40}$$

The model is based on the Germano identity:

$$L_{ij} = T_{ij} - \widetilde{\tau_{ij}} = \widetilde{\overline{u_i}\overline{u_j}} - \tilde{\overline{u}}_i\tilde{\overline{u}}_j \tag{41}$$

The Smagorinsky model (equation (38) and equation (39)) for the deviatoric part of τ_{ij}^d, can be written as:

$$\tau_{ij}^d = \tau_{ij} - \frac{1}{3}\delta_{ij}\tau_{kk} = -2c_s\overline{\Delta}^2\overline{S}\,\overline{S_{ij}} \tag{42}$$

The coefficient has been redefined by c_s (where $c_s = {C_S}^2$) to allow for the possibility of negative values (S. Pope, 2001). The same model equation written for the filter of width $\tilde{\overline{\Delta}}$ is:

$$T_{ij}^d = T_{ij} - \frac{1}{3}\delta_{ij}T_{kk} = -2c_s\tilde{\overline{\Delta}}^2\tilde{\overline{S}}\,\widetilde{\overline{S_{ij}}} \tag{43}$$

Take c_s to be the uniform and define:

$$M_{ij} = 2\overline{\Delta}^2\widetilde{\overline{S}\overline{S}_{ij}} - 2\tilde{\overline{\Delta}}^2\tilde{\overline{S}}\,\widetilde{\overline{S}_{ij}} \tag{44}$$

Equations (42) and (43) lead to the Smagorinksy model for the deviatoric part of L_{ij} that is expressed by L_{ij}^s:

$$L_{ij}^s = T_{ij}^d - \widetilde{\tau_{ij}^d} = -2c_sM_{ij} \tag{45}$$

$$L_{ij}^d = L_{ij} - \frac{1}{3}\delta_{ij}L_{kk} \tag{46}$$

The mean-square error between the deviatoric stress L_{ij}^d and the Smagorinsky model prediction

L_{ij}^{s} is defined by:

$$\epsilon = \left(L_{ij}^{s} - L_{ij}^{d}\right)\left(L_{ij}^{s} - L_{ij}^{d}\right) \tag{47}$$

Differentiate the equation (47) with respect to c_S, the following equation can be obtained that is defined as:

$$c_S = \frac{\langle L_{ij} M_{ij} \rangle}{\langle M_{ij} M_{ij} \rangle} \tag{48}$$

A backward differencing scheme has been used for the discretization of time derivatives, the convection term in momentum equation has been calculated using the Gauss theorem and a pure second order linear interpolation with non-orthogonal correction (Montorfano et al., 2013b). The divergence term in momentum has been calculated using the Gauss Linear-Upwind Stabilized Transport scheme. Other divergence terms have been discretized using Gauss linear schemes. The Courant–Friedrichs–Lewy (CFL) number in the simulation is always smaller than 1 (Source and Consulting, 2014).

4.2. Introduction of the OpenFOAM platform

OpenFOAM (Open Field Operation and Manipulation) is a C++ language developed fully object-oriented open-source fluid dynamics computational software. OpenFOAM was first introduced and written by Hrvoje Jasak in 1993 during his Ph.D., the early OpenFOAM was a commercial software, Henry Weller and others founded OpenCFD company in 2004 to distribute OpenFOAM as an open-source code. With the rapid development of OpenFOAM, OpenFOAM has been widely adopted by scientific researchers and technical engineers. In the thesis, the boundary condition applied in OpenFOAM is introduced in detail here.

OpenFOAM contain many mature fluid dynamics solvers for steady and unsteady flow and incompressible and compressible flow etc. Additionally, the platform supports the user-defined development custom fluid dynamics solver. In this thesis, the large eddy simulation is

applied to calculate the boundary layer flow field, the OpenFOAM's incompressible flow transient solver pimpleFoam is used. The pimpleFoam solver uses the PIMPLE (merged PISO-SIMPLE) algorithm computes transient incompressible flows with large time steps. The PIMPLE algorithm is a hybrid of the PISO (Pressure-Implicit with Splitting of Operators) algorithm and the SIMPLE (Semi-Implicit Method for Pressure-linked Equations) algorithm that can deal with large time-step, non-iterative transient simulation using less computational resources (R.I.Issa, 1991; Holzmann, 2017).

There are three main types of boundary conditions for numerical calculations: Dirichlet boundary condition, Neumann boundary condition and Robin boundary condition. In OpenFOAM, apart from the basic boundary conditions, there are various boundary conditions derived from basic boundary conditions. The boundary conditions including fixedValue, zeroGradient, cyclic, cyclicAMI, symmetry and inletOutlet boundary conditions are applied in this study etc. the introduction of these boundary conditions is shown in Table 4-1. The boundary conditions should be set separately for the velocity field and pressure field for sake of the compatibility of the velocity and pressure boundary conditions, i.e., when the boundary condition of the velocity field is fixedValue, the boundary condition of the pressure field cannot be fixedValue at the same time. The zeroGradient boundary condition can be set for the pressure field (Source and Consulting, 2014).

Table 4-1 Description of boundary conditions commonly applied in openfoam

Boundary condition	Description
fixedValue	The values on the boundary are the fixed values
zeroGradient	The gradient of the values on the boundary is zero
cyclic	Cyclic boundary condition, which requires the meshes of the two cyclic surfaces to be exactly the same

cyclicAMI	Cyclic boundary conditions for arbitrary meshes, the meshes of the two loop faces are not required to be exactly the same
slip	This boundary condition provides a slip constraint
noSlip	This boundary condition fixes the values to zero at walls
symmetry	Symmetric Boundary Conditions
inletOutlet	According to the direction of the velocity on the boundary. The boundary condition is switched between the fixedValue and the zeroGradient, mainly used as the outlet boundary condition

The numerical schemes for dealing with the derivative terms are defined in the 'fvScheme' file in each simulation case folder in OpenFOAM. The numerical schemes for different derivative terms are defined in Table 4-2.

Table 4-2 Description of numerical schemes for derivative terms applied in openfoam

Numerical Scheme	Description
timeScheme	First and second time derivatives
gradSchemes	Gradient ∇
divSchemes	Divergence $\nabla \cdot$
LaplacianSchemes	Laplacian $\nabla^2 \; or \; \Delta$
interpolationSchemes	Cell to face interpolations of values
snGradSchemes	Component of gradient normal to a cell face
wallDist	Distance to wall calculation where required

The detailed instruction of each numerical scheme can be found in the OpenFOAM guidance (CFD Direct, 2020). In this thesis, it is worth explaining the *snGradSchemes* listed in Table 4-2. The basis of the gradient calculation at a face is to subtract the value at the cell centre on one side of the face from the value in the centre on the other side, and then divide by the distance. The calculation is second-order accurate for the gradient if the vector connecting the cell centres is orthogonal to the face. However, the orthogonality requires a regular mesh, and

this mesh configuration does not normally occur in engineering geometries. To maintain the second-order accuracy, an explicit non-orthogonal correction can be added to the orthogonal component which is known as corrected scheme. On the contrary, if the mesh configuration is orthogonal, the uncorrected scheme is applied. Generally, the uncorrected scheme is only implemented at the mesh with very low non-orthogonality. The corrected scheme is recommended in most cases.

Chapter 5

Hump channel flow

5.1. Numerical setup of the hump channel flow

In this chapter, different IBCs implemented in a channel with a hump are examined and discussed. The chord length (c) of the hump is 0.42 m. The flow scenarios are considered under the condition of Mach number equals 0.1. This flow configuration illustrated in Figure 5.1 a,b is one of the test cases considered in NASA Workshop , and experimental data can be accessed from the website of ERCOFTAC ("Classic Collection All cases no.83," n.d.). To generate the target characteristics of inflow turbulence, some essential properties of inflow turbulence are required. Boundary layer thickness, displacement thickness, and momentum thickness are pre-conditions of the Lund method. From the experimental data of ERCOFTAC, free-stream velocity U_{inf} is $34.6 m \cdot s^{-1}$. The Reynolds number based on boundary layer thickness is 6.295×10^4. Figure 5.2 describes the hump model used in the simulation, the origin x = 0 is located on the beginning of the hump. The length of the hump chord c = 0.42 m, the channel height is 0.91c with a small necking over the hump to account for blockage effects, and the channel width is 0.2c. Periodic boundary conditions have been set on the lateral faces due to the periodicity of the geometry in the spanwise direction. At the top surface, the values of velocity gradients and pressure are set to be zero. At the bottom wall, the wall function is used according to the work of Montorfano (2013). In this case, we use the Spalding law wall function since it matches the asymptotic solutions in the inertial sublayer and is not highly affected by the values of y+ near the wall ("Classic Collection All cases no.83," n.d.). Besides, the mesh is non-orthogonal near the hump and the top surface. To maintain the stability of the calculation, the corrected surface normal gradient schemes is used according to the statement in Chapter 4.

The content of Chapter 5 is published by the author of this thesis, the paper is *Effect of the Inlet Boundary Conditions on the Flow Over Complex Terrain Using Large Eddy Simulation*

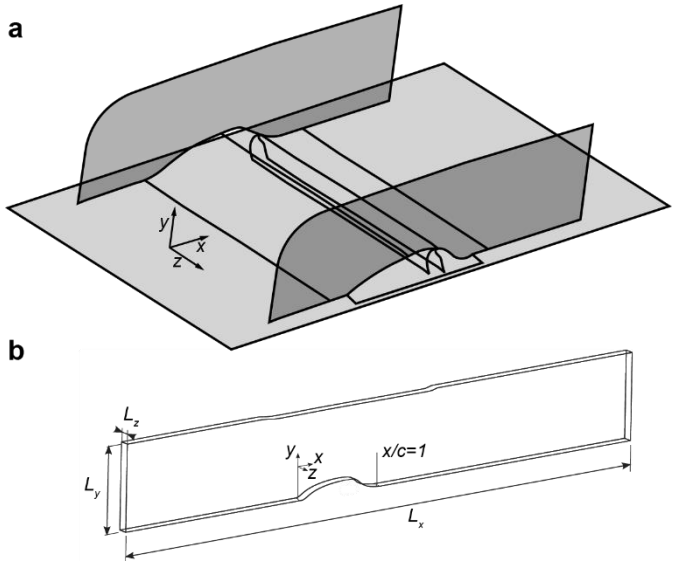


Figure 5.1 (a) Experimental model of the wall-mounted hump given by ERCOFTAC. (b) the simulation domain for hump case: $L_x = 6.14c$; $L_x = 6.14c$; $L_z = 0.2c$ (Greenblatt et al., 2006).

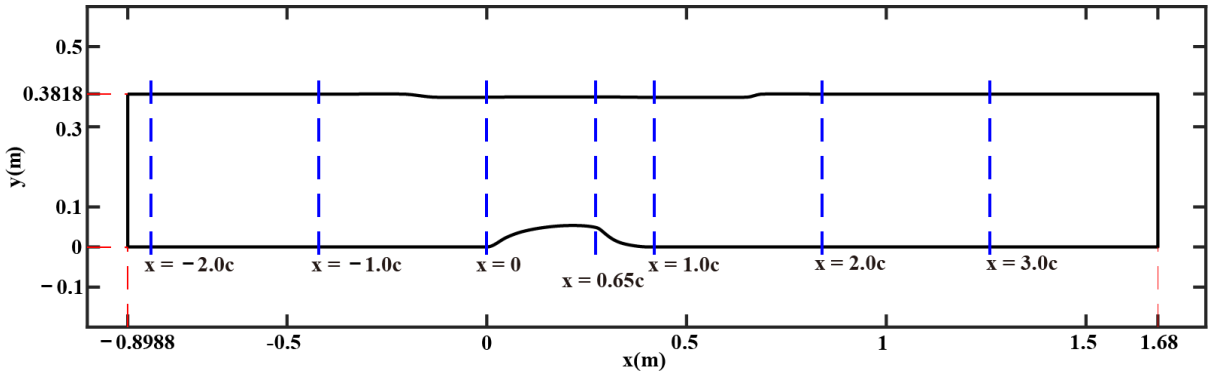


Figure 5.2 Side view of the computational domain with main dimensions expressed in chord unit length. Inlet is located at x/c = −2.14, while hump profile extends from x/c = 0 and x/c = 1. Outflow is at x/c = 4. Channel height is 0.909c. Chanel extends for 0.2c in z direction.

This section elucidates detailed settings of simulations with different IBCs, these details are summarized in Table 5-1, Table 5-2 and Figure 5.3. The specified thickness in Lund method including boundary layer thickness, momentum thickness and displacement thickness are required at the inlet, these properties can be calculated from the experimental data according to the equations (2-(6), where the boundary layer thickness δ is 0.0671c, displacement thickness δ^* is 0.009c, and momentum thickness δ_θ is 0.0069c. With the application of DFSEM, three mean velocity components, turbulent Reynolds stresses, and turbulent length scale at the inlet are needed. The initial setting details of the simulation based on DFSEM are illustrated in Figure 5.3.

The content of Chapter 5 is published by the author of this thesis, the paper is *Effect of the Inlet Boundary Conditions on the Flow Over Complex Terrain Using Large Eddy Simulation*

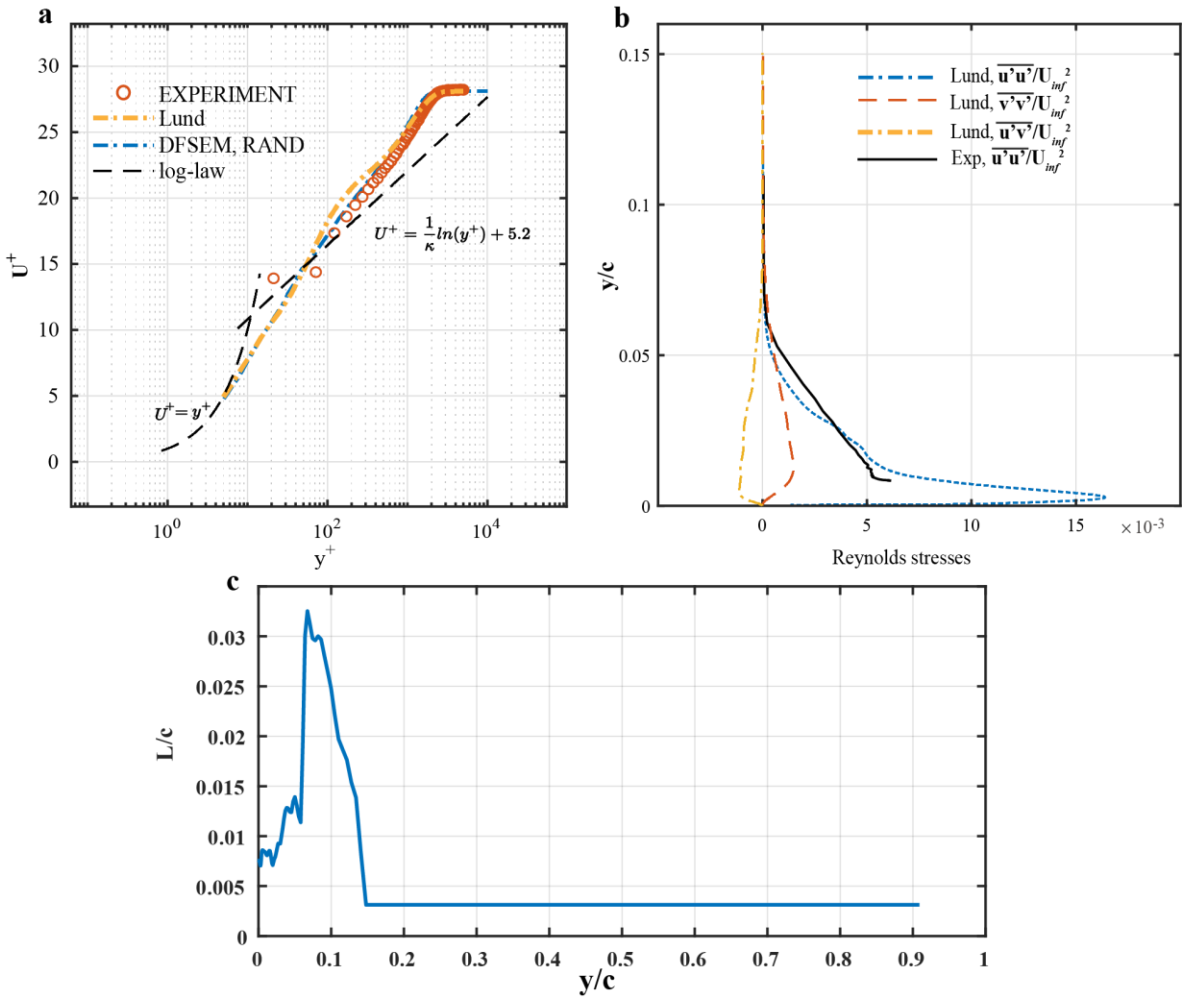


Figure 5.3 Input for the simulation based on DFSEM at the inlet (a) Nondimensional time-averaged velocity profiles at the inlet (b) Distribution of Reynolds stresses components $\overline{u'u'}$, $\overline{v'v'}$ and $\overline{u'v'}$ at the inlet of simulation based on Lund method and experimental data ($\overline{u'u'}$). (c) Profile of the turbulent length scale

From the profiles of the input turbulent length scale shown in Figure 5.3, it can be observed that the values of turbulent length scale show a sharp upward trend closed to the wall and then decrease after y/c=0.08. The input integral length scale is calculated from the simulation data based on the Lund method in this case.

Table 5-1 Summary of the inflow boundary conditions.

	Mean Velocity	Specified Thicknesses	Reynold Stresses	Turbulent Length Scales
Random	X	—	—	—
Lund	X	X	—	—
DFSEM	X	—	X	X

In Table 5-2, distribution of mesh cells along streamwise, vertical and spanwise directions is displayed. Three sets of mesh configuration are used to eliminate the influence of the mesh

The content of Chapter 5 is published by the author of this thesis, the paper is *Effect of the Inlet Boundary Conditions on the Flow Over Complex Terrain Using Large Eddy Simulation*

resolution on the simulation results. Δx^+, Δy^+, and Δz^+ are dimensionless mesh scale at the inlet plane. The mesh in the streamwise direction and vertical direction is not uniform, the mesh in the spanwise direction is uniform. The Smagorinsky model is used as the SGS model in each case and the value of *Cs* is 0.1678 (Mart ńez et al., 2015).

Table 5-2 Summary of the mesh configurations.

Density	**Mesh Size (x, y, z)**	Δx^+	Δy^+	Δz^+
Coarse	$420 \times 88 \times 52$	929	6.35	125.06
Middle	$540 \times 120 \times 64$	658	4.76	101.61
Fine	$630 \times 140 \times 84$	619	3.18	77.42

Figure 5.3a shows the nondimensional time-averaged velocity profile for the experimental data and simulation results obtained by the implementation of three IBCs on the inlet boundary. The non-dimensional time-averaged velocity profiles in the DFSEM and RAND methods are directly set by using the experimental data. In the case based on RAND method. Mean velocity *U*, weighting factor α, and fluctuation scale s for each velocity component should be determined according to the equation (33). In this simulation, the fluctuation scale *s* for each velocity components in *x*, *y*, and *z* direction are 0.02, 0.01 and 0.01 respectively. The weighting factor α is set to be 0.1. Mean velocity is determined from the interpolation of the experimental data as shown in Figure 5.3a.

The velocity profile generated by Lund method is derived from the recycling and rescaling process, the results of which are slightly different from the experimental data. Volume flow rates for all cases are consistent and equal to $1.1\ m^3/s$ though there is small difference between the velocity profiles of different inlet boundary condition methods and experimental data in the near-wall region. However, the nondimensional time-averaged velocity profiles for all cases and the experiment data deviate from the theoretical velocity profile (log-law).

Figure 5.1b reflects the distribution of the Reynolds stresses components, $\overline{u'u'}$, $\overline{v'v'}$ and $\overline{u'v'}$ of the simulation based on the Lund method and $\overline{u'u'}$ distribution of experiment. From

The content of Chapter 5 is published by the author of this thesis, the paper is *Effect of the Inlet Boundary Conditions on the Flow Over Complex Terrain Using Large Eddy Simulation*

the graph, there is a small difference between the simulation results of Lund method and the experimental data close to the wall. The profiles of the Reynolds stresses generated by the Lund method at the inlet are also used as the initial setting for DFSEM to calculate the turbulent intensity at the inlet as explained in Equation (11). Figure 5.1c shows the profile of the turbulent length scale setting for DFSEM. The streamwise integral length scale L_x is characteristic of the larger eddies, which is obtained through:

$$L_x \equiv \int_0^\infty \frac{\overline{u'(x)u'(x+r)}}{\overline{u'^2}} dr \tag{49}$$

where *r* is the space lag in the spanwise direction. The turbulent length scale defined by the integral of autocorrelation function when it reaches *1/e* (Spalding, 1960). $u'(x)$ is fluctuating velocity components along the streamwise direction that is extracted from the prescribed simulation results based on the Lund method. Figure 5.1c illustrates the distribution of the streamwise integral length scale along the vertical direction. The values are used as the initial setting of DFSEM.

5.2. Mesh sensitivity analysis

Figure 5.4-Figure 5.6 reflect the mesh sensitivity of the simulations based on Lund method, DFSEM and RAND method with different mesh resolution. The dimensionless friction velocity u_τ/U is calculated by the square root of wall shear stress at the inlet, which equal 0.035 and the value is fixed for each case since it can ensure that the magnitude of free stream velocity ($y^+ > 3000$) in the log-law plot is the same for each case. Differences of velocity profiles applying different mesh configurations are reflected by the velocity profiles in the near wall region for cases with different IBC methods.

The content of Chapter 5 is published by the author of this thesis, the paper is *Effect of the Inlet Boundary Conditions on the Flow Over Complex Terrain Using Large Eddy Simulation*

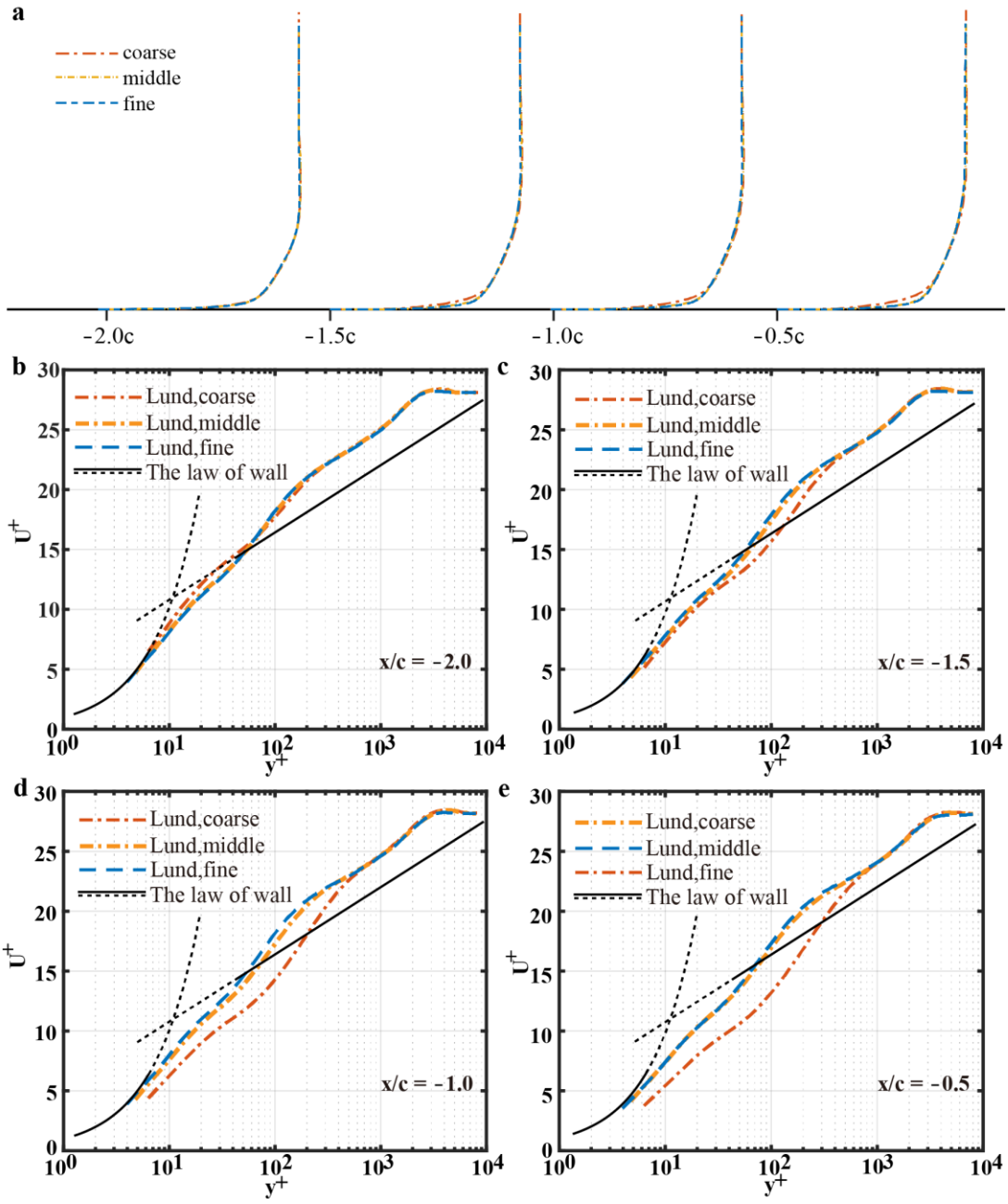


Figure 5.4 Effect of mesh resolution on streamwise mean velocity based on Lund method at (a) 4 positions before the hump (b) x/c = −2 (c) x/c = −1.5 (d) x/c = −1.0 (e) x/c = −0.5.

In Figure 5.4, it is evident that the results are converged when denser mesh is used. However, even though the mesh resolution is fine enough, the simulation results could not fit the theoretical data generated from the law of the wall. Lund method introduce artificial periodicity in the turbulence generation progress, the results are hardly improved by increasing the simulation time. However, the calculation results of mean velocity profiles gradually

The content of Chapter 5 is published by the author of this thesis, the paper is *Effect of the Inlet Boundary Conditions on the Flow Over Complex Terrain Using Large Eddy Simulation*

approach the law of wall at four positions along the streamwise direction, from $x/c = -2$ to $x/c = -0.5$.

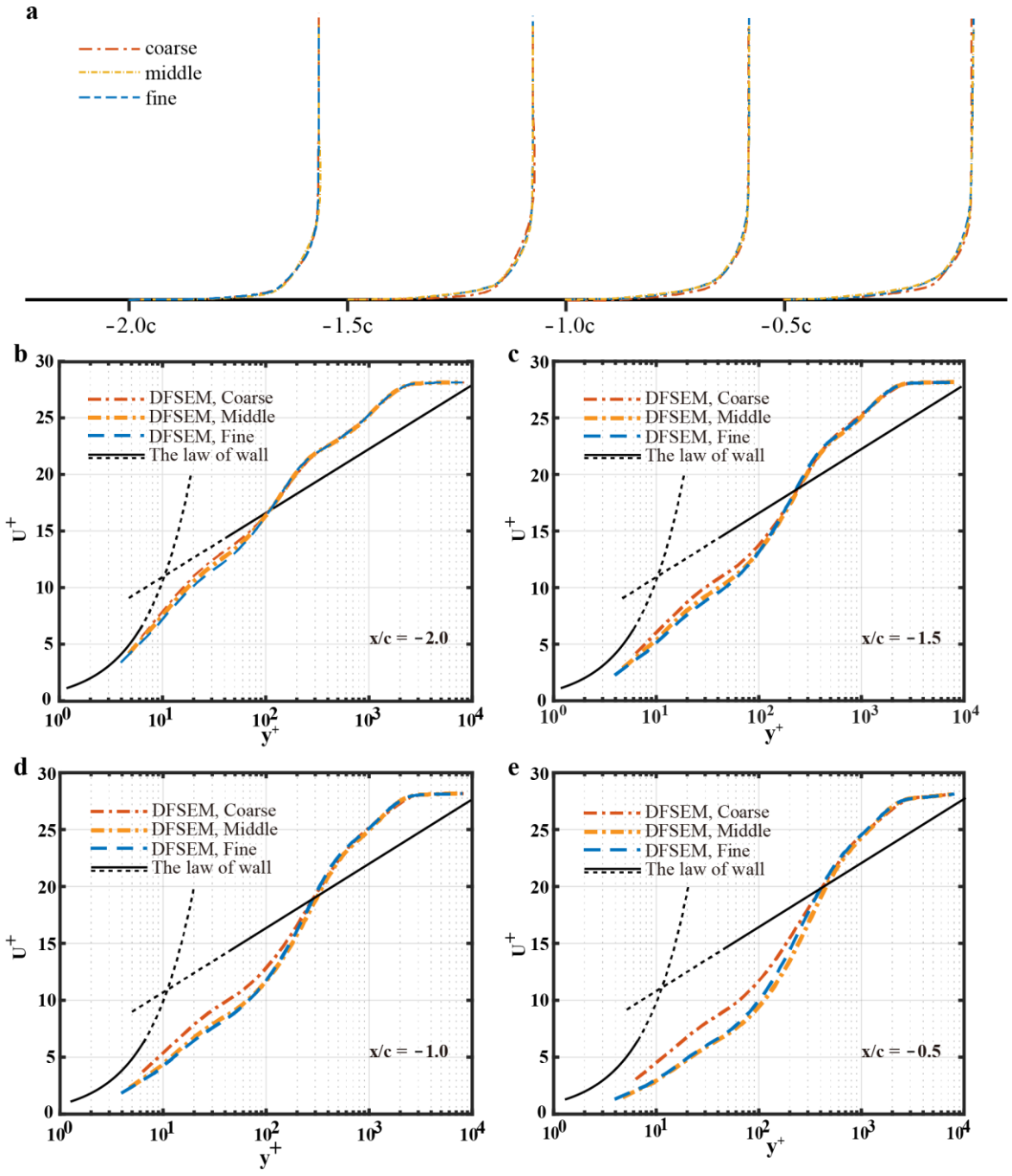


Figure 5.5 Effect of mesh resolution on streamwise mean velocity based on DFSEM at (a) 4 positions before the hump (b) x/c = −2 (c) x/c = −1.5 (d) x/c = −1.0 (e) x/c = −0.5.

In Figure 5.5, the calculation results of mean velocity profiles converge when denser mesh are used. However, the mean velocity profiles of the simulation become further away from the

The content of Chapter 5 is published by the author of this thesis, the paper is *Effect of the Inlet Boundary Conditions on the Flow Over Complex Terrain Using Large Eddy Simulation*

theoretical result as the flow moves from the inlet to the hump at four streamwise positions from $x/c = -2$ to $x/c = -0.5$.

In Figure 5.6, similarly, the calculation results converge as the mesh density increases. The distribution of mean velocity profiles at four streamwise positions has the same trend as the simulation based on DFSEM. Mesh sensitivity analysis after the hump is illustrated by A.1-A.3 in the Appendices. The middle mesh configuration is accurate enough to reflect the simulation results, therefore the results based on the middle mesh configuration is used for the analysis in the following parts in this chapter.

The content of Chapter 5 is published by the author of this thesis, the paper is *Effect of the Inlet Boundary Conditions on the Flow Over Complex Terrain Using Large Eddy Simulation*

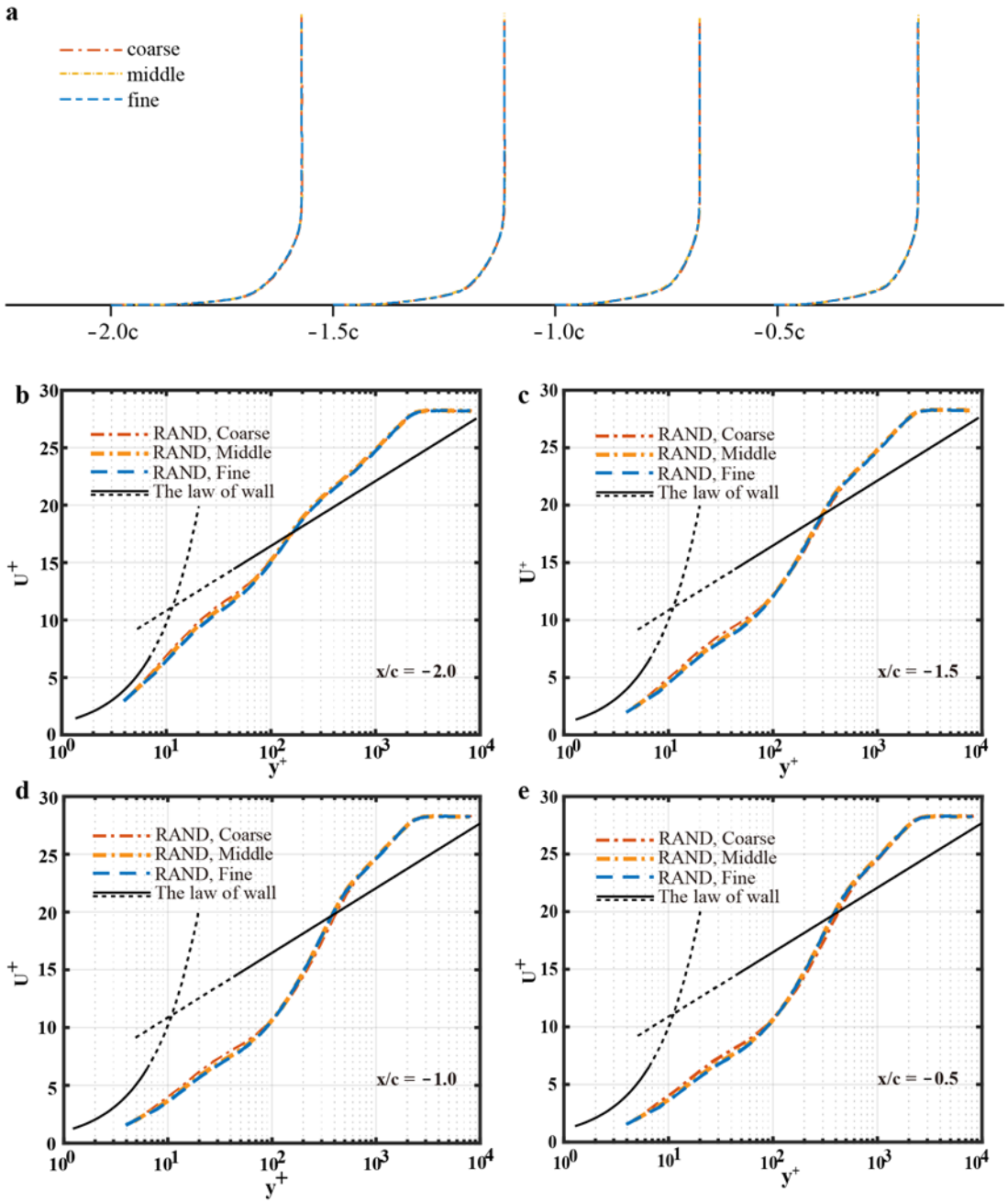


Figure 5.6 Effect of mesh resolution on streamwise mean velocity based on RAND method at (a) 4 positions before the hump (b) x/c = −2 (c) x/c = −1.5 (d) x/c = −1.0 (e) x/c = −0.5.

5.3. Flow properties analysis

5.3.1. Velocity field analysis

Instantaneous streamwise velocity contours and the development of turbulent structure in the boundary layer from $x/c = -2.14$ (inlet plane) until $x/c = 4$ have been demonstrated for 3 IBCs in Figure 5.7a–c. The instantaneous velocity field is captured at the time $T = 3TA$, where

The content of Chapter 5 is published by the author of this thesis, the paper is *Effect of the Inlet Boundary Conditions on the Flow Over Complex Terrain Using Large Eddy Simulation*

TA is the flow-through time, *TA = L/U*. The Q criteria for three cases is the same and set as Q = 10,000. Q is calculated from:

$$Q = \frac{1}{2}(\|\Omega\|^2 - \|S\|^2) \tag{50}$$

where Ω and S are the antisymmetric and symmetric parts of the velocity gradient tensor (Hunt et al., 1988). The Q-criteria defines a vortex as a "connected fluid region with a positive second invariant of ∇u". Q represents the vorticity magnitude as greater than the magnitude of the strain rate, which can be used to indicate the turbulent structures in the flow region.

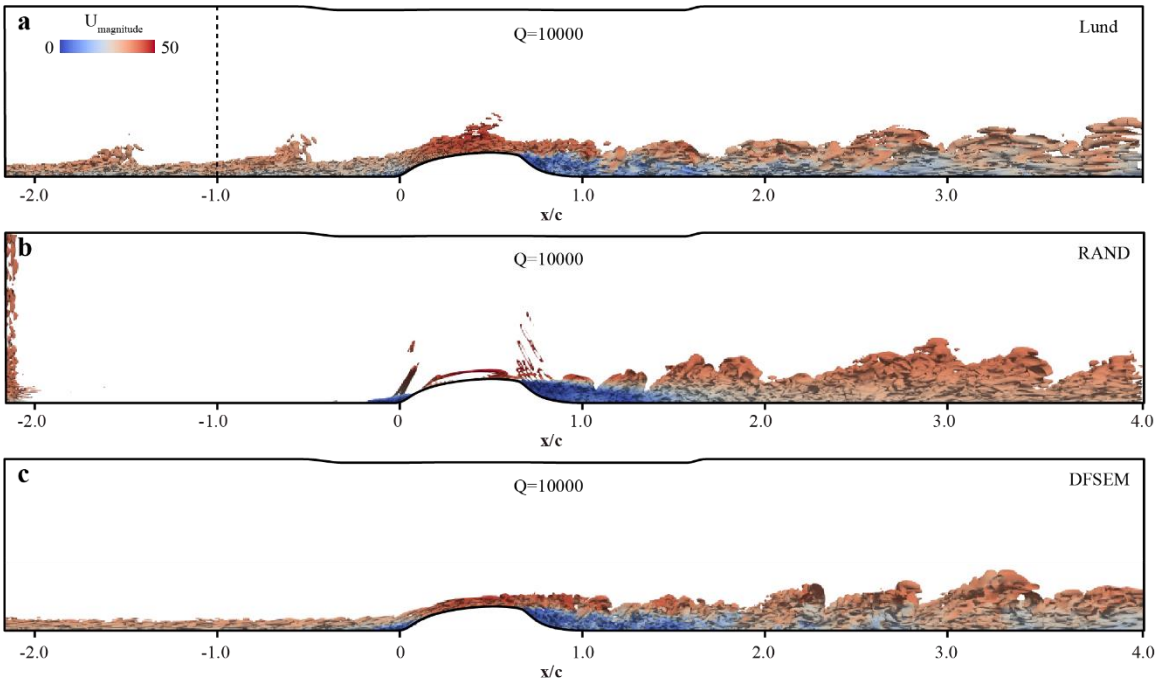


Figure 5.7 Instantaneous velocity field (a–c) at T = 3TA and the corresponding iso-surface at the inlet by using the (a) Lund, (b) RAND, and (c) DFSEM.

For the case of Lund, turbulence is generated in the recycling and rescaling process and then reintroduced in the flow region (Figure 5.7a). The dot line in Figure 5.7a illustrates the position of recycling plane. Turbulence is well developed at the beginning of the flow region and the regular distributed coherent eddies can be observed in the flow region. Moreover, turbulence is generated close to the walls. Turbulence can be maintained over the hump. However, there will be an artificial frequency introduced to the flow region as the boundary layer flow is repeatedly rescaled and fed back again and again. The effect of the artificial

The content of Chapter 5 is published by the author of this thesis, the paper is *Effect of the Inlet Boundary Conditions on the Flow Over Complex Terrain Using Large Eddy Simulation*

frequency is magnified as the distance between the inlet plane and the recycling plane decreases, but it never vanishes even though the distance is long enough. This problem was elucidated and nominated by Keating (2004) as 'spurious' periodicity. This periodicity interacts with some physical frequency of the flow, for instance, the frequency of vortex shedding instability. In addition, the distance between the inlet plane and the recycling plane is determined artificially, which brings uncertainty of simulation results. If this distance is short, there will be less space for turbulence to develop and reach stabilized integral quantities like momentum thickness, on the other hand, there will be more difficulty to obtain a converged solution in the limited distance. Otherwise, if the distance is very long, the computational cost tends to increase sharply. Regardless of whether the distance is short or not, artificial periodicity is inevitable.

For RAND method, some perturbations can be observed close to the inlet plane and in the middle of the vertical direction (Figure 5.7b). These disturbances are further weakened downstream, and it is hardly to observe evident and stabilized turbulent structures before the hump ($x/c = -1 \sim -0.3$). The stabilized turbulent structures can be observed only after the hump (Figure 5.7b). Instantaneous velocity data are generated stochastically, which makes the energy of turbulence signal uniformly distributed over the whole wavenumber range. Due to a lack of energy in the low wave number range, the pseudo turbulence generated in this range damps to zero immediately. The results derived from this method are identical to a laminar flow.

For the case of DFSEM shown in Figure 5.7c, turbulence is developed from the anisotropic turbulent spots randomly distributed at the inlet plane. Turbulent structures are homogeneous before the hump and the thickness of the 'turbulent region' maintains the value of boundary layer thickness at the inlet. Compared with the Lund method, there is no periodic 'turbulent wave' when DFSEM is applied.

For all cases, 'turbulent region' is much thicker after the hump than that before the hump. It reflects that the flow separation could stimulate much stronger turbulence than the artificial

The content of Chapter 5 is published by the author of this thesis, the paper is *Effect of the Inlet Boundary Conditions on the Flow Over Complex Terrain Using Large Eddy Simulation*

inlet boundary condition. Streamline distribution for the three cases are demonstrated in Figure 5.8, where the orange line represents experimental data, and the black line represents simulation results.

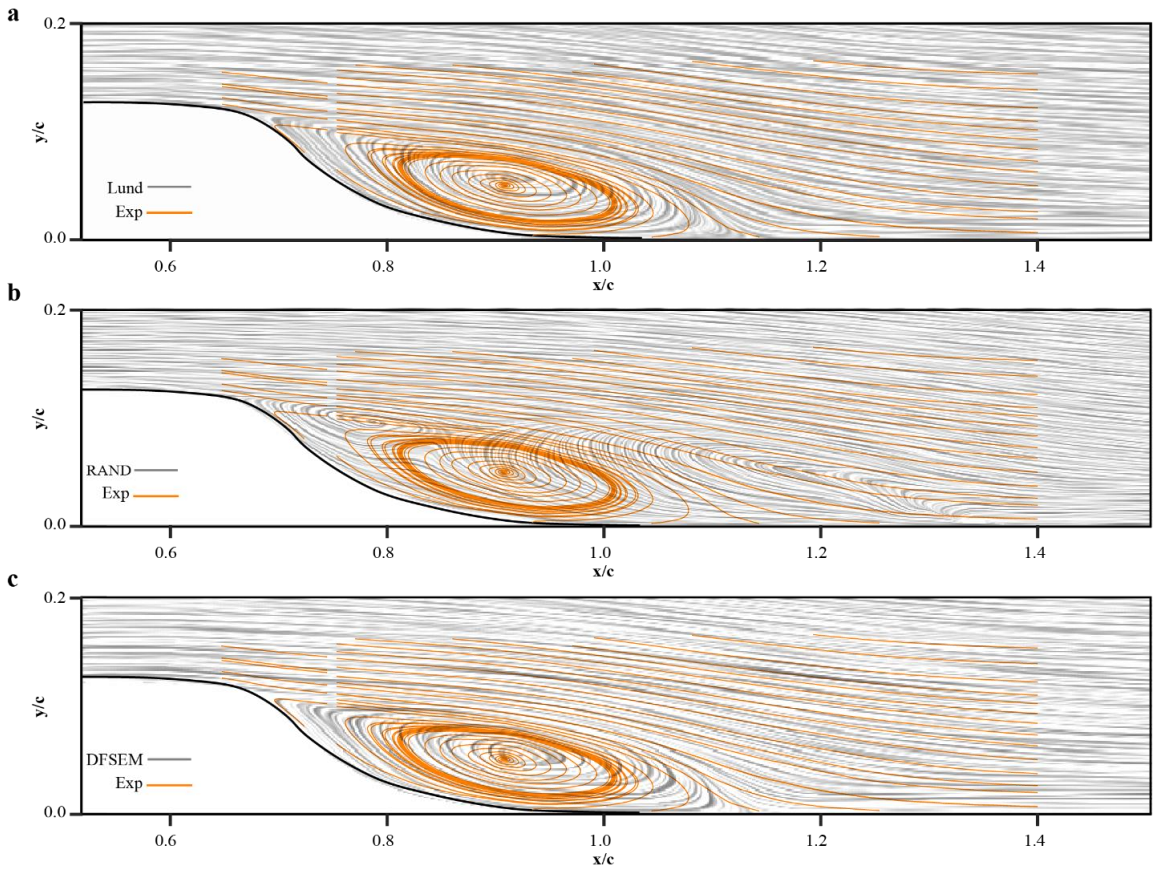


*Figure 5.8 Streamline distribution around the lump plotted from (**a**) Lund method, (**b**) Random method and (**c**) DFSEM method.*

It is apparent that the size of flow separation regions in the simulation based on the Lund method and DFSEM are nearly the same. Besides, the streamlines of simulation based on the Lund method and DFSEM could agree the experimental data (Figure 5.8a, c) better compared with the simulation based on the RAND method (Figure 5.8b). The position of the turbulent separation point of the case with the RAND method is close to others, while there are two vortices after the hump. Hence, the position of the reattachment point in this case is different from that in other cases.

5.3.2. Flow separation and reattachment

The content of Chapter 5 is published by the author of this thesis, the paper is *Effect of the Inlet Boundary Conditions on the Flow Over Complex Terrain Using Large Eddy Simulation*

Table 5-3 presents flow separation and reattachment locations of three IBC methods. "Rel. diff to Exp" represents the relative difference between the simulation results and the experimental data. All these methods could give relatively accurate prediction of the positions of separation points. The relative difference between the prediction and the experiment data is smaller than one percent in cases based on the Lund method and DFSEM. In cases based on the Lund method DFSEM, the relative difference with respect to experiment data is nearly 6%. However, the value is huge in the case based on the RAND method, which is over 22%. Therefore, both simulations with Lund method and DFSEM could capture relatively accurate flow separation region, while the simulation with the RAND method greatly overestimated the size of the separation region after the hump.

Table 5-3 separation and reattachment positions of three IBCs in the flow.

	Exp	**Lund**	**DFSEM**	**RAND**
Separation point (*x/c)*	0.648	0.642	0.645	0.610
Rel. diff to Exp (%)	—	0.93	0.46	5.86
Re-attach. Point (*x/c*)	1.11	1.174	1.175	1.358
Rel. diff to Exp (%)	—	5.77	5.86	22.34

According to the work of Frank T. et al. (2010), the large-scale separation perhaps occurs in the non-fully turbulent regime at sufficiently Reynolds number and the separation is presented be of small scale in fully turbulent regime. The overestimation of the turbulence bubble size based on different IBC methods indicate that turbulence is not fully developed. Comparatively, the results of simulations based on the Lund method and the DFSEM could agree better with the experimental data. A comparison between simulated and measured values of pressure coefficient C_p is illustrated in Figure 5.9, which demonstrates the time-averaged pressure coefficient distribution.

The content of Chapter 5 is published by the author of this thesis, the paper is *Effect of the Inlet Boundary Conditions on the Flow Over Complex Terrain Using Large Eddy Simulation*

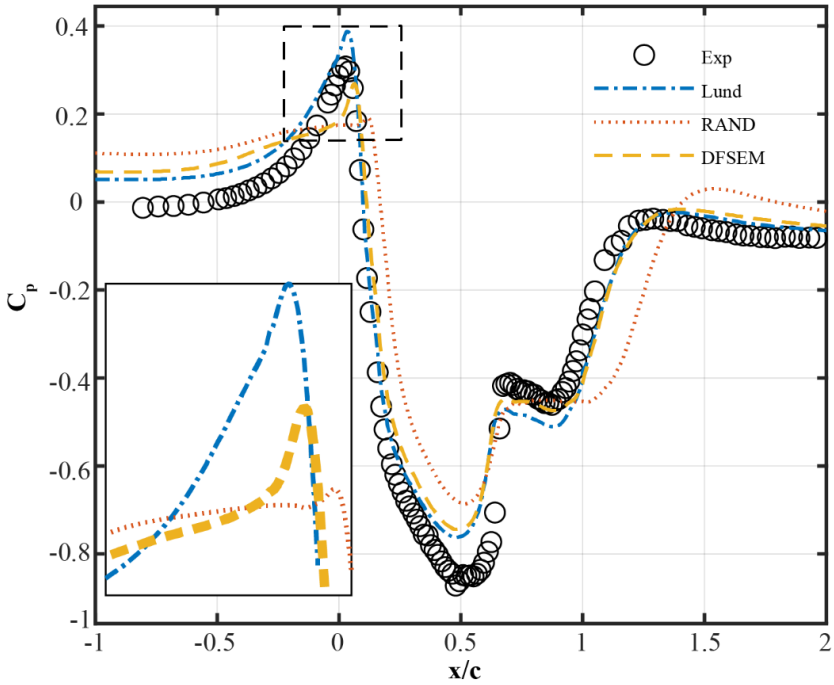


Figure 5.9 Distribution of pressure coefficient for three IBCs

Before the hump, the pressure coefficient for Lund case is slightly larger than the experimental data and other simulations. The peak happened at the head of the hump in all three cases with different IBC methods, and the peak value of Lund case is slightly larger than the experimental value, on the contrary, the values of others are smaller than the experimental value. The information in the dotted line frame without experimental data is zoomed in and put in the bottom left of Figure 5.9. For the case based on DFSEM, it is obvious that the pressure coefficient yields a sharp increase at the position close to the head of hump and then it subjects to the same downward trend as the Lund case does after the peak and the pressure distribution is nearly the same. For the case based on the RAND method, slower growth could be observed before the head of hump compared with cases based on other IBC methods.

In cases based on the Lund method and DFSEM, the distribution of pressure coefficient shows a downward trend on the hump from $x/c = 0$ to $x/c = 0.5$ and then arrives at a 'valley' ($x/c = 0.5$). The values at this point in cases based on these two IBC methods are larger than experimental data. There is a second valley of the pressure coefficient after the hump. Meanwhile, the pressure distribution of cases based on the Lund method and DFSEM are close

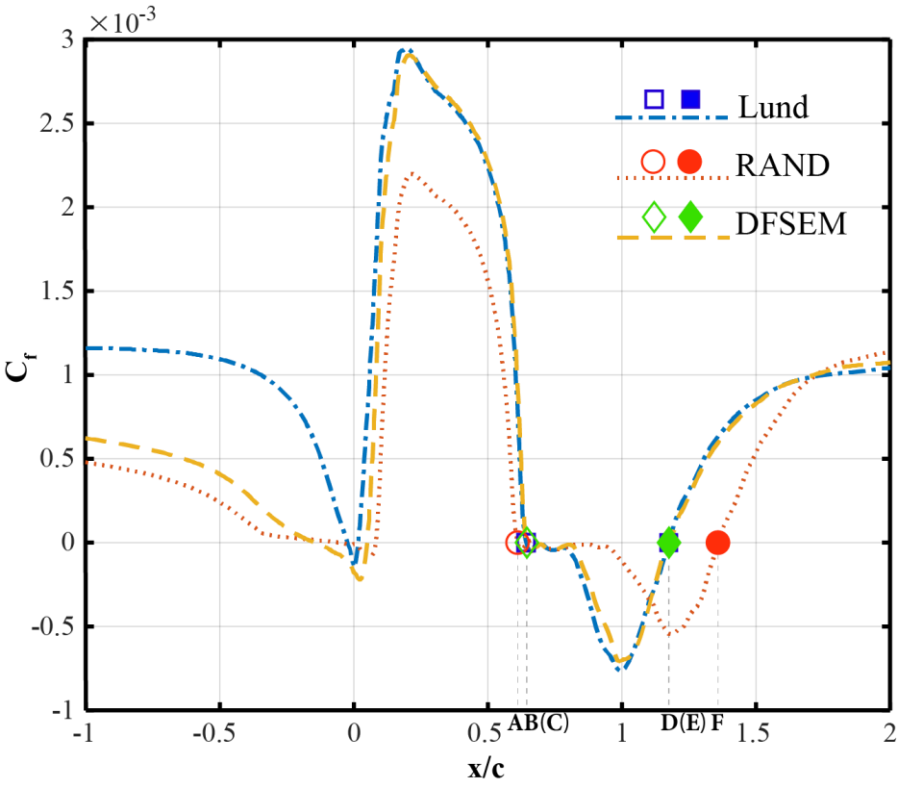
The content of Chapter 5 is published by the author of this thesis, the paper is *Effect of the Inlet Boundary Conditions on the Flow Over Complex Terrain Using Large Eddy Simulation*

from x/c = 0 to x/c = 2. The distribution of pressure coefficient for simulations with RAND is different from simulations with Lund and DFSEM methods. The pressure coefficient is close to the experimental data before the position where $x = -0.5c$. The peak value obtained after the head of the hump, and the magnitude is much smaller than other simulation results and the experimental data. The valley located at $x = 0.5c$ same as other simulations and experiment, but the value is much larger. There is a second valley of the pressure coefficient after the hump, while the pressure coefficient after the second valley rises later than the experimental data.

Figure 5.10 demonstrates the time-averaged friction coefficient for different inflow methods. Before the head of the hump ($-1 \leq x/c \leq 0$), the friction coefficient keeps stable and then decreases for cases using the Lund method, while only the downward trend could be observed when applying RAND method and DFSEM as the inlet boundary condition method. When the flow reaches and cross the middle of the hump ($0 < x/c \leq 0.5$), the friction coefficient increases sharply in all cases at which $x/c \leq 0.15$ and reaches the peak, simulation based on the Lund method and DFSEM has the highest coefficient corresponding to a high rate of velocity acceleration of near-wall flow. The case using the RAND method shows a similar trend at $0 \leq x/c \leq 0.15$, while the peak value is smaller than that in the cases based on the Lund method and DFSEM. After the peak, the same downward trend of C_f can be observed in cases using the Lund method and DFSEM. Simulation based on RAND method shows different rising and descending tendency at $0 \leq x/c \leq 0.15$ and $0.15 < x/c \leq 0.5$ compared to other cases. The growth rate at $0 \leq x/c \leq 0.15$ is smaller than simulations based on the Lund and DFSEM method, besides, the peak value is much smaller than other two cases. After the peak, at the region where flow separation shows up and flow crosses and leaves the second half of the hump ($x/c > 0.5$), C_f shows a similar downward trend and the descending rate is nearly the same in all simulations based on different inlet boundary conditions.

The content of Chapter 5 is published by the author of this thesis, the paper is *Effect of the Inlet Boundary Conditions on the Flow Over Complex Terrain Using Large Eddy Simulation*

The square (B, D), the circle (A, F), and diamond (C, E) marks in Figure 5.10 represent the flow separation and re-attachment point in simulations based on the Lund method, Rand method, and DFSEM respectively. In the case based on the RAND method, a flow separation point shows up firstly at the position A, where x/c = 0.61, and the value of friction coefficient decreases from positive to negative value, in other words, the near wall velocity gradient based on the distance to the wall has a sign reversal at this point. The friction coefficient keeps negative and stable and then drops rapidly until x/c = 1.173. The value of friction coefficient increases from negative value to positive value at the position F, where x/c = 1.252, which represents the flow re-attachment point. In the cases based on the Lund and DFSEM inlet boundary conditions, the positions of separation points at B, C and the positions of re-attachment points at D, E are very close. Therefore, the turbulent bubble sizes of these two simulations are close. This feature is illustrated in Figure 5.9, Figure 5.10 and Table 5-3. The flow separation region in the simulation based on the RAND method is larger than that based on other IBC methods.



The content of Chapter 5 is published by the author of this thesis, the paper is *Effect of the Inlet Boundary Conditions on the Flow Over Complex Terrain Using Large Eddy Simulation*

Figure 5.10 Distribution of friction coefficient for three IBCs

Table 5-4. The position where $C_f = 0$

	A	B	C	D	E	F
x/c	0.61	0.642	0.645	1.174	1.175	1.358

Differences between the flow pattern after the hump for the simulation based on different IBC methods reflect that turbulence generated at the inlet could affect the flow separation after the hump. However, compared with the cases based on RAND method and DFSEM respectively, the distribution of pressure coefficient and drag coefficient shows the same trend before hump until *x/c* = 0. When flow passes through and leaves the hump, the distribution of pressure coefficient and drag coefficient are different in these two cases. The scenario is contrary when comparing the cases based on DFSEM and Lund method respectively. There is a large deviation between these two coefficients, C_p and C_f before the hump, while the values of these two coefficients are nearly the same over and after the hump.

5.3.3. Turbulent properties before the hump

From the perspective of time-averaged velocity distribution and statistical turbulence characteristics (such as Reynolds stresses), it is very important to understand the behaviour of different IBCs and their influence on flow separation and re-attachment positions.

Figure 5.11 shows the time-averaged streamwise velocity profiles of different IBCs before the hump and compares them with theoretical results. Here the profiles in Figure 5.11a are plotted in uniform coordinate while the profiles in Figure 5.11b–e are plotted in logarithmic coordinate. For the simulation based on the Lund method, there is always a small deviation between the Lund results and the theoretical time-average velocity profiles. At *x/c* = −2, the deviation of the time-average velocity profile from the theoretical result is almost 0 at the viscous sublayer region ($y^+ \leq 5$) but large at the log-law region ($y^+ \geq 30$). At *x/c* = −1.5, the time-averaged velocity profile is consistent with the theoretical data in the viscous sublayer, meanwhile the velocity profile in the log-law region approaches the theoretical results. At *x/c*

The content of Chapter 5 is published by the author of this thesis, the paper is *Effect of the Inlet Boundary Conditions on the Flow Over Complex Terrain Using Large Eddy Simulation*

= −1 and *x/c* = −0.5, the time-averaged velocity profiles become much closer to the theoretical results though there is still a deviation between the simulation result and the theoretical result. For the case based on RAND method, the time-averaged velocity profiles close to the wall at *x/c* = −2 has small deviation compared with other simulations and theoretical results, while the deviation becomes larger as the distance from the wall increases. At *x/c* = −1.5, the deviation of the meantime-averaged velocity profile from the theoretical result becomes larger. The same description can be applied to the time-averaged velocity profile at *x/c* = −1, and *x/c* = −0.5. The phenomenon is caused whereby the turbulence is not fully developed in the region before the hump. However, for DFSEM, the distribution of velocity profiles is close to that in the case based on the RAND method. This reflects that there are coherent structures in this region, but the turbulent intensity seems to be small, which makes the flow perform like laminar flow.

The content of Chapter 5 is published by the author of this thesis, the paper is *Effect of the Inlet Boundary Conditions on the Flow Over Complex Terrain Using Large Eddy Simulation*

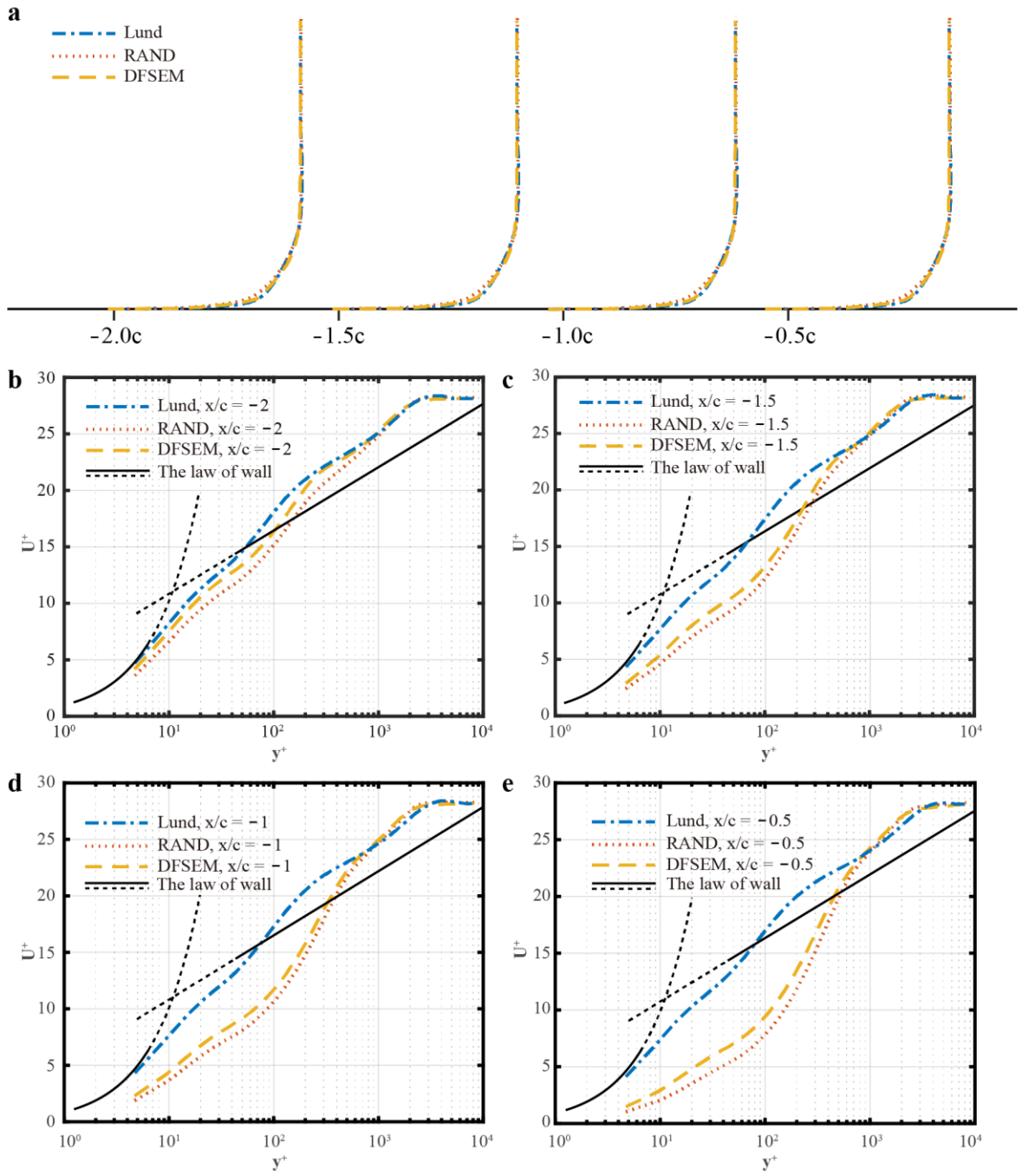


Figure 5.11 Time-averaged streamwise velocity U+ profiles (a) at four stations before the hump: (b) x = -2c, (c) x = -1.5c, (d) x = -1c, (e) x = -0.5c.

Figure 5.12 shows the Reynolds stresses profiles of simulation results based on different IBCs before the hump.

The content of Chapter 5 is published by the author of this thesis, the paper is *Effect of the Inlet Boundary Conditions on the Flow Over Complex Terrain Using Large Eddy Simulation*

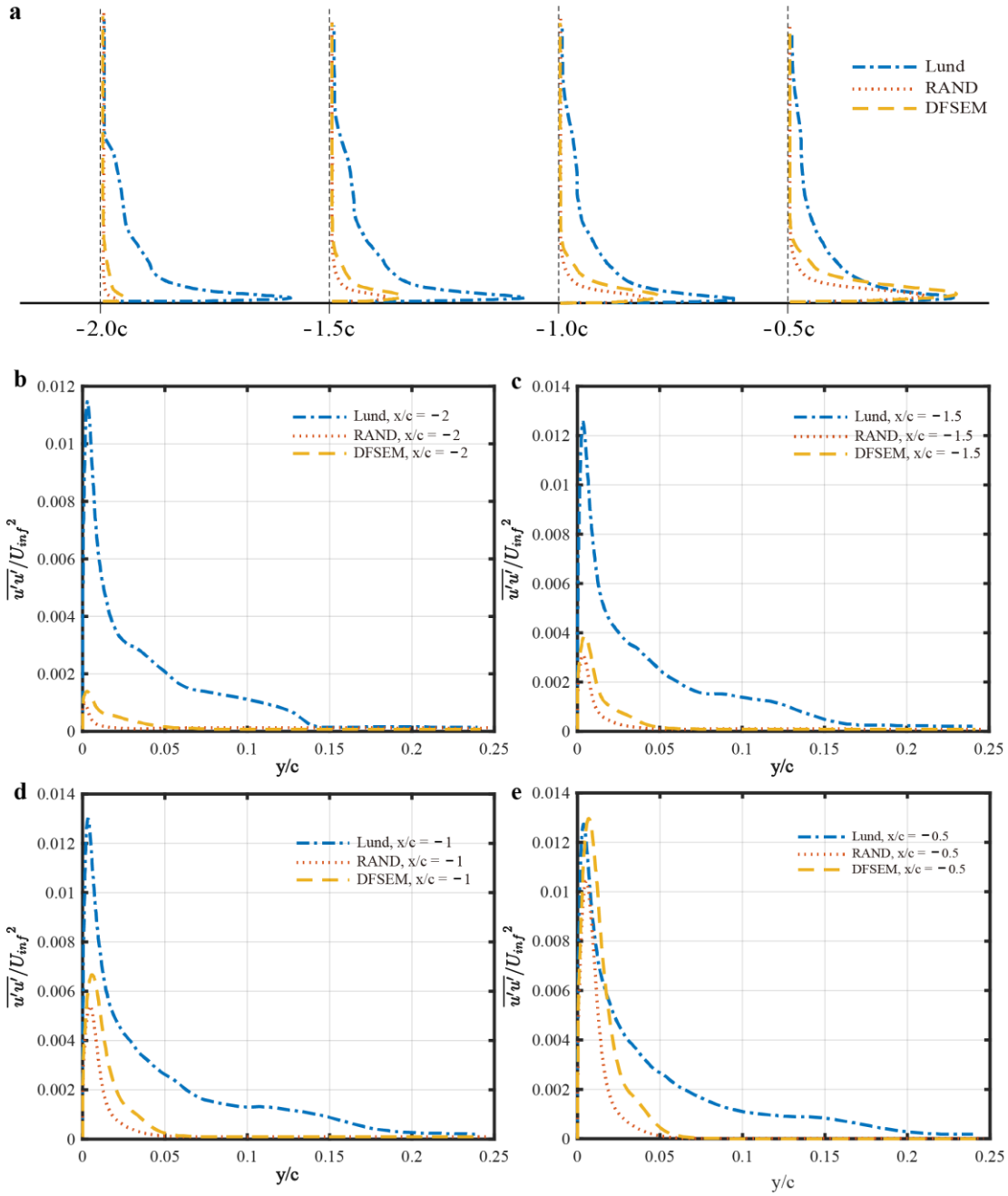


Figure 5.12 Time-averaged streamwise Reynolds stress $\overline{u'u'}/U_{inf}{}^2$ profiles at: (a) four stations before the hump (b) x/c = −2 (c) x/c = −1.5 (d) x/c = −1 (e) x/c = −0.5.

Since the values of $\overline{u'v'}$, $\overline{v'v'}$ and $\overline{w'w'}$ are considerably smaller compared with $\overline{u'u'}$ at the ahead of the hump, it is reasonable to use $\overline{u'u'}/U_{inf}{}^2$ to reflect the turbulent intensity and fluctuating part of the instantaneous velocity in the flow region. For the case based on Lund method, the profiles of $\overline{u'u'}/U_{inf}{}^2$ remain stable and slightly changes at different streamwise positions (x/c = −2, −1.5, −1 and −0.5). For the case based on RAND method and DFSEM, the

The content of Chapter 5 is published by the author of this thesis, the paper is *Effect of the Inlet Boundary Conditions on the Flow Over Complex Terrain Using Large Eddy Simulation*

streamwise turbulence intensity increases from *x/c* = -2 to *x/c* = -0.5, there is slight difference between the results of DFSEM and RAND method. Figure 5.11 and Figure 5.12 reflect that the profiles of mean velocity and streamwise turbulent intensity of the cases based on DFSEM and RAND method are similar before hump. According to Figure 5.12, the fluctuating velocity is not coherent in the case based on RAND method even though the turbulent streamwise intensity increases, while coherent structures can be observed in the case based on DFSEM.

5.3.4. Turbulent properties over the hump

In Figure 5.13a, the time-averaged velocity profiles over and after hump obtained by different IBCs cannot fully match the experimental data at four positions along the streamwise direction. In Figure 5.13b–e, even though the time-averaged velocity profiles and Reynolds stresses profiles are different before the hump, these profiles of cases based on the Lund method and DFSEM are close at certain streamwise positions over and after the hump. At *x/c* = 0.65, all the mean velocity profiles are lower than the experimental profiles in the near wall region but close to the experimental profiles when $y^+ > 500$. The deviation of simulation and experiment is much larger in the case based on RAND method. For all the cases at positions where *x/c* = 0.8 and 1, the mean velocity profiles are close to the experimental data in the near wall region but larger than experimental data when $y^+ \geq 4000$. Velocity profiles in cases based on the Lund method and DFSEM are almost coincidental, whereas that in case based on RAND method differs from the results of cases using the Lund method and DFSEM. Meanwhile, the differences between the results of the cases using the RAND method and the experimental data are larger than those in other cases. At the position *x/c* = 1.2, similarly, the simulation results of cases using Lund method and DFSEM are nearly the same and the results of the case using RAND method differs from the results of other cases. Considering the difference between the simulation and the experimental results, it is obvious to see that the case using the RAND method does not perform as good as cases with other methods.

The content of Chapter 5 is published by the author of this thesis, the paper is *Effect of the Inlet Boundary Conditions on the Flow Over Complex Terrain Using Large Eddy Simulation*

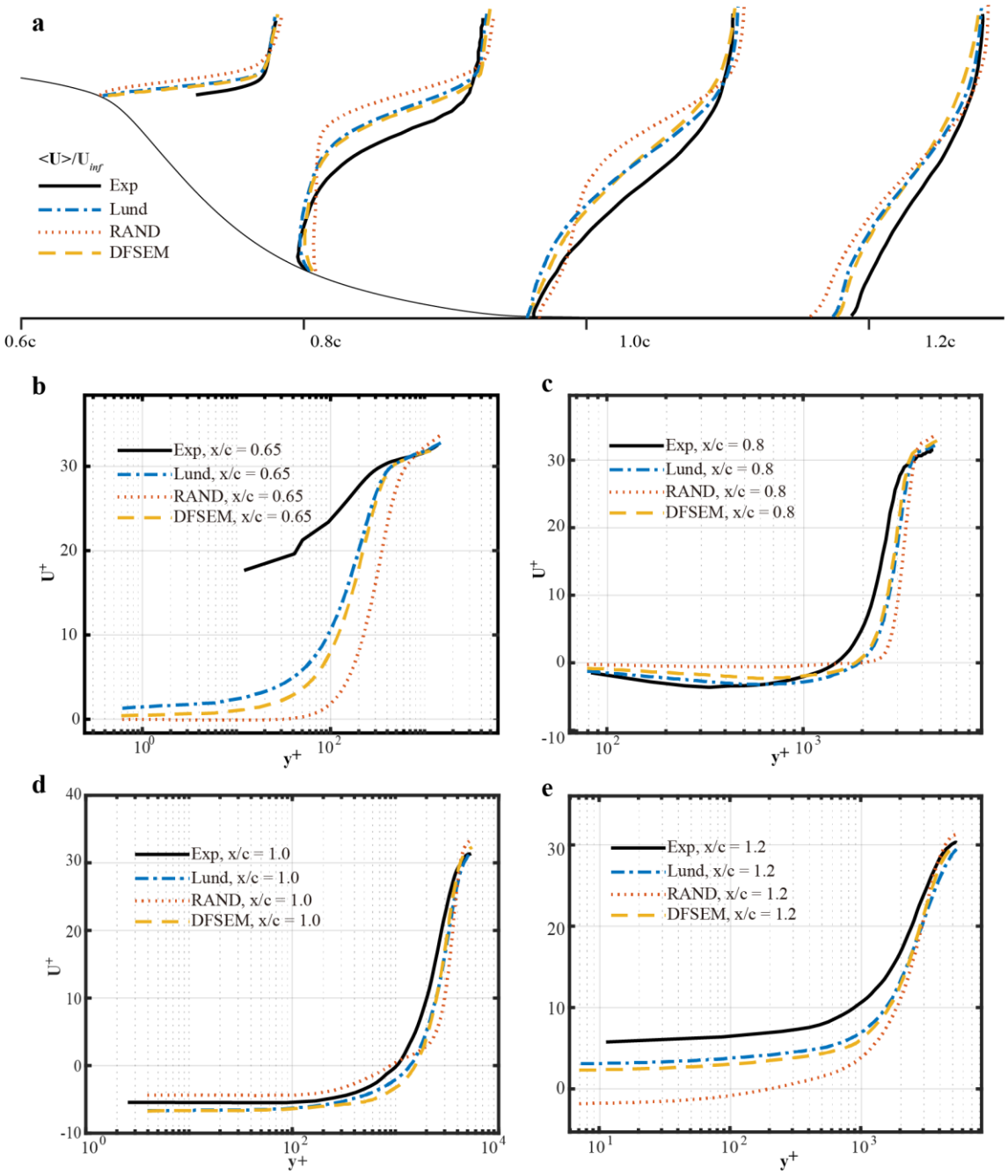


Figure 5.13 Time-averaged streamwise velocity U+ profiles (a) at four stations over the hump (b) x = 0.65c (c) x = 0.8c (d) x = 1.0c (e) x = 1.2c.

By looking at the scales of the graph, streamwise stresses have significantly increased for all methods after flow separation compared with those values before hump. The region close to the surface ($y/c < 0.12$) has gained higher stresses compared to preceding station, which is due to approaching and impingement of separated shear-layer on the surface (Asgari and Tadjfar, 2017). At the four sample positions (x/c = 0.65, 0.8, 1 and 1.2) shown in Figure 5.14,

The content of Chapter 5 is published by the author of this thesis, the paper is *Effect of the Inlet Boundary Conditions on the Flow Over Complex Terrain Using Large Eddy Simulation*

profiles of $\overline{u'u'}/{U_{inf}}^2$ show the same trend for simulations based on three IBC methods but the values are different. The main difference between the simulation results based on all IBC methods and the experimental data exists in the near wall region ($y/c < 0.12$). At the position $x/c = 0.65$, there is a slight drop of the peak values of $\overline{u'u'}/{U_{inf}}^2$ in cases based on the RAND method, Lund method, and DFSEM, respectively, and all peak values from simulations are larger than the experimental data. At the position $x/c = 0.8$, the distribution of cases based on all IBC methods are similar as well. Results of cases based on the Lund method and DFSEM are close, while the result of case based on RAND differs from simulation with other methods but becomes much close to the experimental data. At $x/c = 1, 1.2$, the difference between simulation results and the experimental data becomes much larger compared with the results at $x/c = 0.65$ and 0.8. The most likely cause of the difference is that simulations using these IBC methods could not predict the position of re-attachment point as precisely as the position of the separation point since the turbulence generated based on these methods is not fully-developed. Compared with the case based on the RAND method and DFSEM, the case using the Lund method performs more reliably at these two positions.

The content of Chapter 5 is published by the author of this thesis, the paper is *Effect of the Inlet Boundary Conditions on the Flow Over Complex Terrain Using Large Eddy Simulation*

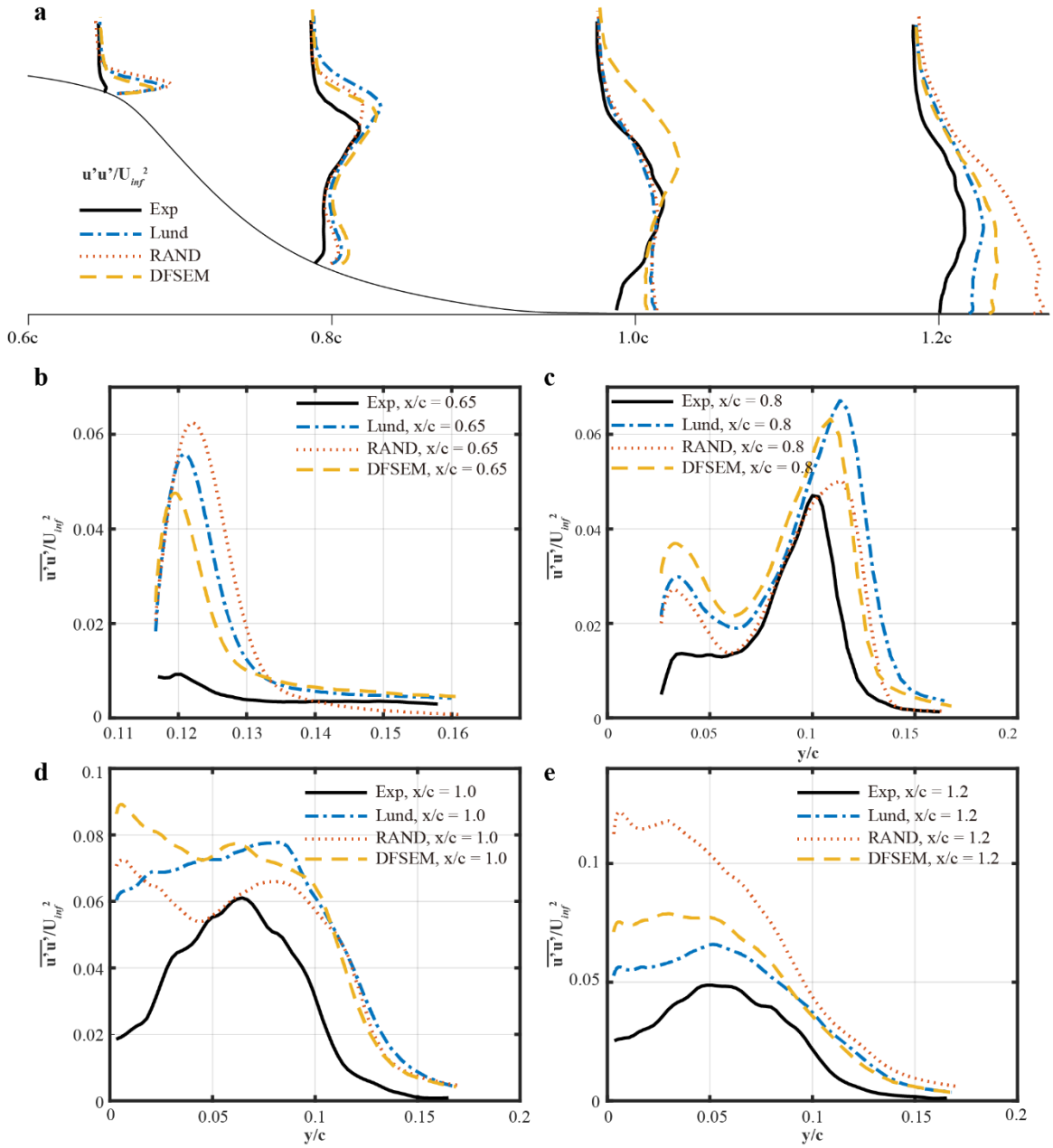


Figure 5.14 Time-averaged streamwise velocity $\overline{u'u'}$ profiles (a) at four stations over the hump (b) x = 0.65c (c) x = 0.8c (d) x = 1.0c (e) x = 1.2c.

Profiles of $\overline{v'v'}/{U_{inf}}^2$ for simulations with different IBCs and experiment are shown in Figure 5.15. At *x/c* = 0.65, the trend of the cases based on the Lund method and DFSEM are same to the experimental data, but the magnitude of $\overline{v'v'}/{U_{inf}}^2$ in cases based on these two methods is as twice as the experimental data when *y/c* = 0.12~0.16, the trend of the simulation based on the RAND method is different. At *x/c* = 0.8, there is a slight deviation between the cases based on the Lund method and DFSEM, the difference between the results of cases using

The content of Chapter 5 is published by the author of this thesis, the paper is *Effect of the Inlet Boundary Conditions on the Flow Over Complex Terrain Using Large Eddy Simulation*

three IBC methods is close to the experimental data. At *x/c* = 1 and 1.2, profiles of simulation case based on RAND method shows large difference to the experimental data, while the results of the simulation cases based on the Lund and RAND methods are closer to the experimental data compared with the simulation based on the RAND method.

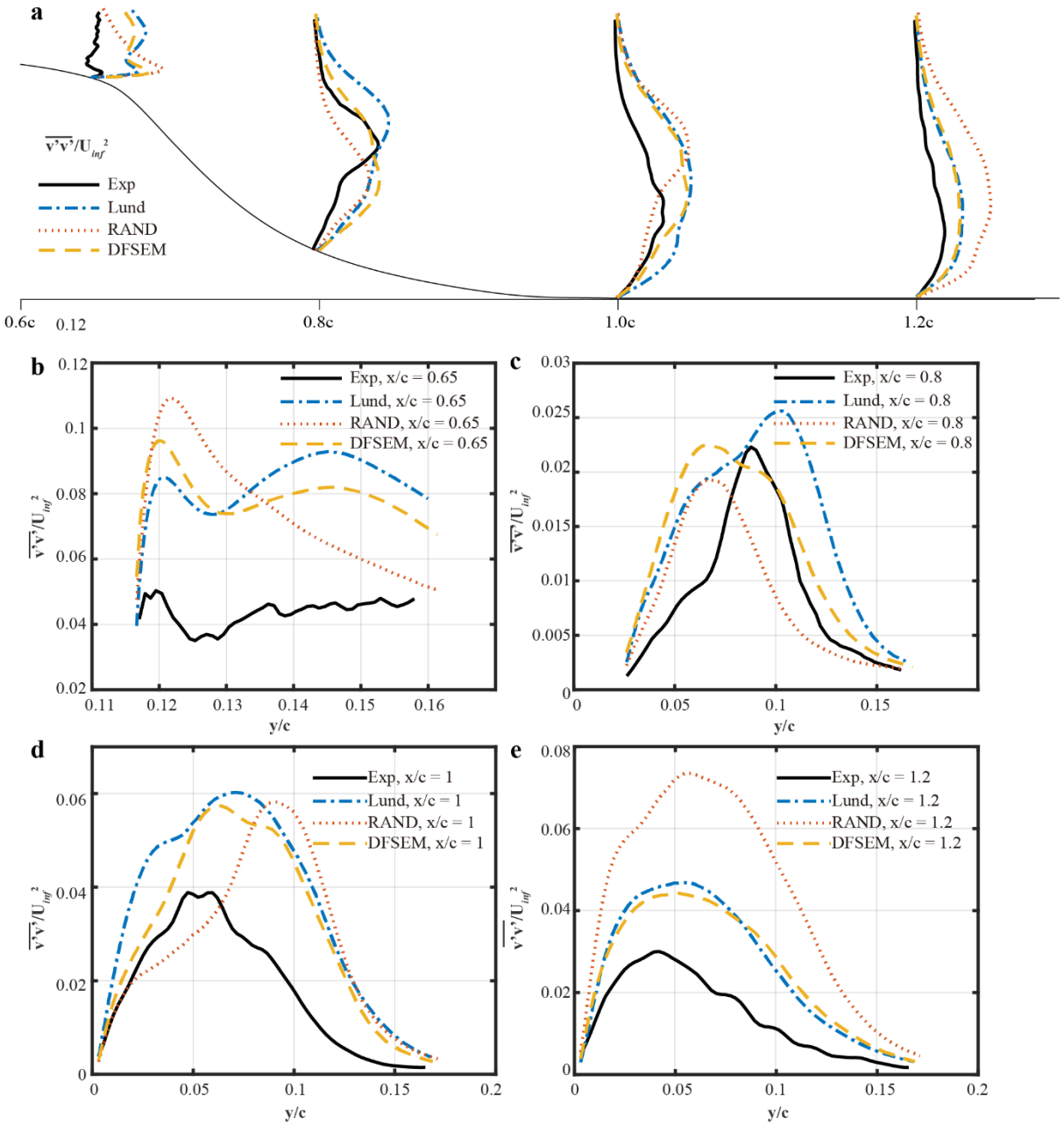
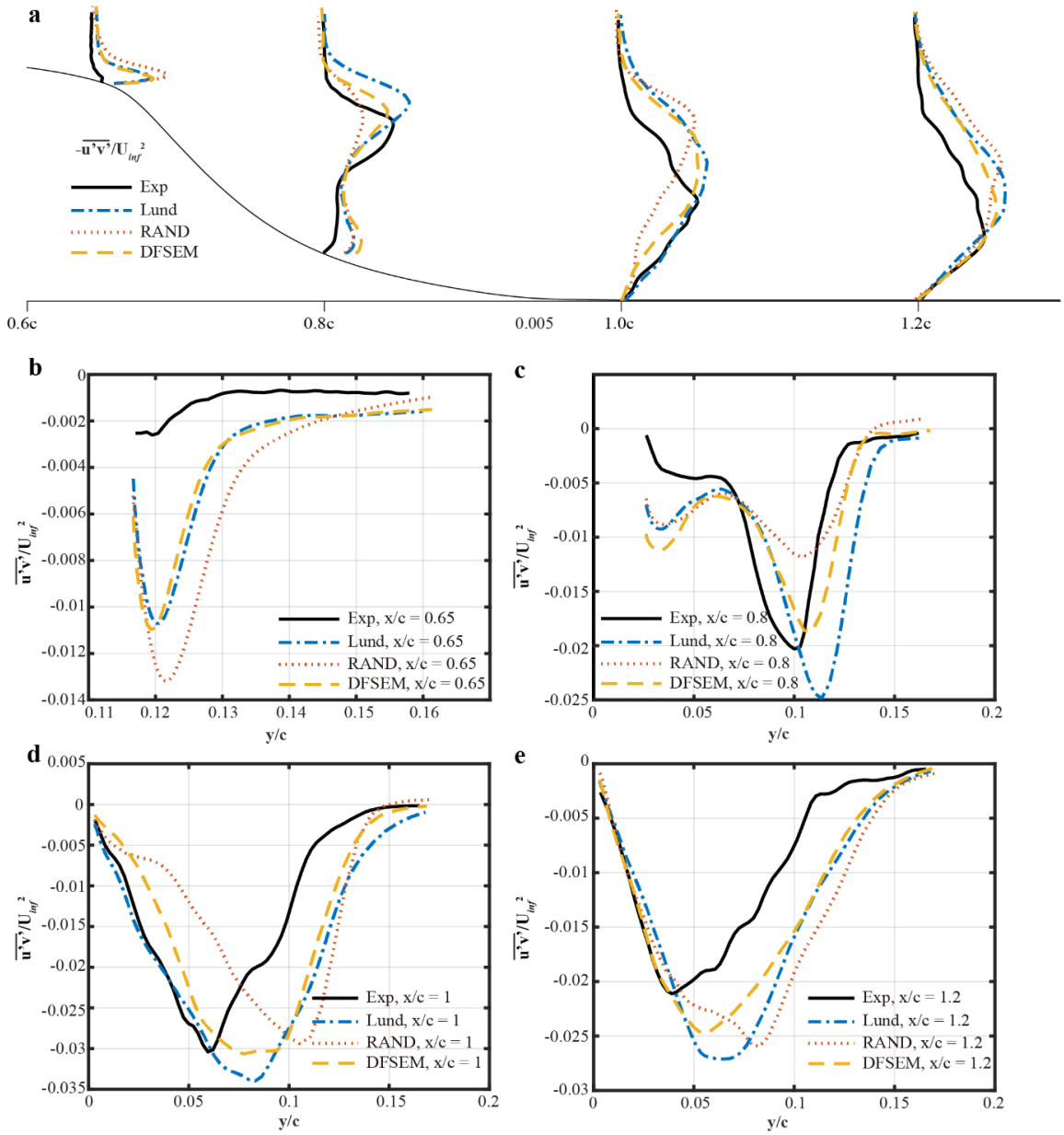


Figure 5.15 Time-averaged Reynolds stress component $\overline{v'v'}/U_{inf}^2$ profiles (a) at four stations over the hump (b) x = 0.65c (c) x = 0.8c (d) x = 1.0c (e) x = 1.2c.

The distribution of $\overline{u'v'}/U_{inf}^2$ along the vertical direction illustrated by Figure 5.16 shows the similar behavior as the profiles of $\overline{u'u'}/U_{inf}^2$ and $\overline{v'v'}/U_{inf}^2$, at the flow separation

The content of Chapter 5 is published by the author of this thesis, the paper is *Effect of the Inlet Boundary Conditions on the Flow Over Complex Terrain Using Large Eddy Simulation*

region (x/c = 0.65 and 0.8). The results of simulation based on the Lund method and DFSEM are closer to the experimental data than the results of simulation based on the Lund and RAND methods, but the deviation is still large at x/c = 0.65. At x/c = 0.8, the simulation results based on three IBC methods are close to the experimental data, especially the case based on DFSEM. In the flow re-attachment region (x/c = 1 and 1.2), the simulation results based on three IBC methods are closer compared with the results in the flow separation region. There is always a slight deviation between the simulation results and the experimental data.



The content of Chapter 5 is published by the author of this thesis, the paper is *Effect of the Inlet Boundary Conditions on the Flow Over Complex Terrain Using Large Eddy Simulation*

Figure 5.16 Time-averaged Reynolds stress component $\overline{u'v'}/{U_{inf}}^2$ profiles (a) at four stations over the hump (b) x = 0.65c (c) x = 0.8c (d) x = 1.0c (e) x = 1.2c.

5.4. Conclusion of this chapter

In this chapter, the impact of three different IBC methods used in LES in the boundary-layer flow with a hump were investigated. Re_θ at the inlet in this flow configuration is 6473.5. It is challengeable to capture the flow details with the extensive flow separation region with this high Reynolds number. Nevertheless, the flow separation after the hump could reflect more details of the effects from different IBC methods.

From the qualitative results, turbulence generated from different IBCs at the region before hump shows apparent differences. In the simulation based on the Lund method, clear turbulent structure can be observed. Due to the artificial periodicity imposed in the flow region during this recycling and rescaling process, the turbulent signal is periodic. In the simulation based on RAND method, it is hard to see the clear coherent turbulent structure before the hump. As the flow develops and gradually approaches the hump, the turbulence generated at the inlet quickly dissipates. In the simulation based on DFSEM, compared with the simulation based on the Lund method, coherent turbulent structures can be observed apparently in the boundary layer. In the region over and after the hump, the differences between the simulation results based on the Lund method and DFSEM method are not great. However, there are still obvious differences between the simulation results based on the RAND method and simulation results based on other methods, which indicates that the coherent turbulence in the approach flow region will significantly affect the flow separation after the hump.

From the quantitative results, mean velocity and turbulent Reynolds stresses profiles are used to reflect the flow details of each simulation. In the simulation based on the Lund method, there is a deviation between the simulation and theoretical results at the beginning, while the deviation gradually decreases as flow moves towards the hump from $x/c = -2$ to $x/c = -0.5$. The scenario is different in the cases based on the RAND method and DFSEM. It is hard to

The content of Chapter 5 is published by the author of this thesis, the paper is *Effect of the Inlet Boundary Conditions on the Flow Over Complex Terrain Using Large Eddy Simulation*

observe the difference between the simulation results and theoretical results at $x/c = -2$, but the difference increases as the main flow approaches the hump from $x/c = -2$ to $x/c = -0.5$. The statement above reflects that turbulence generated by Lund method is likely fully developed in the approach flow region. According to the differences of Reynolds stresses profiles in these simulations with different IBCs, it is obvious that the profiles of streamwise turbulent stresses in Lund method are maintained at different positions before the hump, while the profiles of streamwise Reynolds stresses increase from $x/c = -2$ to $x/c = -0.5$ in the case based on DFSEM and RAND method, there is barely turbulence in the case of RAND at different positions before the hump. This phenomenon indicates that the generated turbulence is stable in the case of Lund and not stable in the case of DFSEM and RAND method. In the flow region after the hump, even if the location of flow separation is nearly the same in these three cases, the effects of different IBCs are more manifested. Firstly, the relative differences between the mean velocity and Reynolds stresses profiles of the simulations based on Lund and DFSEM methods are smaller than 2%. The turbulent bubble size can be predicted relative precisely in these two simulations, there is only a slight deviation (6.6% and 6.4%) in the turbulent statistics profiles between the simulation results and the experimental data. Compared with other simulations, the simulation based on the RAND method shows obvious difference. It cannot capture the flow separation and re-attachment point. Meanwhile, turbulent bubble size in the base based on the RAND method is highly overestimated about 28% larger than the experimental data, hence the RAND method cannot predict the velocity and Reynolds stresses profiles accurately.

From the analysis above, it can be found that the statistical properties of the case based on DFSEM shows a special trend before and after the hump. In the approach flow, the mean velocity profiles of the case based on DFSEM cannot fit the theoretical results and performs like the simulation using the RAND method though the coherent structures could be observed in the approach flow. However, in the flow region over and after the hump, the results of the

The content of Chapter 5 is published by the author of this thesis, the paper is *Effect of the Inlet Boundary Conditions on the Flow Over Complex Terrain Using Large Eddy Simulation*

simulation using DFSEM become much close to the simulation results based on the Lund method, though the mean velocity profiles before the hump is significantly different between these two cases. These features indicate that the stable coherent structure before the hump is not fully developed turbulence, therefore it is hard to gain the mean velocity profiles that are agree well with the wall function. Nevertheless, the not fully developed turbulence is still able to delay the flow separation. Therefore, different turbulent inflow generation methods have a manifested impact on the flow separation after the hump. If the coherent turbulence is maintained in the approach flow, even though turbulent intensity cannot agree well with the experimental date, the simulation can still predict the flow separation and turbulent bubble size relative precisely.

However, there are still some limitations of this study. Firstly, the spanwise width of the simulation domain is relatively small. In the future, spanwise width sensitivity analysis should be applied, and a wider domain would be adopted. Secondly, the LES sub-grid scale model has a great impact on the results. In the future, a more advanced SGS model such as the dynamic Smagorinsky model could be applied. Finally, in the simulation based on DFSEM, the setting of turbulent length scale at the inlet is an important factor affecting the simulation results. In the following work, the influence of turbulent length scales should be considered.

The content of Chapter 5 is published by the author of this thesis, the paper is *Effect of the Inlet Boundary Conditions on the Flow Over Complex Terrain Using Large Eddy Simulation*

Chapter 6

Flat plate boundary layer

6.1. Computational domain and mesh configuration

To validate simulation results based on different IBC methods, a zero pressure gradient flat plate boundary layer is simulated which is identified to the simulation domain used by Lund et al (1998) and the simulation results are compared with the DNS database (Philipp, 2011). The DNS case is used as the benchmark and the description of it can be referred to the work of Philipp (Schlatter and Örlü, 2012).

In this research, the DNS data at the position where $Re_\theta = 1410$ is used as the inlet values for LES cases based on different IBC methods. These IBC methods are Lund method, DFSEM and DFM, respectively. In the simulation based on Lund method, the computational domain consists of two subdomains illustrated in Figure 6.1(a). The first subdomain is called the precursor (or auxiliary) subdomain while the second one is the successor subdomain (Vasaturo et al., 2018). The spatial and temporal correlated instantaneous velocity are generated after the recycling and rescaling procedure in the precursor domain and then introduced in the successor domain. The dimension of the precursor subdomain is $10\delta \times \pi/2\delta \times 3.3\delta$ with the mesh configuration $n_{x_1} \times n_{y_1} \times n_{z_1} = 319 \times 45 \times 64$, where n_{x_1}, n_y and n_z represent the number of cells along the x, y, and z direction respectively and δ represents the boundary layer thickness. The dimension of the successor subdomain is $50\delta \times \pi/2\delta \times 3.3\delta$ with the mesh consists of $n_{x_2} \times n_y \times n_z = 1794 \times 45 \times 64$ cells. Likewise, n_{x_2} represents the number of cells along the x direction in this subdomain. The spanwise and streamwise mesh configuration is the same for both precursor domain and the successor subdomains. The mesh cells are uniformly placed along the streamwise and spanwise directions and exponentially distributed

The content of Chapter 6 is published by the author of this thesis, the paper is *Influence of Turbulent Inlet Boundary Condition on Large Eddy Simulation Over a Flat Plate Boundary Layer*

along the vertical direction. In addition, a cell size ratio 1.12 is adopted in the vertical (y) direction with a first cell height of $y^+ = 1.02$ at the inlet plane.

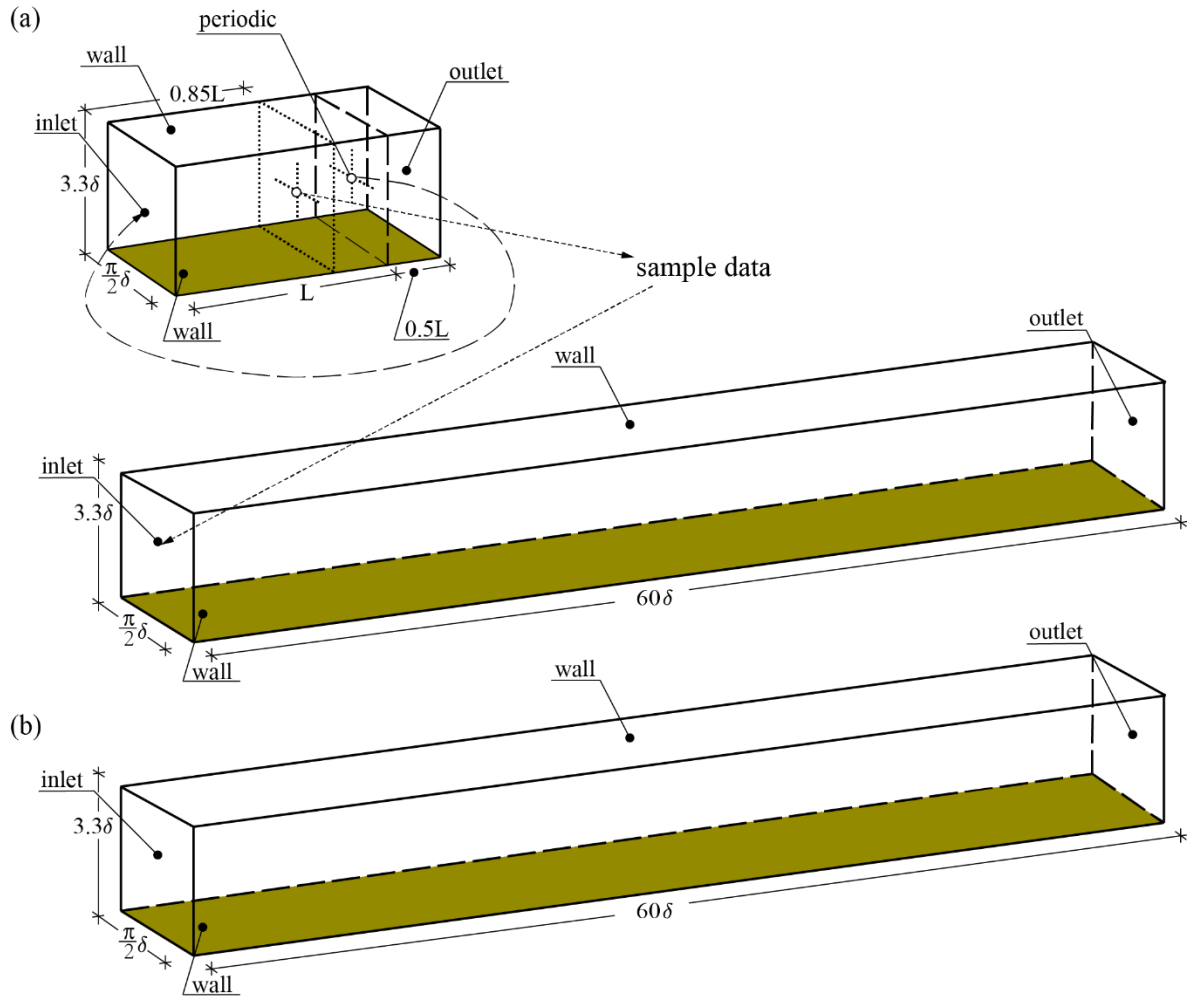


Figure 6.1 Schematic of the computational domains used for the different simulations: (a) Simulation based on Lund method (precursor domain), (b) Simulation based on all methods Lund, DFSEM and DFM (main domain).

Figure 6.1(a) shows how the instantaneous velocity profiles are captured in a periodic plane inside the precursor subdomain and imposed at the inlet plane. The simulation data at the sampled plane of the precursor subdomain is mapped into the inlet of the main computational domain. Figure 6.1(b) shows the computational domain where the DFM and DFSEM are used to generate the instantaneous velocity profiles. According to the statement above, the mesh configuration in this case is strictly orthogonal. Therefore, the uncorrected surface normal gradient scheme is used for each IBC method.

For the turbulent inlet boundary condition, there are three IBC methods implemented in

The content of Chapter 6 is published by the author of this thesis, the paper is *Influence of Turbulent Inlet Boundary Condition on Large Eddy Simulation Over a Flat Plate Boundary Layer*

this work and the first one is based on the Lund method. As described above, Lund method is an approach to extract instantaneous velocity data at a fixed plane in an auxiliary simulation. The auxiliary simulation is spatially developing but generates its own inflow conditions through a sequence of operations where the velocity field at a downstream station is rescaled and re-introduced at the inlet. The rescaling factors are determined by the parameters of turbulent boundary layer thickness (δ), displacement thickness (δ^*) and the momentum thickness (θ) at the beginning. The velocity field should be initialized in the precursor and successor domain firstly, and the mean velocity field is initialized by the δ^* (Araya et al., 2011).

Figure 6.1(a) illustrates the recycling and rescaling procedure of the Lund method, the distance between the inlet plane and the recycle plane is 10 δ. The values of δ and θ are determined from the mean velocity profiles at the inlet, where $\delta^+ = u_\tau \delta/\nu = 5.3$ and $\theta^+ = u_\tau \delta/\nu = 0.68$. In addition, the average time interval is required according to the equation (9). In this case, $\Delta t = 0.09\delta/U_\infty$, T is set as $10\delta/U_\infty$ at the beginning according to the suggestions of Lund. When the flow equilibrates, the averaging interval is increased simultaneously to $100\delta/U_\infty$ to stabilize the statistics and then switching to a simple running average $T = T_0 + t - t_0$, t is the current time in the simulation, t_0 is the time where the running average was initiated, and T_0 is the value of the averaging interval adopted prior to t_0.

The second and third IBC methods used in this work are the DFSEM and the DFM respectively. The target profiles of mean velocity and turbulence quantities are used as input when these methods are employed to generate inflow turbulence. In DFSEM, the synthetic eddies represent a set of velocity fluctuations in the vicinity of the inlet plane where a turbulent field is required. These eddies are determined by their centres and the formula of the velocity distribution around these centres. All these synthetic eddies and the inlet plane are encompassed by a virtual box. Eddies generated at the head of the virtual box are convected by mean flow at each time step. Then, they transverse the inlet plane encircled by the virtual box and finally

The content of Chapter 6 is published by the author of this thesis, the paper is *Influence of Turbulent Inlet Boundary Condition on Large Eddy Simulation Over a Flat Plate Boundary Layer*

leave the box. When they leave the box, they will regenerate anywhere on the head of the box and repeat the process described above. Digital Filter method can be regarded as a tool to deal with a random velocity field. The uncorrelated velocity field is generated at the inlet plane at the beginning, then a specific filter with a defined correlation function is imported to deal with the random field. The procedure of the implementation of these two methods is elaborated in Chapter 3.

Both DFSEM and DFM require the input parameters over the inlet plane incorporating profiles of the mean velocity, the turbulent Reynolds stresses, and the turbulent length scale. Generally, these input parameters can be obtained from the DNS database or from experimental results of interest. From the definition, turbulent length scale is the spatial structure of the fluctuating velocity field that is defined by the two-point correlation, for example:

$$L_i^j(x) \equiv \int_0^\infty \frac{\overline{u_i'(x)u_i'(x+\boldsymbol{e_j}r)}}{\overline{u_i'(x)u_i'(x)}}dr \tag{51}$$

In equation (51), r is the space lag in the j direction. There are 9 components that should be determined according to this equation if there are sufficient DNS results or high-resolution results of experimental data. Otherwise, the integral length scale is computed by Taylor's hypothesis with autocorrelation and only one components needs to be considered (Lamberti et al., 2018a). As the description of Vita et al. (2020), the streamwise integral length scale L_u is estimated from the autocorrelation coefficient:

$$L_u = U\int_0^\infty \frac{\overline{u_i'(x)u_i'(x+\boldsymbol{e_j}r)}}{\overline{u_i'(x)u_i'(x)}}dr = U\int_0^{\tau_0}\rho(\tau)\,d\tau \tag{52}$$

In equation (52), $\rho(\tau)$ is the autocorrelation coefficient, τ is the time lag and τ_0 is the value of τ where $\rho(\tau_0) = 0$. From the work of Boris (Boris, 2012), $L_u = UT_u$ where T_u is the integral time scale obtained from the area comprised by the $\rho(\tau)$ curve, which can be approximated by a simplified approximation that $\rho(T_u) = 1/e$. However, it is generally hard to have access to the data applied for the calculation of turbulent length scales. In this work, the profiles of the

The content of Chapter 6 is published by the author of this thesis, the paper is *Influence of Turbulent Inlet Boundary Condition on Large Eddy Simulation Over a Flat Plate Boundary Layer*

mean velocity and turbulent Reynolds stresses are accessible while the profiles of the turbulent length scales are inaccessible. Moreover, there is no instantaneous velocity data accessible, hence the profiles of the turbulent length scale should be obtained by other method such as the Lund method. As the statement above concluded, the simulation results based on DFM are not sensitive to the slight difference of profiles of the turbulent length scale (Lee et al., 2021). Therefore, it is reasonable to adopt the constant values as the turbulent length scale.

Table 6-1 Turbulent length scales applied at the inlet boundary together with DFM

	Giacomo (2018)	Xie (2008)	Lee (2021)	Present study
L_u^x	UT_u	Two-point correlation	UT_u	$(0.1-10)\delta$
L_v^x	UT_v	Two-point correlation	UT_v	$0.33L_u^x$
L_w^x	UT_w	Two-point correlation	UT_w	$0.33L_u^x$
L_u^y	$0.2UT_u$	$0.67L_u^z$	$0.67L_u^z$	$0.235L_u^x$
L_v^y	$0.2UT_u$	L_u^y	L_u^y	$0.235L_u^x$
L_w^y	$0.2UT_u$	L_u^y	L_u^y	$0.235L_u^x$
L_u^z	$0.3UT_u$	$\frac{(0.35-0.57)}{max(L_u^x)}$	$\frac{(0-1.2)}{max(L_u^x)}$	$0.35L_u^x$
L_v^z	$0.3UT_u$	L_u^z	L_u^z	$0.35L_u^x$
L_w^z	$0.3UT_u$	L_u^z	L_u^z	$0.35L_u^x$

Table 6-1 shows the input of the values of turbulent length scales in different studies based on DFM. The values of turbulent length scale in the x-direction are calculated through (51) and (52) with the previous DNS data or the experimental data. In other words, simulations in these studies are on basis of the previous temporal DNS or experimental database. According to the previous research, in the context of wall-bounded flows where there are large variations in length scales. Therefore the imposition of precise length scales at the inlet was not attempted (Veloudis et al., 2007).

The content of Chapter 6 is published by the author of this thesis, the paper is *Influence of Turbulent Inlet Boundary Condition on Large Eddy Simulation Over a Flat Plate Boundary Layer*

Table 6-2 Turbulent length scales applied at the inlet boundary together with SEM or DFSEM

	(Jarrin et al., 2006)	Poletto et al. (2013)	Present study
L	0.1δ, 0.2δ and 0.4δ	$min\left(k^{3/2}/\varepsilon\,, \kappa\delta, \max(\Delta x, \Delta y, \Delta z)\right)$	$(0.1-10)\delta$

From previous studies shown in the Table 6-1, L_y is simply taken as $0.67L_z$. The profile of the turbulent length scale in the work of Iwamoto (2002) are shown like the quadratic profile, which means that the turbulent length scale in the near wall region ($y^+ < 15$) is much smaller than that in the middle of buffer layer zone, log layer zone and the outer region in the boundary layer ($15 < y^+ < \delta$). Lee et al (2021) found that the length scale variation in the region of approximately $15 < y^+ < 30$ contributed significantly to the generation of turbulent energy near the wall surface. From their simulation results, turbulent length scale variation in other regions ($y^+ < 15, y^+ > 30$) have limited effects on the development length, i.e., the recovery of the wall shear stress. This indicates that the constant turbulent length scale as the input parameter is accessible.

Table 6-2 shows the settings of input turbulent length scale in different studies based on SEM or DFSEM. In the work of Jarrin et al, L is selected corresponding roughly to the Prandtl mixing length at the top of log-layer (Jarrin et al., 2006). In the work of Poletto (2013), L is determined by the empirical equation, where $k^{3/2}/\varepsilon$ is the local length-scale provided by the DNS data or come from the RANS model in a typical embedded LES application, κ is the Von-Karman constant and δ is the channel half-height. $\Delta x, \Delta y, \Delta z$ is the local mesh size along different directions. In the present study, due to the limitation of the database, it is hard to obtain the data applied for the calculation of turbulent length scale with (51) or (52). Hence, it is reasonable to adopt a constant value as the input turbulent length for the simulation based on DFM and DFSEM. Prandtl introduced the concept of a mixing length and the Prandt's mixing length closure model has been used extensively to describe the eddy viscosity (Hutchinson et al., 2021). The mixing length theory was successfully applied in free shear flows and turbulent

The content of Chapter 6 is published by the author of this thesis, the paper is *Influence of Turbulent Inlet Boundary Condition on Large Eddy Simulation Over a Flat Plate Boundary Layer*

wall flows (Egolf, 1994). In a Smagorinksy scheme (Smagorinsky, 1963), the eddy-diffusivity depends on the shear and the mixing length. The latter usually represents the typical size of the energy-containing sub-grid eddies (Honnert et al., 2021). For LES, the turbulent length scale input for the DFSEM and DFM should be larger than the scale of sub-grid eddies, therefore it can be determined by Prandtl mixing length at the top of log-layer, like the value determined in the research of Jarrin (2006), in which the value of the mixing length $L_m = \kappa\delta$ ($\kappa = 0.41$). The similar settings can be found in the commercial software, Fluent. For wall-bounded flows where the inlets involve a turbulent boundary layer, the turbulent length scale is calculated by using the boundary layer thickness, and the turbulent length scale $L = 0.4\delta$. In this study, there is $L_u^x = L = 0.4\delta$ (Fluent Inc, 2006). L_u^x and L are the input turbulent length scales for simulations based on DFM and DFSEM respectively. From the two-point correlation DNS data of Iwamoto (2002), the relationship between different turbulent length scales can be estimated as the values shown in the last column of the Table 6-1. Likewise, L_y is set as $0.67L_z$. However, the crude guess of the constant turbulent length scale as the input parameter is not reliable. Therefore, it is significant to explore the influence of the values of L_u^x and L for simulations based on DFM and DFSEM, the analysis is shown in the section 6.2.

Table 6-3 Summary of the mesh configurations

IBC	**Mesh Size (x, y, z)**	$\Delta x^+ = 14.5$
Lund (Precursor)	$319 \times 45 \times 64$	$\Delta y^+ = 1.025$
Lund (Main)	$1794 \times 45 \times 64$	$\Delta z^+ = 13.75$
DFM/DFSEM	$2113 \times 45 \times 64$	$\Delta x^+/\Delta y^+ \approx 4.5\pi$ $\Delta z^+/\Delta y^+ \approx 4.3\pi$

According to the discussion above, detailed settings of simulations with different IBCs are summarized in Table 6-3. Table 6-4 shows the cases of mesh sensitivity analysis for the LES. In this study, i.e., cases based on different IBC methods with different mesh configuration is described.

The content of Chapter 6 is published by the author of this thesis, the paper is *Influence of Turbulent Inlet Boundary Condition on Large Eddy Simulation Over a Flat Plate Boundary Layer*

Table 6-4 Mesh configurations for different mesh size

	Mesh Size (x, y, z)	Δx^+	Δy^+	Δz^+
Coarse	$1850 \times 40 \times 56$	16.56	1.89	15.71
Middle	$2113 \times 45 \times 64$	14.5	1.025	13.75
Fine	$2419 \times 51 \times 73$	12.67	0.945	12.05

The results are reflected by Figure A4 to Figure A12 into the appendices. It is apparent that the middle mesh size is enough in this study. Table 6-3 and Table 6-4 present the mesh configuration, the values of Δx^+, Δy^+ and Δz^+ and the values of the largest aspect ratio along the vertical and streamwise directions respectively.

Table 6-5 Summary of the inflow boundary conditions

	Mean velocity(m/s)	Specified thicknesses	Turbulent Reynolds stresses	Turbulent length scales
Lund	DNS	DNS	—	—
DFSEM	DNS	—	DNS	Constant
DFM	DNS	—	DNS	Constant

Table 6-5 shows the input parameters required in simulations based on different IBC methods. The specified thicknesses here indicate δ, $\delta^*$and θ. The profiles of mean velocity and turbulent Reynolds stresses are determined by the DNS data while the profiles of turbulent length scale are set as different constant values. The sensitivity of the spanwise length scales is explored by Lee, which indicates that the larger spanwise length scale used in the simulation can reduce the development length. When the spanwise length is large enough, it is hardly to see the effect of this value on the development length from the simulation results (Lee et al., 2021).

A no-slip condition on the bottom walls and a slip condition on the top wall is used. Periodic boundary condition in the lateral direction and zero-gradient condition with no diffusion of all the flow variables on the outlet is adopted.

The content of Chapter 6 is published by the author of this thesis, the paper is *Influence of Turbulent Inlet Boundary Condition on Large Eddy Simulation Over a Flat Plate Boundary Layer*

6.2. Length sensitivity analysis

The decision of the turbulent length scale is still hard. From the previous studies, there is a conclusion that the vertical and spanwise turbulent length scales have limited effect on the simulation results while the cordial parameter is the streamwise turbulent length scale. However, all these studies determined the values of streamwise length scale by using two-correlation or one-point correlation with Taylor's hypothesis. This operation is still not convenient. Therefore, it is reasonable to explore whether we can use the constant values of the input parameters for turbulent length scale and investigate the comparison between input parameters of constant turbulent length scale. According to the analysis in the Section 6.1, the input turbulent length scale can be determined by the Prandtl's mixing length i.e., the boundary layer thickness multiplied by a factor and the value of the factor is around 0.4.

. However, there might be a series of values can be selected as the factor. In the zero pressure gradient boundary layer, the fully developed turbulence can only be observed in the boundary layer (S. B. Pope, 2001). The turbulent length scale input for the DFM and DFSEM probably lies in the range that is $(0.4-1)\delta$. To verify this assumption, it is important to make a sensitivity analysis of the turbulent length scale determined by different factors multiplied by the boundary layer thickness. The cases based on DFM and DFSEM in this study are listed in Table 6-6.

Table 6-6 Inlet turbulent length scales applied in the simulation

	DFM(L_u^x)		**DFSEM**(L)
Case 1	0.02δ	**Case 8**	0.02δ
Case 2	0.1δ	**Case 9**	0.1δ
Case 3	0.2δ	**Case 10**	0.2δ
Case 4	0.4δ	**Case 11**	0.4δ
Case 5	0.6δ	**Case 12**	0.6δ

The content of Chapter 6 is published by the author of this thesis, the paper is *Influence of Turbulent Inlet Boundary Condition on Large Eddy Simulation Over a Flat Plate Boundary Layer*

Case 6	1δ	**Case 13**	1δ
Case 7	2δ	**Case 14**	2δ

Non-dimensional turbulent kinetic energy budgets have been computed in these simulations. The budget terms are described in equations:

$$\mathrm{P} = -\langle u_i u_j \rangle \frac{\partial \langle U_i \rangle}{\partial x_j} \tag{53}$$

$$\overline{\mathrm{T}} = \underbrace{\frac{1}{2}\langle u_i u_j u_j \rangle}_{\overline{T_t}} + \underbrace{\frac{\langle u_i p' \rangle}{\rho}}_{\overline{T_p}} - \underbrace{2\upsilon \langle u_j s_{ij} \rangle}_{\overline{T_\upsilon}} \tag{54}$$

$$\varepsilon = 2\upsilon \langle s_{ij} s_{ij} \rangle \tag{55}$$

The production term P plays a critical role in removing kinetic energy from the mean flow and transferring it to the fluctuating velocity field. The term $\nabla \cdot \bar{T}$ represents the rate of turbulent kinetic energy transportation from the large eddies to the successively smaller and smaller eddies. It consists of three terms, including the turbulent convection term, the pressure term, and the viscous diffusion term. ε is the dissipation rate. The friction velocity u_τ is used to non-dimensionalize these turbulent kinetic energies (TKE) budget terms.

6.2.1. The Digital Filter Method (DFM))

Figure 6.2-Figure 6.8 show the typical properties of the flow details of the simulation based on DFM with different input turbulent length scale (L_u^x).

The content of Chapter 6 is published by the author of this thesis, the paper is *Influence of Turbulent Inlet Boundary Condition on Large Eddy Simulation Over a Flat Plate Boundary Layer*

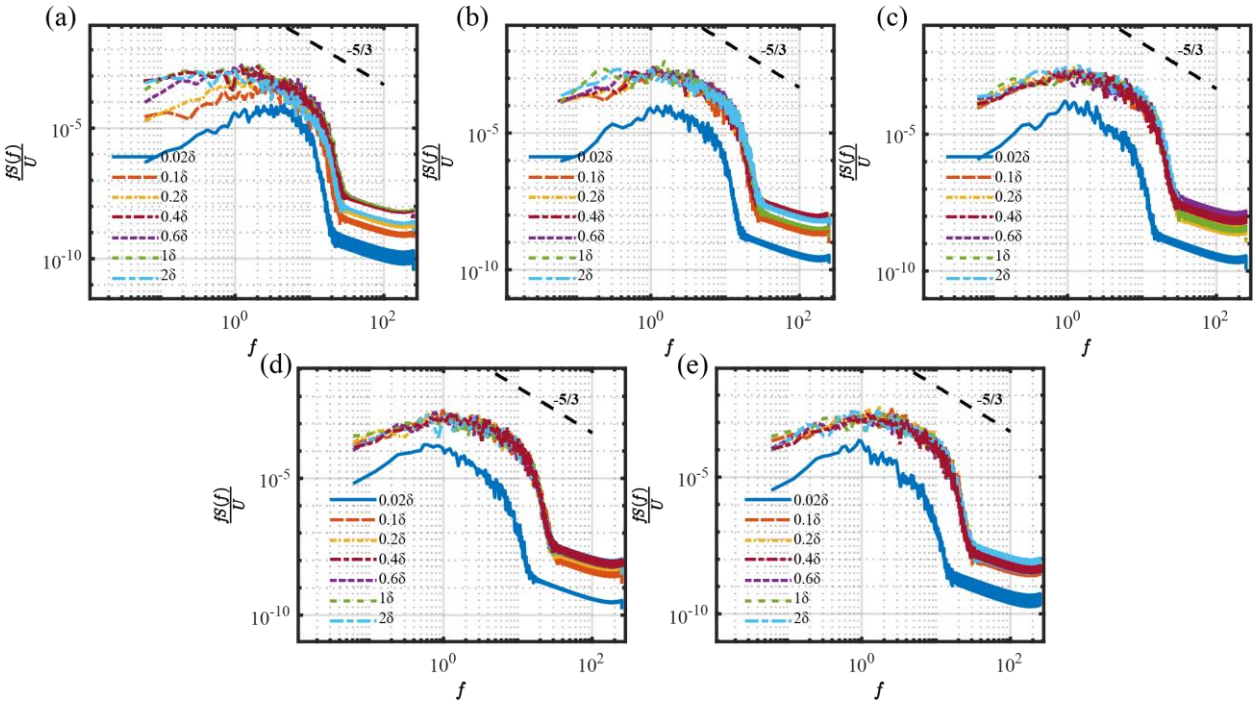


Figure 6.2 The profiles of the turbulent kinetic energy spectrum of the simulation based on DFM with different input turbulent length scales at the same vertical position where $y = 0.5\delta$ $(y^+ = 300)$ *and distinctive horizontal positions where (a)* $x = 10\delta$ *(b)* $x = 20\delta$ *(c)* $x = 30\delta$ *(d)* $x = 40\delta$ *(e)* $x = 50\delta$

Figure 6.2 presents the spectra of velocity at the downstream location of interest at a height of 0.5δ. The highest frequency captured by the LES was approximately 50 Hz, as indicated by the energy decay above this frequency. In the inertial sub-range of resolved scales where $f = 1{\sim}50Hz$, the LES spectra were in good agreement with the -5/3 power law when different values of the input turbulent length scale were used apart from $L_u^x = 0.02\delta$. Moreover, the deviations between simulations with different input turbulent length scales were clearly observed at $x = 10\delta$, whereas the differences at other downstream locations were not significant, except for the simulation with $L_u^x = 0.02\delta$. The results indicate that the profiles of the power spectrum of the inflow turbulence generated by DFM with $L_u^x = 0.02\delta$ could not match the profiles of that generated by the DFM with other turbulent length scales. The profiles of the power spectrum with $L_u^x = 0.4\delta$, $0.6\,\delta$ and 1δ were nearly coincident from $x = 10\delta$–50δ.

The content of Chapter 6 is published by the author of this thesis, the paper is *Influence of Turbulent Inlet Boundary Condition on Large Eddy Simulation Over a Flat Plate Boundary Layer*

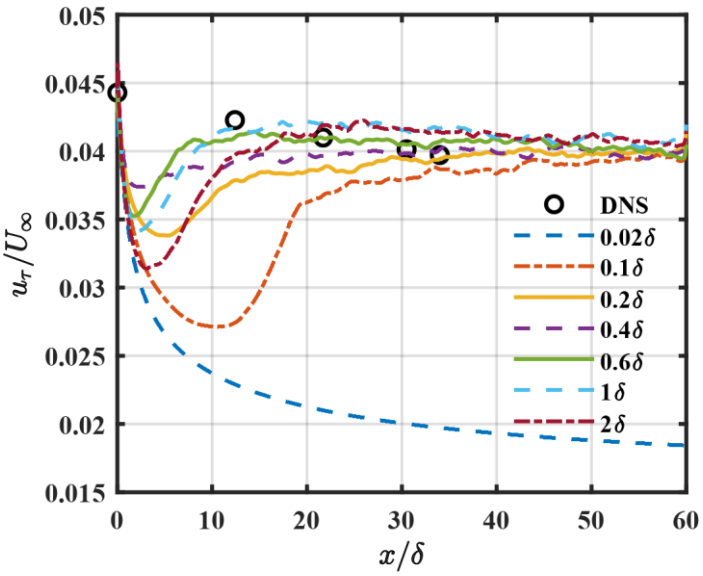


Figure 6.3 The profiles of friction velocity along the streamwise direction based on DFM with different input turbulent length scale

Figure 6.3 presents the development of the wall friction velocity downstream of the inlet for simulations based on the DFM with six input turbulent length scales. When the input turbulent length scale L_u^x was in the range of $(0.1-2)\delta$, there was an abrupt decrease in the friction velocity downstream before recovery to the fully developed value. For the cases where $L_u^x = 0.1\delta, 0.2\delta$ and 0.4δ, the friction velocity exhibited a downward trend at the early stage, and then profiles of the friction velocity gradually increased. In comparison, for the case where $L_u^x = 0.6\delta, 1\delta,$ and 2δ, there was a typical decrease and recovery after the inlet, whereas the friction velocity exhibited a slight downward trend. The shape of the distribution of the friction velocity is like the T3A experiment, where the friction coefficient has a faster rate of decline in the laminar flow than that in the turbulent flow when the value of Re_x was rising (Roach and Brierlay, 1989). Therefore, the trend of friction velocity in the cases where $L_u^x = 0.6\delta, 1\delta,$ and 2δ can reflect the transition of the flow from the laminar condition to the turbulent condition. For a turbulent boundary layer, the distribution of the friction coefficient is monotonically decreasing as indicated by Shahinfar et al. (2013). Besides, the monotonicity of the friction velocity and the friction coefficient is the same and the monotonicity of the value of x/δ and Re_x is the same in the turbulent boundary layer. In this study, in the simulations

The content of Chapter 6 is published by the author of this thesis, the paper is *Influence of Turbulent Inlet Boundary Condition on Large Eddy Simulation Over a Flat Plate Boundary Layer*

based on the DFM, the velocity coefficient increased at the early stage, and then gradually decreased. This process indicates that physical turbulent structures were established in this domain. Therefore, the profiles of the friction velocity in the simulation cases where $L_u^x = 0.6\delta, 1\delta$ and 2δ were accurate, and the simulation case where $L_u^x = 0.6\delta$ exhibited a shorter recovery length of the friction velocity. However, the values of friction velocity of the cases with $L = 0.6, 1\delta$ and 2δ are slightly smaller than the DNS results. In the case where $L_u^x = 0.02\delta$, the friction velocity decreased abruptly without increasing after a long distance, which indicates that turbulence generated at the inlet could not be maintained and dissipated.

Figure 6.4 presents the distribution of the mean velocity profiles of the simulations based on the DFM. As observed, the case with $L_u^x = 0.02\delta$ could not capture the law of the wall at the different positions along the streamwise direction. Moreover, the deviation between the mean velocity profile in this case and the law of the wall increased from $x/\delta = 10$ to $x/\delta = 50$. The deviation indicates that the turbulent boundary layer was not formed in this case. In contrast, in the simulation cases with $L_u^x = (0.1-2)\delta$, mean velocity profiles in these cases were in good agreement with the law of the wall after a sufficiently long distance. The cases with $L_u^x = 0.4\delta, 0.6\delta$ and 1δ required shorter distances to generate velocity profiles in accordance with the law of the wall, and the distance for cases with $L_u^x = 0.1\delta, 0.2\delta,$ and 2δ exceeded 20δ. Therefore, the profiles of the mean velocity confirm that the cases with $L_u^x = 0.4\delta, 0.6\delta$ and 1δ corresponded to shorter development lengths.

The content of Chapter 6 is published by the author of this thesis, the paper is *Influence of Turbulent Inlet Boundary Condition on Large Eddy Simulation Over a Flat Plate Boundary Layer*

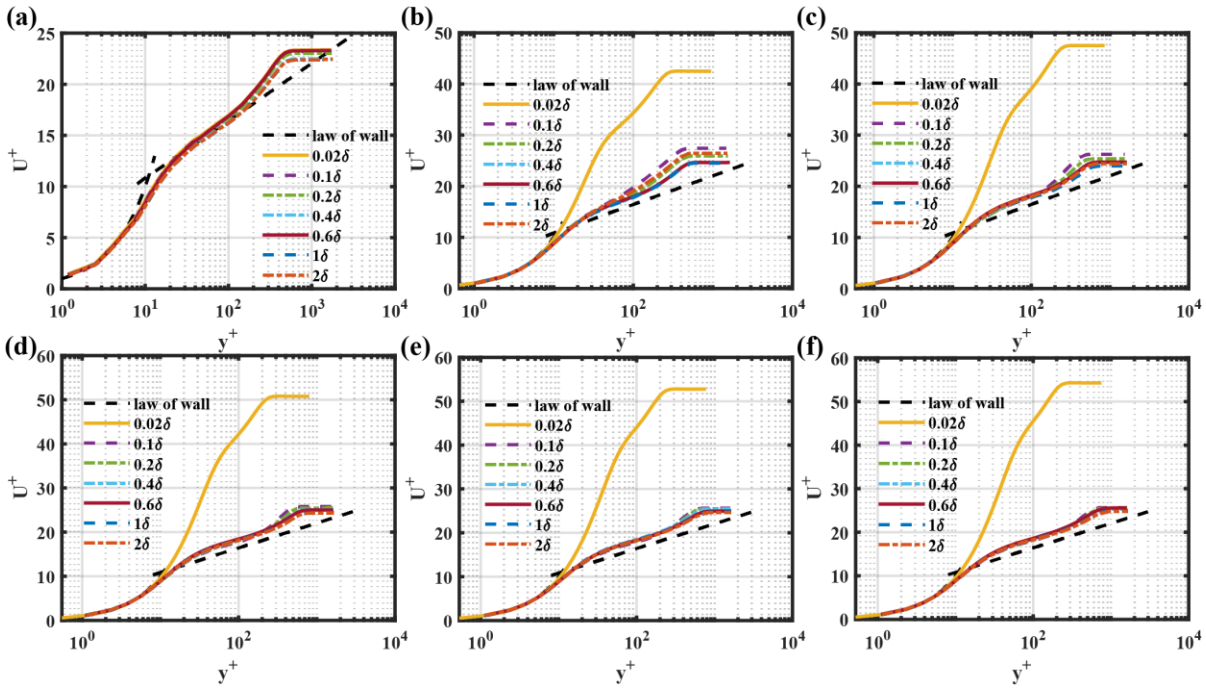


Figure 6.4 Distribution of the mean velocity profiles of simulations based on DFM with different input turbulent length scales at different positions: (a) x=inlet (b) $x/\delta = 10$ *(c)* $x/\delta = 20$ *(d)* $x/\delta = 30$ *(e)* $x/\delta = 40$ *(f)* $x/\delta = 50$

Figure 6.5-Figure 6.7 present the profiles of different turbulent Reynolds stresses components at different positions along the streamwise direction. The profiles of $\sqrt{\overline{u'u'}}$ are presented in Figure 6.5. As can be seen from the figure, the profiles of the streamwise component of the turbulent Reynolds stresses in different cases gradually approached the DNS results at different downstream positions, except for $L_u^x = 0.02\delta$. Besides, there was a deviation between the profiles of the Reynolds stresses of simulations with different L_u^x values and the DNS results. The deviation was distributed over the region of $8 < \mathrm{y}^+ \leq 20$ and $\mathrm{y}^+ > 700$. In these regions, the streamwise fluctuating velocity profiles of simulations with different values of L_u^x exceeded those of the DNS. The case with $L_u^x = 0.6\delta$ could reach a stable condition within a shorter distance of approximately 10δ when compared with the other cases. Besides, all the profiles of $\sqrt{\overline{u'u'}}$ were nearly coincident after approximately $\frac{x}{\delta} = 40$, except for $L_u^x = 0.02\delta$. The vertical fluctuating profiles of $\sqrt{\overline{v'v'}}$ are shown in Figure 6.6. Likewise, the case with $L_u^x = 0.02\delta$ is not capable of fitting the profiles of DNS. For the profiles of $\sqrt{\overline{v'v'}}$

The content of Chapter 6 is published by the author of this thesis, the paper is *Influence of Turbulent Inlet Boundary Condition on Large Eddy Simulation Over a Flat Plate Boundary Layer*

the case with $L_u^x = 0.02\delta$ was not in good agreement with the DNS profiles. For the profiles of $\sqrt{\overline{v'v'}}$ in the cases with other values of L_u^x, the difference was significant at positions where $x/\delta \leq 40$, and the $\sqrt{\overline{v'v'}}$ profiles of cases with $L_u^x = 0.4\delta$, 0.6δ and 1δ could agree well with the DNS results. However, a phrase difference between the LES and DNS results was observed even at $x/\delta = 50$.

Figure 6.7 presents the distribution of the spanwise fluctuating velocity $\sqrt{\overline{w'w'}}$ along the vertical direction. Similar to the profiles of $\sqrt{\overline{v'v'}}$ and $\sqrt{\overline{u'u'}}$ presented in Figure 6.5 and Figure 6.6, respectively, the profiles of $\sqrt{\overline{w'w'}}$ in the case with $L_u^x = 0.02\delta$ did not match the DNS results at different downstream positions. Besides, there was no apparent difference between the LES results with $L_u^x = (0.1 - 2)\delta$ at positions where $x/\delta \geq 40$. At the position where $x/\delta = 10$, the profiles of $\sqrt{\overline{w'w'}}$ in the case with $L_u^x = 0.4\delta$ and 0.6δ is more closed to the DNS result when compared with the other cases. In addition, the profiles of $\sqrt{\overline{w'w'}}$ in the cases with $L_u^x = 0.1\delta$ and 0.2δ were lower than the DNS result, whereas the profiles of $\sqrt{\overline{w'w'}}$ in the cases with $L_u^x = 1\delta$ and 2δ were slightly larger than the DNS result. All the profiles of the cases with different L_u^x values, except for $L_u^x = 0.02\delta$, gradually approached the DNS results at different downstream positions. Moreover, the deviation between the LES and DNS results was not apparent after $x/\delta = 40$, except for the case with $L_u^x = 0.02\delta$. The profiles of the turbulent shear stress component $\overline{u'v'}$ are presented in Figure 6.7. As can be seen from the figure, the results of cases with different values of L_u^x values did not match the DNS profiles at $x/\delta = 10$; whereas the deviation between the LES and DNS results gradually decreased at different downstream locations. The case with $L_u^x = 0.4\delta$ and 0.6δ is more closed to the profiles of the DNS.

The content of Chapter 6 is published by the author of this thesis, the paper is *Influence of Turbulent Inlet Boundary Condition on Large Eddy Simulation Over a Flat Plate Boundary Layer*

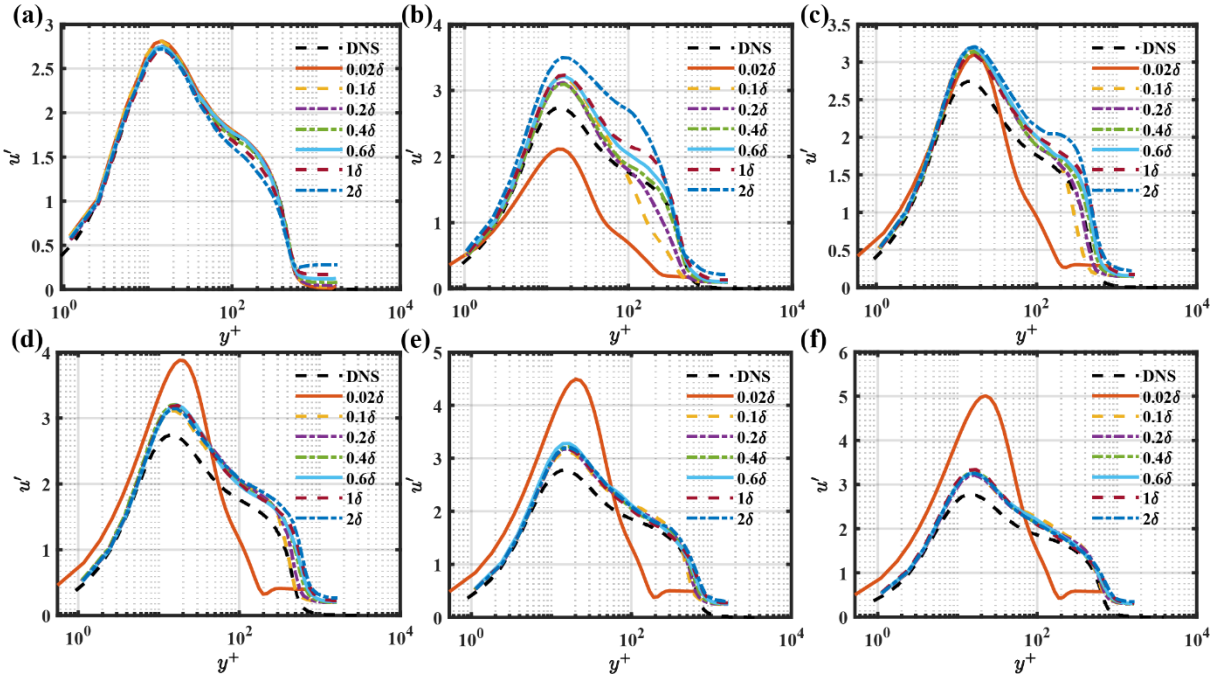


Figure 6.5 Distribution of the streamwise fluctuating velocity profiles of simulations based on DFM with different input turbulent length scales at different positions: (a) x=inlet (b) $x/\delta = 10$ (c) $x/\delta = 20$ (d) $x/\delta = 30$ (e) $x/\delta = 40$ (f) $x/\delta = 50$

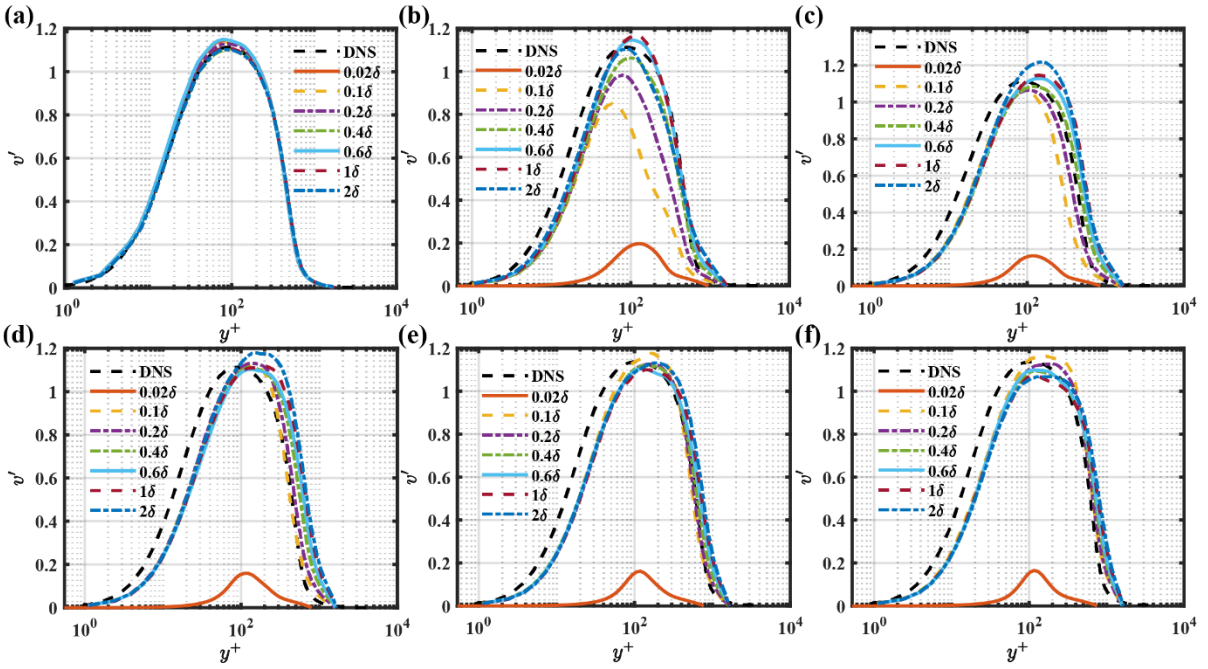


Figure 6.6 Distribution of the vertical fluctuating velocity profiles of simulations based on DFM with different input turbulent length scales at different positions: (a) x=inlet (b) $x/\delta = 10$ (c) $x/\delta = 20$ (d) $x/\delta = 30$ (e) $x/\delta = 40$ (f) $x/\delta = 50$

The content of Chapter 6 is published by the author of this thesis, the paper is *Influence of Turbulent Inlet Boundary Condition on Large Eddy Simulation Over a Flat Plate Boundary Layer*

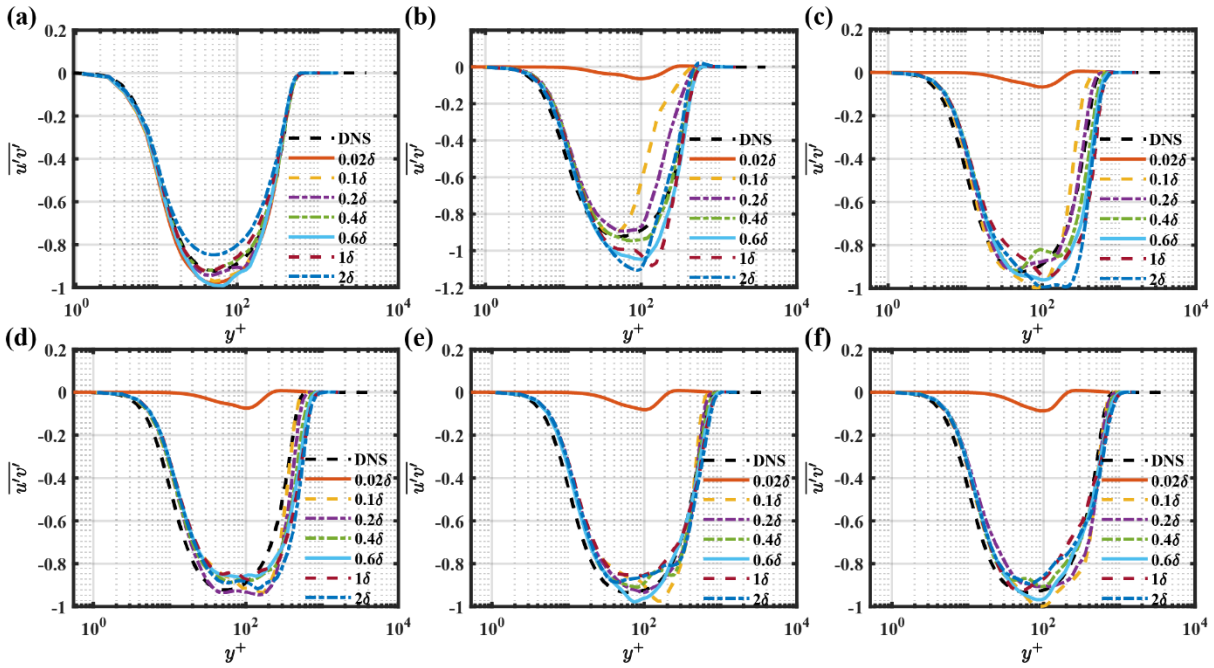


Figure 6.7 Distribution of the Reynolds shear stresses profiles of simulations based on DFM with different input turbulent length scales at different positions: (a) x=inlet (b) $x/\delta = 10$ (c) $x/\delta = 20$ (d) $x/\delta = 30$ (e) $x/\delta = 40$ (f) $x/\delta = 50$

Figure 6.8 and Figure 6.9 illustrate the profiles of the production and dissipation terms of the turbulent kinetic energy. In Figure 6.8 (a), it can be observed that the values of turbulent kinetic energy production in the simulation case with $L_u^x \geq 0.2\delta$ is larger than that of the DNS data and the profile of the case with $L_u^x = 0.1\delta$ is slightly smaller than that of the DNS data, while the distinction of these profiles is relatively small. However, when $L_u^x = 0.02\delta$, there is a big gap between the results of LES and DNS, the production term of the case with $L_u^x = 0.02\delta$ is much smaller than the values of the DNS result. At different positions along the streamwise direction from $x/\delta = 10$ to $x/\delta = 50$, the difference between the simulation results of LES and DNS can be nearly neglected except the case with $L_u^x = 0.02\delta$. Figure 6.9 illustrates the turbulent kinetic energy dissipation of the cases based on DFM with different L_u^x. The big difference between the profiles of LES and DNS can be observed at the inlet as shown in Figure 6.9 (a). At the position where $x/\delta = 10$ as shown in Figure 6.9 (b), the deviation between the results of cases with different L_u^x except $L_u^x = 0.02\delta$ and the DNS result becomes apparently smaller compared with that at the inlet. At the positions where $x/\delta > 10$, the results

The content of Chapter 6 is published by the author of this thesis, the paper is *Influence of Turbulent Inlet Boundary Condition on Large Eddy Simulation Over a Flat Plate Boundary Layer*

of cases with $L_u^x \geq 0.1\delta$ nearly coincide each other, and an obvious gap can be observed between the profiles of the results of LES and DNS. The gap can maintain and keep stable at different downstream positions. It means that the dissipation of the LES based on DFM with different L_u^x is not large enough.

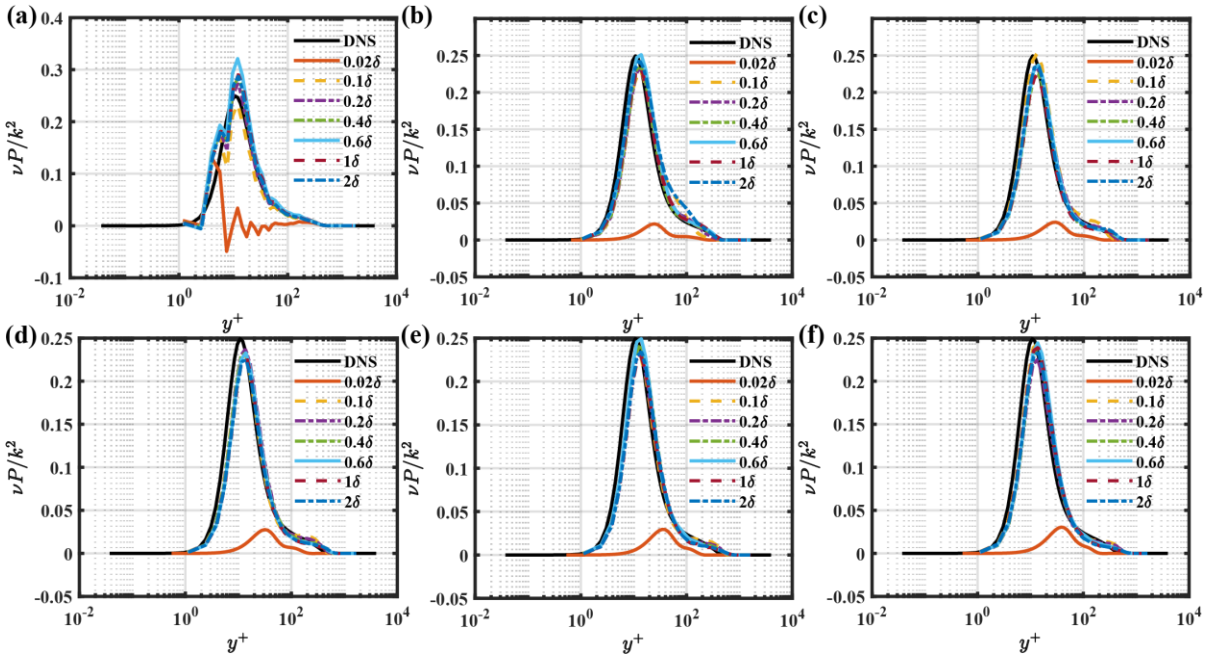
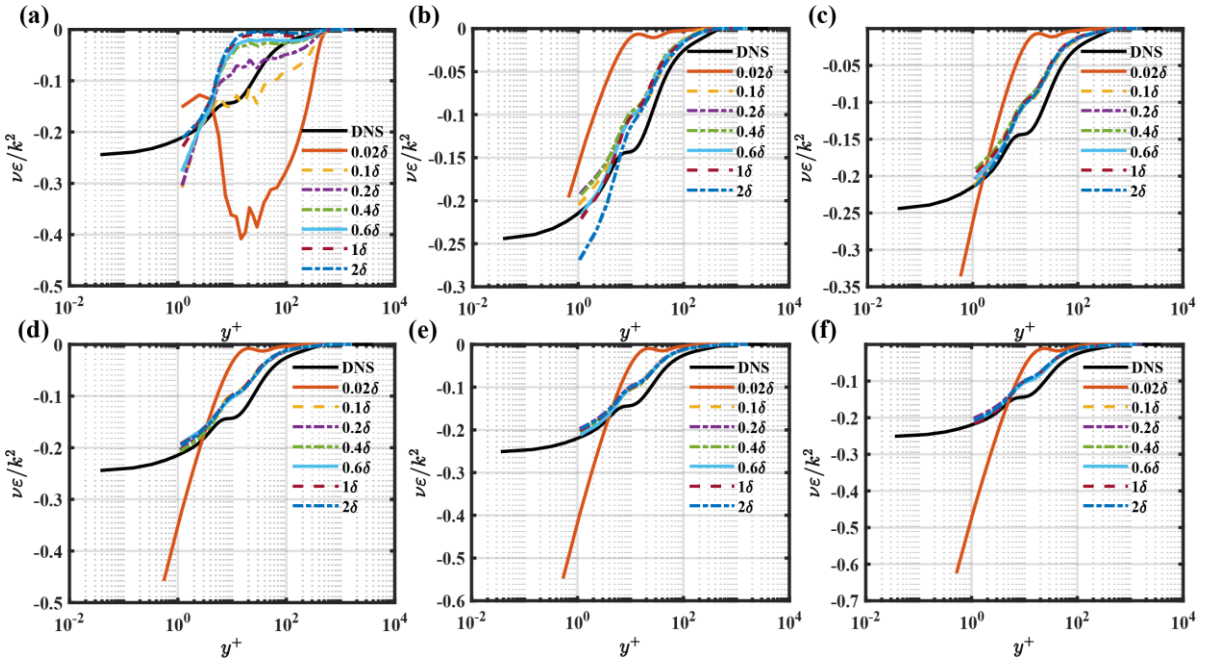


Figure 6.8 Distribution of the profiles of the production rate in simulations based on DFM with different input turbulent length scales at different positions: (a) x=inlet (b) $x/\delta = 10$ (c) $x/\delta = 20$ (d) $x/\delta = 30$ (e) $x/\delta = 40$ (f) $x/\delta = 50$

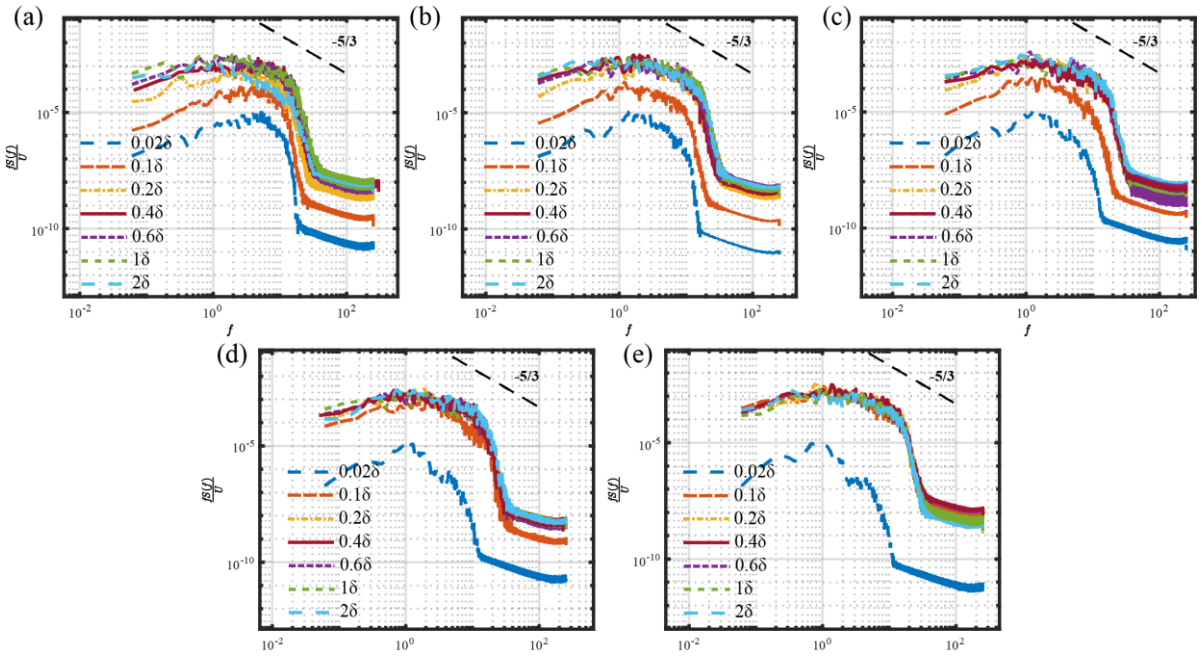


The content of Chapter 6 is published by the author of this thesis, the paper is *Influence of Turbulent Inlet Boundary Condition on Large Eddy Simulation Over a Flat Plate Boundary Layer*

Figure 6.9 Distribution of the profiles of the dissipation in simulations based on DFM with different input turbulent length scales at different positions: (a) x=inlet (b) $x/\delta = 10$ (c) $x/\delta = 20$ (d) $x/\delta = 30$ (e) $x/\delta = 40$ (f) $x/\delta = 50$

6.2.2. The Divergence Free Synthetic Eddies Method (DFSEM)

Figure 6.10-Figure 6.18 present the typical properties of the flow details of the simulation based on the DFSEM with different input turbulent length scales (L). Figure 6.10 presents the spectra of three velocity components at the downstream locations of interest, at a height of 0.5δ. The deviation of profiles obtained from the simulations based on DFSEM with different L values was apparent at $x = 10\delta$. When $x \geq 20\delta$, the profiles of the LES cases based on the DFSEM with different input turbulent length scales ranging from 0.2δ~2δ were coincident. In the LES case based on the DFSEM with $L = 0.1\delta$, 40δ was required to fit the profiles of cases with $0.2\delta \leq L \leq 2\delta$. However, in the case with $L = 0.02\delta$, the profiles of the spectrum at different downstream positions were not coincident with those of other cases. This indicates that the profiles of the power spectrum of the inflow turbulence generated by the DFSEM with $L = 0.02\delta$ did not match the profiles of those generated by the DFSEM with other turbulent length scales. The profiles of the power spectrum with $L = 0.4\delta, 0.6\delta$ and $L = 1\delta$ were nearly coincident from $x = 10\delta - 50\delta$.



The content of Chapter 6 is published by the author of this thesis, the paper is *Influence of Turbulent Inlet Boundary Condition on Large Eddy Simulation Over a Flat Plate Boundary Layer*

Figure 6.10 The profiles of the turbulent kinetic energy spectrum of the simulation based on DFSEM with different input turbulent length scales at the same vertical position where $y = 0.5\delta$ $(y^+ = 300)$ and distinctive horizontal positions where (a) $x = 10\delta$ (b) $x = 20\delta$ (c) $x = 30\delta$ (d) $x = 40\delta$ (e) $x = 50\delta$

Figure 6.11 presents the development of the wall friction velocity downstream of the inlet for the simulations based on the DFSEM with six input turbulent length scales. With reference to a study conducted Poletto et al (Poletto et al., 2013). when synthetic turbulence is applied at a flow inlet, there is typically an abrupt decrease in the friction coefficient downstream before recovery to the fully developed value, which occurs further downstream. The distance required for this coefficient to be restored its fully developed value is defined as the development length (Poletto et al., 2013). In the case where $L = 0.02\delta$, the friction velocity decreased abruptly without increasing after a long distance, which indicates that turbulence generated at the inlet could not be maintained and was dissipated after a short distance. For the cases where $L = 0.1\delta$ and 0.2δ, the friction velocity exhibited a downward trend at the early stage, and the profiles of the friction velocity gradually increased with a slight fluctuation. In contrast, in the case where $L = 0.4\delta, 0.6\delta, 1\delta,$ and 2δ, there was a typical decrease and recovery after the inlet, and the friction velocity exhibited a slight downward trend. Therefore, the profiles of the friction velocity in the simulation cases where $L = 0.4\delta, 0.6\delta, 1\delta,$ and 2δ were accurate, and the simulation case where $L = 0.4\delta$ and 0.6δ exhibited a shorter recovery length of the friction velocity.

The content of Chapter 6 is published by the author of this thesis, the paper is *Influence of Turbulent Inlet Boundary Condition on Large Eddy Simulation Over a Flat Plate Boundary Layer*

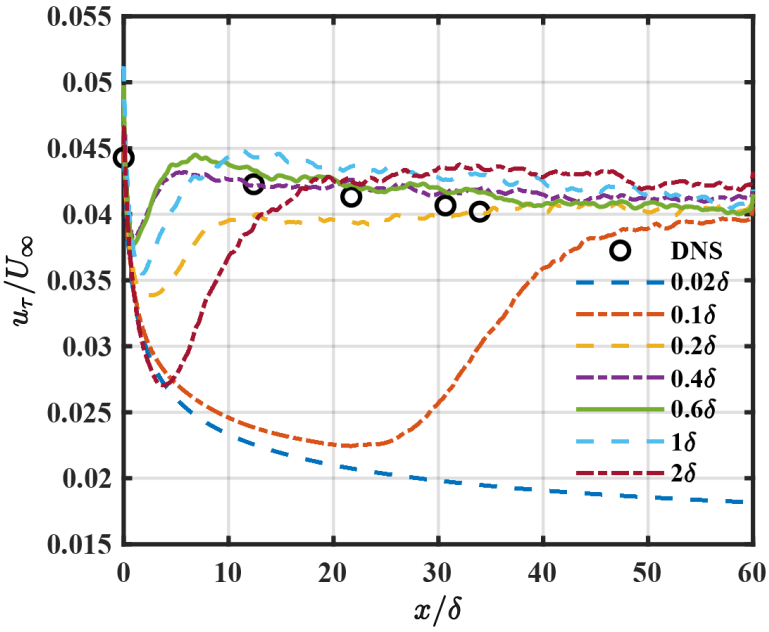


Figure 6.11 The profiles of friction velocity along the streamwise direction based on DFSEM with different input turbulent length scale

Figure 6.12 presents the distribution of the mean velocity profiles of the simulations based on the DFSEM. The velocity profiles of the LES cases based on the DFSEM were not in accordance with the law of the wall at the inlet; although, several cases gradually matched the law of wall at different downstream positions. As observed, the case with $L = 0.02\delta$ was not in accordance with the law of the wall at different positions along the streamwise direction, and the deviation between the mean velocity profile and the law of the wall increased by 16.4% from $x/\delta = 10$ to $x/\delta = 50$. The deviation indicates that the turbulent boundary layer was not formed when $L = 0.02\delta$. In contrast, in the simulation cases with $L = (0.1\text{–}2)\delta$, the mean velocity profiles were in accordance with the law of the wall after a sufficiently long distance. The cases with $L = 0.4\delta, 0.6\delta$ and 1δ required a shorter distance of less than 10δ to generate a velocity profile in accordance with the law of the wall; whereas the distances for the cases with $L = 0.1\delta$ and 0.2δ exceeded 40δ, and that for the case where $L = 2\delta$ exceeded 20δ. Therefore, the profiles of the mean velocity confirm that the cases with $L = 0.4\delta, 0.6\delta$ and 1δ exhibited a shorter development length that is about 10δ. Besides, the cases with $L = 0.4\delta, 0.6\delta$ and 1δ agree well with the DNS data.

The content of Chapter 6 is published by the author of this thesis, the paper is *Influence of Turbulent Inlet Boundary Condition on Large Eddy Simulation Over a Flat Plate Boundary Layer*

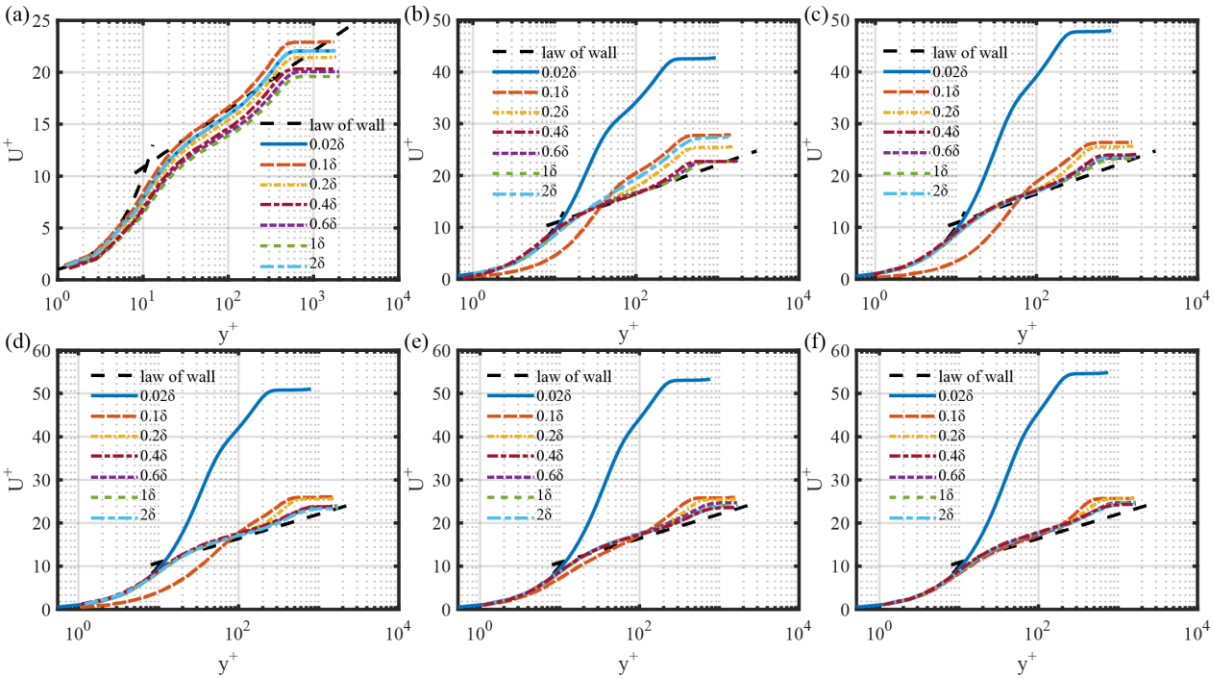


Figure 6.12 Distribution of the mean velocity profiles of simulations based on DFSEM with different input turbulent length scales at different positions: (a) x=inlet (b) $x/\delta = 10$ (c) $x/\delta = 20$ (d) $x/\delta = 30$ (e) $x/\delta = 40$ (f) $x/\delta = 50$

Figure 6.13-Figure 6.16 present the profiles of different turbulent Reynolds stresses components at different positions along the streamwise direction. The profiles of $\sqrt{\overline{u'u'}}$ are presented in Figure 6.13. As can be seen from the figure, the profiles of the streamwise component of the turbulent Reynolds stresses in different cases gradually approached the DNS results at different downstream positions, except for $L = 0.02\delta$. Like the simulation results based on the DFM, there was a deviation between the profiles of the Reynolds stresses from the simulations with different values of L and the DNS results. In particular, the deviations were distributed over the region of $8 < y^+ \leq 20$ and $y^+ > 700$. Among the cases with $0.1\delta \leq L \leq 2\delta$, the case with $L = 0.4\delta$ and 0.6δ was in accordance with the DNS results within a shorter distance of approximately 10δ after the inlet; whereas the case with $L = 1\delta$ required a longer distance of approximately 20δ to match the DNS profile. The distance for the case with $L = 2\delta$ ranged from $20\delta - 30\delta$.

The content of Chapter 6 is published by the author of this thesis, the paper is *Influence of Turbulent Inlet Boundary Condition on Large Eddy Simulation Over a Flat Plate Boundary Layer*

Besides, the profiles of $\sqrt{\overline{u'u'}}$ in the cases with $0.1\delta \leq L \leq 2\delta$ were nearly coincident before $x/\delta = 50$. As observed, the case with $L = 0.1\delta$ required a longer distance to match the DNS profile, and the case with $L = 0.02\delta$ was not in agreement with the DNS profile. The vertical fluctuating profiles of $\sqrt{\overline{v'v'}}$ are shown in Figure 6.14. Likewise, the case with $L = 0.02\delta$ was not in accordance with the DNS profile. For the profiles of $\sqrt{\overline{v'v'}}$ in cases with other values of L, the difference was significant at positions where $x/\delta \leq 40$, and the $\sqrt{\overline{v'v'}}$ profiles of cases with $L = 0.6\delta$ and 1δ were more in accordance with the DNS results. However, an apparent phrase difference between the LES and DNS results was observed, especially at $x/\delta = 50$. Figure 6.15 presents the distribution of the spanwise fluctuating velocity $\sqrt{\overline{w'w'}}$ along the vertical direction. Like the profiles of $\sqrt{\overline{v'v'}}$ and $\sqrt{\overline{u'u'}}$, as presented in Figure 6.13 and Figure 6.14, the profiles of $\sqrt{\overline{w'w'}}$ in the case with $L = 0.02\delta$ were not in agreement with the DNS results at different downstream positions.

Besides, there was no significant difference (<1%) between the LES results with $L = (0.1 - 2)\delta$ at positions where $x/\delta \geq 40$. At the position of $x/\delta = 10$, the profiles of $\sqrt{\overline{w'w'}}$ in the case with $L = 0.6\delta$ were more closed to the DNS result when compared with the other cases. In addition, the profiles of $\sqrt{\overline{w'w'}}$ in cases with $L = 0.1\delta$ and 0.2δ were lower than the DNS results, whereas the profiles of $\sqrt{\overline{w'w'}}$ in cases with $L = 1\delta$ and 2δ were slightly larger than the DNS results. All the profiles, except for $L = 0.02\delta$, gradually approached the DNS results at different downstream positions; and the deviation between the LES and DNS results, except for the case with $L = 0.02\delta$, was not observed after $x/\delta = 40$. The profiles of the turbulent shear stress component $\overline{u'v'}$ are presented in Figure 6.16. As can be seen from the figure, the results for the cases with different values of L were not in agreement with the DNS profiles at $x/\delta = 10$, and the deviation between the LES and DNS results gradually decreased

The content of Chapter 6 is published by the author of this thesis, the paper is *Influence of Turbulent Inlet Boundary Condition on Large Eddy Simulation Over a Flat Plate Boundary Layer*

at different downstream locations to 5.3%. At positions where $x/\delta = 40$ and $x/\delta = 50$, the case with $L = 0.4\delta$ and 0.6δ was more closed to the DNS profiles.

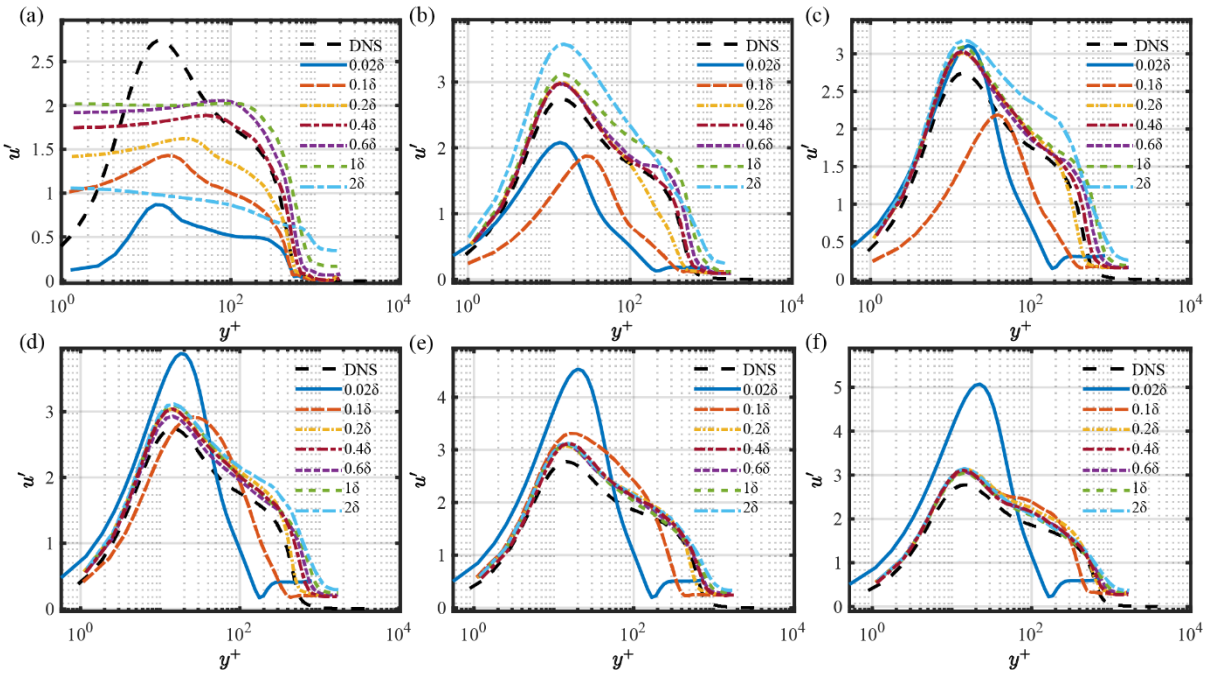


Figure 6.13 Distribution of the streamwise fluctuating velocity profiles of simulations based on DFSEM with different input turbulent length scales at different positions: (a) x=inlet (b) $x/\delta = 10$ (c) $x/\delta = 20$ (d) $x/\delta = 30$ (e) $x/\delta = 40$ (f) $x/\delta = 50$

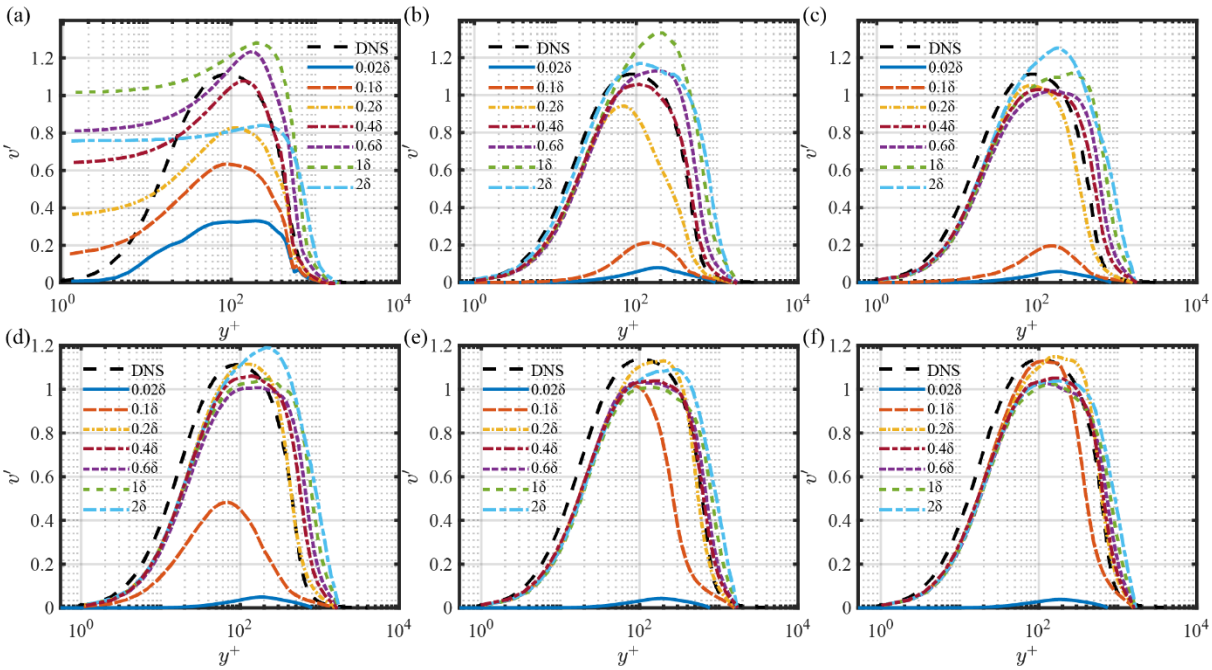


Figure 6.14 Distribution of the vertical fluctuating velocity profiles of simulations based on DFSEM with different input turbulent length scales at different positions: (a) x=inlet (b) $x/\delta = 10$ (c) $x/\delta = 20$ (d) $x/\delta = 30$ (e) $x/\delta = 40$ (f) $x/\delta = 50$

The content of Chapter 6 is published by the author of this thesis, the paper is *Influence of Turbulent Inlet Boundary Condition on Large Eddy Simulation Over a Flat Plate Boundary Layer*

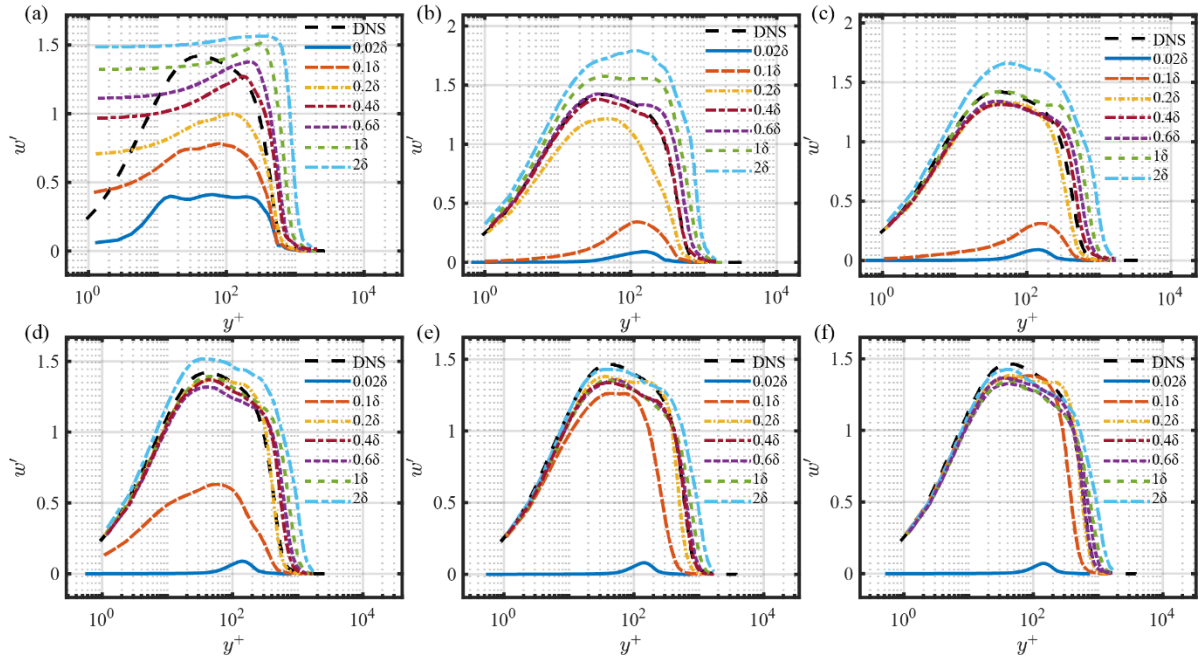


Figure 6.15 Distribution of the spanwise fluctuating velocity profiles of simulations based on DFSEM with different input turbulent length scales at different positions: (a) x=inlet (b) $x/\delta = 10$ (c) $x/\delta = 20$ (d) $x/\delta = 30$ (e) $x/\delta = 40$ (f) $x/\delta = 50$

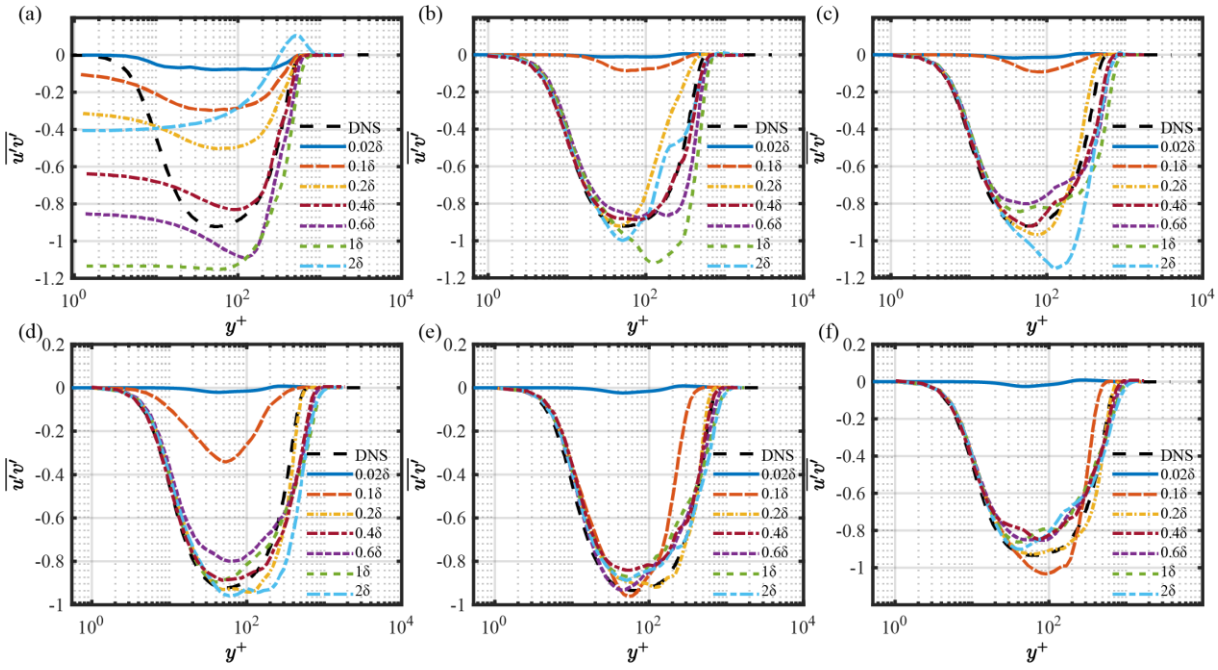


Figure 6.16 Distribution of the turbulent shear stresses profiles of simulations based on DFSEM with different input turbulent length scales at different positions: (a) x=inlet (b) $x/\delta = 10$ (c) $x/\delta = 20$ (d) $x/\delta = 30$ (e) $x/\delta = 40$ (f) $x/\delta = 50$

Figure 6.17 and Figure 6.18 reflect the profiles of TKE production and dissipation. In Figure 6.16, it can be observed that the case with $L = 0.02\delta$ cannot fit the DNS profiles after the inlet whatever the distance is away from the inlet along the streamwise direction. It means

The content of Chapter 6 is published by the author of this thesis, the paper is *Influence of Turbulent Inlet Boundary Condition on Large Eddy Simulation Over a Flat Plate Boundary Layer*

that there is little turbulent kinetic energy obtained from the mean flow and transferred into the turbulent field. In the case with $L = 0.1\delta$, the profile of it can fit the DNS result when after a much longer distance that $x/\delta = 50$. In comparison, the distance is about 20δ for the case with $L = 0.1\delta$ and 2δ while the distance is about 10δ for the case with $L = 0.4\delta, 0.6\delta$ and 1δ. The scenario can match the conclusion obtained from the results above that the case with $L = 0.4\delta, 0.6\delta$ and 1δ can generate the physical turbulent structures in a short distance about 10δ away from the inlet. In Figure 6.17, similarly, the profile of the case with $L = 0.02\delta$ cannot fit the DNS result whatever the distance is away from the inlet along the streamwise direction. Besides, the case with $L = 0.1\delta$ requires a quite large distance about 50δ to approach the DNS profile enough like the scenario in the production term. The performance of cases with $L = 0.6\delta$ and 1δ show an agreement with the DNS profile in a short distance. However, like the analysis in the simulation based on DFM, there is an obvious gap between the results of LES cases can the DNS profile when $5 \leq y^+ \leq 200$.

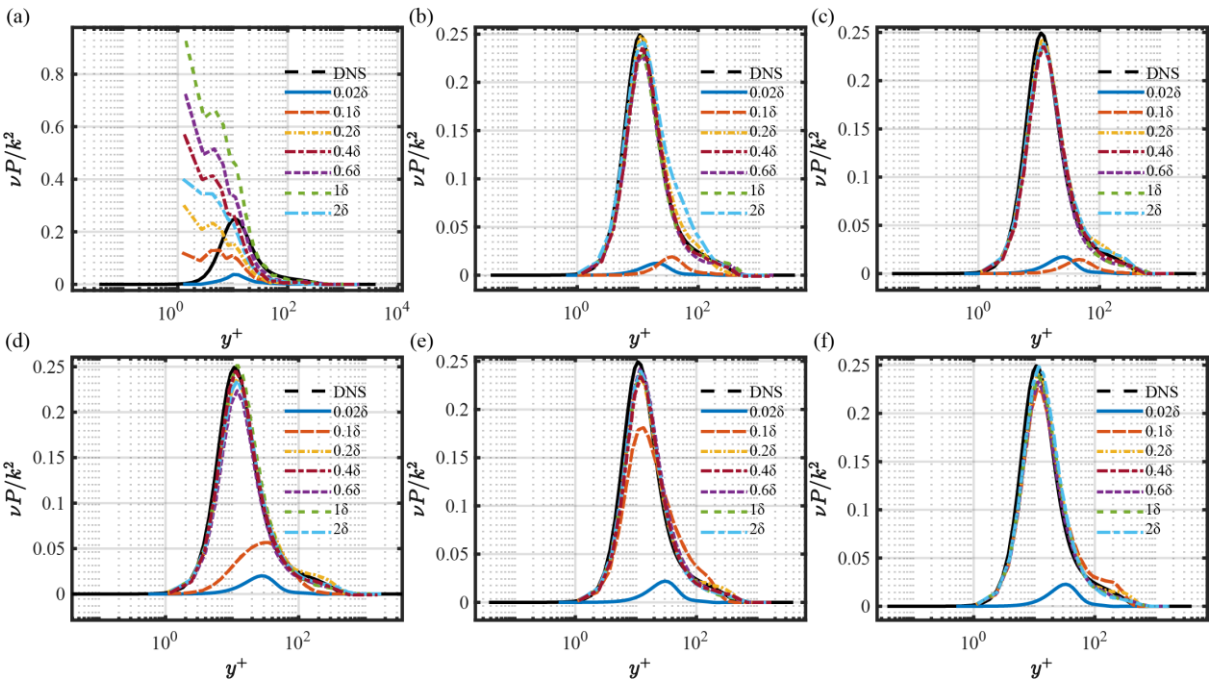


Figure 6.17 Distribution of the profiles of the production rate in simulations based on DFSEM with different input turbulent length scales at different positions: (a) x=inlet (b) $x/\delta = 10$ (c) $x/\delta = 20$ (d) $x/\delta = 30$ (e) $x/\delta = 40$ (f) $x/\delta = 50$

The content of Chapter 6 is published by the author of this thesis, the paper is *Influence of Turbulent Inlet Boundary Condition on Large Eddy Simulation Over a Flat Plate Boundary Layer*

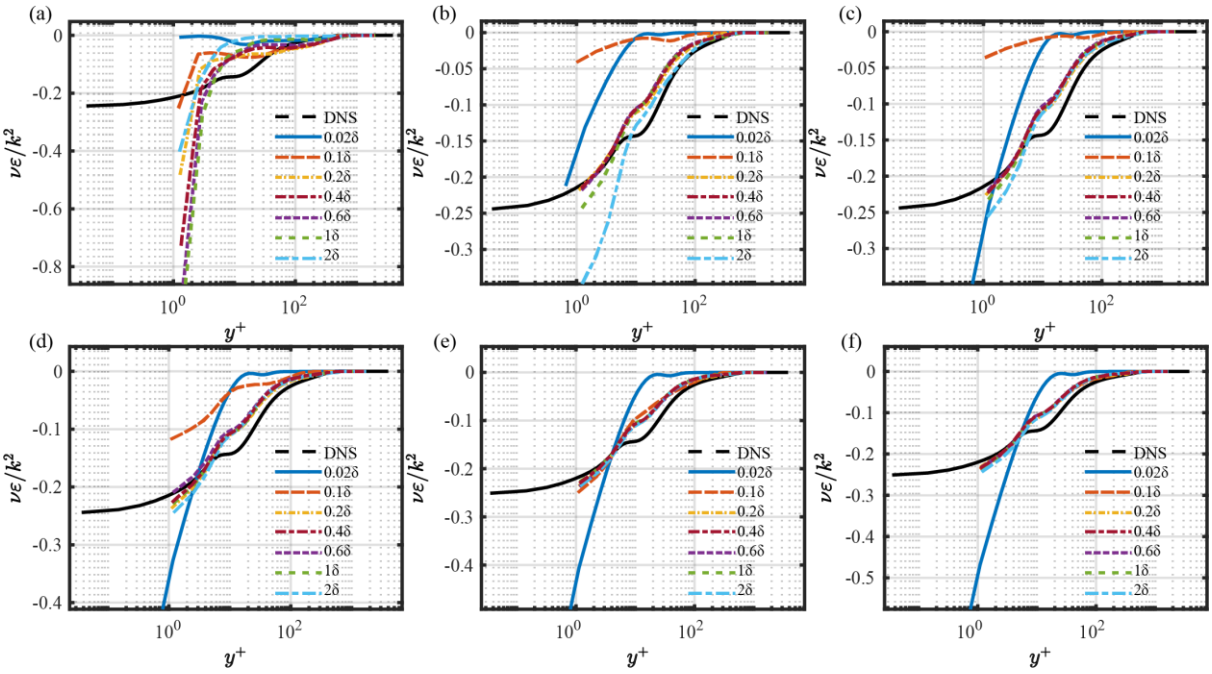


Figure 6.18 Distribution of the profiles of the turbulent dissipation in simulations based on DFSEM with different input turbulent length scales at different positions: (a) x=inlet (b) $x/\delta = 10$ (c) $x/\delta = 20$ (d) $x/\delta = 30$ (e) $x/\delta = 40$ (f) $x/\delta = 50$

6.2.3. The Lund method

Compared with the simulations based on the DFM and DFSEM, the simulation based on the Lund method has a high computational cost based on the previous statements. The simulation was therefore conducted in triplicate with different time average values. During this process, the turbulent statistics were accumulated until an instant of 1400 inertial time units (U_∞/δ_0). The instantaneous simulation data, including the velocity and the pressure, were extracted from the sample plane, as shown in Figure 6.1(a). Figure 6.1(a) presents the domain of the simulation based on the Lund method. The value of L was determined as $10\delta, 20\delta$, and 30δ, respectively. Compared with the DFM and DFSEM, the time consuming of the Lund method is nearly 3 times of the simulation based on the DFSEM and DFM. While the cost of the simulation based on DFM and DFSEM is nearly the same.

The content of Chapter 6 is published by the author of this thesis, the paper is *Influence of Turbulent Inlet Boundary Condition on Large Eddy Simulation Over a Flat Plate Boundary Layer*

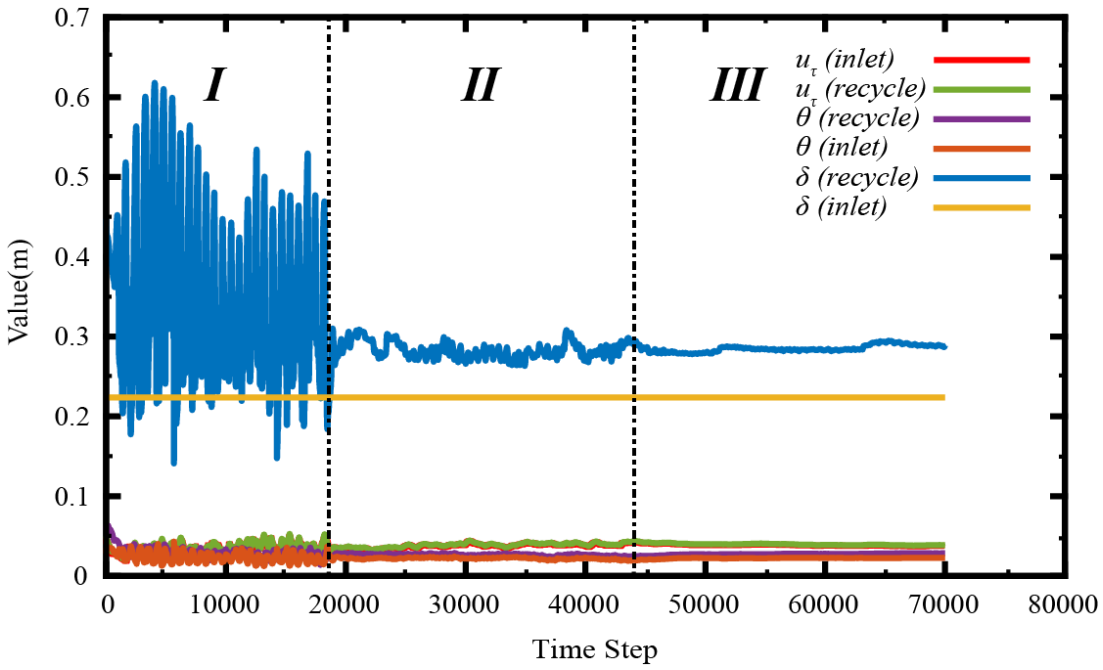


Figure 6.19 Instantaneous turbulent boundary layer thickness, momentum thickness and the friction velocity at the inlet plane at different time step with different average time applied for the simulation based on the Lund method

Figure 6.19 presents the turbulent statistics at the inlet plane with different average time as described above. According to the statement in the Chapter 3, the average time should be modified until the flow equilibrates during each stage i.e., the turbulent statistics become stationary. As is shown in Figure 6.19, the violent fluctuation of turbulent statistics can be observed in the first stage, when turbulent statistics become stationary, the value of the time average is increased. The fluctuation of these turbulent statistics decreases at each time when the time average value is modified. After this procedure, the turbulent flow is generated by the Lund method.

Figure 6.20 presents the mean velocity profiles from the simulations at different streamwise positions. As can be seen from the figure, different lengths of the precursor domain had minimal influences on the results. Hence, the simulation results were not sensitive to the length of the precursor domain. It is an advantage of the Lund method that the simulation results remain stable with respect to changes in the length of the precursor domain. However, the velocity profiles were not in good agreement with the law of the wall in each case. This

The content of Chapter 6 is published by the author of this thesis, the paper is *Influence of Turbulent Inlet Boundary Condition on Large Eddy Simulation Over a Flat Plate Boundary Layer*

indicates that turbulence generated by the Lund method was not fully developed along the streamwise direction, irrespective of changes in the size of the precursor domain.

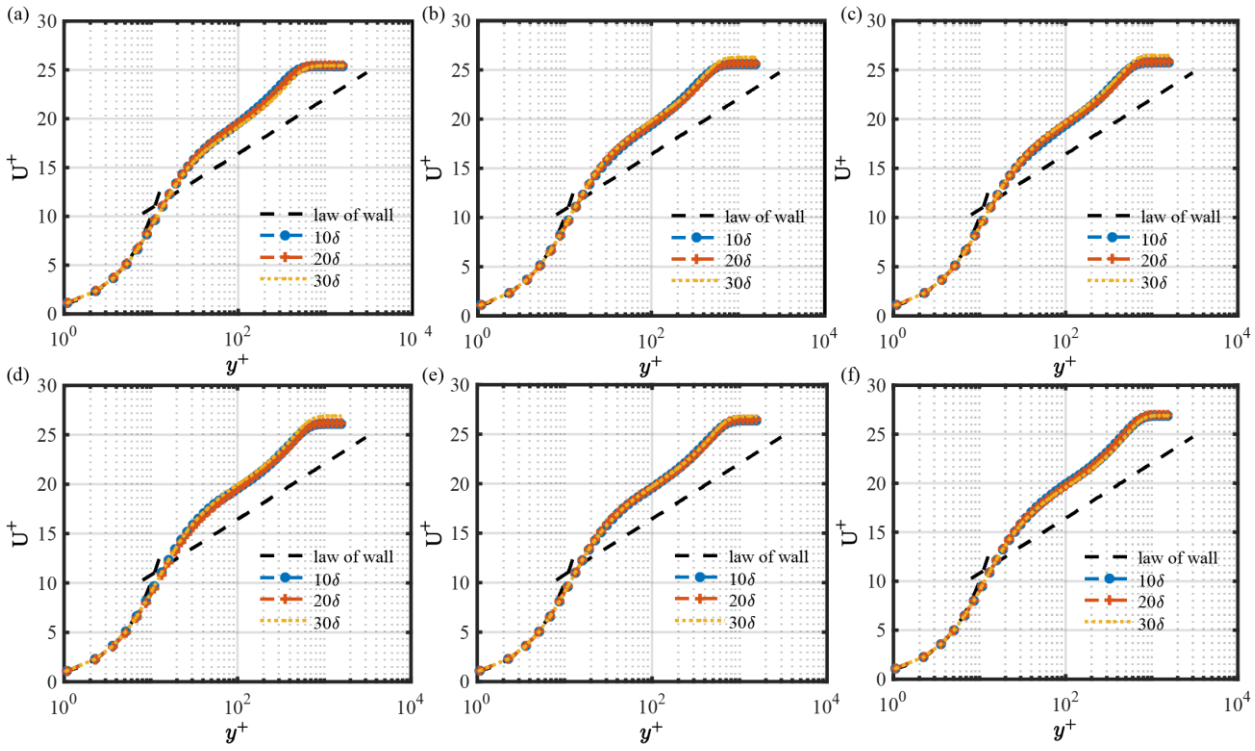


Figure 6.20 Distribution of the mean velocity profiles of simulations based on Lund with different length of the precursor domain: (a) x=inlet (b) $x/\delta = 10$ (c) $x/\delta = 20$ (d) $x/\delta = 30$ (e) $x/\delta = 40$ (f) $x/\delta = 50$

The profiles of the Reynolds stresses and TKE budgets can provide more information on the turbulence generated by the Lund method. Figure 6.21 presents the profiles of the turbulent Reynolds stresses. Different lengths of the precursor domain had a less significant influence on the simulation results at different streamwise positions. At different streamwise positions, $\sqrt{\overline{u'u'}}$ was overvalued, and $\sqrt{\overline{v'v'}}$ and $\sqrt{\overline{w'w'}}$ were undervalued. The profiles of $\overline{u'v'}$ were in accordance with the DNS data to an extent. No significant improvement along the streamwise direction was observed, i.e., the difference between the simulation results based on the Lund method and the DNS data was stable at different streamwise positions. While the Reynolds stresses profiles reflect that the TKE distribution is not correct. In particular, the $\sqrt{\overline{u'u'}}$ component gained more energy, and the other two components gained less energy.

The content of Chapter 6 is published by the author of this thesis, the paper is *Influence of Turbulent Inlet Boundary Condition on Large Eddy Simulation Over a Flat Plate Boundary Layer*

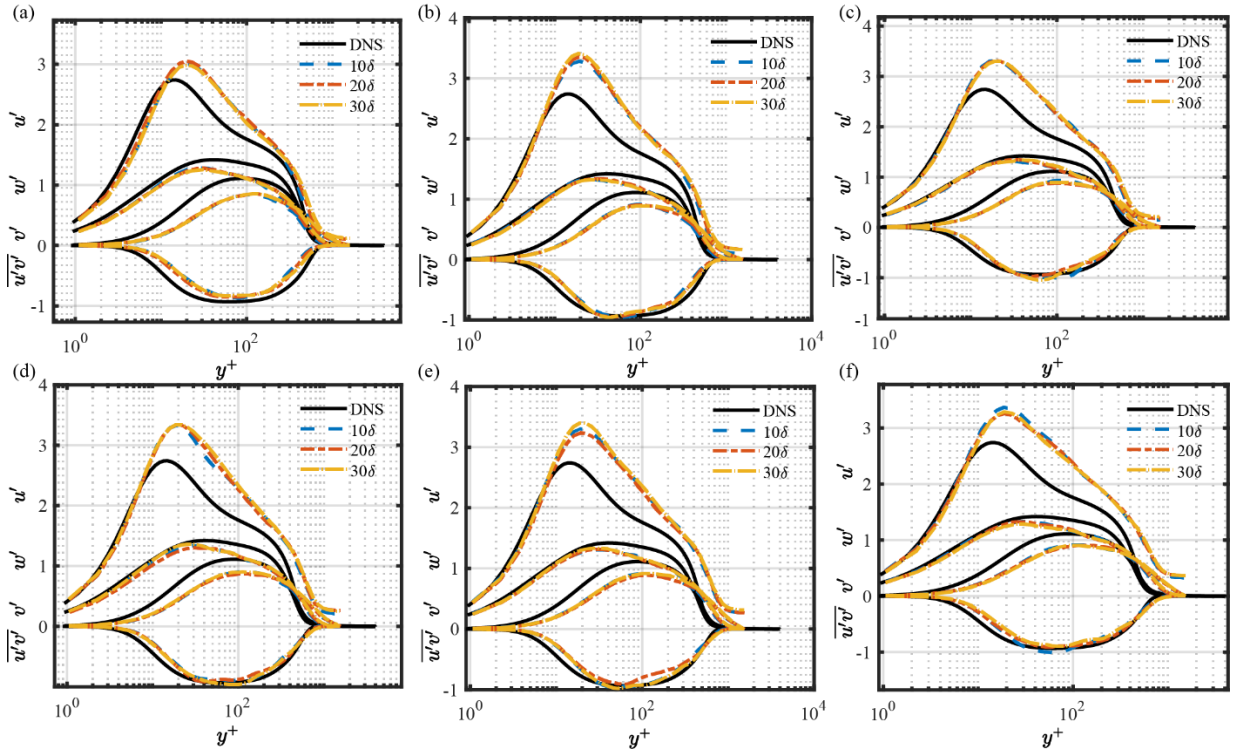


Figure 6.21 Distribution of the turbulent Reynolds stresses profiles of simulations based on Lund with different length of the precursor domain at: (a) x=inlet (b) $x/\delta = 10$ *(c)* $x/\delta = 20$ *(d)* $x/\delta = 30$ *(e)* $x/\delta = 40$ *(f)* $x/\delta = 50$

The profiles of the TKE budget terms can reflect the TKE production, transportation, and dissipation at different streamwise and vertical positions based on a study conducted by Spalart (1988). As can be seen from Figure 6.22, there was less TKE generation and dissipation when compared with the DNS results. As can be seen from Figure 6.21, the TKE was generated by the turbulent shear stresses $\overline{u'v'}$, and the shear stress profiles were in good agreement with the DNS data. Therefore, the mean velocity gradient along the vertical direction was small according to the TKE production equation. Hence, the mean velocity profiles of the simulation based on the Lund method were not in good agreement with the DNS profiles. And it illustrates that turbulence generated by the Lund method is not fully developed again. The TKE distribution is mainly dependent on the TKE transportation term (S. Pope, 2001). When $x/\delta \geq 20$, there was a phase difference in the TKE transportation term between the simulation based on the Lund method and the DNS data. Given that the LES cannot accurately resolve the

The content of Chapter 6 is published by the author of this thesis, the paper is *Influence of Turbulent Inlet Boundary Condition on Large Eddy Simulation Over a Flat Plate Boundary Layer*

Kolmogorov-scale eddies, the TKE production and the transportation terms were more critical in this study.

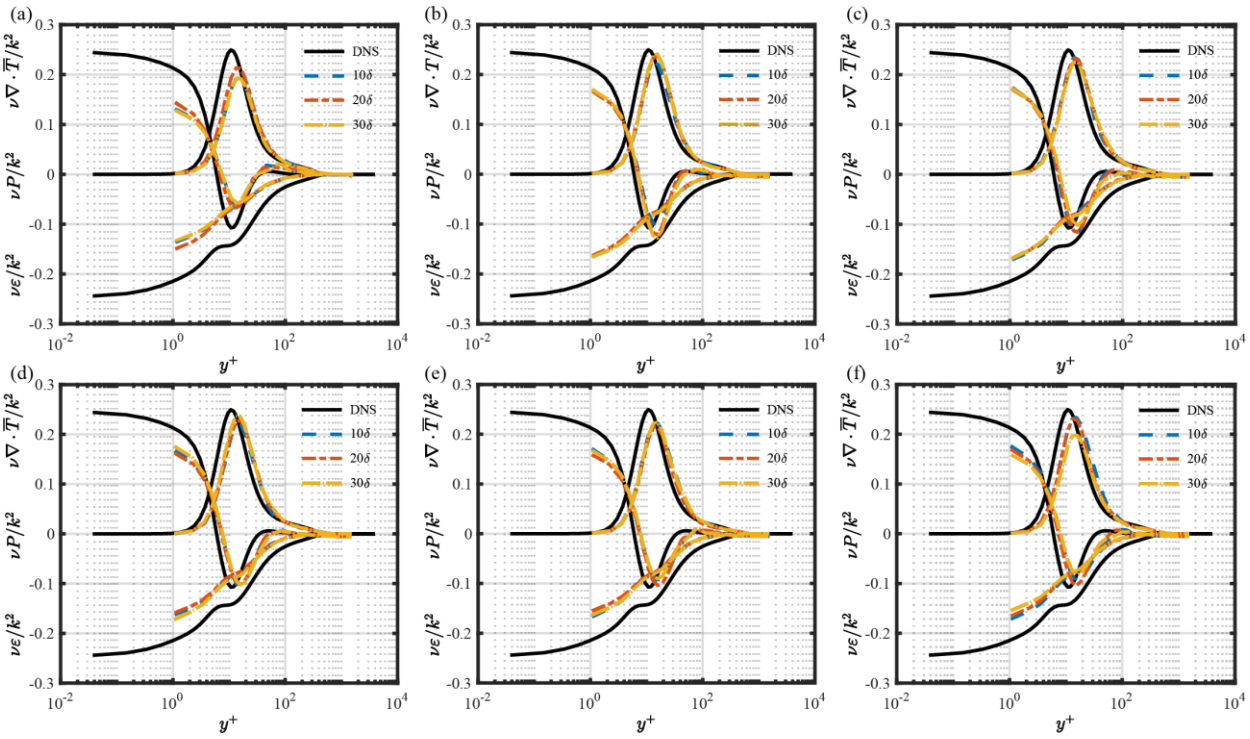


Figure 6.22 Distribution of the TKE budget terms profiles of simulations based on Lund with different length of the precursor domain at: (a) x=inlet (b) $x/\delta = 10$ (c) $x/\delta = 20$ (d) $x/\delta = 30$ (e) $x/\delta = 40$ (f) $x/\delta = 50$

6.3. Flow properties analysis

6.3.1. Analysis of velocity field

The Q criterion is used to analyze the turbulent structures in the instantaneous velocity field.

The content of Chapter 6 is published by the author of this thesis, the paper is *Influence of Turbulent Inlet Boundary Condition on Large Eddy Simulation Over a Flat Plate Boundary Layer*

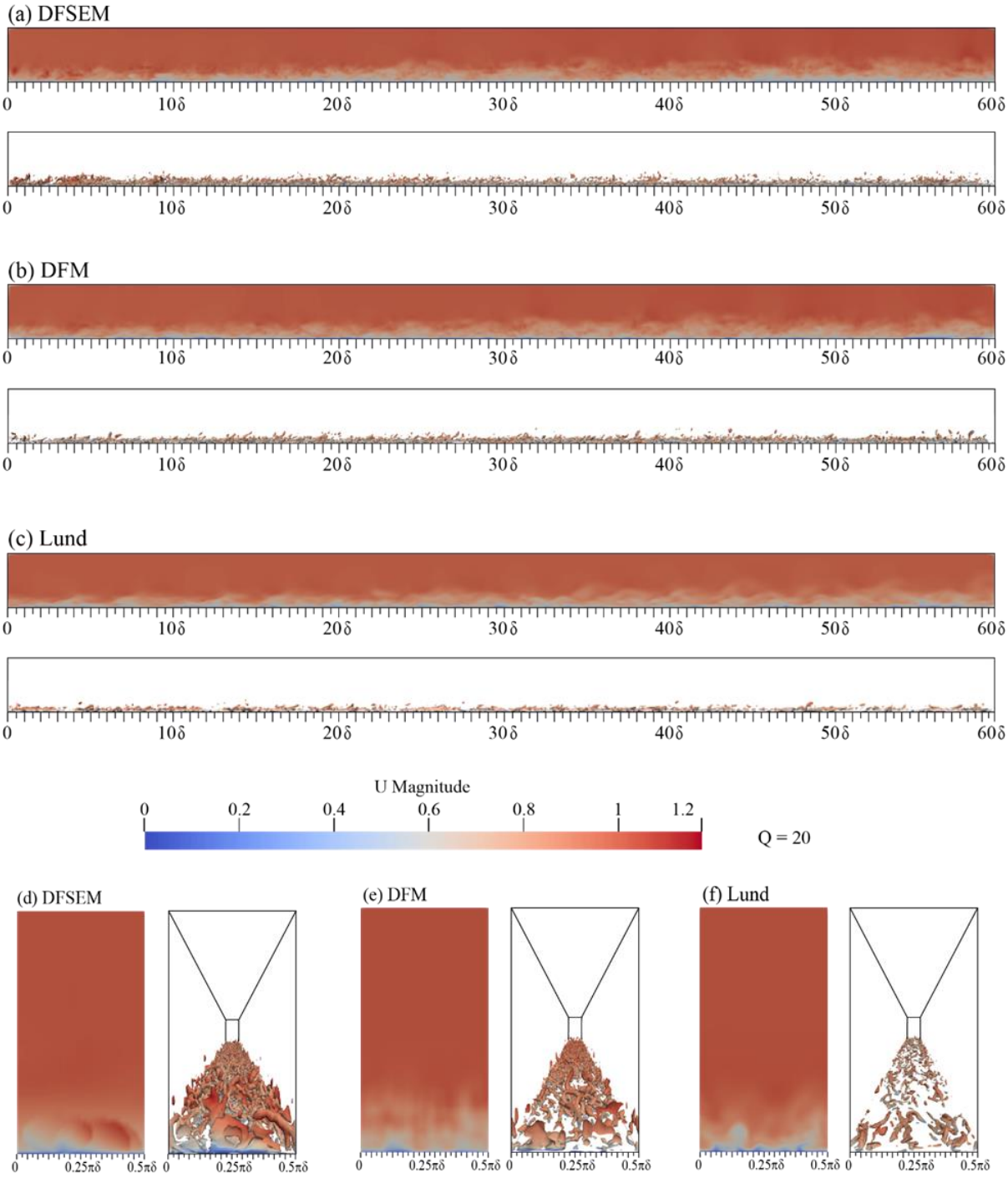


Figure 6.23 Instantaneous velocity field (a-c) and the corresponding iso-surface of $Q = 20$ in the x-y plane of different cases using the (a) DFSEM, (b) DFM, and (c) Lund method. Instantaneous velocity field (d-f) and the corresponding iso-surface of $Q = 20$ in the y-z plane (at the inlet) of different cases using the (d) DFSEM, (e) DFM, and (f) Lund method.

Figure 6.23 presents the instantaneous velocity fields with the iso-surface of $Q = 20$ in different cases based on three inflow generation methods. As can be seen from Figure 6.23 (a)-(c), the instantaneous velocity field was turbulent, and turbulence structures were formed at the inlet, irrespective of the turbulent inlet boundary condition method. Besides, the turbulence

The content of Chapter 6 is published by the author of this thesis, the paper is *Influence of Turbulent Inlet Boundary Condition on Large Eddy Simulation Over a Flat Plate Boundary Layer*

generated at the inlet could be maintained and kept stable, which indicates that the physical turbulent structures were formed without rapid dissipation. In comparison, more turbulent structures were observed in the case based on the DFSEM. Figure 6.23 (d)-(f) present the instantaneous velocity fields and the corresponding iso-surface of $Q = 20$ at the inlet for three cases based on different inlet boundary condition methods. In Figure 6.23 (d), the instantaneous velocity field based on the DFSEM at the inlet was not as spatially correlated as that based on Lund method shown in Figure 6.23 (f). However, more turbulent structures were observed in the case based on the DFSEM. In contrast, sparse turbulent structures were observed in the case based on the Lund method. Figure 6.23 (e) presents the abovementioned properties in the case based on the DFM. Similarly, the instantaneous velocity field at the inlet did not reflect actual turbulence, and the stable turbulent structures were observed after the inlet. Moreover, more turbulent structures were observed in the case based on the DFM when compared with that based on the Lund method. In comparison with the DFSEM, relatively less turbulent structures were observed in the case based on the DFM within a short distance after the inlet.

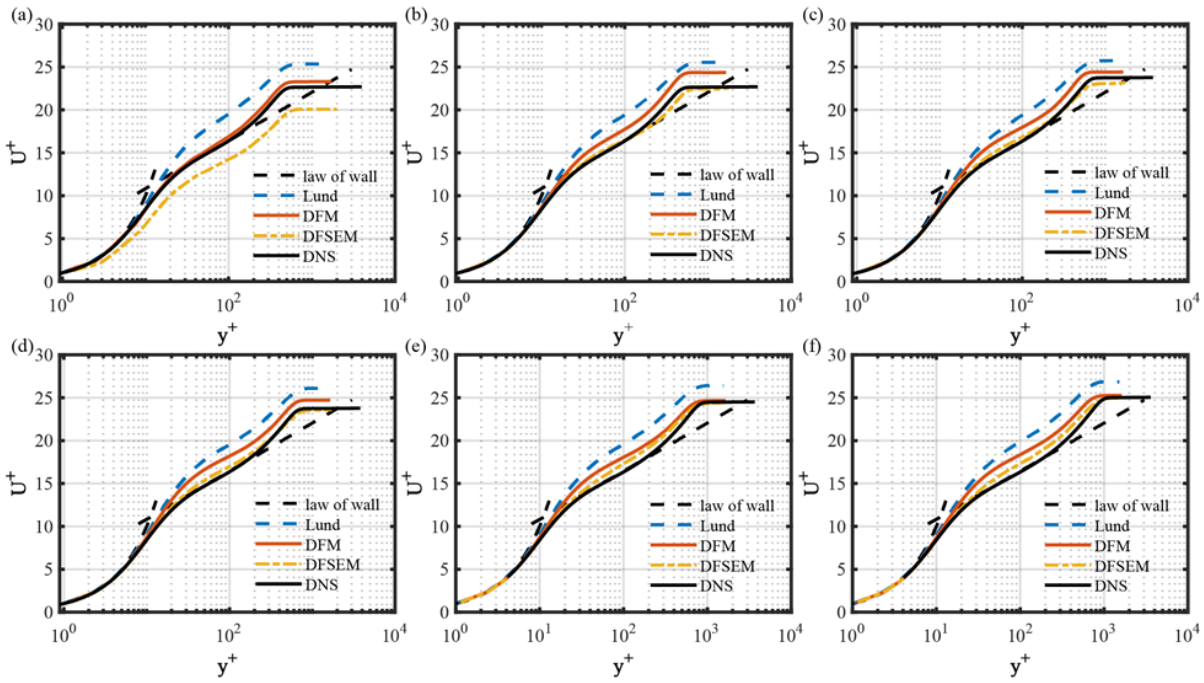


Figure 6.24 Distribution of the mean velocity profiles of simulations based on different IBC methods at different positions: (a) at x=inlet (b) at $x/\delta = 10$ (c) $x/\delta = 20$ (d) $x/\delta = 30$ (e) $x/\delta = 40$ (f) $x/\delta = 50$

The content of Chapter 6 is published by the author of this thesis, the paper is *Influence of Turbulent Inlet Boundary Condition on Large Eddy Simulation Over a Flat Plate Boundary Layer*

The velocity profiles from the simulations based on different turbulent IBC methods at different streamwise positions ($\frac{x}{\delta} = 0, 10, 20, 30, 40, \text{and } 50$) are shown in Figure 6.24 (a)-(f). The mean velocity profiles from the simulations based on the DFM were in good agreement at the inlet and in accordance with the law of the wall; whereas those from the simulations based on the Lund method and DFSEM deviated from the law of the wall at the inlet. As can be seen from Figure 6.24 (b)-(f), the mean velocity profiles of the DFSEM were in good agreement with the law of the wall. Comparatively, there is a small deviation between the mean velocity profiles of the simulation based on DFM and the law of wall. For the Lund method, the deviation to the law of wall can be clearly observed at the inlet and becomes a little smaller at different downstream positions, however, it still exists and looks larger than that of the simulation based on the Lund method at $x/\delta = 50$. For the mean velocity profiles, the simulation based on DFSEM seems to have a better performance than that based on DFM, and the simulation based on DFM has a better performance than that based on Lund method.

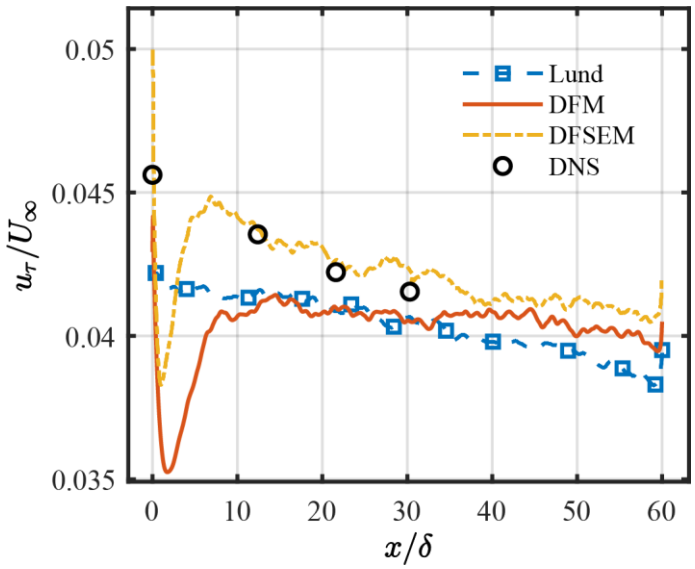


Figure 6.25 The profiles of friction velocity along the streamwise direction based on DFM with different input turbulent length scale

The content of Chapter 6 is published by the author of this thesis, the paper is *Influence of Turbulent Inlet Boundary Condition on Large Eddy Simulation Over a Flat Plate Boundary Layer*

Based on the friction velocity profiles along the streamwise direction, the simulation based on the DFSEM was in better agreement with the DNS data than the simulations based on the DFM and the Lund method.

6.3.2. Analysis of Turbulent Budget terms

Figure 6.26-Figure 6.30 illustrate the distribution of turbulent kinetic energy budget terms of simulations based on different IBC methods at different downstream positions along the streamwise direction.

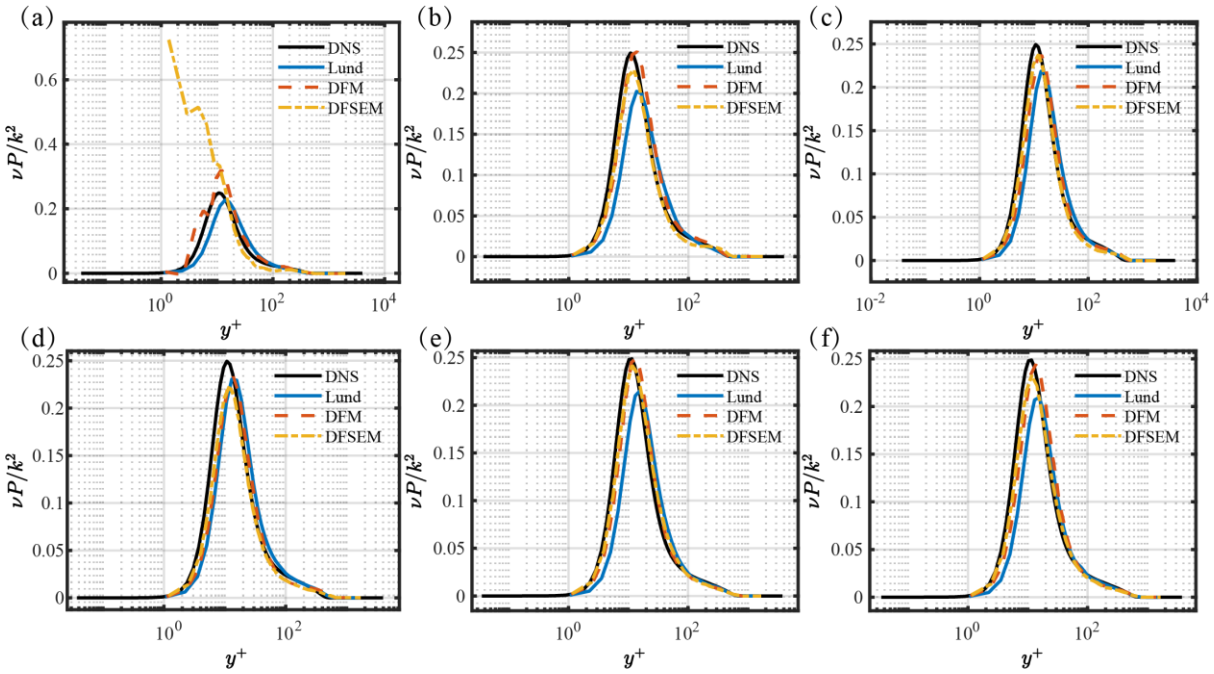


Figure 6.26 The profiles of the production of simulations based on different IBC methods at different downstream positions: (a) at x=inlet (b) at $x/\delta = 10$ (c) $x/\delta = 20$ (d) $x/\delta = 30$ (e) $x/\delta = 40$ (f) $x/\delta = 50$

The distribution of the production term is shown in Figure 6.26. At the inlet, it is obvious that the simulation based on DFM, and Lund method could fit the profile of DNS, while the profile of the simulation based on DFSEM cannot fit the DNS result. After the inlet as shown in Figure 6.26 (b)-(f), simulations based on DFM and DFSEM can nearly fit the profile of DNS, while there is tiny difference between the profiles of the simulation based on Lund method and the DNS result. The scenario indicates that turbulent kinetic energy transferred to the

The content of Chapter 6 is published by the author of this thesis, the paper is *Influence of Turbulent Inlet Boundary Condition on Large Eddy Simulation Over a Flat Plate Boundary Layer*

fluctuating velocity field is fulfill for cases based on DFM and DFSEM and relatively smaller for the case based on Lund method.

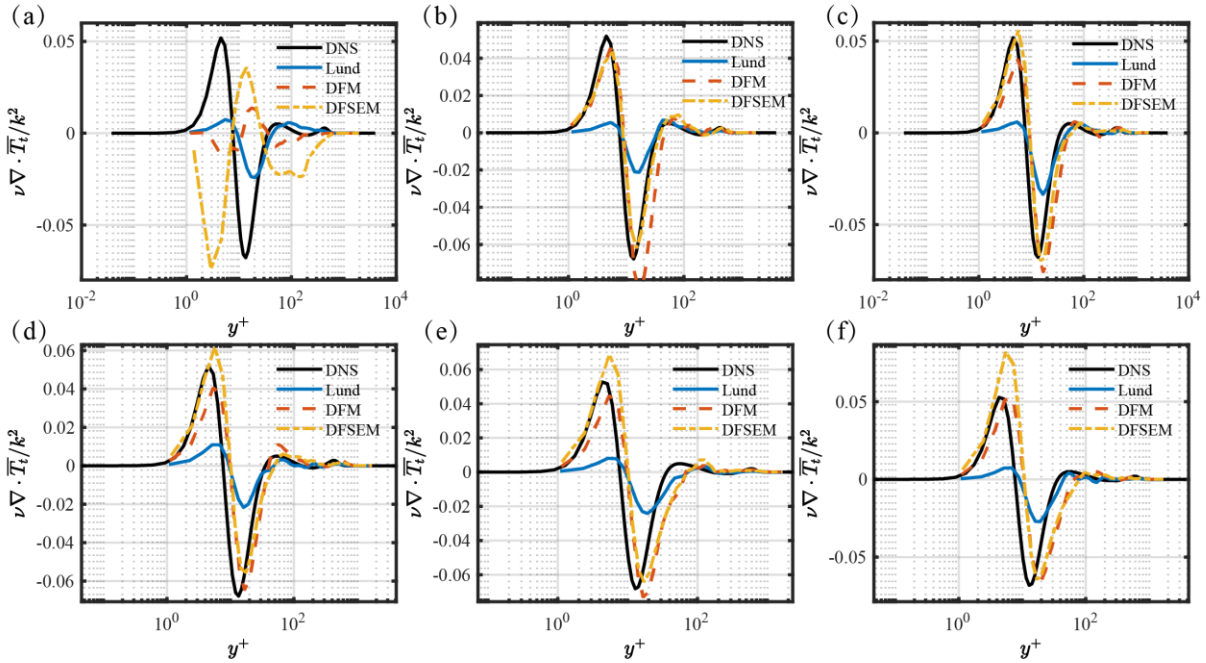


Figure 6.27 The profiles of the turbulent convection of simulations based on different IBC methods at different downstream positions: (a) at x=inlet (b) at $x/\delta = 10$ (c) $x/\delta = 20$ (d) $x/\delta = 30$ (e) $x/\delta = 40$ (f) $x/\delta = 50$

Figure 6.27 to Figure 6.29 perform the results of the transportation of the turbulent kinetic energy. As demonstrated above, the transportation term consists of the turbulent convection term (T_t), pressure term (T_p) and the viscous diffusion term (T_v). Figure 6.27 shows the comparison of the profiles of T_t of simulations based on different IBC methods and that of DNS. At the inlet, the distinction between the results of the LES and the DNS is apparent for all IBC methods. At different downstream positions from $x/\delta = 10$ to $x/\delta = 50$, the simulation with Lund method cannot capture the turbulent convection while simulations based on other methods can relatively fit the profile of the DNS. Simulation based on DFSEM apparently overpredicts the values of the turbulent convection about 20% when $x/\delta \geq 30$. In comparison, the simulation based on DFM has much more stable results even though it under predicts the values of T_t at positions where $20 \leq x/\delta \leq 40$. The profiles of T_p of LES cases based on different IBC methods and the DNS results are illustrated in Figure 6.28. Similarly,

The content of Chapter 6 is published by the author of this thesis, the paper is *Influence of Turbulent Inlet Boundary Condition on Large Eddy Simulation Over a Flat Plate Boundary Layer*

the T_p profiles of LES cases are apparently different from the result of DNS at the inlet. However, the difference for the case based on Lund method is still relatively large that is over 50%. For cases based on DFSEM and DFM, the deviation between the profiles of LES and DNS is much smaller, only 11.35% and 4.13%, and the case based on DFM has more accurate magnitude of the results in viscous region and log region. The distribution of the T_ν term is shown in Figure 6.29. The effect of the viscous diffusion is significant in the viscous wall region and negligible in the log region and outer region. At the different downstream positions along the streamwise direction from $x/\delta = 10$ to $x/\delta = 50$. It can be observed that simulations based on DFM and DFSEM could precisely fit the DNS profile, while there is an apparent difference between the results of the simulation based on Lund method and the profile of DNS.

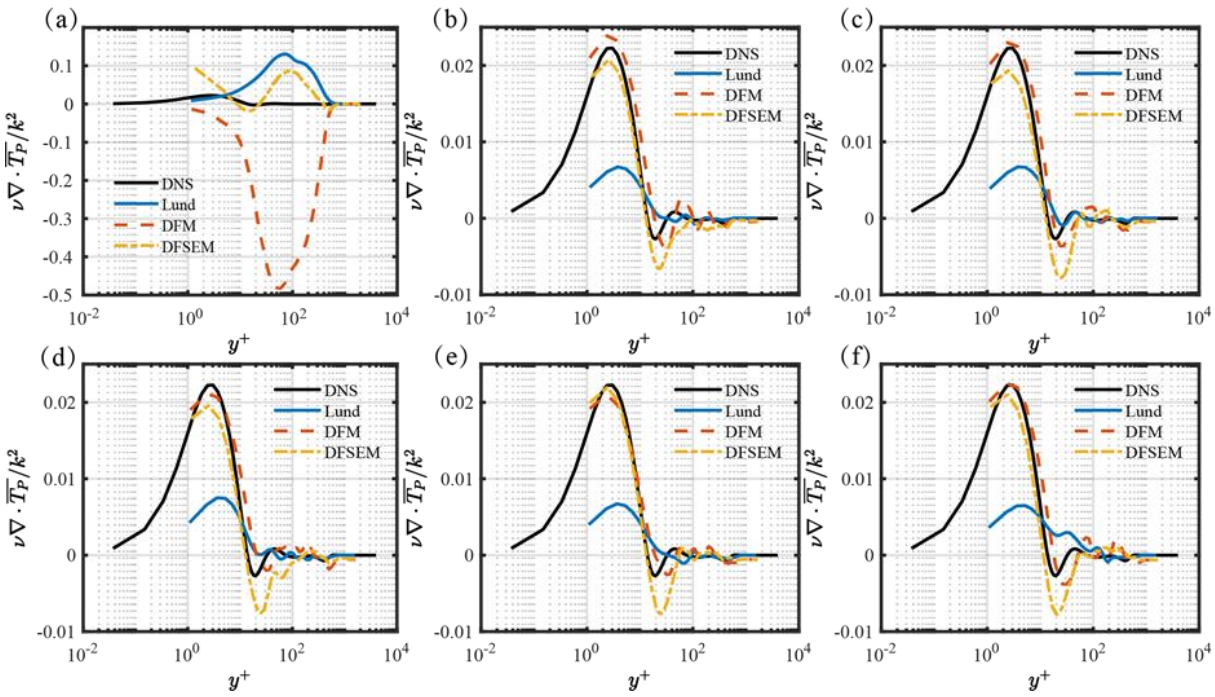


Figure 6.28 The profiles of the pressure of simulations based on different IBC methods at different downstream positions: (a) at x=inlet (b) at $x/\delta = 10$ (c) $x/\delta = 20$ (d) $x/\delta = 30$ (e) $x/\delta = 40$ (f) $x/\delta = 50$

The content of Chapter 6 is published by the author of this thesis, the paper is *Influence of Turbulent Inlet Boundary Condition on Large Eddy Simulation Over a Flat Plate Boundary Layer*

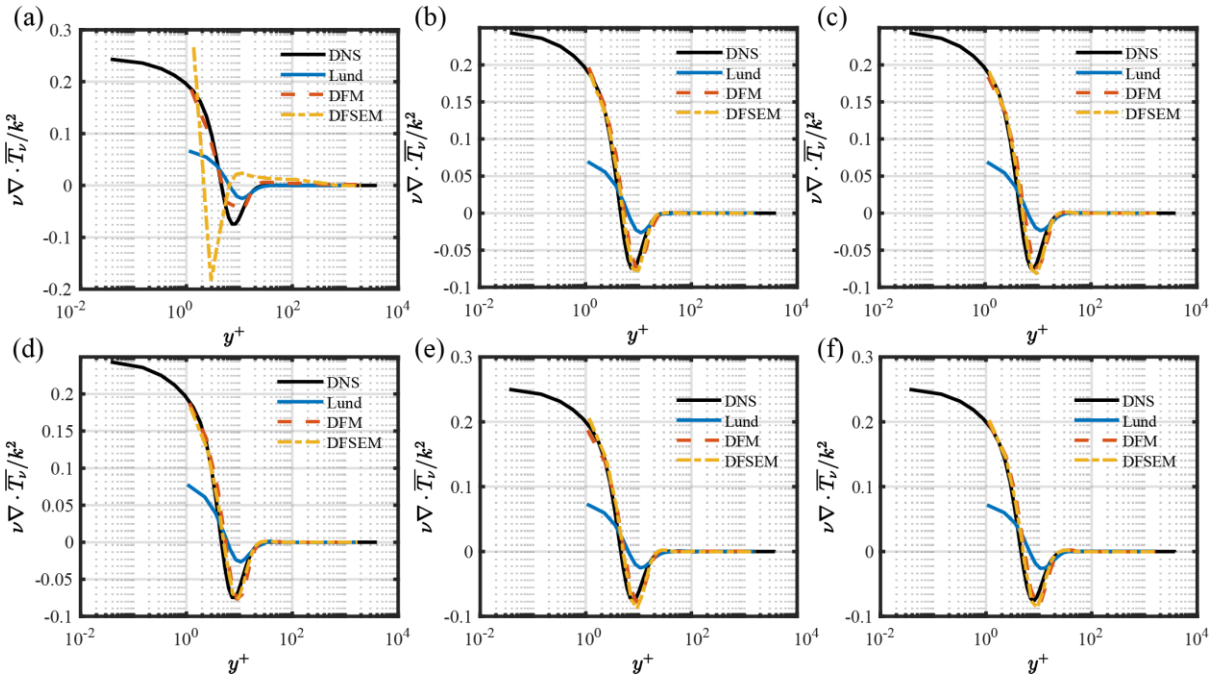


Figure 6.29 The profiles of the viscous diffusion of simulations based on different IBC methods at different downstream positions: (a) at x=inlet (b) at $x/\delta = 10$ (c) $x/\delta = 20$ (d) $x/\delta = 30$ (e) $x/\delta = 40$ (f) $x/\delta = 50$

The dissipation evolution is shown in Figure 6.30. The distribution of the profiles of ε in LES cases based on DFM and DFSEM is nearly the same at different downstream positions $x/\delta = 10$ to $x/\delta = 50$. Meanwhile, the results of LES cases based on these two IBC methods can capture the DNS result. However, the difference between the results of the LES and the DNS in the region where $5 \leq y^+ \leq 200$ is obvious whatever positions along the streamwise direction as shown in Figure 6.30 (b)-(f). The case based on Lund method, like other TKE budget terms referred above, the profile of it has a large deviation to the DNS result.

The content of Chapter 6 is published by the author of this thesis, the paper is *Influence of Turbulent Inlet Boundary Condition on Large Eddy Simulation Over a Flat Plate Boundary Layer*

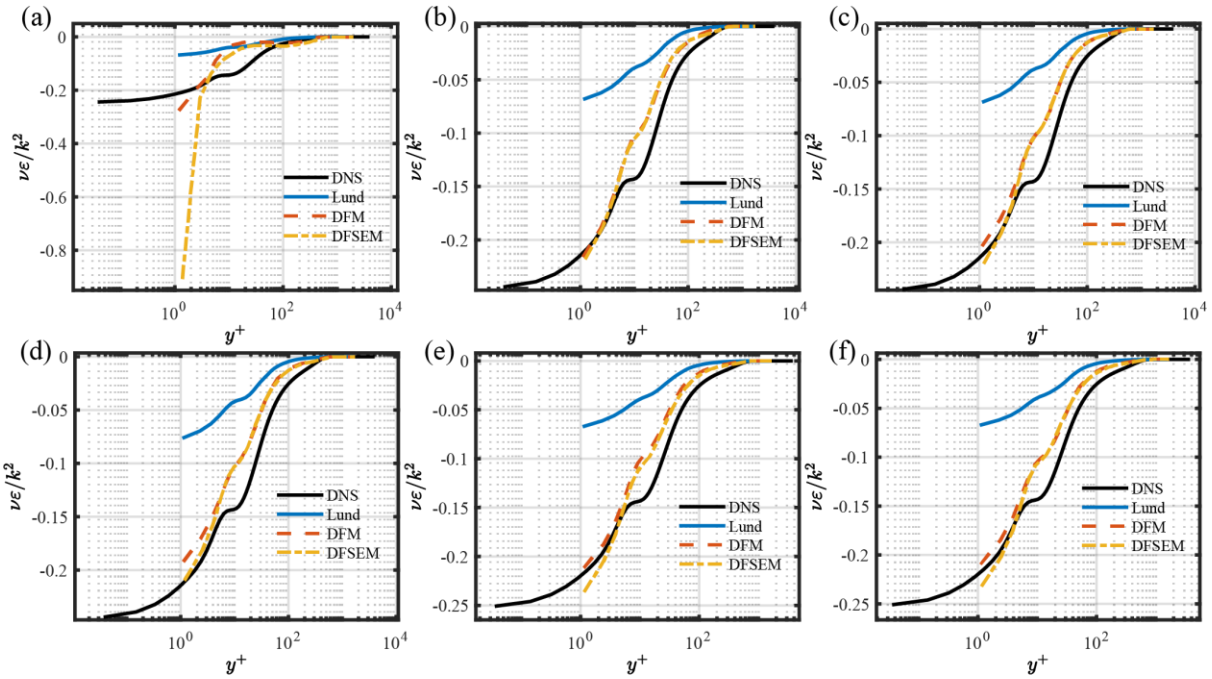


Figure 6.30 The profiles of the dissipation of simulations based on different IBC methods at different downstream positions: (a) at x=inlet (b) at $x/\delta = 10$ (c) $x/\delta = 20$ (d) $x/\delta = 30$ (e) $x/\delta = 40$ (f) $x/\delta = 50$

From the previous researches (Lund et al., 1998; Araya et al., 2011), simulations based on the Lund method can have a better performance, while the input parameters for the Lund method referred to above are the values of boundary layer thickness, momentum thickness and displacement thickness. These values can only define the mean velocity profile at the inlet indirectly. In addition, the position of the recycle plane is not rigorous for different cases. Moreover, the artificial periodicity is hardly avoided in the case with Lund method. Therefore, it is possible to obtain high-performance results with the Lund method, however, it should undertake a try-and-error process to adjust the values of different physical thickness and the position of the recycle plane.

6.3.3. Analysis of Turbulent Reynolds stresses

The content of Chapter 6 is published by the author of this thesis, the paper is *Influence of Turbulent Inlet Boundary Condition on Large Eddy Simulation Over a Flat Plate Boundary Layer*

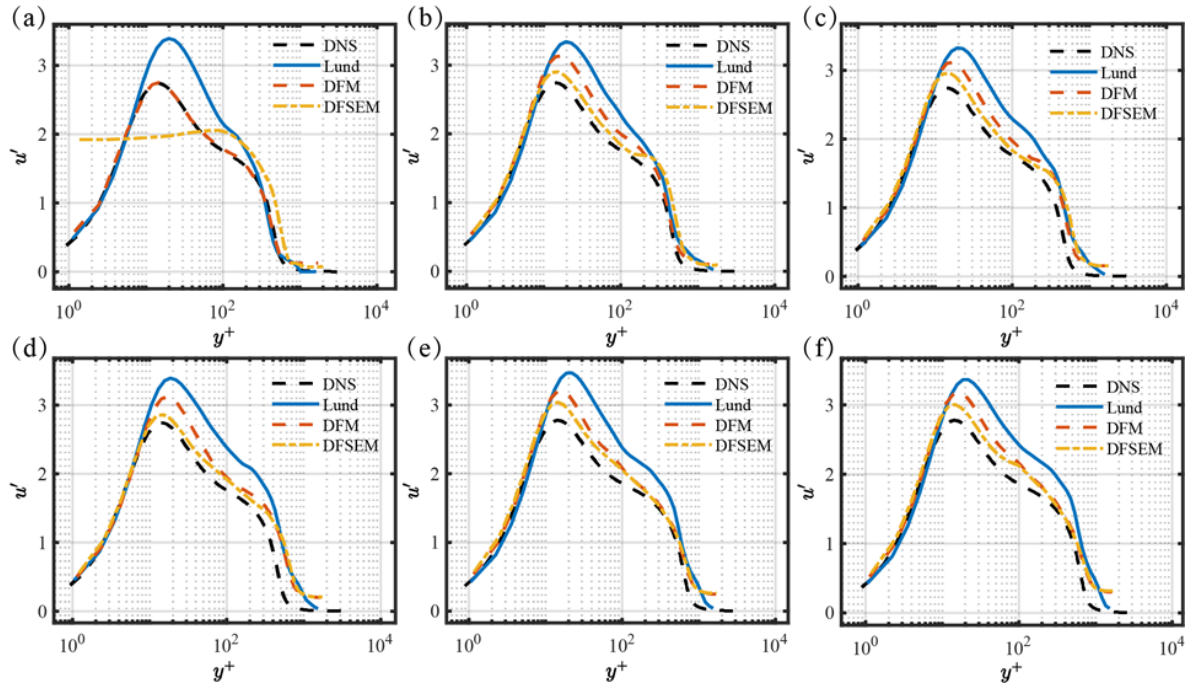


Figure 6.31 Distribution of the streamwise velocity fluctuation of simulations based on different IBC methods at different positions: (a) at x=inlet (b) at $x/\delta = 10$ (c) $x/\delta = 20$ (d) $x/\delta = 30$ (e) $x/\delta = 40$ (f) $x/\delta = 50$

Streamwise velocity fluctuation (u_{rms}) in simulations based on different IBC methods are shown in Figure 6.31. At the inlet, there is significant deviation of the results of u_{rms} of the simulation based on Lund method and DFSEM to the DNS results. For the simulation based on DFM, the profiles of u_{rms} could fit the DNS results where $Re_\theta = 1410$. At different downstream positions along the streamwise direction, it can be clearly observed that the mean velocity profile of the simulation based on DFSEM is more closed to that of the DNS compared with the simulation based on DFM and Lund method. There is a slight difference between the profiles of the simulation based on DFM and DFSEM. Comparatively, the discrepancy between the profile of the simulation based on Lund method and that of simulations based on other methods is apparent. For all simulations, the discrepancy occurs when y^+ increases from 30 to 300, and the discrepancy defined by $\langle \frac{|u'_{inlet} - u'_{DNS}|}{|u'_{DNS}|} \rangle \times 100\%$ is illustrated by Table 6-7. Besides, when y^+ is larger than 400, results of DFM and DFSEM could not decay to zero.

Table 6-7 Discrepancy of $\sqrt{u'u'}$ between the LES and the DNS result in the region $5 \leq y^+ \leq 300$

The content of Chapter 6 is published by the author of this thesis, the paper is *Influence of Turbulent Inlet Boundary Condition on Large Eddy Simulation Over a Flat Plate Boundary Layer*

	10δ	20δ	30δ	40δ	50δ
Lund	24.12	18.88	18.02	16.7	17.29
DFM	13.05	4.52	7.74	6.68	6.15
DFSEM	7.43	3.61	4.68	5.56	4.96

Figure 6.32 illustrated distribution of vertical velocity fluctuation (v_{rms}) at different streamwise positions. The deviation between the simulation results based on different inlet boundary conditions and the DNS data are more apparent. For the simulation based on Lund method, it can be observed that the profiles of v_{rms} at the inlet is much lower than the results of DNS data. As the distance away from the inlet becomes much larger, there is not apparent difference of the discrepancy between the simulation results based on Lund method and DNS data. For the simulation based on DFM and DFSEM, the difference between the v_{rms} profiles and the profile of the DNS at different streamwise positions is not as obvious as that of the simulation based on Lund method.

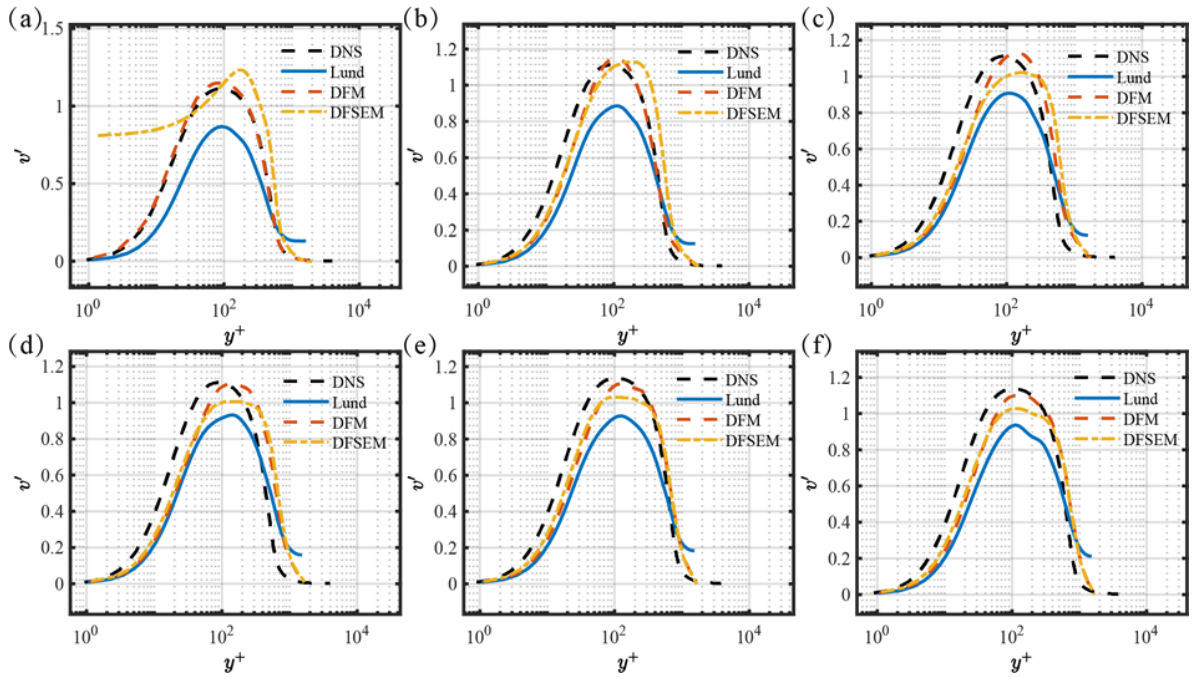


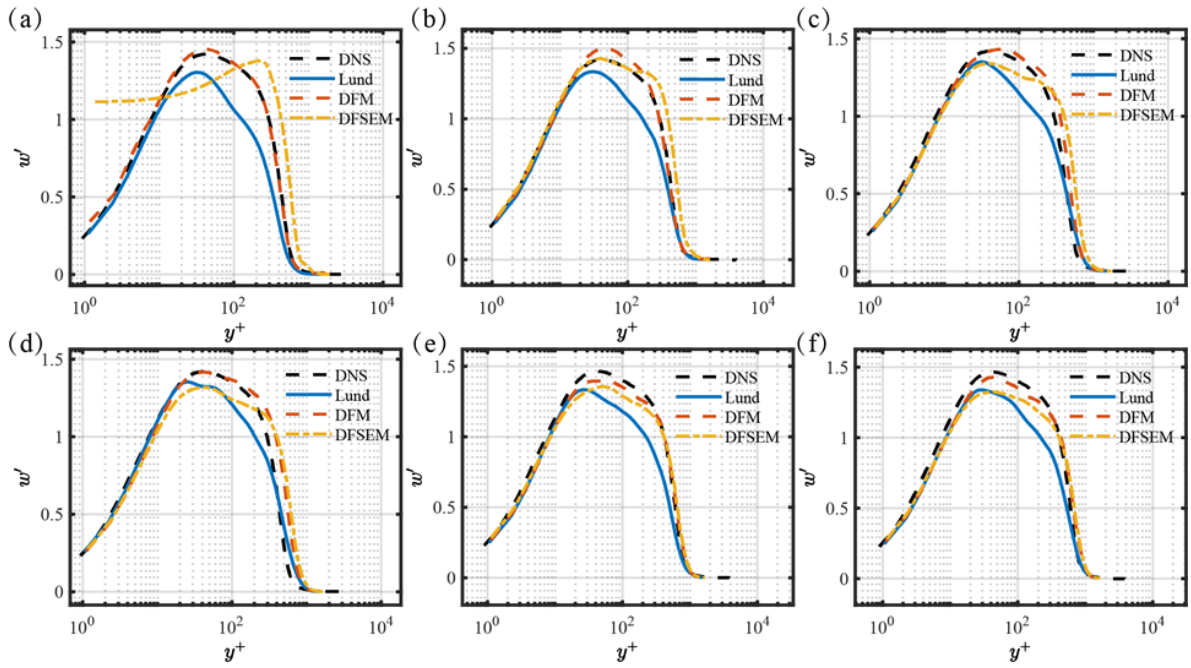
Figure 6.32 Distribution of the streamwise velocity fluctuation of simulations based on different IBC methods at different positions: (a) at x=inlet (b) at $x/\delta = 10$ (c) $x/\delta = 20$ (d) $x/\delta = 30$ (e) $x/\delta = 40$ (f) $x/\delta = 50$

The content of Chapter 6 is published by the author of this thesis, the paper is *Influence of Turbulent Inlet Boundary Condition on Large Eddy Simulation Over a Flat Plate Boundary Layer*

Compared with the DFSEM, the v_{rms} profiles of the simulation based on DFM are more closed to the profile of the DNS. But there is still apparent discrepancy at the position between $y^+ = 5$ and $y^+ = 100$ even after a long distance until $x/\delta = 50$. In the simulation based on DFSEM, the v_{rms} profiles approach the DNS results and keeps stable in a much longer distance than that in the simulation based on DFM. The results in the vertical position where $y^+ \geq 100$ could fit the DNS results but at the position where $5 \leq y^+ \leq 300$, there is apparent discrepancy between the simulation results and the DNS data. The mean relative difference defined by $\langle \frac{|v'_{IBC} - v'_{DNS}|}{|v'_{DNS}|} \rangle \times 100\%$ is applied to describe the discrepancy in this region as shown in Table 6-8.

Table 6-8 Discrepancy of $\sqrt{v'v'}$ between the LES and the DNS result in the region $5 \leq y^+ \leq 300$

	10δ	20δ	30δ	40δ	50δ
Lund	28.9	28.91	28.97	29.01	29.08
DFM	4.24	4.29	4.5	4.66	5
DFSEM	8.11	8.08	7.97	7.89	7.78



The content of Chapter 6 is published by the author of this thesis, the paper is *Influence of Turbulent Inlet Boundary Condition on Large Eddy Simulation Over a Flat Plate Boundary Layer*

Figure 6.33 Distribution of the spanwise velocity fluctuation of simulations based on different IBC methods at different positions: (a) at x=inlet (b) at $x/\delta = 10$ *(c)* $x/\delta = 20$ *(d)* $x/\delta = 30$ *(e)* $x/\delta = 40$ *(f)* $x/\delta = 50$

Figure 6.33 shows the distribution of the w_{rms} in simulations based on different inflow boundary condition methods. The simulation based on DFM produces results that are in good agreement with the profiles of DNS at the inlet and different downstream positions. Simulation performed using the DFSEM results in profiles that yield an underprediction at the positions from $x/\delta = 30$ to $x/\delta = 50$. Simulation with the Lund method produces the results that show larger underprediction than DFSEM between $y^+ = 30$ and $y^+ = 300$. The discrepancy between the simulations based on different IBC methods and the DNS result defined by $\langle \frac{|w\prime - w\prime_{DNS}|}{|w\prime_{DNS}|} \rangle \times 100\%$ is shown in Table 6-9. The profiles of the simulation based on Lund method shows apparent difference. There is always a slight deviation between the DNS results and the simulation results. The results keep stable when $x/\delta \geq 20$ for all simulations.

Table 6-9 Discrepancy of $\sqrt{w'w'}$ *between the LES and the DNS result in the region* $5 \leq y^+ \leq 300$

	10δ	20δ	30δ	40δ	50δ
Lund	14.01	13.52	12.48	13.05	11.7
DFM	3.18	3.75	4.73	4.4	3.9
DFSEM	4.61	7.33	8.42	6.47	7.26

The shear stress profiles are captured by Figure 6.34. The simulation performed using the DFSEM show a large discrepancy with the DNS profile at the inlet. The deviation is barely observed in cases based on DFSEM and Lund method. At different downstream positions along the streamwise direction, it is obvious that simulations based on different inlet turbulent boundary conditions produce results that are in good agreement with the profiles of DNS. Comparatively, simulations based on the DFM and Lund method could agree with the DNS profile much better.

The content of Chapter 6 is published by the author of this thesis, the paper is *Influence of Turbulent Inlet Boundary Condition on Large Eddy Simulation Over a Flat Plate Boundary Layer*

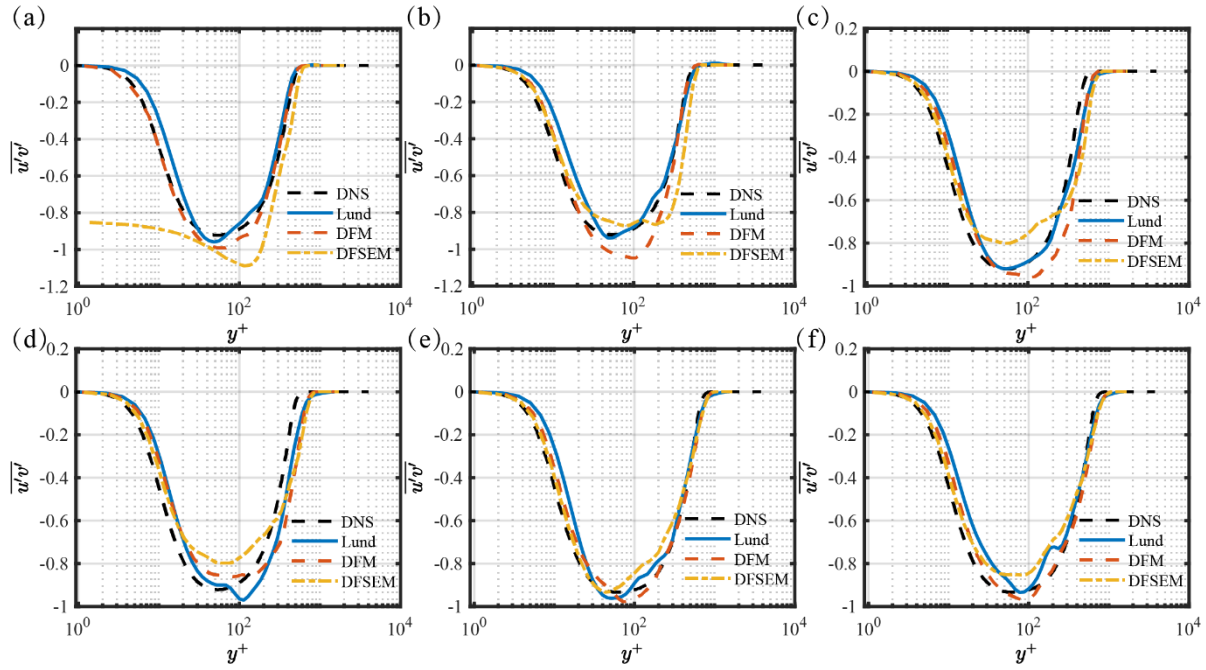


Figure 6.34 Distribution of the turbulent shear stresses $\overline{u'v'}$ of simulations based on different IBC methods at different positions: (a) at x=inlet (b) at $x/\delta = 10$ (c) $x/\delta = 20$ (d) $x/\delta = 30$ (e) $x/\delta = 40$ (f) $x/\delta = 50$

Besides the IBC methods, different SGS models applied have effects on the simulation results as well. To investigate the effects of interaction between different SGS models and different IBC methods, the cases based on DFSEM and DFM with different turbulent length scales and different SGS models are simulated. The results are displayed by Figure A13-Figure A48. Four SGS models are investigated including the Smagorinsky model (SM), the Wall-Adapting Local Eddy-viscosity (WALE) model, the one-equation k_{sgs} (KEqn) model and the dynamic Smagorinsky model (DSM). And the results reflect that the DSM and the WALE model can obtain the reliable simulation results, and there is no interaction between the input turbulent length scale and the turbulent SGS models. It means that even though the input turbulent length scale is changed, the simulation results with DSM and WALE models are still more reliable than those with other SGS models and the simulation results with DSM and WALE models are the same for simulations based on either DFSEM or DFM with different input turbulent length scales.

6.4. Conclusion of this chapter

The content of Chapter 6 is published by the author of this thesis, the paper is *Influence of Turbulent Inlet Boundary Condition on Large Eddy Simulation Over a Flat Plate Boundary Layer*

In this chapter, two topics were investigated. The first was the influence of the implementation of the constant input turbulent length scales on the LES cases based on the DFM and DFSEM and the influence of the length of the precursor domain on the LES cases based on the Lund method. The second was the influence of three different IBC methods used in the boundary-layer flow of the LES, and Re_θ at the inlet in this flow region was 1410.

The constant input turbulent length scales for the LES based on the DFM and DFSEM generated the physical turbulence about 10δ away from the inlet. Therefore, it is not necessary to use the one-point correlation with Taylor's hypothesis and two-point correlation to determine the values of the input turbulent length scales for simulations based on the DFM and DFSEM. When the value of the input turbulent length scale was approximately 0.4δ or 0.6δ for both IBC methods, the LES results agree well with those of DNS. The variance of simulation results based on the DFM was smaller than that based on the DFSEM, which indicates that the LES cases based on the DFM were not as sensitive to the constant input turbulent length scale as those based on the DFSEM. Moreover, the simulation based on the DFSEM when $L = 0.6\delta$ was in better agreement with the mean velocity profiles of DNS than that based on the DFM. This indicates that simulation based on DFSEM could obtain relatively reliable results. Besides, it is hard to see the difference between the cases with $L_u^x = 0.4\delta$, 0.6δ and 1δ. Similarly, the conclusion was nearly the same for the LES cases based on the DFSEM. Therefore, it is appropriate to use a value in the range of $0.4\delta - 1\delta$ as the input turbulent length scale for a zero pressure gradient boundary layer.

As observed, turbulence generated from different IBCs exhibited differences, and the iso-surface when $\mathrm{Q} = 20$ indicated that the order of the number of turbulent structures generated were as follows: $\mathrm{DFSEM} > \mathrm{DFM} > \mathrm{Lund\ method}$. The turbulent structures generated by these IBC methods could be maintained and stabilised without significant dissipation at different downstream positions, which indicates that coherent turbulent structures were formed in these

The content of Chapter 6 is published by the author of this thesis, the paper is *Influence of Turbulent Inlet Boundary Condition on Large Eddy Simulation Over a Flat Plate Boundary Layer*

cases. In comparison, the DFM and DFSEM are simpler; hence, these two synthetic turbulence methods are more applicable, although they require development lengths of approximately 10δ. In the simulation based on the Lund method, a clear turbulent structure was observed. With respect to the DFM and DFSEM results, the instantaneous velocity fields at the inlet were distinctive and non-physical; however, the non-physical inlet velocity fields had a significantly limited influence on the turbulent generation along the streamwise direction.

Based on the quantitative results, mean velocity, and turbulent Reynolds stresses, TKE budget profiles were used to reflect the flow details of each simulation. In the simulation based on the Lund method, the mean velocity profiles at the early stages were not in accordance with the law of the wall, and the deviations were mainly observed in the buffer region and log-law region. Moreover, the values of U^+ of the simulation results were larger than theoretical results when the values of y^+ were the same. These differences indicate that turbulence was not fully developed after the recycling and re-scaling process. This is in contrast with the simulations based on the DFSEM, wherein the values of U^+ from the simulation results were smaller than the theoretical results. The inlet profiles of the LES cases based on the DFM were in good agreement with the DNS profiles. At the different downstream positions along the streamwise direction, the extents of agreement with the law of the wall for the simulations were in the following order: $\mathrm{DFSEM} > \mathrm{DFM} > \mathrm{Lund\ method}$. The same pattern was observed for the profiles of $\sqrt{\overline{u'u'}}$ in the LES cases based on the three IBC methods.

From this chapter, two conclusions can be drawn. The first one is that input turbulent length scale for the DFM and DFSEM can be constant, and it is appropriate to use a value in the range of $0.6\delta - 1\delta$ as the input turbulent length scale. The second one is that simulation based on the DFSEM demonstrated a higher performance than other two IBC methods. It should be noted that there were several limitations to this study. First, there is a significant mismatch between DNS results and the LES results at the inlet plane when the DFSEM method

The content of Chapter 6 is published by the author of this thesis, the paper is *Influence of Turbulent Inlet Boundary Condition on Large Eddy Simulation Over a Flat Plate Boundary Layer*

is used. This problem is probably due to the implementation of the DFSEM, since the Lumley triangle mapping process is used instead of applying Lund transformation matrix. Second, the proportion of the input turbulent length scales in the different cases based on the DFM was fixed in this study. Maybe this condition results in the imperfect performance of the DFM in this study. The investigation of the influence of the proportion is therefore within the scope of future research. Third, the range of $0.6\delta - 1\delta$ should be tested in different cases such as the periodic hill flow and the flow over a hump as described in Chapter 5.

The content of Chapter 6 is published by the author of this thesis, the paper is *Influence of Turbulent Inlet Boundary Condition on Large Eddy Simulation Over a Flat Plate Boundary Layer*

Chapter 7

Conclusion

7.1. Original Research Contribution

Table 7-1 Objectives and relevant outcome of the research

Objective	Outcome of the research
O1	Turbulent IBC methods have a great impact on the LES in both complex terrain and flat plate boundary layer. The application of the Lund method is difficult. The limitation of the DFSEM and DFM is observed. Different turbulent IBC methods have a manifested impact on the flow separation after the hump. If the coherent turbulence is maintained in the approach flow such as the turbulence generated by the Lund method and the DFSEM, even though turbulent intensity is not large enough, the simulation can still predict the flow separation and turbulent bubble size relative precisely. In this work, except the RAND method, the DFSEM and the Lund method applied in the simulation could obtain the results that agree well with the experimental data after the hump, the clear difference can be only observed before the hump.
O2	In the flat plate boundary layer. It can be observed that the results of the simulation based on DFSEM with the turbulent length scale about 0.4-1.0δ could agree better with the experimental data compared with other methods.
O3	For the DFM and DFSEM, it is obvious that the turbulent length scale is a critical parameter that should be predefined at the inlet. In this research, according to the scale of the mixing length, we found that in the flat plate boundary layer we can use the boundary layer thickness by a factor of 0.4-1.0 as the input turbulent length scale for these two methods.

O4	The Lund method is more expensive compared with the method based on other methods since the time average value should be modified and the a temporal velocity data should be restored. There is no apparent difference on the simulation cost between other methods. For the Lund method, the improvement is more difficult, for the simulation based on the DFSEM and the DFM, it can be observed that the value of the turbulent length scale can be modified to make the simulation result agree well with the DNS results.

Table 7-1 shows the comprehensiveness of results towards the establishment of a methodological framework. The main research contributions are listed as follows:

i) Different turbulent inflow generation methods have an obvious effect on the flow separation after the hump. If the coherent turbulence is maintained in the approach flow, even though turbulent intensity is not large enough, the simulation can still capture the flow separation and turbulent bubble size precisely.

ii) For the flat plate boundary layer. The input turbulent length scale for the DFM and DFSEM can be constant, and it is appropriate to use a value in the range of $0.4\delta - 1\delta$ as the input turbulent length scale. And the simulation based on the DFSEM demonstrated a higher performance than other two IBC methods.

7.2. Further steps of the research

The thesis compared the effects of different IBC methods on 2 LES cases. The first one is the flow over a hump and the second one is the boundary layer flow. For the flow over a hump, it can be observed that there is relatively big difference between the simulation results and the experimental results. Even if the simulation based on the Lund method and DFSEM have a better performance than the simulation based on the RAND method, the results still cannot agree well with the experimental data. There are some possible reasons that result in the big difference. Firstly, the spanwise width of the simulation domain is relatively small. In the future,

the spanwise width sensitivity analysis should be comprised to examine if this property will make a big difference on the simulation results. Additionally, the LES sub-grid scale model has a slight impact on the results according to the previous research, in the future, the more advanced SGS model such as dynamic Vreman model (You and Moin, 2007) could be applied to investigate the influence of different SGS models. Finally, the DFSEM is sensitive to the surface normal gradient schemes, therefore the method should be optimized in the future.

The second case fully discussed in this thesis is the boundary flow. According to the conclusion as shown above. Similarly, the effect of LES sub-grid scale models should be investigated explicitly in that different SGS models might have a great impact on the results. In the future, the simulations based on different IBC methods with different SGS models should be put together with comparison. Besides, the value of the turbulent length scale for this case is obtained. In the future, it is reasonable to explore whether the optimal turbulent length scale for this case is still accessible for other cases. In addition, the proportion of the input turbulent length scales in cases based on DFM is fixed in this study. Currently, there is little research could elaborate the how each component of the turbulent length scale affects the artificial instantaneous velocity field generated at the inlet. And the mechanism of the impact of the turbulent length scale is still not clear. Therefore, the effect of each component of the turbulent length scale and the proportion between them should be further explored in the future. And it is significant to explore the mechanism of the impact of the turbulent length scale on the artificial turbulence generated at the inlet.

References

Aboshosha, H., Elshaer, A., Bitsuamlak, G.T., El Damatty, A., 2015. Consistent inflow turbulence generator for LES evaluation of wind-induced responses for tall buildings. J. Wind Eng. Ind. Aerodyn. 142, 198–216.

Aliabadi, A.A., Veriotes, N., Pedro, G., 2018. A Very Large-Eddy Simulation (VLES) model for the investigation of the neutral atmospheric boundary layer. J. Wind Eng. Ind. Aerodyn. 183, 152–171.

Allegrini, J., Carmeliet, J., 2017. Evaluation of the Filtered Noise Turbulent Inflow Generation Method. Flow, Turbul. Combust. 98, 1087–1115.

Araya, G., Castillo, L., Meneveau, C., Jansen, K., 2011. A dynamic multi-scale approach for turbulent inflow boundary conditions in spatially developing flows. J. Fluid Mech. 670, 581–605.

Asgari, E., Tadjfar, M., 2017. Assessment of four inflow conditions on large-eddy simulation of a gently curved backward-facing step. J. Turbul. 18, 61–86.

Bechmann, A., Sørensen, N.N., Johansen, J., 2007. Atmospheric flow over terrain using hybrid RANS/LES. Eur. Wind Energy Conf. Exhib. 2007, EWEC 2007 1, 107–113.

Benedicto, A., Rives, T., Soliva, R., 2014. The 3D Fault Segmentation Development - A Conceptual Model. Implications of Fault Sealing.

Blackman, K., Perret, L., Calmet, I., Rivet, C., 2017. Turbulent kinetic energy budget in the boundary layer developing over an urban-like rough wall using PIV. Phys. Fluids 29.

Boris, C., 2012. Wind resource accessment in complex terrain by wind tunnel modelling.

Cao, S.J., 2019. Challenges of using CFD simulation for the design and online control of ventilation systems. Indoor Built Environ. 28, 3–6.

Castro, H.G., Paz, R.R., Sonzogni, V.E., 2011. Generation of Turbulent Inlet Velocity Conditions XXX, 1–4.

CFD Direct, 2020. OpenFOAM v6 User Guide: 4.4 Numerical schemes (date accessed: 13.02.2020) [WWW Document]. URL https://cfd.direct/openfoam/user-guide/v6-fvschemes/

Classic Collection All cases no.83 [WWW Document], n.d. URL http://cfd.mace.manchester.ac.uk/ercoftac/index.html

Davidson, L., 2022. Synthetic turbulence generator for lattice Boltzmann method at the interface between Synthetic turbulence generator for lattice Boltzmann method at the interface between RANS and LES 055118.

Davidson, L., Billson, M., 2006. Hybrid LES-RANS using synthesized turbulent fluctuations for forcing in the interface region. Int. J. Heat Fluid Flow 27, 1028–1042.

Dhamankar, N.S., Blaisdell, G.A., Lyrintzis, A.S., 2018. Overview of turbulent inflow boundary conditions for large-eddy simulations. AIAA J. 56, 1317–1334.

di Mare, L., Klein, M., Jones, W.P., Janicka, J., 2006. Synthetic turbulence inflow conditions for large-eddy simulation. Phys. Fluids 18.

Druault, P., Lardeau, S., Bonnet, J.P., Coiffet, F., Delville, J., Lamballais, E., Largeau, J.F., Perret, L., 2004. Generation of Three-Dimensional Turbulent Inlet Conditions for Large-Eddy Simulation. AIAA J. 42, 447–456.

Druilhet, A., Durand, P., 1997. Experimental investigation of atmospheric boundary layer turbulence. Atmos. Res. 43, 345–388.

Drummond, I.T., Duane, S., Horgan, R.R., 1984. Scalar diffusion in simulated helical turbulence with molecular diffusivity. J. Fluid Mech. 138, 75–91.

Egolf, P.W., 1994. Difference-quotient turbulence model: A generalization of Prandtl's mixing-length theory. Phys. Rev. E 49, 1260–1268.

Elghorab, M., Ahmed, M., 2020. Numerical analysis for active control of drag over flat plate using sinusoidal travelling wave method.

Fagbade Afagbade@Uwyo.Edu, A., Heinz, S., 2022. Application of Mode-Controlled Hybrid RANS-LES to the NASA Wall-Mounted Hump Flow. AIAA Sci. Technol. Forum Expo. AIAA SciTech Forum 2022.

Fluent Inc, 2006. FLUENT 6.3 User's Guide.

Fröhlich, J., Mellen, C.P., Rodi, W., Temmerman, L., Leschziner, M.A., 2005. Highly resolved large-eddy simulation of separated flow in a channel with streamwise periodic constrictions. J. Fluid Mech. 526, 19–66.

Fukami, K., Nabae, Y., Kawai, K., Fukagata, K., 2019. Synthetic turbulent inflow generator using machine learning. Phys. Rev. Fluids 4, 1–26.

Germano, M., 1992. Turbulence : the filtering approach. J. Fluid Mech. 238, 325–336.

Greenblatt, D., Paschal, K.B., Yao, C., Harris, J., Schaeffler, N.W., Washburn, A.E., 2006. Part 1 : Baseline & Steady Suction. AIAA J. 44, 1–17.

Hepffner, J., Naka, Y., Fukagata, K., 2011. Realizing turbulent statistics. J. Fluid Mech. 676, 54–80.

Holzmann, T., 2017. Mathematics, Numerics, Derivations and OpenFOAM. Config. Distrib. Syst. 1992., Int. Work. 68–79.

Honnert, R., Masson, V., Lac, C., Nagel, T., 2021. A Theoretical Analysis of Mixing Length for Atmospheric Models From Micro to Large Scales. Front. Earth Sci. 8, 1–15.

Huang, S.H., Li, Q.S., Wu, J.R., 2010. A general inflow turbulence generator for large eddy simulation. J. Wind Eng. Ind. Aerodyn. 98, 600–617.

Hunt, J.C.R., Wray, a a, Moin, P., 1988. Eddies, streams, and convergence zones in turbulent flows. Cent. Turbul. Res. Proc. Summer Progr. 193–208.

Hutchinson, A.J., Hale, N., Born, K., Mason, D.P., 2021. Prandtl's extended mixing length model applied to the two-dimensional turbulent classical far wake. Proc. R. Soc. A Math. Phys. Eng. Sci. 477.

I.Park, G., 2015. Wall-modeled large-eddy simulation of a separated flow over the NASA wall-mounted hump. Annu. Res. Briefs (Center Turbul. Res. 145–160.

Immer, M.C., 2016. Time-resolved measurement and simulation of local scale turbulent urban flow.

Inoue, M., 2012. Large-Eddy Simulation of the Flat-plate Turbulent Boundary Layer at High Reynolds numbers. Caltech Dr. thethis 2012, 1–111.

Iwamoto, K., 2002. Database for fully developed channel flow [WWW Document]. THTLAB Intern. Rep. (ILR- 0201).

Jarrin, N., Benhamadouche, S., Laurence, D., Prosser, R., 2006. A synthetic-eddy-method for generating inflow conditions for large-eddy simulations. Int. J. Heat Fluid Flow 27, 585–593.

Ji, B., Lei, W., Xiong, Q., 2022. An inflow turbulence generation method for large eddy simulation and its application on a standard high-rise building. J. Wind Eng. Ind. Aerodyn. 226, 105048.

Kanchi, H., Sengupta, K., Mashayek, F., 2013. Effect of turbulent inflow boundary condition in les of flow over a backward-facing step using spectral element method. Int. J. Heat Mass Transf. 62, 782–793.

Karras, T., Aila, T., Laine, S., Lehtinen, J., 2018. Progressive growing of GANs for improved quality, stability, and variation. 6th Int. Conf. Learn. Represent. ICLR 2018 - Conf. Track Proc. 1–26.

Karras, T., Laine, S., Aila, T., 2021. A Style-Based Generator Architecture for Generative Adversarial Networks. IEEE Trans. Pattern Anal. Mach. Intell. 43, 4217–4228.

Keating, A., Piomelli, U., Balaras, E., Kaltenbach, H.J., 2004. A priori and a posteriori tests of inflow conditions for large-eddy simulation. Phys. Fluids 16, 4696–4712.

Khosronejad, A., Flora, K., Kang, S., 2020. Effect of Inlet Turbulent Boundary Conditions on Scour Predictions of Coupled LES and Morphodynamics in a Field-Scale River: Bankfull Flow Conditions. J. Hydraul. Eng. 146, 1–24.

Kim, J., Lee, C., 2020. Deep unsupervised learning of turbulence for inflow generation at various Reynolds numbers. J. Comput. Phys. 406, 1–26.

Kim, W.W., Menon, S., 1995. A new dynamic one-equation subgrid-scale model for large eddy simulations. 33rd Aerosp. Sci. Meet. Exhib.

Kim, Y., Castro, I.P., Xie, Z.T., 2013. Divergence-free turbulence inflow conditions for large-eddy simulations with incompressible flow solvers. Comput. Fluids 84, 56–68.

Klein, M., Sadiki, A., Janicka, J., 2003. A digital filter based generation of inflow data for spatially developing direct numerical or large eddy simulations. J. Comput. Phys. 186, 652–665.

Kondo, K., Murakami, S., Mochida, A., 1997. Generation of velocity fluctuations for inflow boundary condition of LES. J. Wind Eng. Ind. Aerodyn. 67–68, 51–64.

Kornev, N., Hassel, E., 2003. A new method for generation of artificial turbulent inflow data with prescribed statistic properties for LES and DNS simulations. Schiffbauforschung 42, 35–44.

Kraichnan, R.H., 1970. Diffusion by a Random Velocity Field 22.

Krishna, V., Squires, K.D., Forsythe, J.R., 2004. Prediction of separated flow characteristics over a hump using RANS and DES. 2nd AIAA Flow Control Conf. 44.

Kröger, H., Kornev, N., 2018. Generation of divergence free synthetic inflow turbulence with arbitrary anisotropy. Comput. Fluids 165, 78–88.

Lamberti, G., García-Sánchez, C., Sousa, J., Gorlé, C., 2018a. Optimizing turbulent inflow conditions for large-eddy simulations of the atmospheric boundary layer. J. Wind Eng. Ind. Aerodyn. 177, 32–44.

Lamberti, G., García-Sánchez, C., Sousa, J., Gorlé, C., 2018b. Optimizing turbulent inflow conditions for large-eddy simulations of the atmospheric boundary layer. J. Wind Eng. Ind. Aerodyn. 177, 32–44.

Lee, Y.T., Gutti, L.K., Lim, H.C., 2021. Numerical study of the influence of the inlet turbulence length scale on the turbulent boundary layer. Appl. Sci. 11.

Leonard, A., 1975. Energy cascade in large-eddy simulations of turbulent fluid flows. Adv. Geophys. 18, 237–248.

Li, N., Balaras, E., Piomelli, U., 2000. Inflow conditions for large-eddy simulations of mixing layers. Phys. Fluids 12, 935–938.

Lilly, D.K., 1992. A proposed modification of the German0 closure method h J axi. Phys. Fluids 4, 633–635.

Liu, K., Pletcher, R.H., 2006. Inflow conditions for the large eddy simulation of turbulent boundary layers: A dynamic recycling procedure. J. Comput. Phys. 219, 1–6.

Lund, T.S., Wu, X., Squires, K.D., 1998. Generation of Turbulent Inflow Data for Spatially-Developing Boundary Layer Simulations. J. Comput. Phys. 140, 233–258.

Luo, Y., Liu, H., Huang, Q., Xue, H., Lin, K., 2017. A multi-scale synthetic eddy method for generating inflow data for LES. Comput. Fluids 156, 103–112.

M. R. Maxey, 1987. The gravitational settling of aerosol particles in homogeneous turbulence and random flow fields. J. Fluid Mech. 174, 441–465.

Mahdizadehaghdam, S., Panahi, A., Krim, H., 2019. Sparse generative adversarial network. Proc. - 2019 Int. Conf. Comput. Vis. Work. ICCVW 2019 3063–3071.

Mansouri, Z., Panneer, R., Gan, A., 2022. Journal of Wind Engineering & Industrial Aerodynamics Performance of different inflow turbulence methods for wind engineering applications. J. Wind Eng. Ind. Aerodyn. 229, 105141.

Martínez, J., Piscaglia, F., Montorfano, A., Onorati, A., Aithal, S.M., 2015. Influence of spatial discretization schemes on accuracy of explicit LES: Canonical problems to engine-like geometries. Comput. Fluids 117, 62–78.

McMullan, W.A., Gao, S., Coats, C.M., 2009. The effect of inflow conditions on the transition to turbulence in large eddy simulations of spatially developing mixing layers. Int. J. Heat Fluid Flow 30, 1054–1066.

Minguez, M., Pasquetti, R., Serre, E., 2008. High-order large-eddy simulation of flow over the "Ahmed body" car model. Phys. Fluids 20.

Moin, P., Mahesh, K., 1998. DIRECT NUMERICAL SIMULATION: A Tool in Turbulence Research. Annu. Rev. Fluid Mech. 30, 539–578.

Montorfano, A., Piscaglia, F., Ferrari, G., 2013a. Inlet boundary conditions for incompressible LES: A comparative study. Math. Comput. Model. 57, 1640–1647.

Montorfano, A., Piscaglia, F., Ferrari, G., 2013b. Inlet boundary conditions for incompressible LES: A comparative study. Math. Comput. Model. 57, 1640–1647.

Mordant, N., Metz, P., Michel, O., Pinton, J.F., 2001. Measurement of lagrangian velocity in fully developed turbulence. Phys. Rev. Lett. 87, 214501-1-214501–4.

Mukha, T., Liefvendahl, M., 2017. The generation of turbulent inflow boundary conditions using precursor channel flow simulations. Comput. Fluids 156, 21–33.

Nicoud, F., Ducros, F., 2006. Subgrid-scale stress modelling based on the square of the velocity. Agric. Econ. Res. Rev. 19, 37–48.

OpenFOAM-v2006, n.d. Turbulent inlet boundary condition based on pseudo-random numbers and a given spatiotemporal-invariant mean field [WWW Document]. URL https://www.openfoam.com/documentation/guides/latest/api/classFoam_1_1turbulentInletFvPatchField.html

Pamiès, M., Weiss, P.É., Garnier, E., Deck, S., Sagaut, P., 2009. Generation of synthetic turbulent inflow data for large eddy simulation of spatially evolving wall-bounded flows. Phys. Fluids 21.

Patruno, L., Ricci, M., 2017. On the generation of synthetic divergence-free homogeneous anisotropic turbulence. Comput. Methods Appl. Mech. Eng. 315, 396–417.

Perret, L., Delville, J., Manceau, R., Bonnet, J.P., 2008. Turbulent inflow conditions for large-eddy simulation based on low-order empirical model. Phys. Fluids 20.

Philipp, S., 2011. Boundary Layer DNS/LES Data [WWW Document]. 7th Int. Symp. Turbul. Shear Flow Phenom. URL https://www.mech.kth.se/~pschlatt/DATA/

Piomelli, U., 1999. Large-eddy simulation: achievements and challenges. Prog. Aerosp. Sci. 35, 335–362.

Poletto, R., Craft, T., Revell, A., 2013. A new divergence free synthetic eddy method for the reproduction of inlet flow conditions for les. In: Flow, Turbulence and Combustion. pp. 519–539.

Pope, S., 2001. Turbulent flows.

Pope, S.B., 2001. Turbulent flows.

Quon, E.W., Ghate, A.S., Lele, S.K., 2018. Enrichment methods for inflow turbulence generation in the atmospheric boundary layer. In: Journal of Physics: Conference Series. Institute of Physics Publishing.

R.I.Issa, 1991. Solution of the Implicity Discretized Reacting Flow Equations by Operator-Splitting. J. Comput. Phys. 388–410.

Radford, A., Metz, L., Chintala, S., 2016. Unsupervised representation learning with deep convolutional generative adversarial networks. 4th Int. Conf. Learn. Represent. ICLR 2016 - Conf. Track Proc. 1–16.

Rai, M.M., Parviz, M., 1993. Direct Numerical Simulation of Transition and Turbulence in a Spatially Evolving Boundary Layer. J. Comput. Phys. 109, 169–192.

Roach, P., Brierlay, D., 1989. The influence of a turbulent freestream on zero pressure gradient transitional boundary layer development including the condition test cases T3A and T3B. Cambridge Univ. Press 319–347.

Roth, K., Lucchi, A., Nowozin, S., Hofmann, T., 2017. Stabilizing training of generative adversarial networks through regularization. Adv. Neural Inf. Process. Syst. 2017-Decem, 2019–2029.

Sagaut, P., 2006. Large eddy simulation for incompressible flows: an introduction. Springer Science & Business Media.

Sagaut, P., Garnier, E., Tromeurz, E., Larchevêque, L., Labourasse, E., 2003. Turbulent inflow conditions for LES of supersonic and subsonic wall bounded flows. 41st Aerosp. Sci. Meet. Exhib. 1–11.

Šarić, S., Jakirlić, S., Tropea, C., 2005. A periodically perturbed backward-facing step flow by means of LES, des and T-RANS: An example of flow separation control. J. Fluids Eng. Trans. ASME 127, 879–887.

Schlatter, P., Örlü, R., 2012. Turbulent boundary layers at moderate Reynolds numbers: Inflow length and tripping effects. J. Fluid Mech. 710, 5–34.

Shahinfar, S., Fransson, J.H.M., Sattarzadeh, S.S., Talamelli, A., 2013. Scaling of streamwise boundary layer streaks and their ability to reduce skin-friction drag. J. Fluid Mech. 733, 1–32.

Smagorinsky, J., 1963. General circulation experiments with the primitive equations: I. The basic equations. Mon. Weather Rev. 91,99-164.

Smirnov, A., Shi, S., Celik, I., 2001. Random Flow Generation Technique for Large Eddy Simulations and Particle-Dynamics Modeling. J. Fluid Mech. 123, 359–371.

Smith, F.T., Scheichl, B., Kluwick, A., 2010. On turbulent separation. J. Eng. Math. 68, 373–400.

Source, O., Consulting, C.F.D., 2014. OpenFoam Utilities.

Spalart, P.R., 1988. Direct simulation of a turbulent boundary layer up to Rθ= 1410. J. Fluid Mech. 187, 61–98.

Spalding, D.B., 1960. A single formula for the “law of the wall.” J. Appl. Mech. Trans. ASME 28, 455–458.

Tabor, G.R., Baba-Ahmadi, M.H., 2010. Inlet conditions for large eddy simulation: A review. Comput. Fluids 39, 553–567.

Tominaga, Y., Stathopoulos, T., 2011. CFD modeling of pollution dispersion in a street canyon: Comparison between LES and RANS. J. Wind Eng. Ind. Aerodyn. 99, 340–348.

Treleaven, N.C.W., Staufer, M., Spencer, A., Garmory, A., Page, G.J., 2020. Application of the PODFS method to inlet turbulence generated using the digital filter technique. J. Comput. Phys. 1, 109541.

Tyacke, J.C., Tucker, P.G., 2015. Future use of large eddy simulation in aero-engines. J. Turbomach. 137, 1–16.

Uzun, A., Malik, M.R., 2018. Large-eddy simulation of flow over a wall-mounted hump with separation and reattachment. AIAA J. 56, 715–730.

Vasaturo, R., Kalkman, I., Blocken, B., van Wesemael, P.J.V., 2018. Large eddy simulation of the neutral atmospheric boundary layer: performance evaluation of three inflow methods for terrains with different roughness. J. Wind Eng. Ind. Aerodyn. 173, 241–261.

Veloudis, I., Yang, Z., McGuirk, J.J., Page, G.J., Spencer, A., 2007. Novel implementation and assessment of a digital filter based approach for the generation of les inlet conditions. Flow, Turbul. Combust. 79, 1–24.

Vita, G., Hemida, H., Andrianne, T., Baniotopoulos, C., 2020. The effect of the integral length scale of turbulence on a wind turbine aerofoil. J. Wind Eng. Ind. Aerodyn. 204, 104235.

Wu, X., 2016. Inflow Turbulence Generation Methods. Annu. Rev. Fluid Mech. 49, 23–49.

Wu, X., Moin, P., 2009. Direct numerical simulation of turbulence in a nominally zero-pressure-gradient flat-plate boundary layer. J. Fluid Mech. 630, 5–41.

Xiao, F., Dianat, M., McGuirk, J.J., 2013. Large eddy simulation of liquid-jet primary breakup in air crossflow. AIAA J. 51, 2878–2893.

Xie, Z.T., Castro, I.P., 2008. Efficient generation of inflow conditions for large eddy simulation of street-scale flows. Flow, Turbul. Combust. 81, 449–470.

Yan, B.W., Li, Q.S., 2015. Computers & Fluids Inflow turbulence generation methods with large eddy simulation for wind effects on tall buildings 116, 158–175.

Yang, Q., Zhou, T., Yan, B., Van Phuc, P., Hu, W., 2020. LES study of turbulent flow fields over hilly terrains — Comparisons of inflow turbulence generation methods and SGS models. J. Wind Eng. Ind. Aerodyn. 204.

You, D., Moin, P., 2007. Application of a dynamic global-coefficient subgrid-scale model for large-eddy simulation in complex geometries. 2007 Proc. 5th Jt. ASME/JSME Fluids Eng. Summer Conf. FEDSM 2007 1 SYMPOSIA, 1429–1437.

You, D., Wang, M., Moin, P., 2006. Large-eddy simulation of flow over a wall-mounted hump with separation control. AIAA J. 44, 2571–2577.

Yu, Y., Yang, Y., Xie, Z., 2018. A new inflow turbulence generator for large eddy simulation evaluation of wind effects on a standard high-rise building. Build. Environ. 138, 300–313.

Zhong, J., Cai, X., Xie, Z.-T., 2019. Implementation of a synthetic inflow turbulence generator in idealised WRF v3.6.1 large eddy simulations under neutral atmospheric conditions. Geosci. Model Dev. Discuss. 1–24.

Appendices

A1. The grid independency analysis after the hump

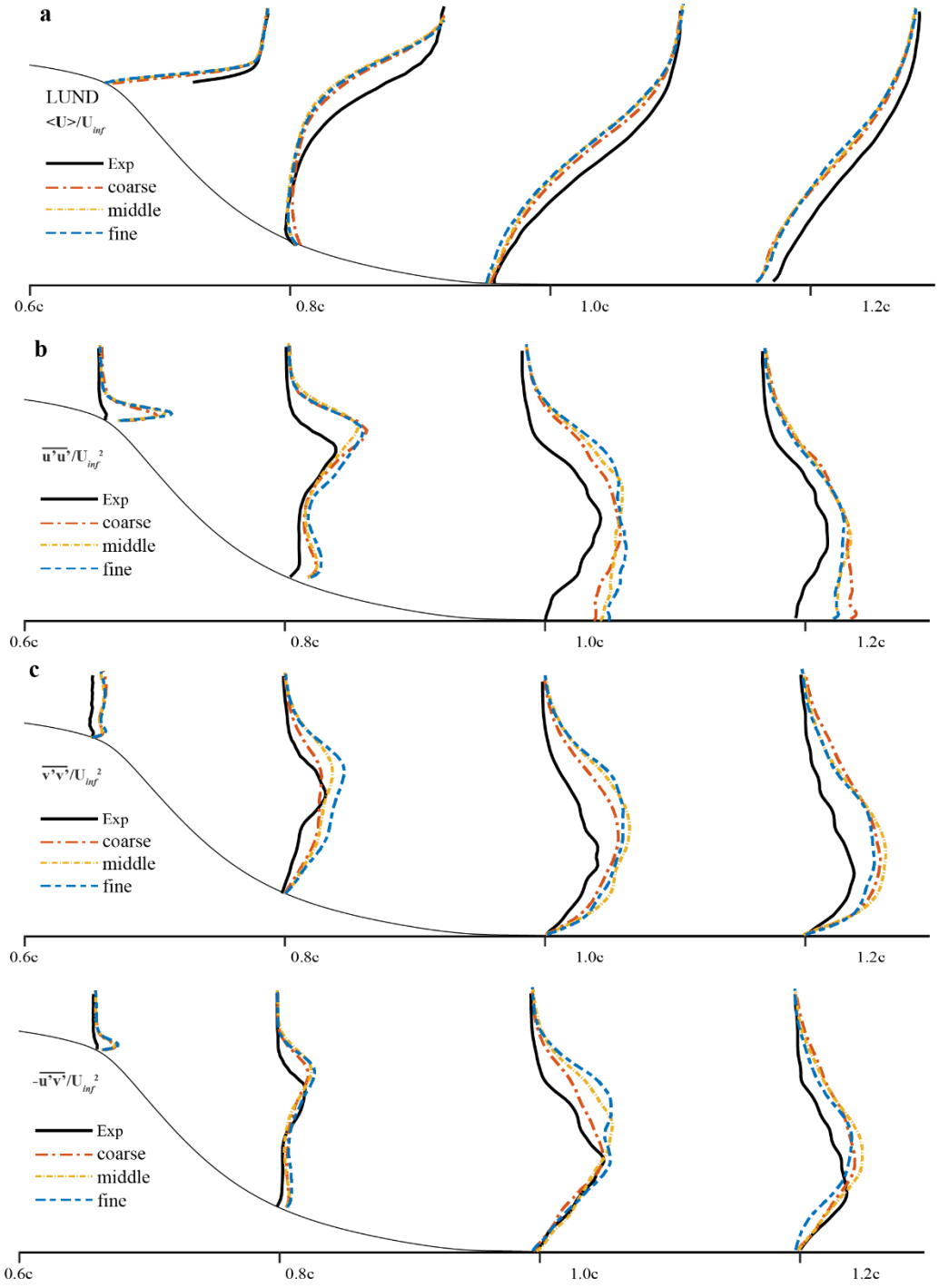


Figure A1. Grid independency analysis after the hump for the simulation based on Lund method: (a) Mean velocity profiles (b) profiles of Reynolds stresses component $\overline{u'u'}$ (c) profiles of Reynolds stresses component $\overline{v'v'}$ (d) profiles of Reynolds stresses component $\overline{u'v'}$

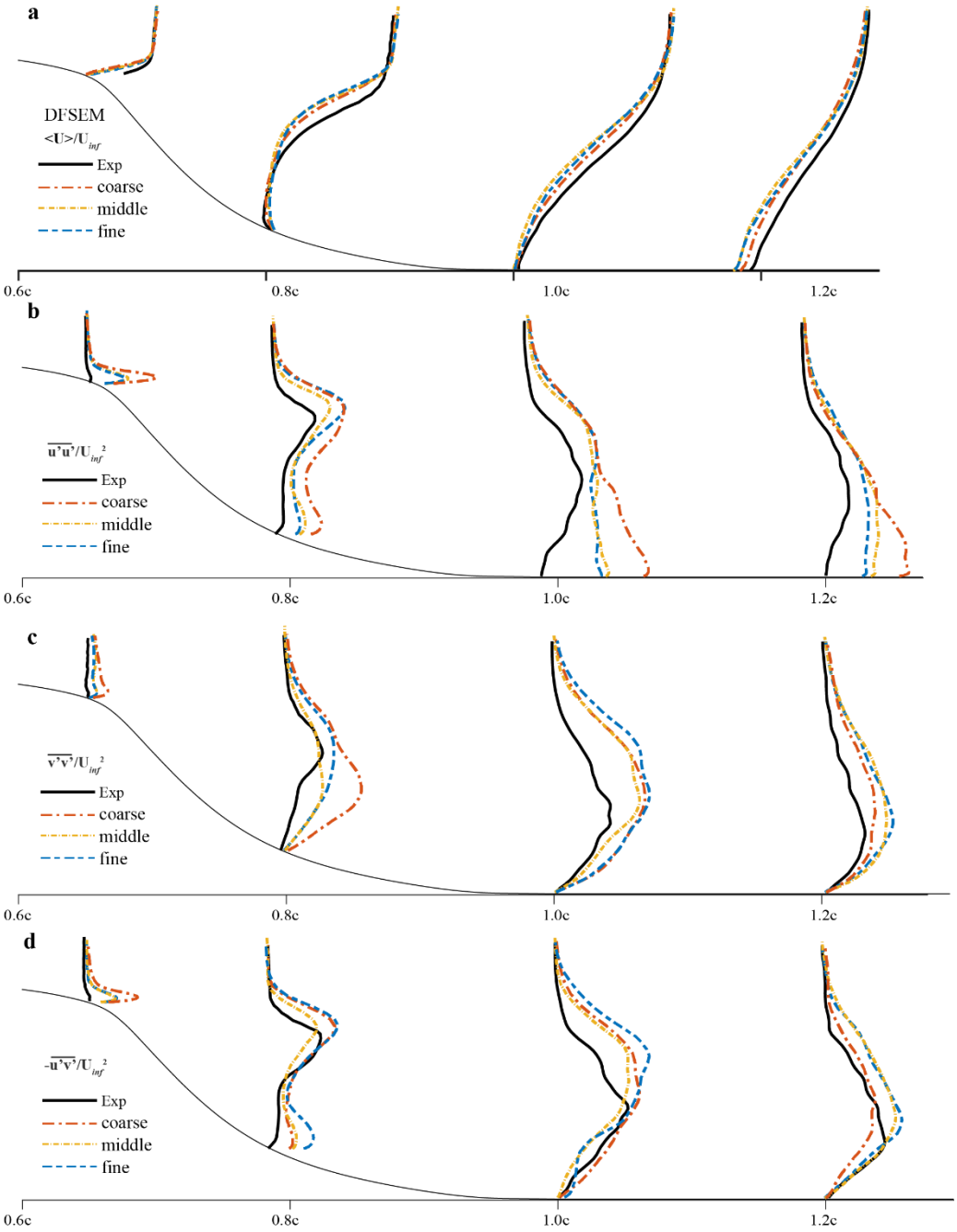


Figure A2. Grid independency analysis after the hump for the simulation based on DFSEM: (a) Mean velocity profiles (b) profiles of Reynolds stresses component $\overline{u'u'}$ (c) profiles of Reynolds stresses component $\overline{v'v'}$ (d) profiles of Reynolds stresses component $\overline{u'v'}$

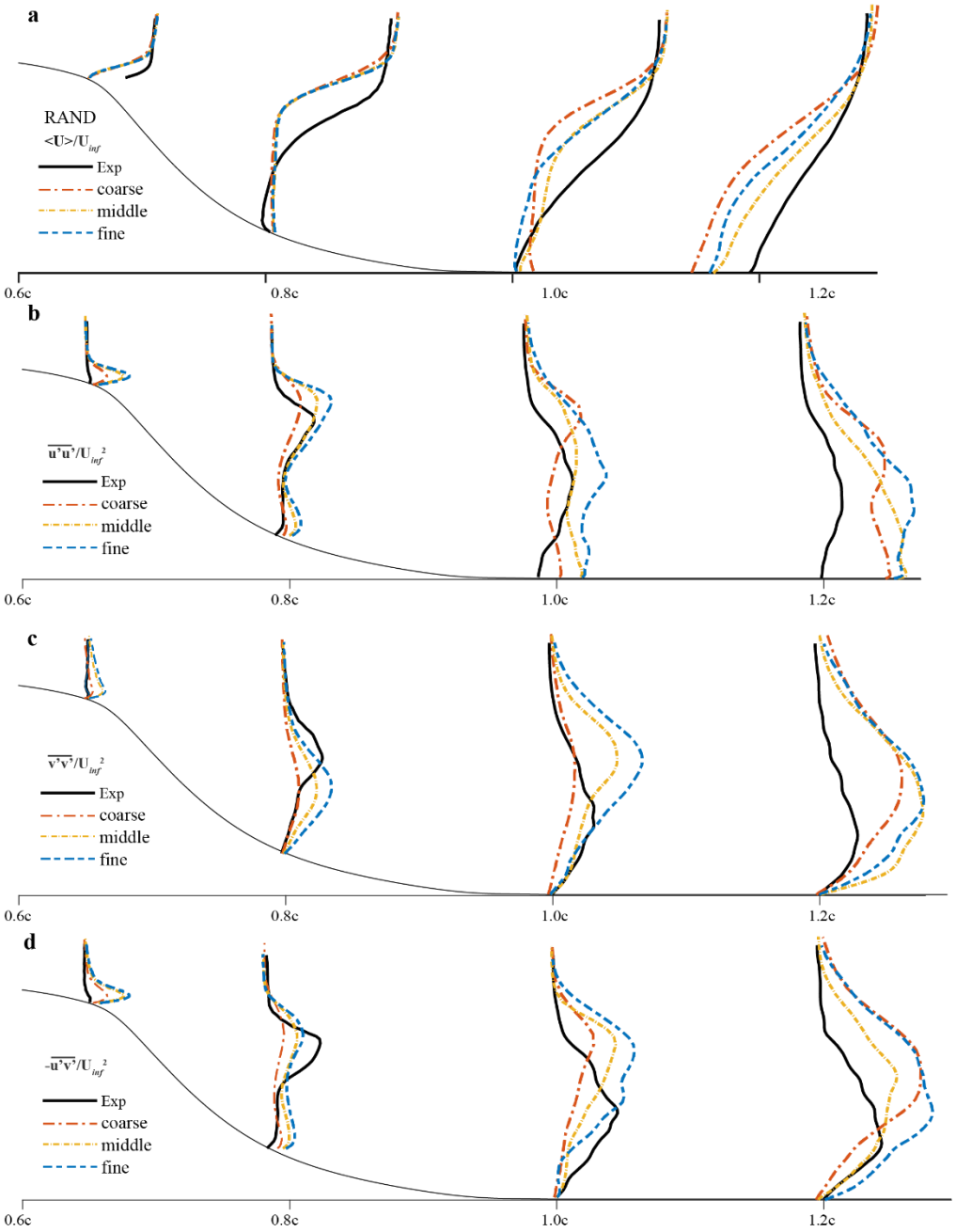


Figure A3. Grid independency analysis after the hump for the simulation based on RAND method: (a) Mean velocity profiles (b) profiles of Reynolds stresses component $\overline{u'u'}$ (c) profiles of Reynolds stresses component $\overline{v'v'}$ (d) profiles of Reynolds stresses component $\overline{u'v'}$

A2. The grid independency analysis for the flat plate boundary layer

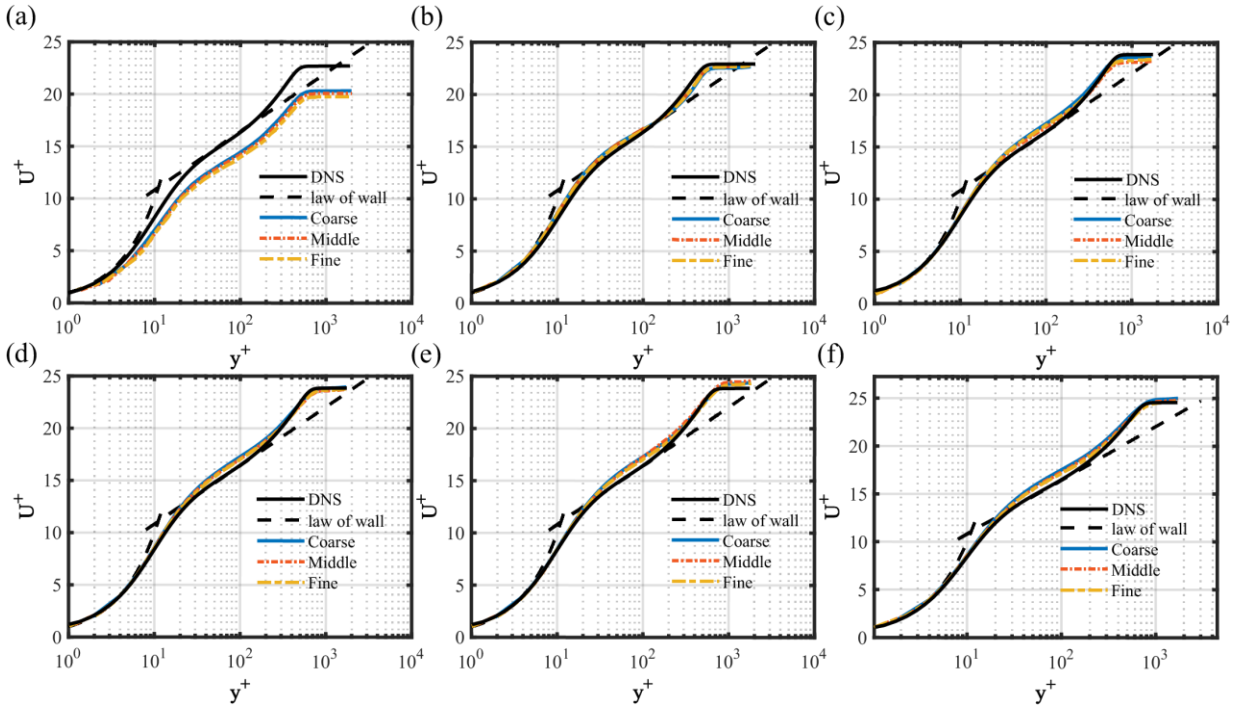


Figure A4. Distribution of the mean velocity profiles of simulations based on DFSEM with different mesh size at different positions: (a) at x=inlet (b) at $x/\delta = 10$ (c) $x/\delta = 20$ (d) $x/\delta = 30$ (e) $x/\delta = 40$ (f) $x/\delta = 50$

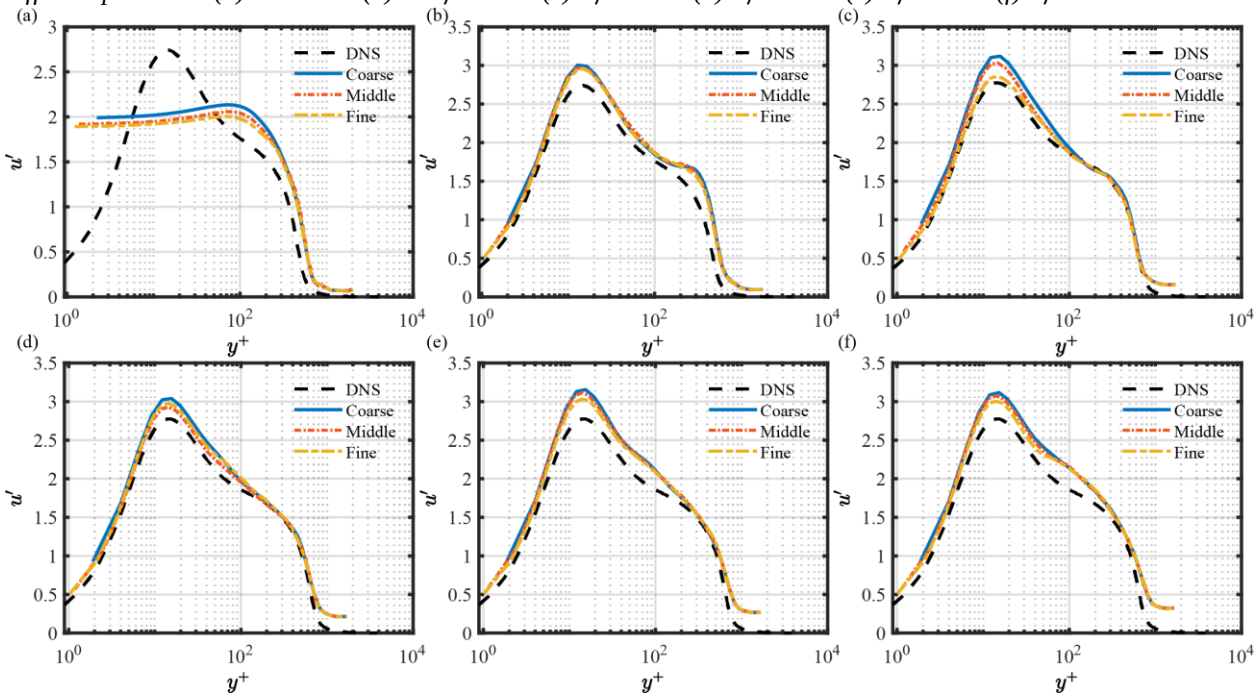


Figure A5. Distribution of the profiles of Reynolds stresses component $\overline{u'u'}$ in simulations based on DFSEM with different mesh size at different positions: (a) at x=inlet (b) at $x/\delta = 10$ (c) $x/\delta = 20$ (d) $x/\delta = 30$ (e) $x/\delta = 40$ (f) $x/\delta = 50$

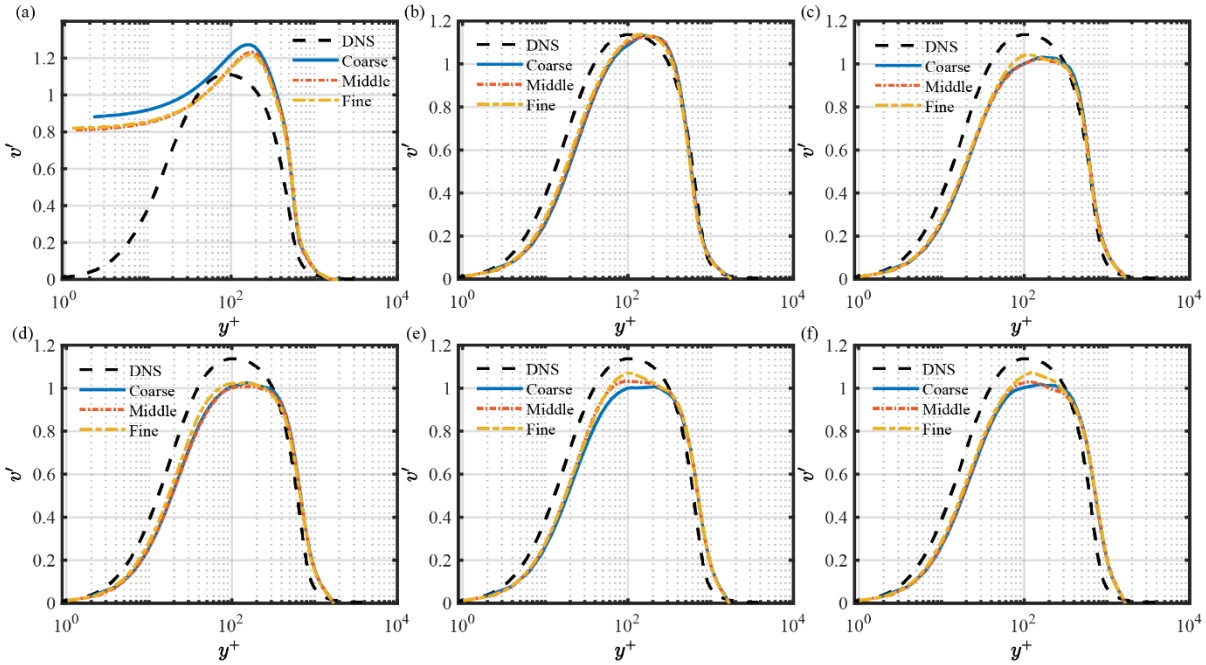


Figure A6. Distribution of the profiles of Reynolds stresses component $\overline{v'v'}$ in simulations based on DFSEM with different mesh size at different positions: (a) at x=inlet (b) at $x/\delta = 10$ (c) $x/\delta = 20$ (d) $x/\delta = 30$ (e) $x/\delta = 40$ (f) $x/\delta = 50$

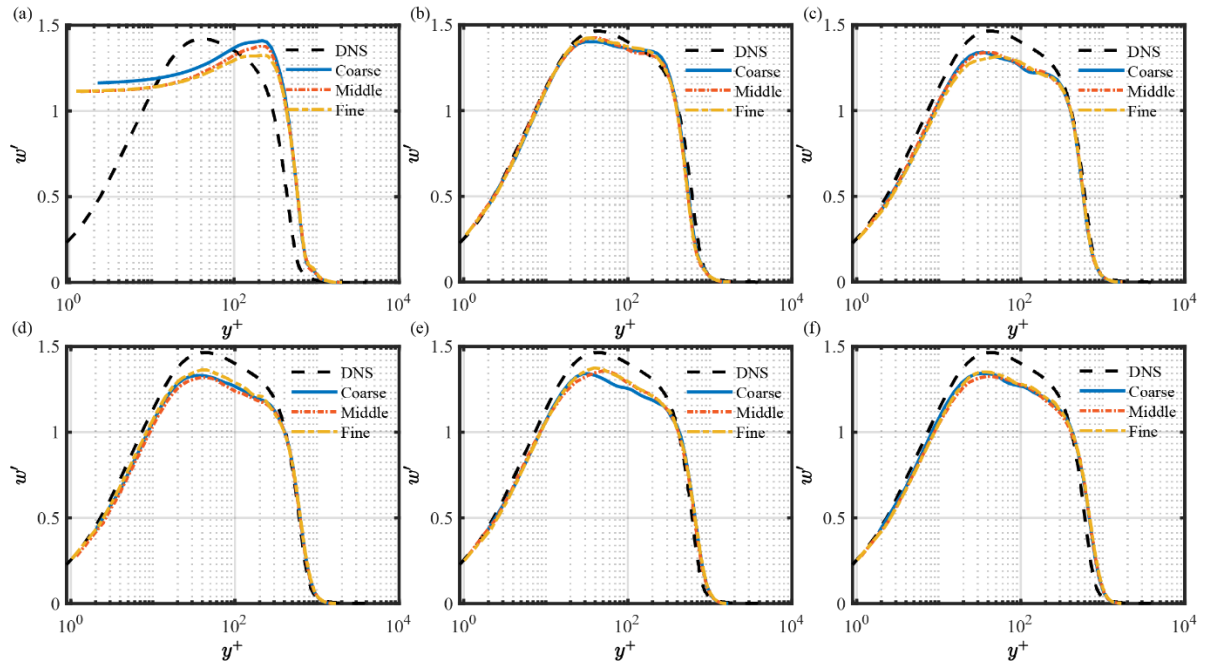


Figure A7. Distribution of the profiles of Reynolds stresses component $\overline{w'w'}$ in simulations based on DFSEM with different mesh size at different positions: (a) at x=inlet (b) at $x/\delta = 10$ (c) $x/\delta = 20$ (d) $x/\delta = 30$ (e) $x/\delta = 40$ (f) $x/\delta = 50$

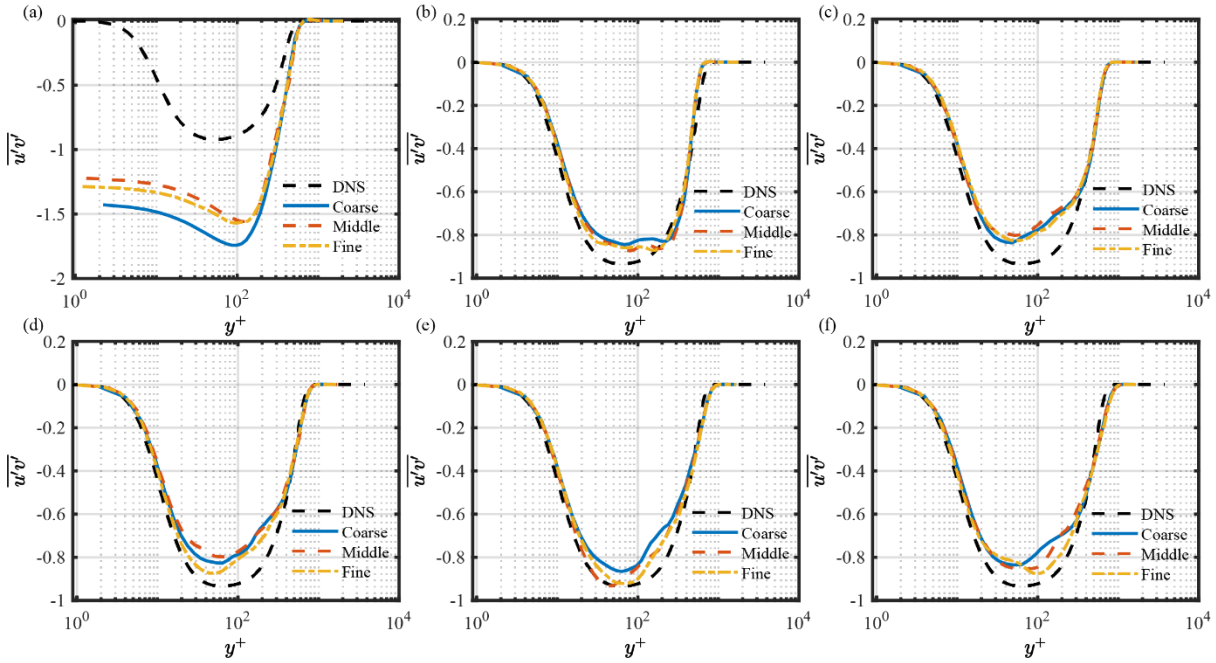


Figure A8. Distribution of the profiles of Reynolds stresses component $\overline{u'v'}$ in simulations based on DFSEM with different mesh size at different positions: (a) at x=inlet (b) at $x/\delta = 10$ (c) $x/\delta = 20$ (d) $x/\delta = 30$ (e) $x/\delta = 40$ (f) $x/\delta = 50$

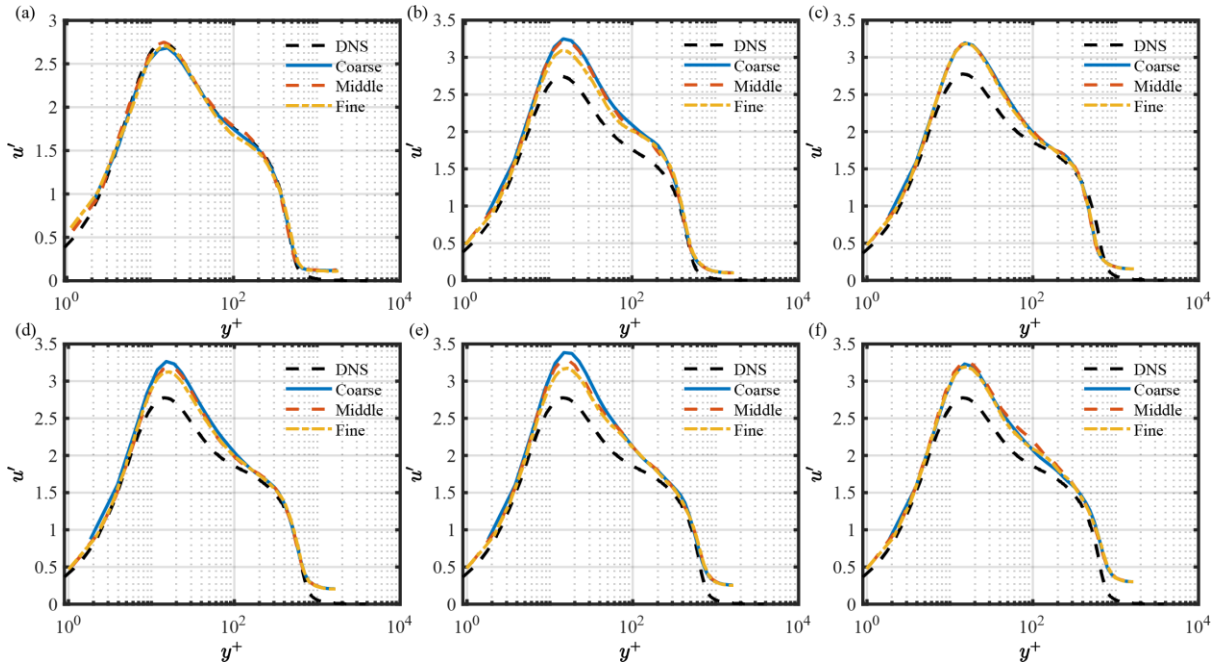


Figure A9. Distribution of the profiles of Reynolds stresses component $\overline{u'u'}$ in simulations based on DFSEM with different mesh size at different positions: (a) at x=inlet (b) at $x/\delta = 10$ (c) $x/\delta = 20$ (d) $x/\delta = 30$ (e) $x/\delta = 40$ (f) $x/\delta = 50$

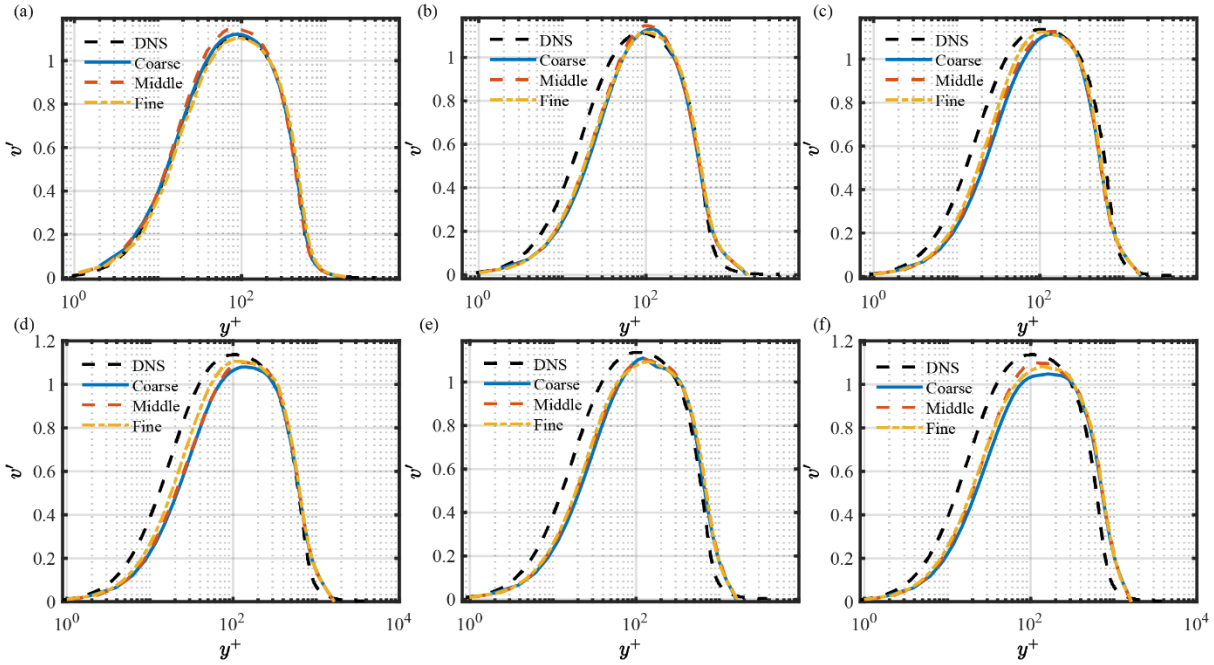


Figure A10. Distribution of the profiles of Reynolds stresses component $\overline{v'v'}$ in simulations based on DFM with different mesh size at different positions: (a) at x=inlet (b) at $x/\delta = 10$ (c) $x/\delta = 20$ (d) $x/\delta = 30$ (e) $x/\delta = 40$ (f) $x/\delta = 50$

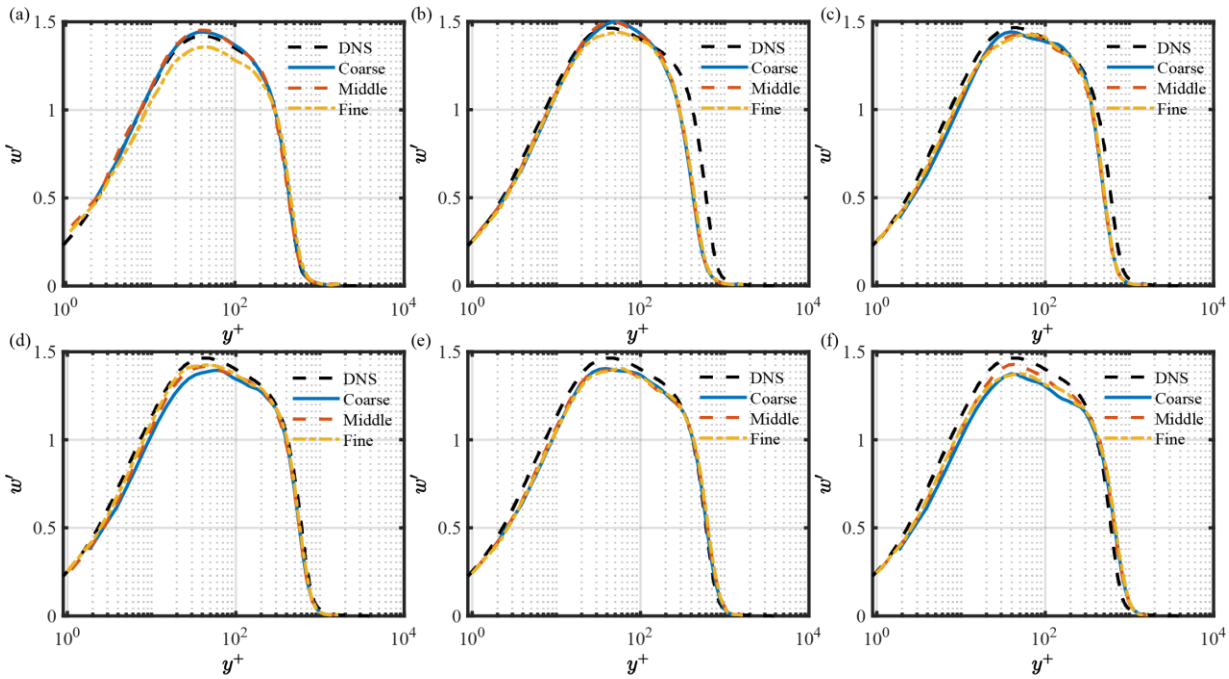


Figure A11. Distribution of the profiles of Reynolds stresses component $\overline{w'w'}$ in simulations based on DFM with different mesh size at different positions: (a) at x=inlet (b) at $x/\delta = 10$ (c) $x/\delta = 20$ (d) $x/\delta = 30$ (e) $x/\delta = 40$ (f) $x/\delta = 50$

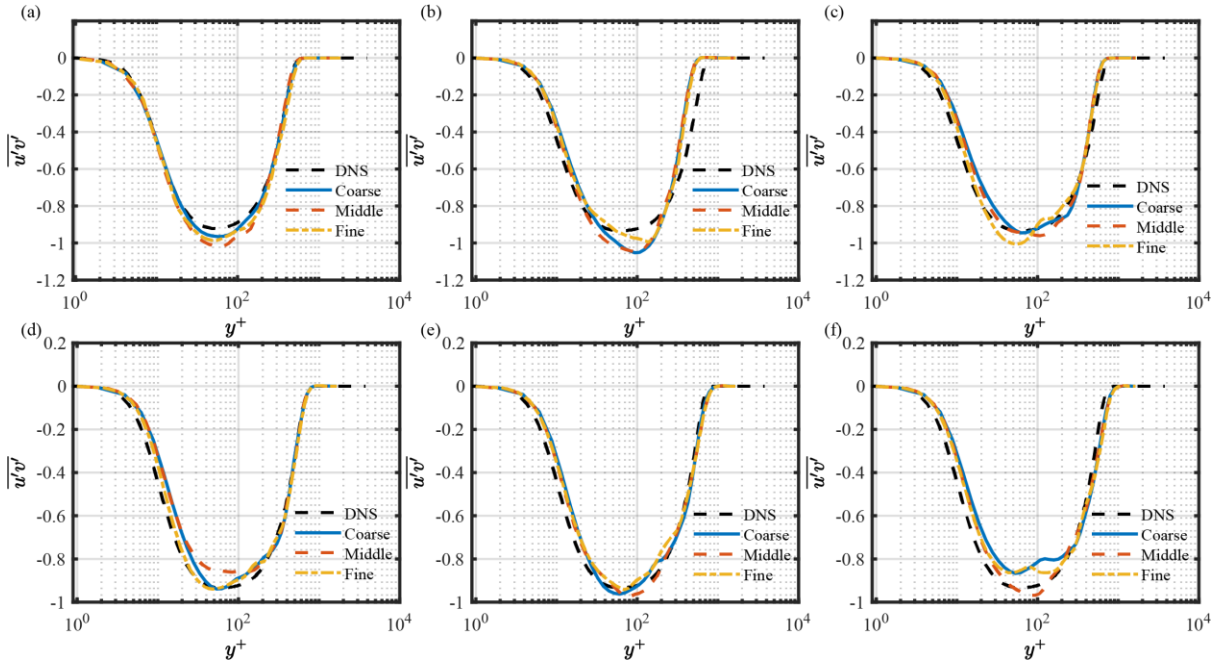


Figure A12. Distribution of the profiles of Reynolds stresses component $\overline{u'v'}$ in simulations based on DFM with different mesh size at different positions: (a) at x=inlet (b) at $x/\delta = 10$ (c) $x/\delta = 20$ (d) $x/\delta = 30$ (e) $x/\delta = 40$ (f) $x/\delta = 50$

A3. Simulations based on DFSEM with different turbulent length scales and SGS models

The subgrid-scale (SGS) models are introduced in the section 4.1 including the Smagorinsky model (SM) and the dynamic Smagorinsky model (DSM). There are also other SGS models such as the one-equation k_{sgs} model that can be applied to model the SGS turbulent kinetic energy, k_{sgs} and the equation can be written on the same form as the RANS k-equation, i.e.,

$$\begin{aligned} \frac{\partial k_{sgs}}{\partial t} + \frac{\partial}{\partial x_j}(\overline{v}_j k_{sgs}) \quad &= \frac{\partial}{\partial x_j}[(\nu + \nu_{sgs})\frac{\partial k_{sgs}}{\partial x_j}] + P_{k_{sgs}} - \varepsilon \\ \nu_{sgs} = c_k \Delta k_{sgs}^{1/2}, P_{k_{sgs}} \quad &= 2\nu_{sgs}\overline{s}_{ij}\overline{s}_{ij}, \varepsilon = C_\varepsilon \frac{k_{sgs}^{3/2}}{\Delta} \end{aligned} \tag{56}$$

The production $P_{k_{sgs}}$ term is equivalent to the SGS dissipation in the equation for the resolved turbulent kinetic energy (Davidson and Billson, 2006).

The wall adapting local eddy viscosity (WALE) model is another SGS model based on a tensor invariant that can reproduce the proper scaling at the wall, which reads:

$$\begin{aligned} g_{ij} = \frac{\partial \overline{v}_i}{\partial x_j}, g_{ij}^2 = g_{ik}g_{kj} \\ \overline{s}_{ij}^d = \frac{1}{2}(g_{ij}^2 + g_{ji}^2) - \frac{1}{3}\delta_{ij}g_{kk}^2 \\ \nu_{sgs} \quad = (C_m\Delta)^2 \frac{(\overline{s}_{ij}^d \overline{s}_{ij}^d)^{3/2}}{(\overline{s}_{ij}\overline{s}_{ij})^{5/2} + (\overline{s}_{ij}^d \overline{s}_{ij}^d)^{5/4}} \end{aligned} \tag{57}$$

The $\delta_{ij}^d = \frac{1}{2}(\overline{g}_{ij}^2 + \overline{g}_{ji}^2) - \frac{1}{3}\delta_{ij}\overline{g}_{kk}^2$ represents the traceless symmetric part of the square of the velocity gradient tensor. A value of C_m lies in the range $[0.55, 0.60]$ (Nicoud and Ducros, 2006). Simulation based on DFSEM with different turbulent length scales and SGS models are illustrated by Figure A13-Figure A30.

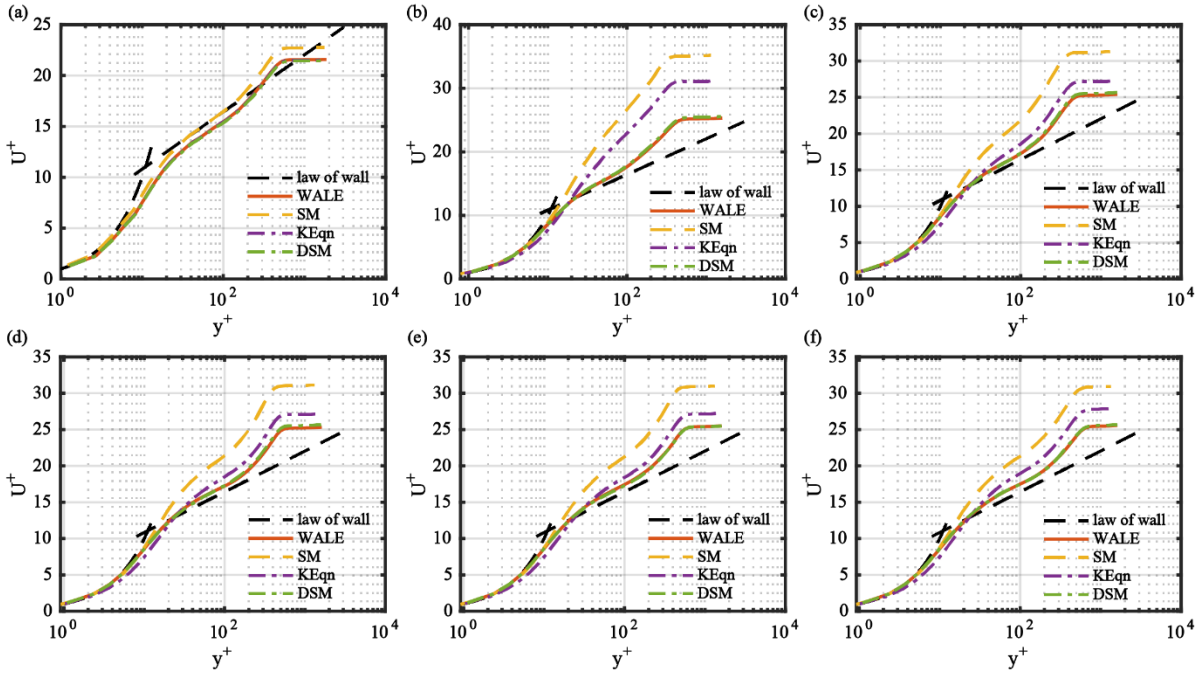


Figure A13. Distribution of the mean velocity profiles of simulations based on DFSEM where the turbulent length scale is 0.2δ *with different sub-grid scale models at different positions: (a) at x=inlet (b) at* $x/\delta = 10$ *(c)* $x/\delta = 20$ *(d)* $x/\delta = 30$ *(e)* $x/\delta = 40$ *(f)* $x/\delta = 50$

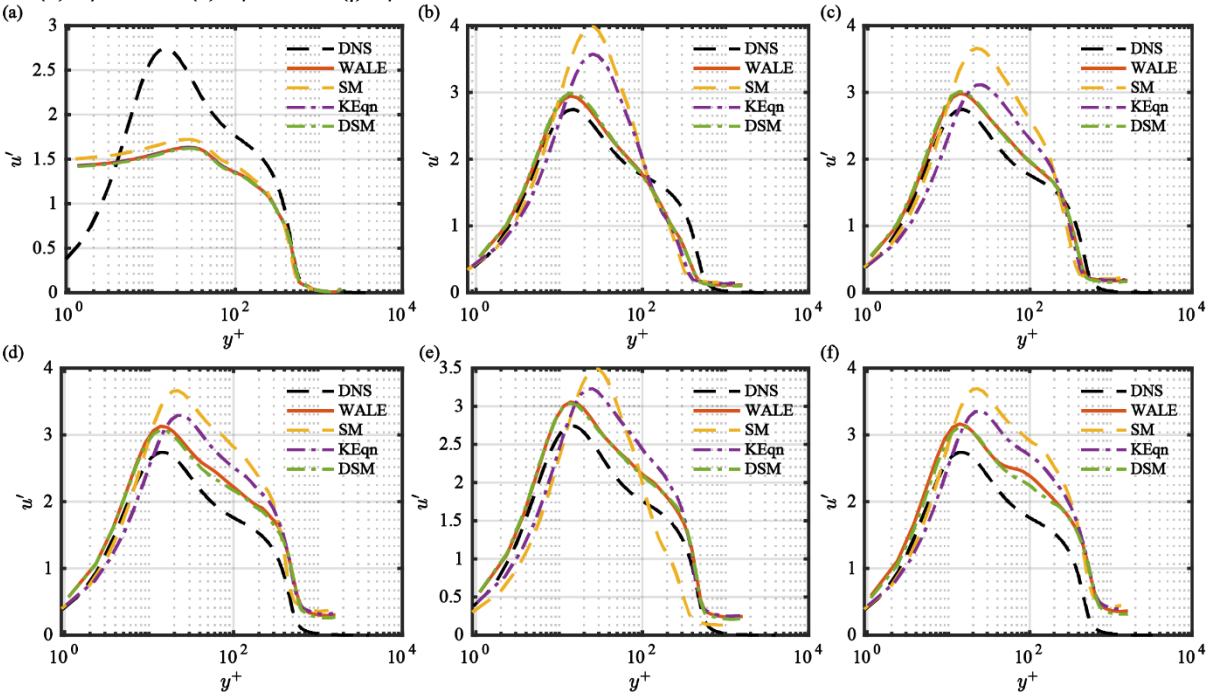


Figure A14. Distribution of the profiles of Reynolds stresses component $\overline{u'u'}$ *in simulations based on DFSEM where the turbulent length scale is* 0.2δ *with different sub-grid scale models at different positions: (a) at x=inlet (b) at* $x/\delta = 10$ *(c)* $x/\delta = 20$ *(d)* $x/\delta = 30$ *(e)* $x/\delta = 40$ *(f)* $x/\delta = 50$

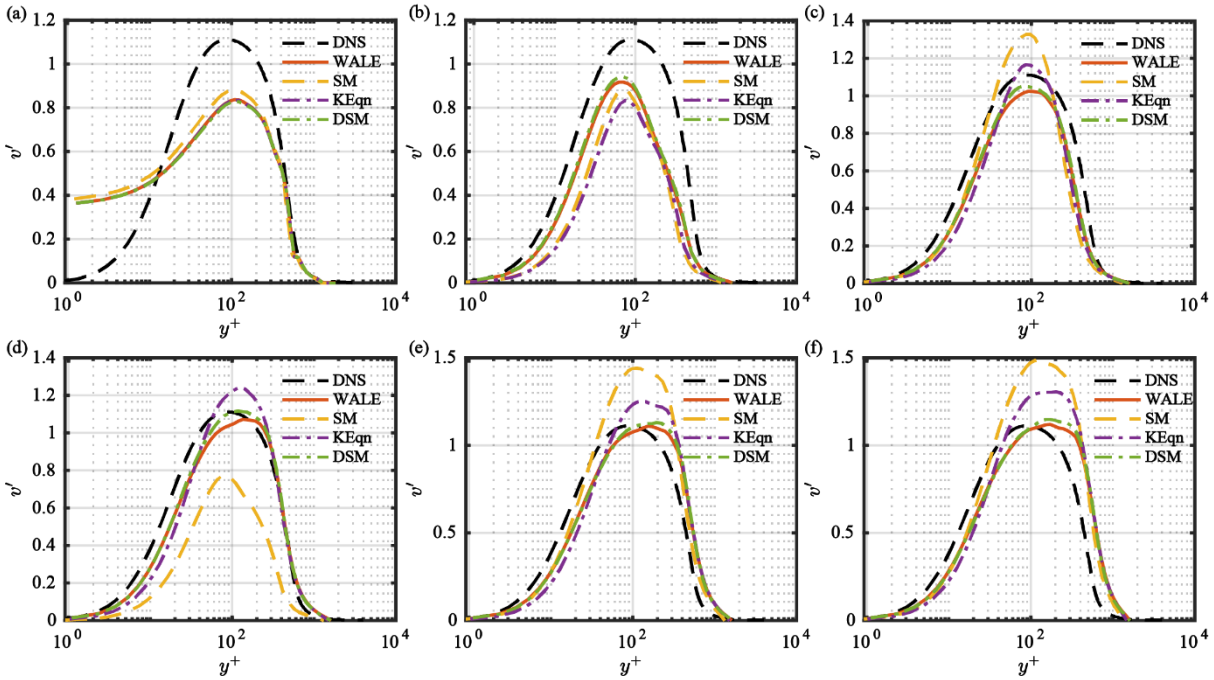


Figure A15. Distribution of the profiles of Reynolds stresses component $\overline{v'v'}$ in simulations based on DFSEM where the turbulent length scale is 0.2δ with different sub-grid scale models at different positions: (a) at x=inlet (b) at $x/\delta = 10$ (c) $x/\delta = 20$ (d) $x/\delta = 30$ (e) $x/\delta = 40$ (f) $x/\delta = 50$

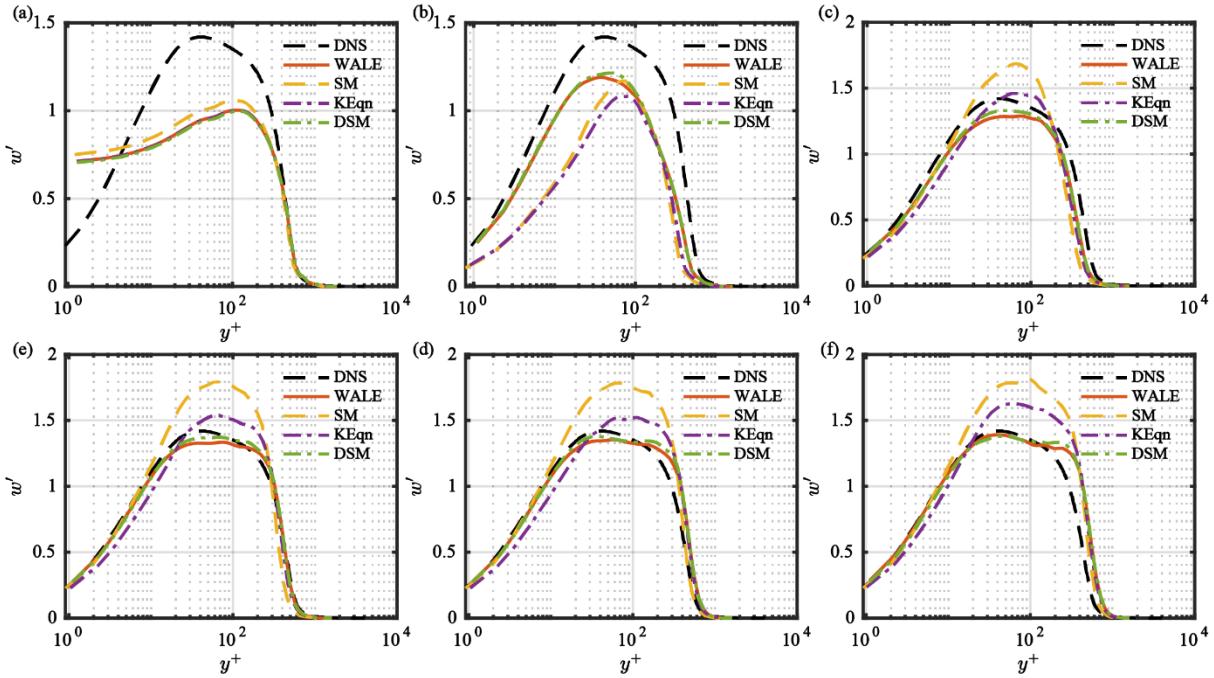


Figure A16. Distribution of the profiles of Reynolds stresses component $\overline{w'w'}$ in simulations based on DFSEM where the turbulent length scale is 0.2δ with different sub-grid scale models at different positions: (a) at x=inlet (b) at $x/\delta = 10$ (c) $x/\delta = 20$ (d) $x/\delta = 30$ (e) $x/\delta = 40$ (f) $x/\delta = 50$

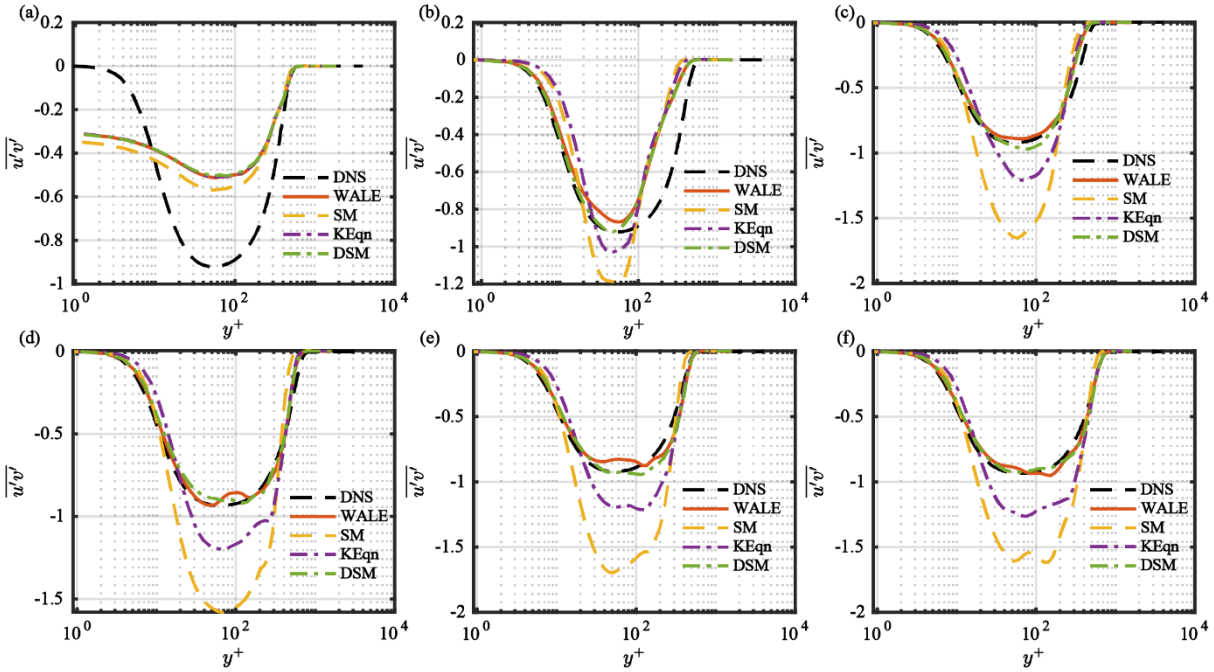


Figure A17. Distribution of profiles of Reynolds stresses component $\overline{u'v'}$ in simulations based on DFSEM where the turbulent length scale is 0.2δ with different sub-grid scale models at different positions: (a) at x=inlet (b) at $x/\delta = 10$ (c) $x/\delta = 20$ (d) $x/\delta = 30$ (e) $x/\delta = 40$ (f) $x/\delta = 50$

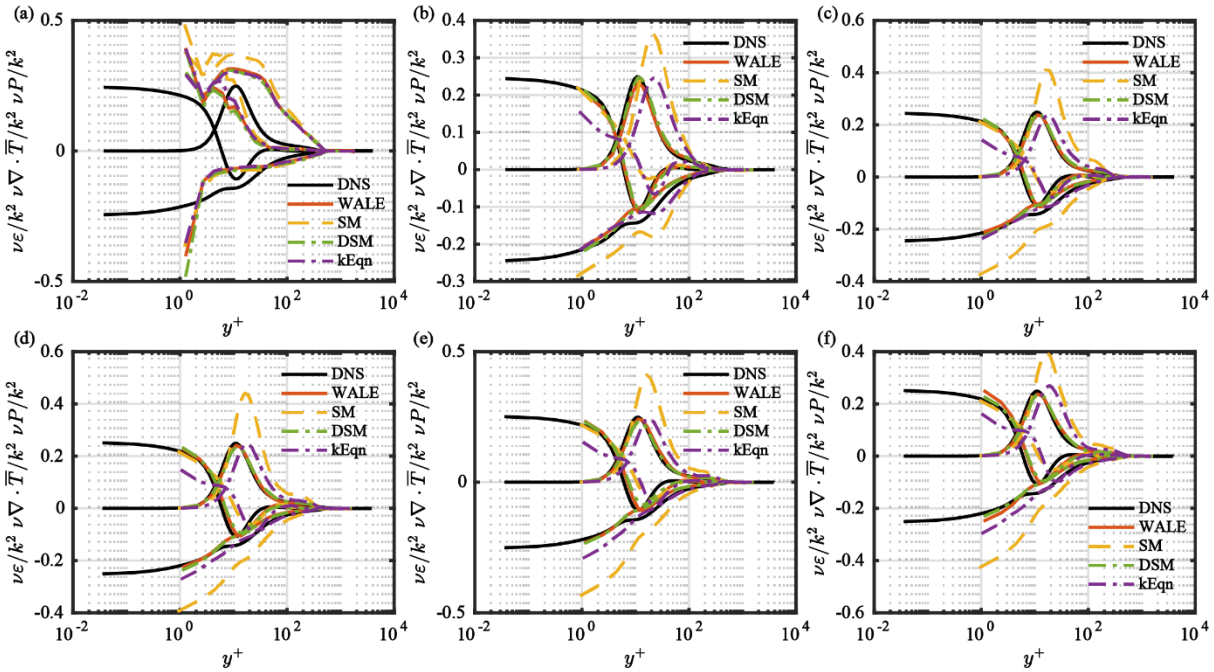


Figure A18. Distribution of the TKE budget terms profiles in simulations based on DFSEM where the turbulent length scale is 0.2δ with different sub-grid scale models at different positions: (a) at x=inlet (b) at $x/\delta = 10$ (c) $x/\delta = 20$ (d) $x/\delta = 30$ (e) $x/\delta = 40$ (f) $x/\delta = 50$

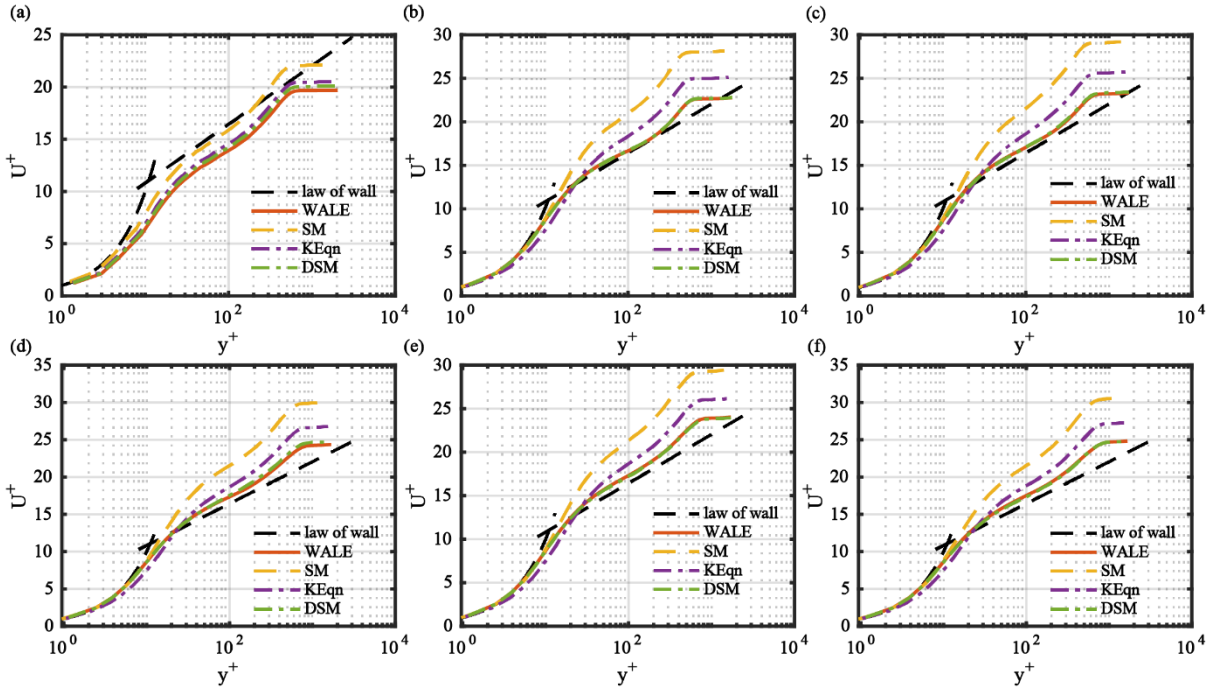


Figure A19. Distribution of the mean velocity profiles of simulations based on DFSEM where the turbulent length scale is 0.6δ *with different sub-grid scale models at different positions: (a) at x=inlet (b) at* $x/\delta = 10$ *(c)* $x/\delta = 20$ *(d)* $x/\delta = 30$ *(e)* $x/\delta = 40$ *(f)* $x/\delta = 50$

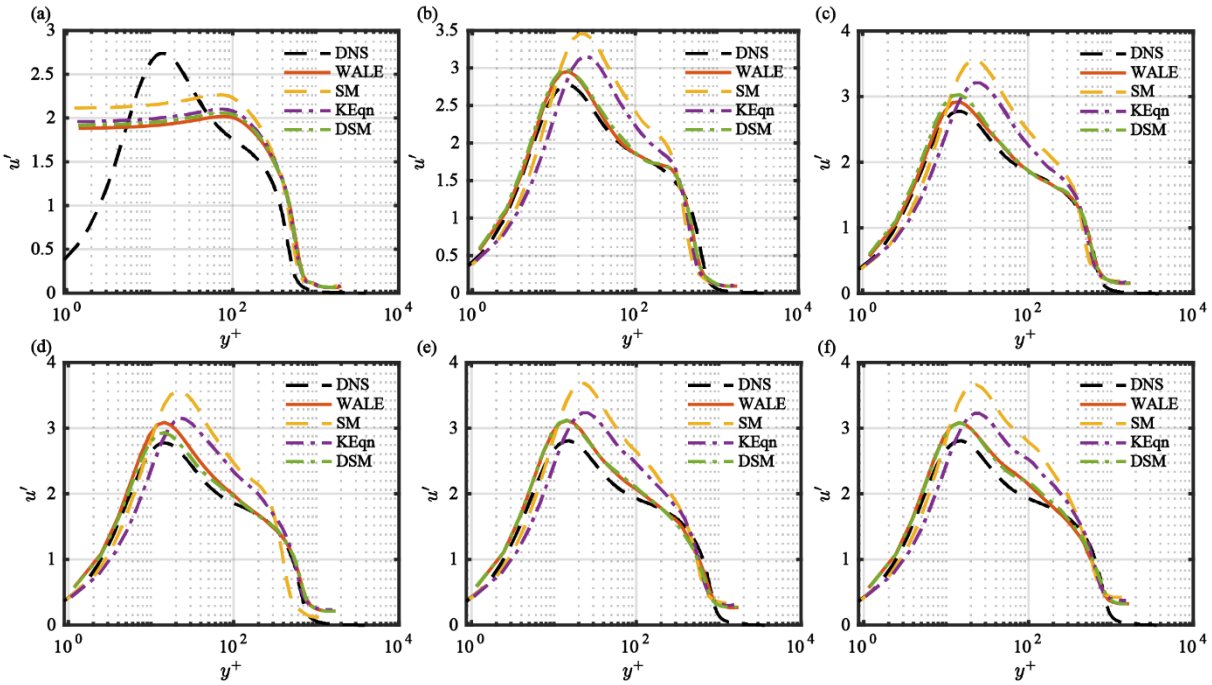


Figure A20. Distribution of the profiles of Reynolds stresses component $\overline{u'u'}$ *in simulations based on DFSEM where the turbulent length scale is* 0.6δ *with different sub-grid scale models at different positions: (a) at x=inlet (b) at* $x/\delta = 10$ *(c)* $x/\delta = 20$ *(d)* $x/\delta = 30$ *(e)* $x/\delta = 40$ *(f)* $x/\delta = 50$

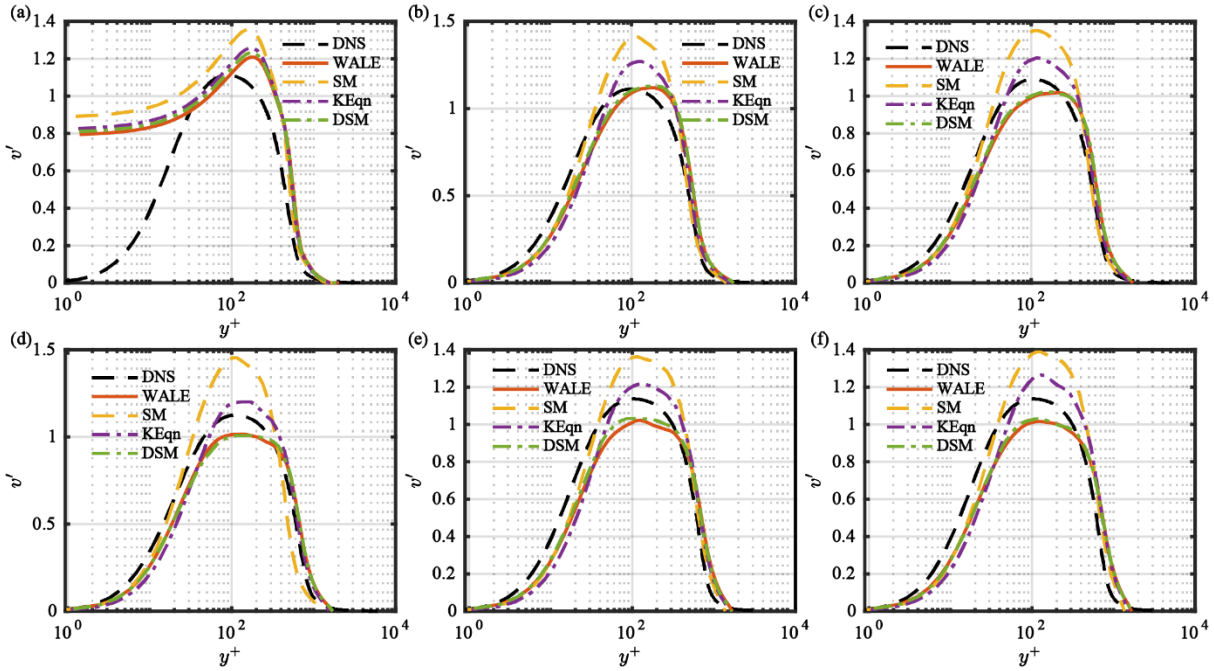


Figure A21. Distribution of the profiles of Reynolds stresses component $\overline{v'v'}$ in simulations based on DFSEM where the turbulent length scale is 0.6δ with different sub-grid scale models at different positions: (a) at x=inlet (b) at $x/\delta = 10$ (c) $x/\delta = 20$ (d) $x/\delta = 30$ (e) $x/\delta = 40$ (f) $x/\delta = 50$

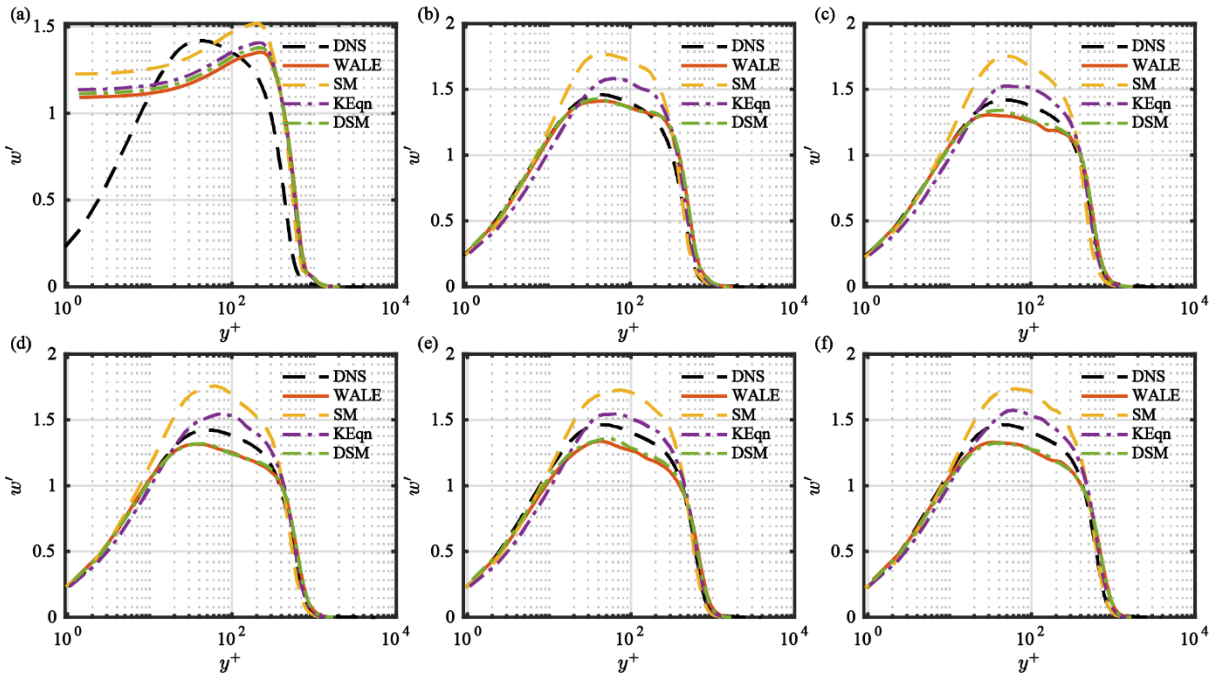


Figure A22. Distribution of the profiles of Reynolds stresses component $\overline{w'w'}$ in simulations based on DFSEM where the turbulent length scale is 0.6δ with different sub-grid scale models at different positions: (a) at x=inlet (b) at $x/\delta = 10$ (c) $x/\delta = 20$ (d) $x/\delta = 30$ (e) $x/\delta = 40$ (f) $x/\delta = 50$

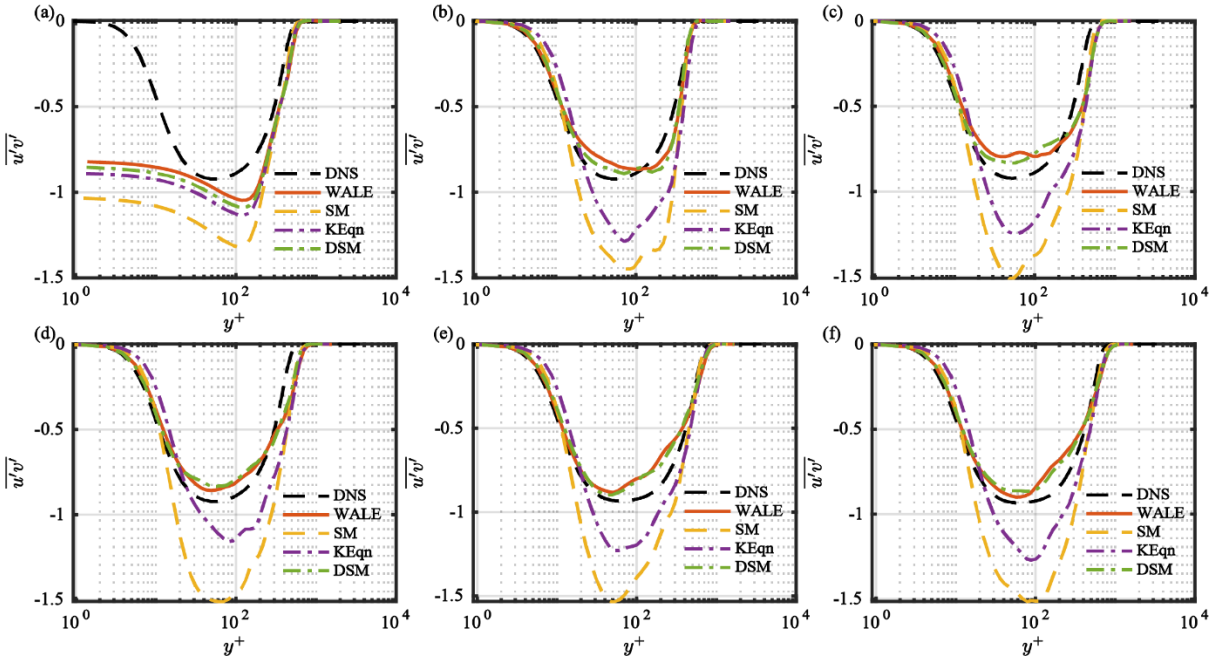


Figure A23. Distribution of the profiles of Reynolds stresses component $\overline{u'v'}$ in simulations based on DFSEM where the turbulent length scale is 0.6δ with different sub-grid scale models at different positions: (a) at x=inlet (b) at $x/\delta = 10$ (c) $x/\delta = 20$ (d) $x/\delta = 30$ (e) $x/\delta = 40$ (f) $x/\delta = 50$

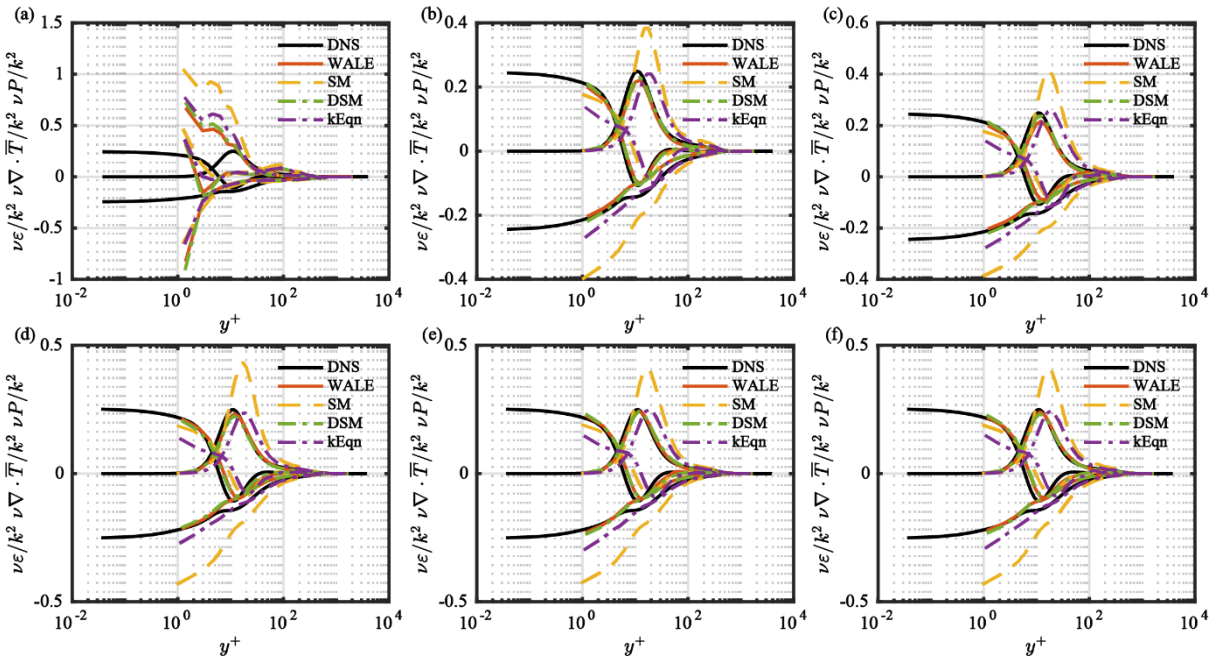


Figure A24. Distribution of the TKE budget terms profiles in simulations based on DFSEM where the turbulent length scale is 0.6δ with different sub-grid scale models at different positions: (a) at x=inlet (b) at $x/\delta = 10$ (c) $x/\delta = 20$ (d) $x/\delta = 30$ (e) $x/\delta = 40$ (f) $x/\delta = 50$

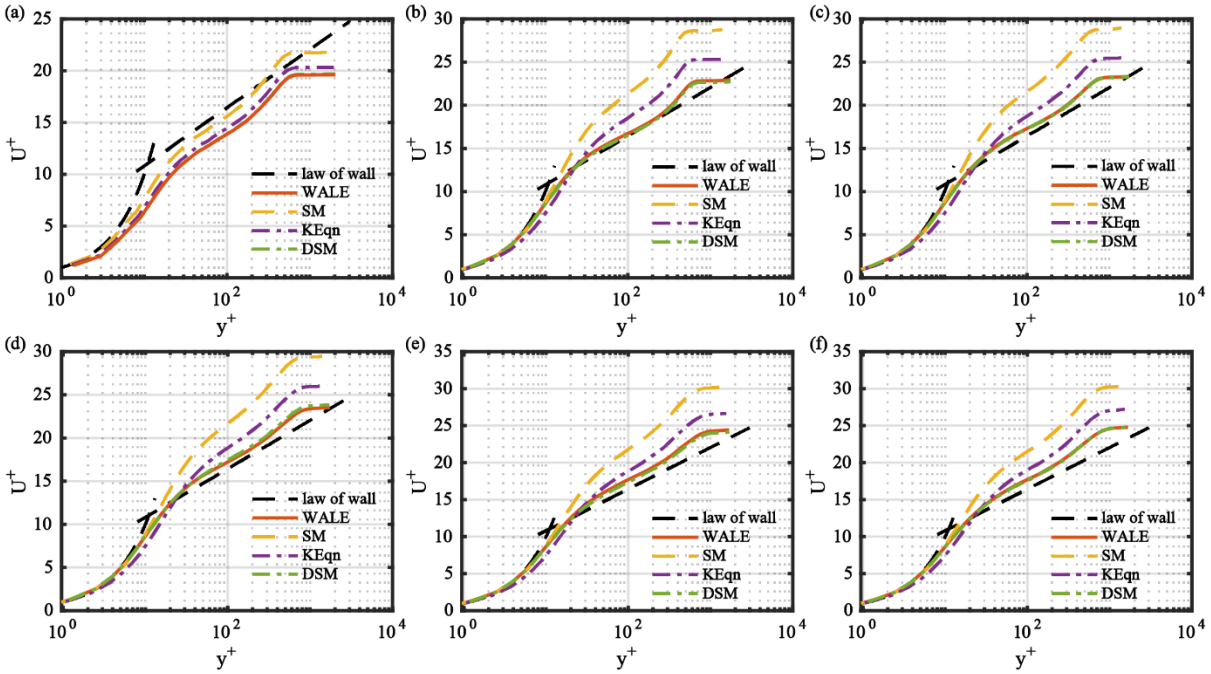


Figure A25. Distribution of the mean velocity profiles of simulations based on DFSEM where the turbulent length scale is 1.0δ *with different sub-grid scale models at different positions: (a) at x=inlet (b) at* $x/\delta = 10$ *(c)* $x/\delta = 20$ *(d)* $x/\delta = 30$ *(e)* $x/\delta = 40$ *(f)* $x/\delta = 50$

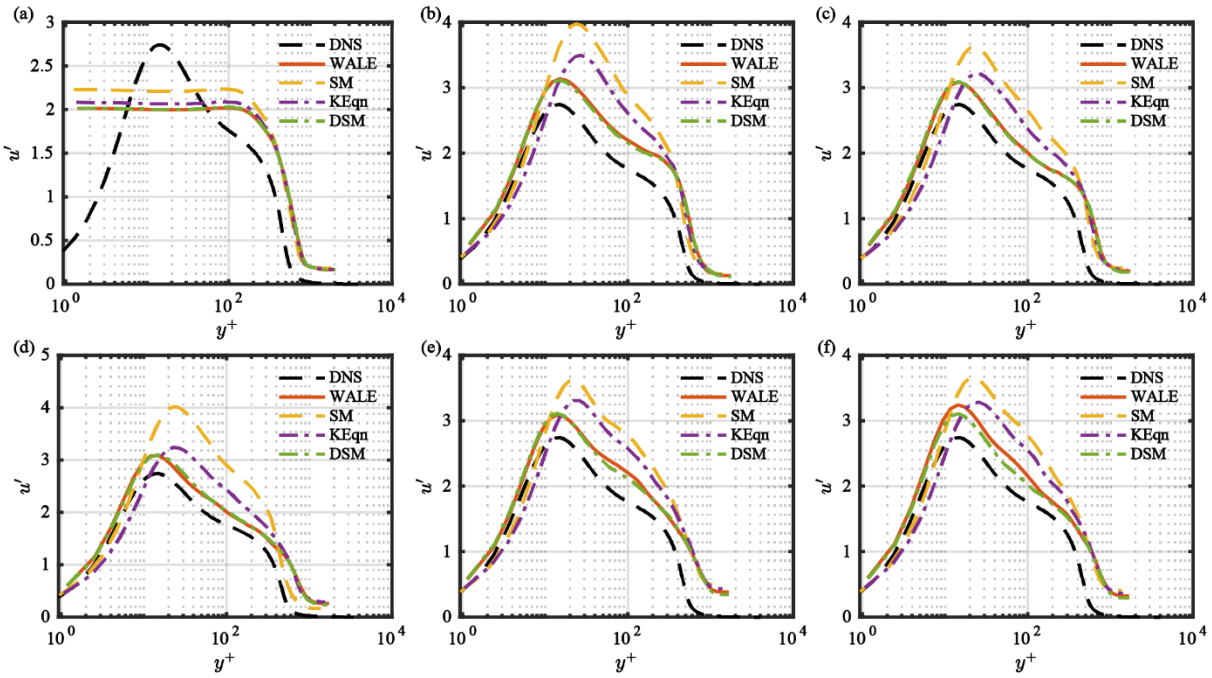


Figure A26. Distribution of the profiles of Reynolds stresses component $\overline{u'u'}$ *in simulations based on DFSEM where the turbulent length scale is* 1.0δ *with different sub-grid scale models at different positions: (a) at x=inlet (b) at* $x/\delta = 10$ *(c)* $x/\delta = 20$ *(d)* $x/\delta = 30$ *(e)* $x/\delta = 40$ *(f)* $x/\delta = 50$

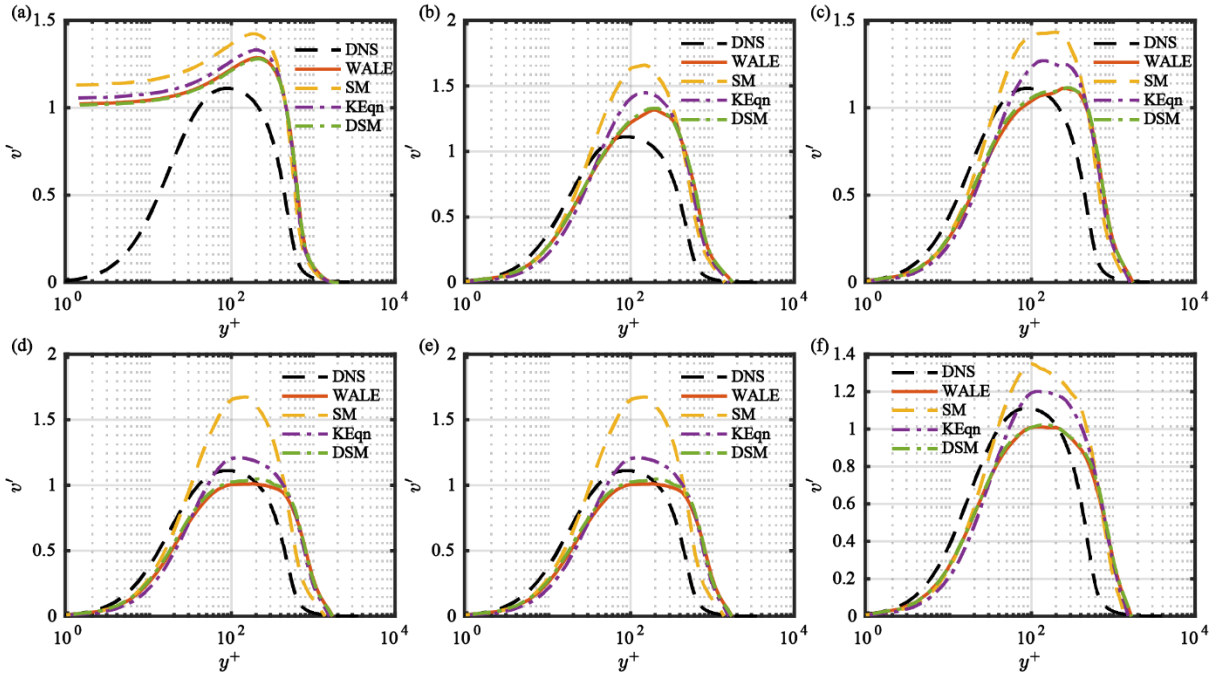


Figure A27. Distribution of the profiles of Reynolds stresses component $\overline{v'v'}$ in simulations based on DFSEM where the turbulent length scale is 1.0δ with different sub-grid scale models at different positions: (a) at x=inlet (b) at $x/\delta = 10$ (c) $x/\delta = 20$ (d) $x/\delta = 30$ (e) $x/\delta = 40$ (f) $x/\delta = 50$

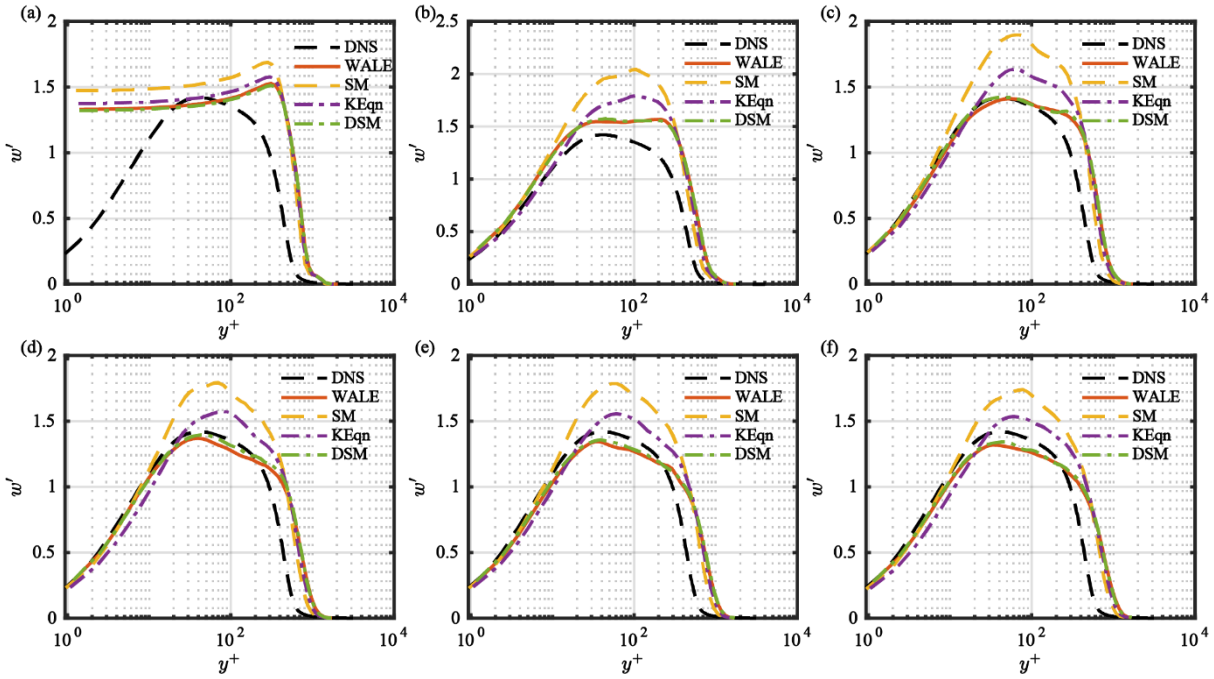


Figure A28. Distribution of the profiles of Reynolds stresses component $\overline{w'w'}$ in simulations based on DFSEM where the turbulent length scale is 1.0δ with different sub-grid scale models at different positions: (a) at x=inlet (b) at $x/\delta = 10$ (c) $x/\delta = 20$ (d) $x/\delta = 30$ (e) $x/\delta = 40$ (f) $x/\delta = 50$

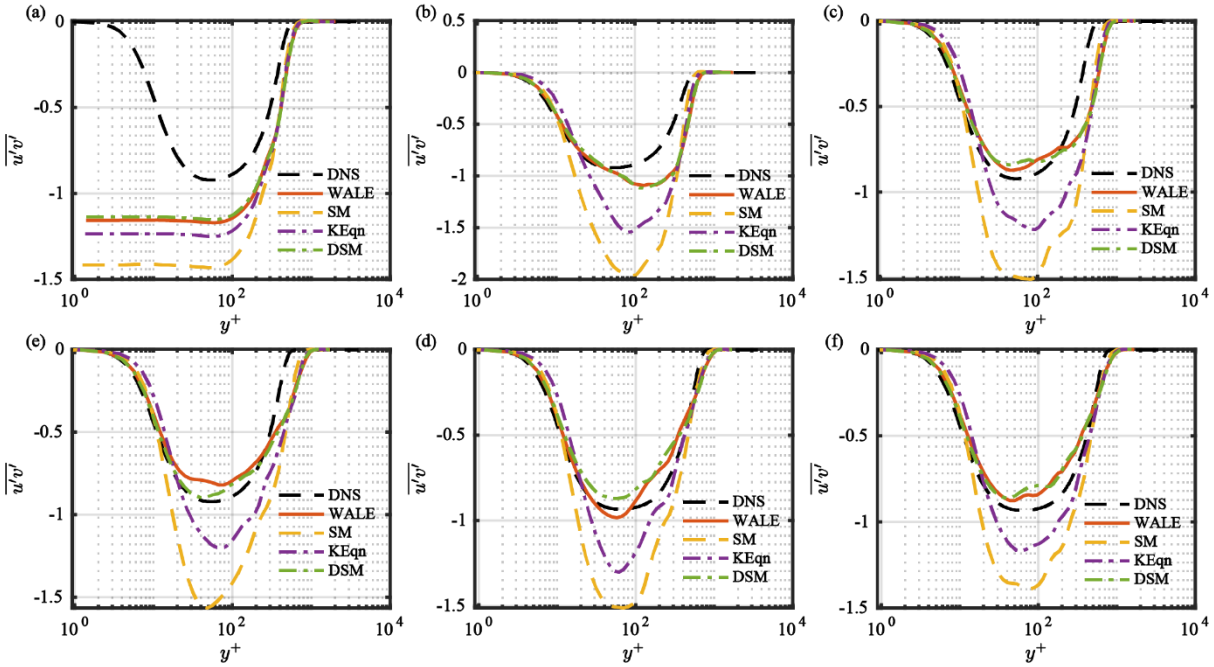


Figure A29. Distribution of the profiles of Reynolds stresses component $\overline{u'v'}$ in simulations based on DFSEM where the turbulent length scale is 1.0δ with different sub-grid scale models at different positions: (a) at x=inlet (b) at $x/\delta = 10$ (c) $x/\delta = 20$ (d) $x/\delta = 30$ (e) $x/\delta = 40$ (f) $x/\delta = 50$

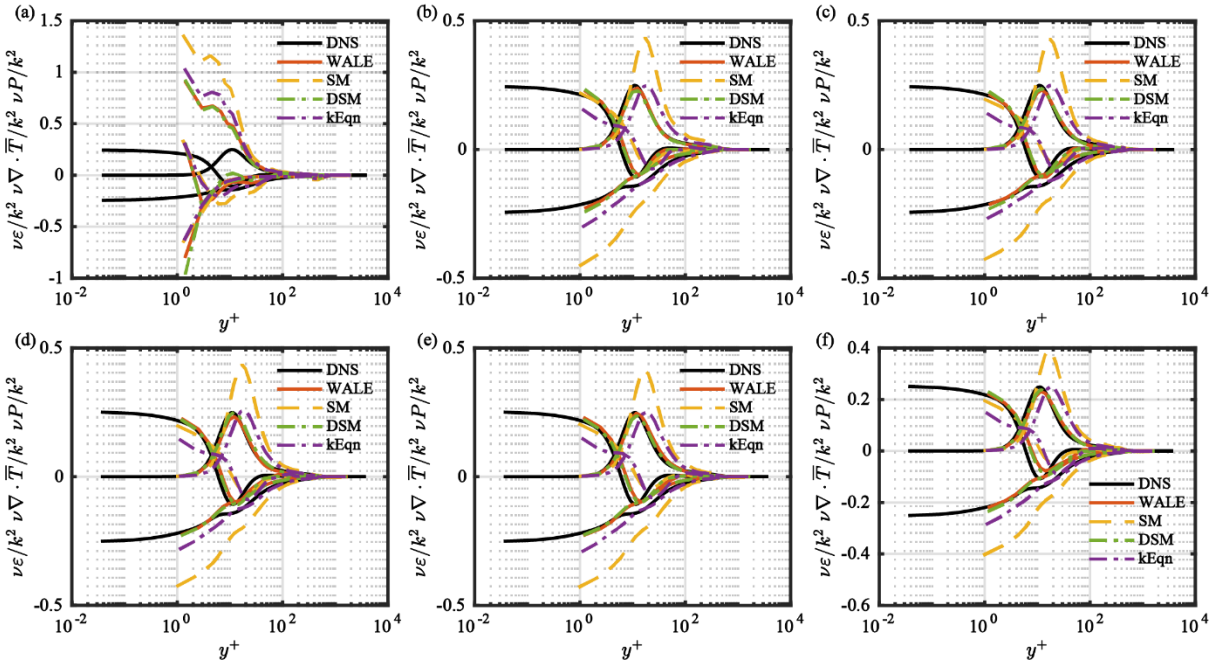


Figure A30. Distribution of the TKE budget terms profiles in simulations based on DFSEM where the turbulent length scale is 1.0δ with different sub-grid scale models at different positions: (a) at x=inlet (b) at $x/\delta = 10$ (c) $x/\delta = 20$ (d) $x/\delta = 30$ (e) $x/\delta = 40$ (f) $x/\delta = 50$

A4. Simulations based on DFM with different turbulent length scales and SGS models

Simulation based on DFM with different turbulent length scales and SGS models are illustrated by Figure A31-Figure A48.

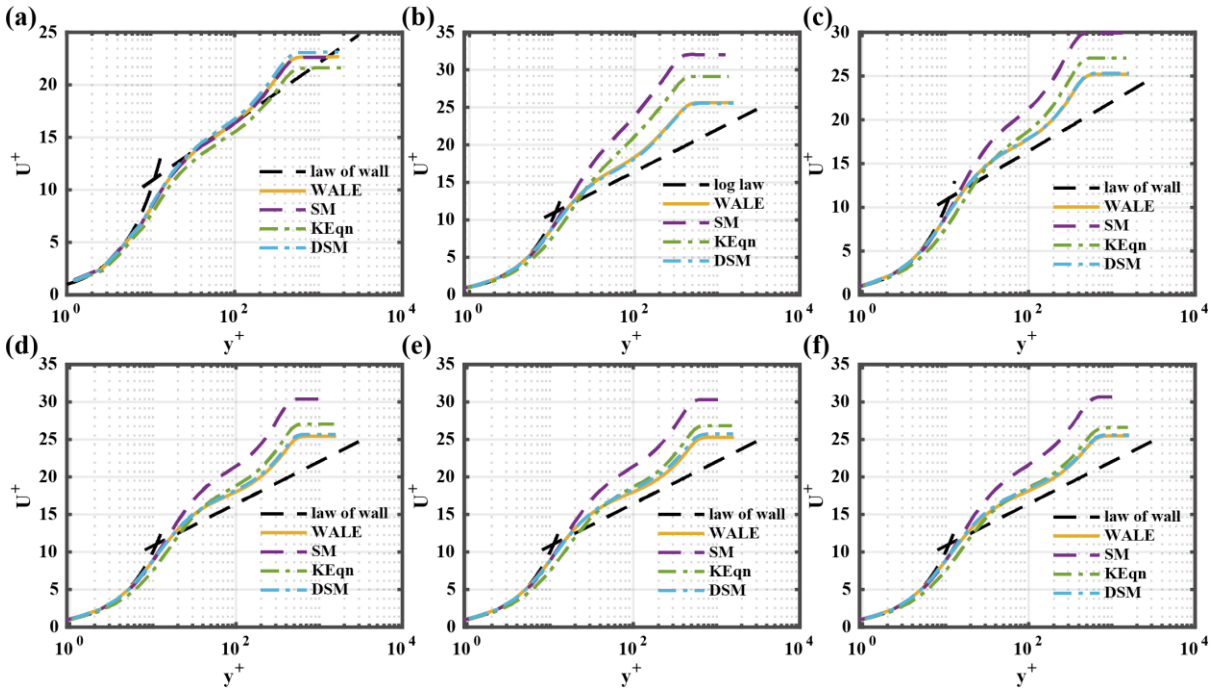


Figure A31. Distribution of the mean velocity profiles of simulations based on DFM where the turbulent length scale is 0.2δ *with different sub-grid scale models at different positions: (a) at x=inlet (b) at* $x/\delta = 10$ *(c)* $x/\delta = 20$ *(d)* $x/\delta = 30$ *(e)* $x/\delta = 40$ *(f)* $x/\delta = 50$

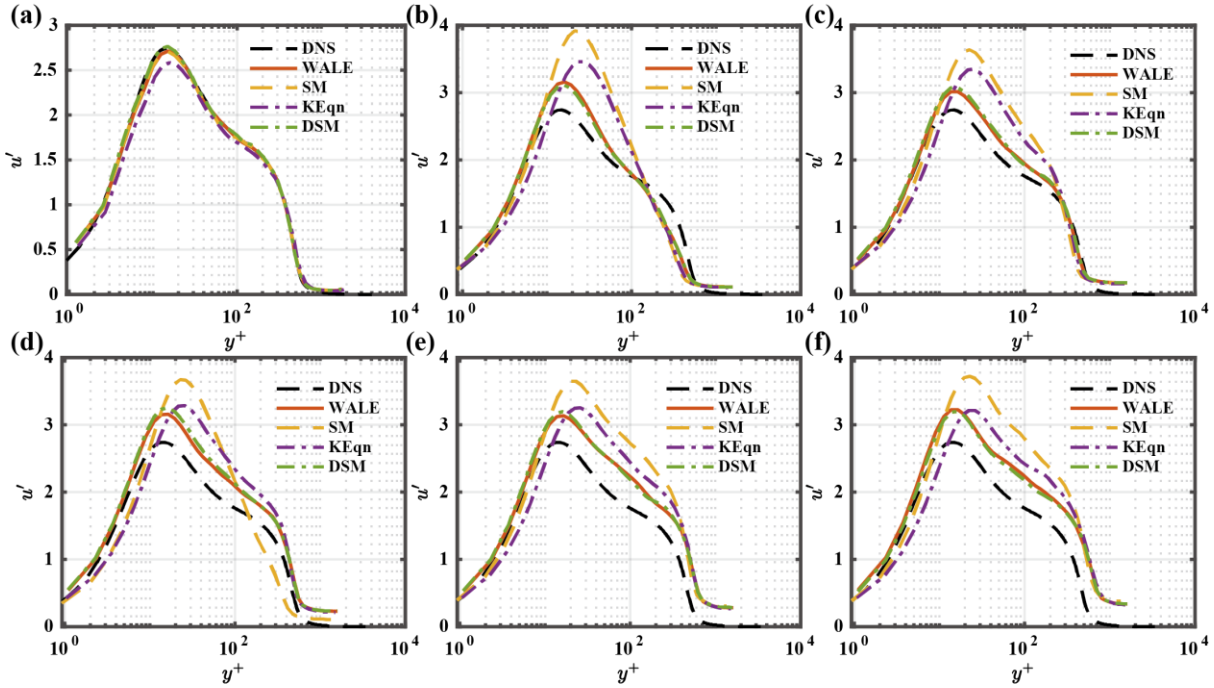


Figure A32. Distribution of the Reynolds stresses component $\overline{u'u'}$ of simulations based on DFM where the turbulent length scale is 0.2δ with different sub-grid scale models at different positions: (a) at x=inlet (b) at $x/\delta = 10$ (c) $x/\delta = 20$ (d) $x/\delta = 30$ (e) $x/\delta = 40$ (f) $x/\delta = 50$

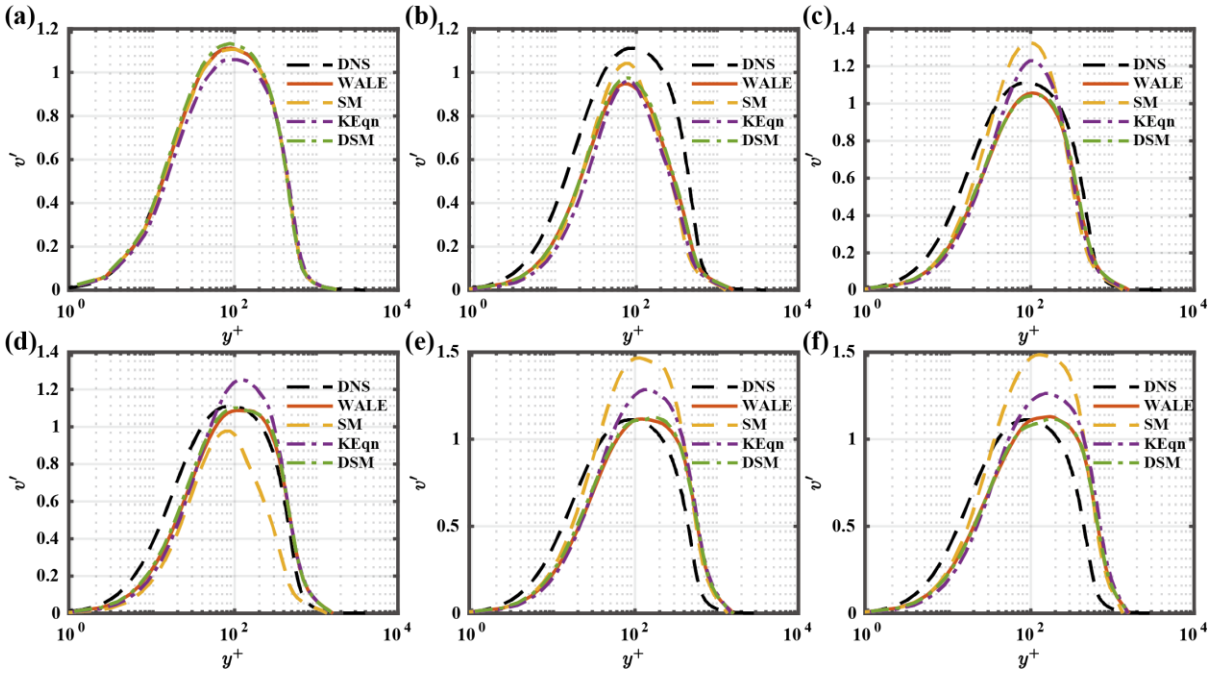


Figure A33. Distribution of the Reynolds stresses component $\overline{v'v'}$ of simulations based on DFM where the turbulent length scale is 0.2δ with different sub-grid scale models at different positions: (a) at x=inlet (b) at $x/\delta = 10$ (c) $x/\delta = 20$ (d) $x/\delta = 30$ (e) $x/\delta = 40$ (f) $x/\delta = 50$

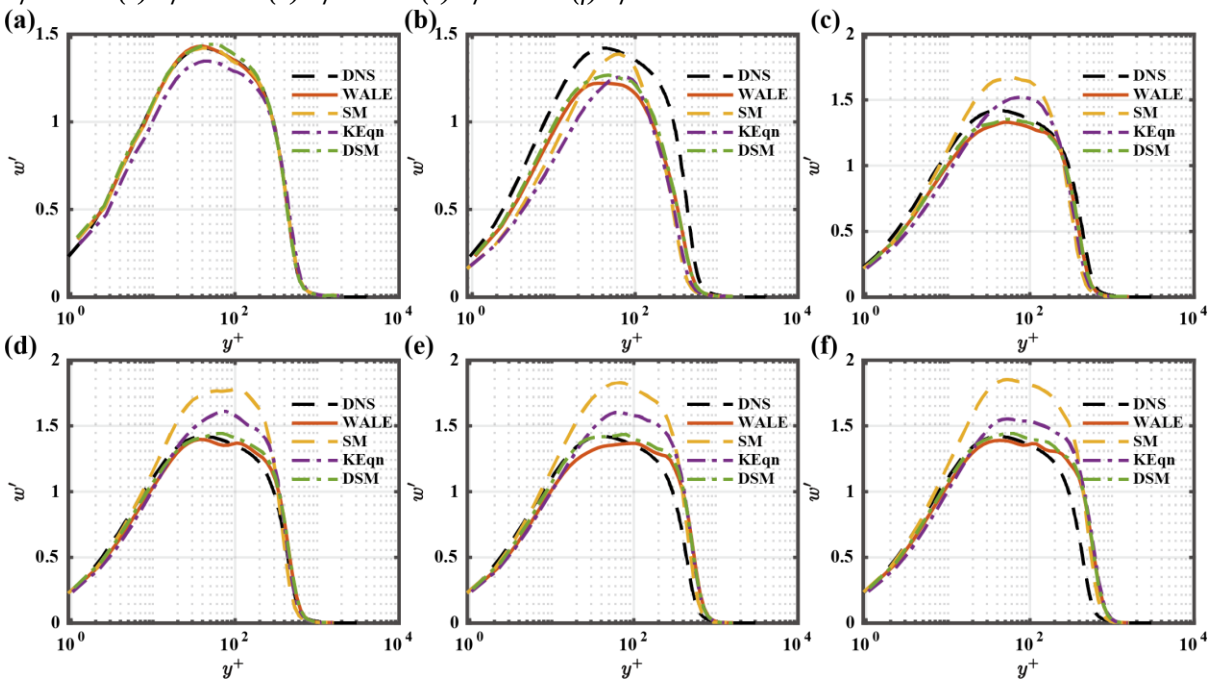


Figure A34. Distribution of the Reynolds stresses component $\overline{w'w'}$ of simulations based on DFM where the turbulent length scale is 0.2δ with different sub-grid scale models at different positions: (a) at x=inlet (b) at $x/\delta = 10$ (c) $x/\delta = 20$ (d) $x/\delta = 30$ (e) $x/\delta = 40$ (f) $x/\delta = 50$

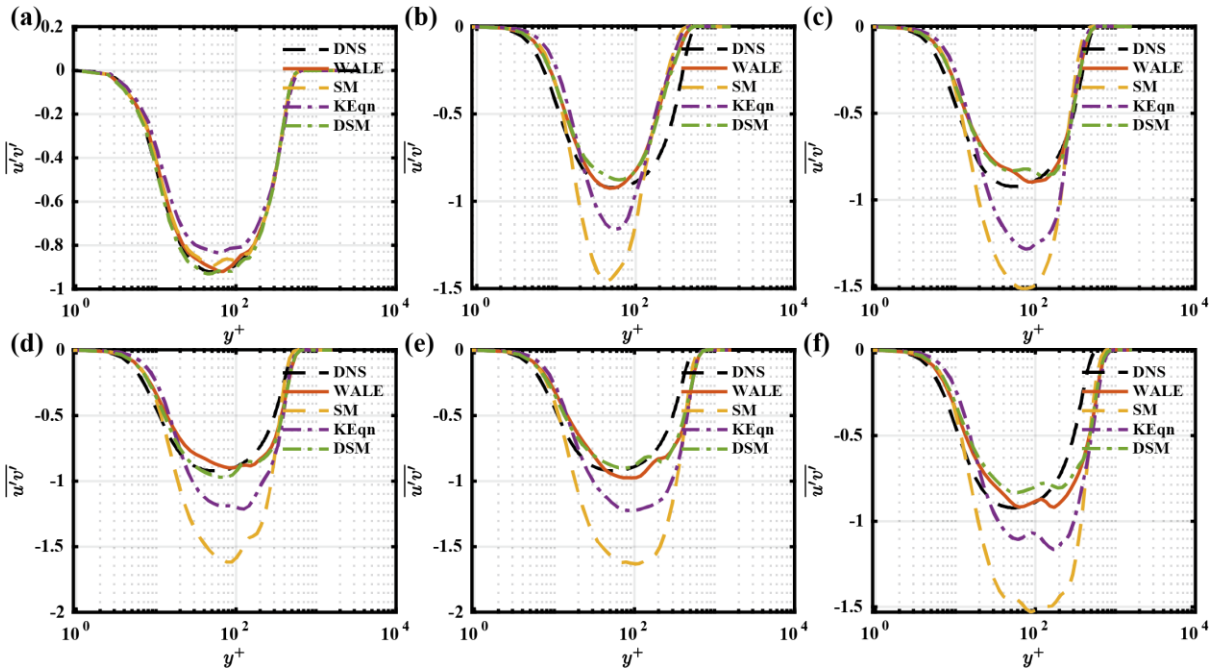


Figure A35. Distribution of the Reynolds stresses component $\overline{u'v'}$ of simulations based on DFM where the turbulent length scale is 0.2δ with different sub-grid scale models at different positions: (a) at x=inlet (b) at $x/\delta = 10$ (c) $x/\delta = 20$ (d) $x/\delta = 30$ (e) $x/\delta = 40$ (f) $x/\delta = 50$

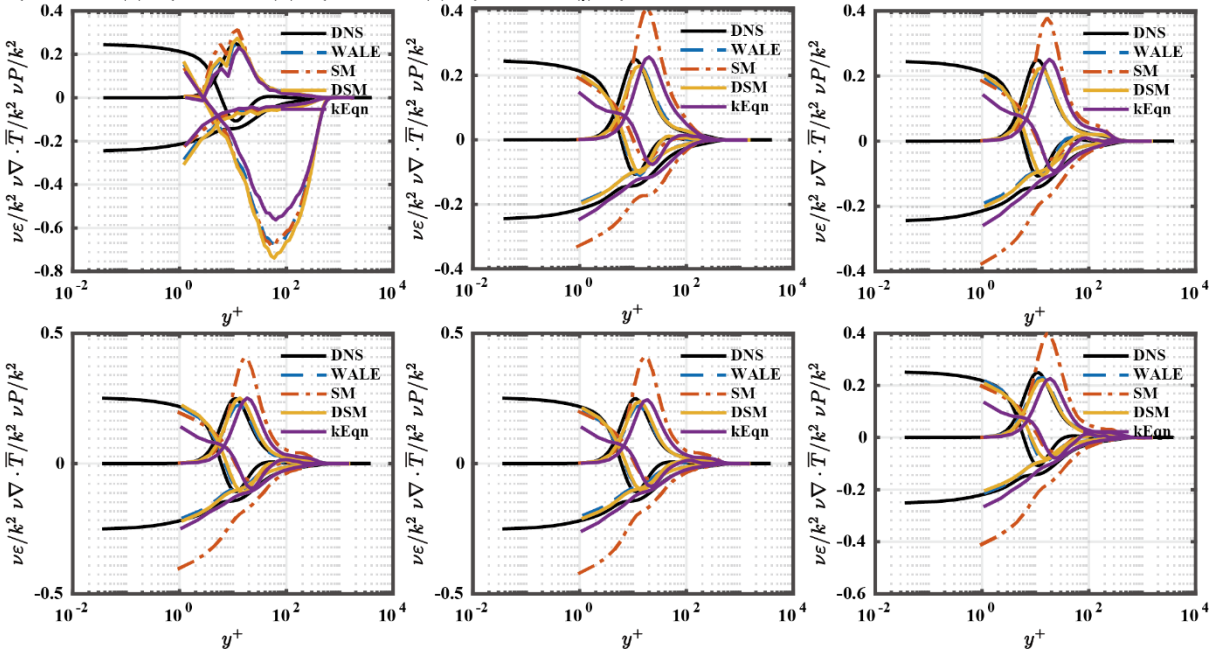


Figure A36. Distribution of the TKE budget terms profiles in simulations based on DFM where the turbulent length scale is 0.2δ with different sub-grid scale models at different positions: (a) at x=inlet (b) at $x/\delta = 10$ (c) $x/\delta = 20$ (d) $x/\delta = 30$ (e) $x/\delta = 40$ (f) $x/\delta = 50$

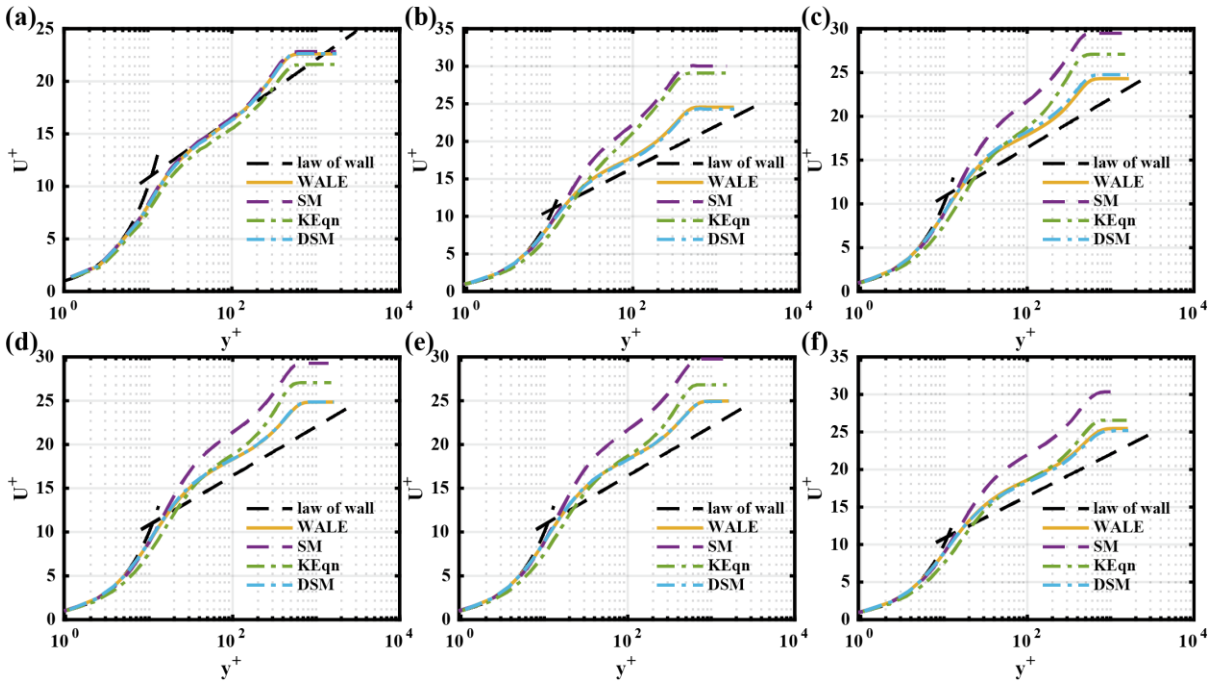


Figure A37. Distribution of the mean velocity profiles of simulations based on DFM where the turbulent length scale is 0.6δ *with different sub-grid scale models at different positions: (a) at x=inlet (b) at* $x/\delta = 10$ *(c)* $x/\delta = 20$ *(d)* $x/\delta = 30$ *(e)* $x/\delta = 40$ *(f)* $x/\delta = 50$

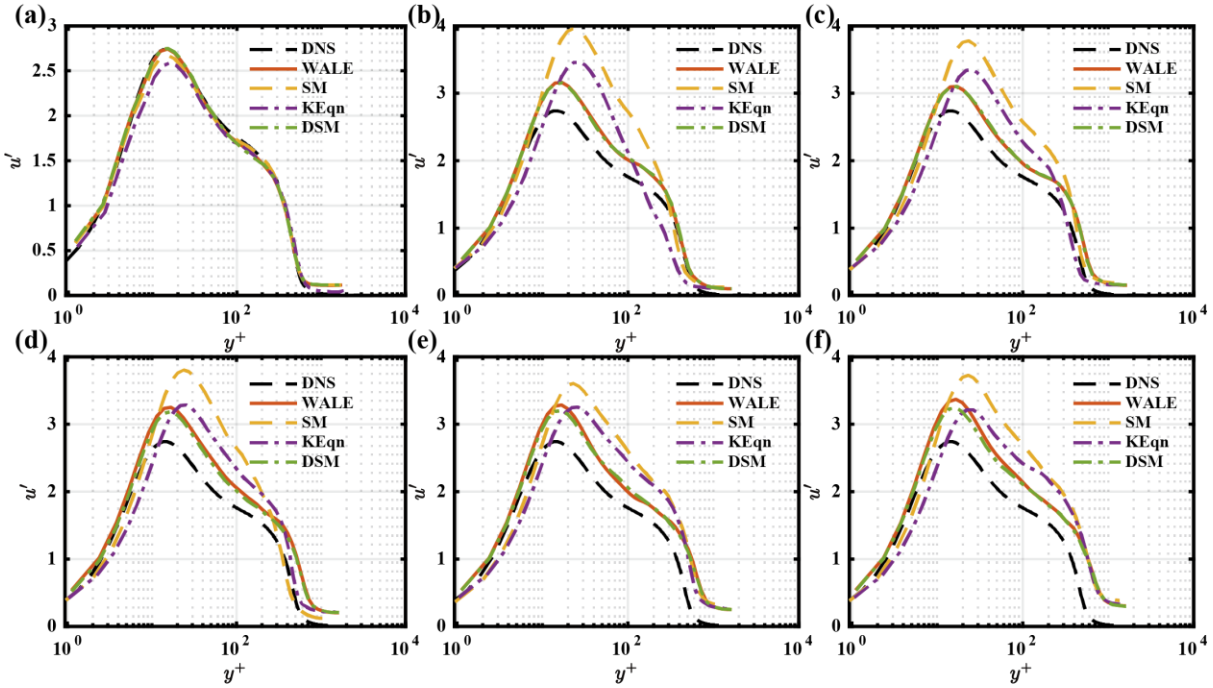


Figure A38. Distribution of the Reynolds stresses component $\overline{u'u'}$ *of simulations based on DFM where the turbulent length scale is* 0.6δ *with different sub-grid scale models at different positions: (a) at x=inlet (b) at* $x/\delta = 10$ *(c)* $x/\delta = 20$ *(d)* $x/\delta = 30$ *(e)* $x/\delta = 40$ *(f)* $x/\delta = 50$

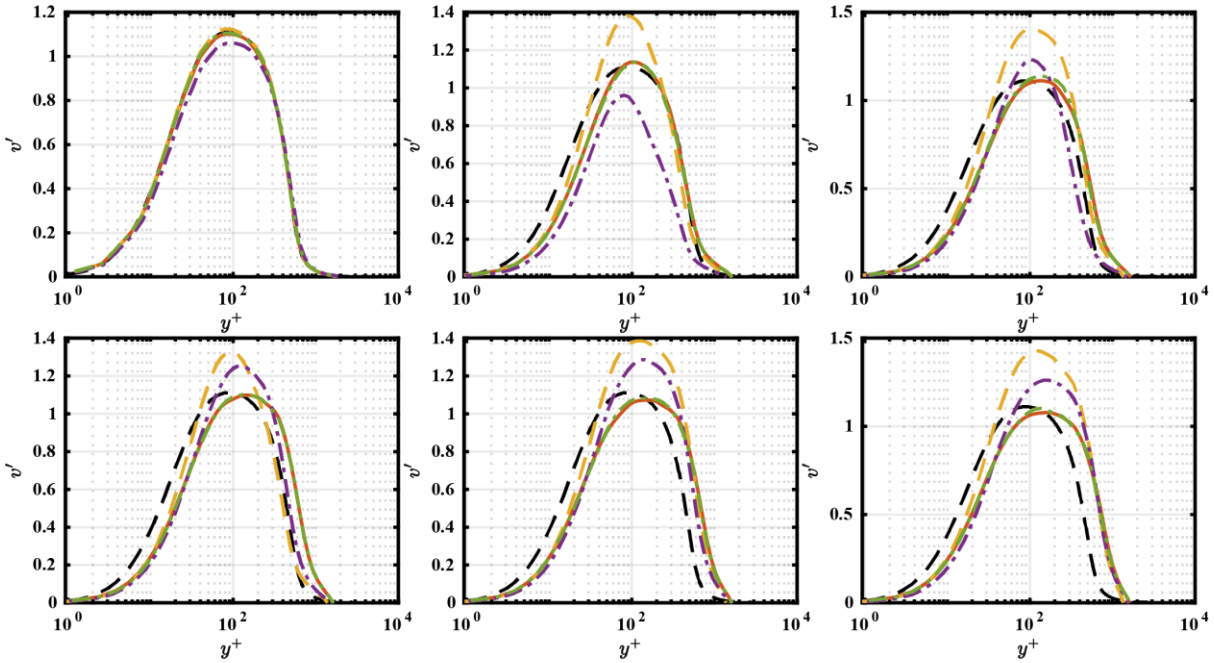


Figure A39. Distribution of the Reynolds stresses component $\overline{v'v'}$ of simulations based on DFM where the turbulent length scale is 0.6δ with different sub-grid scale models at different positions: (a) at x=inlet (b) at $x/\delta = 10$ (c) $x/\delta = 20$ (d) $x/\delta = 30$ (e) $x/\delta = 40$ (f) $x/\delta = 50$

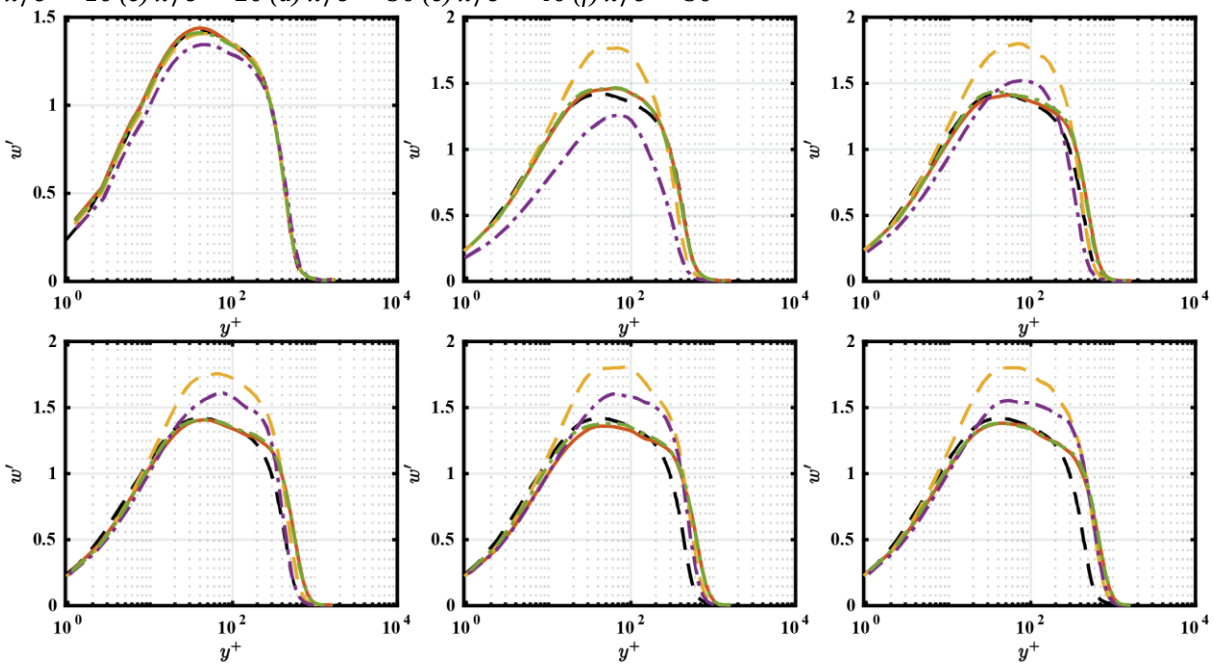


Figure A40. Distribution of the Reynolds stresses component $\overline{w'w'}$ of simulations based on DFM where the turbulent length scale is 0.6δ with different sub-grid scale models at different positions: (a) at x=inlet (b) at $x/\delta = 10$ (c) $x/\delta = 20$ (d) $x/\delta = 30$ (e) $x/\delta = 40$ (f) $x/\delta = 50$

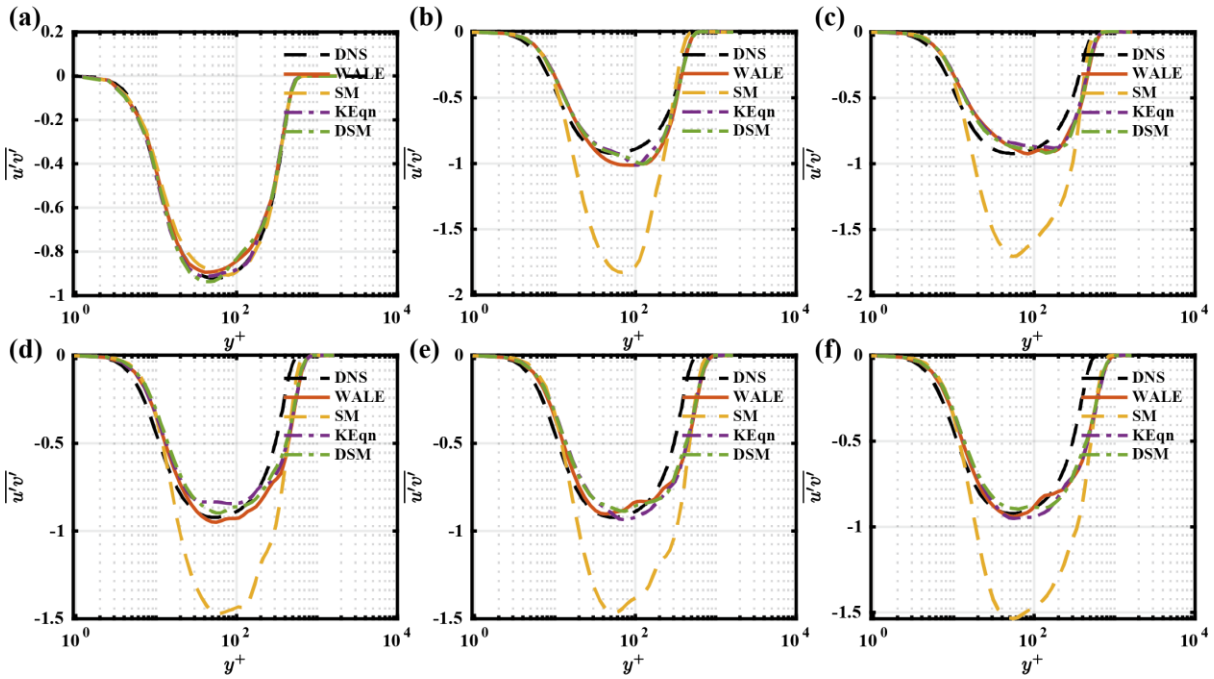


Figure A41. Distribution of the Reynolds stresses component $\overline{u'v'}$ of simulations based on DFM where the turbulent length scale is 0.6δ with different sub-grid scale models at different positions: (a) at x=inlet (b) at $x/\delta = 10$ (c) $x/\delta = 20$ (d) $x/\delta = 30$ (e) $x/\delta = 40$ (f) $x/\delta = 50$

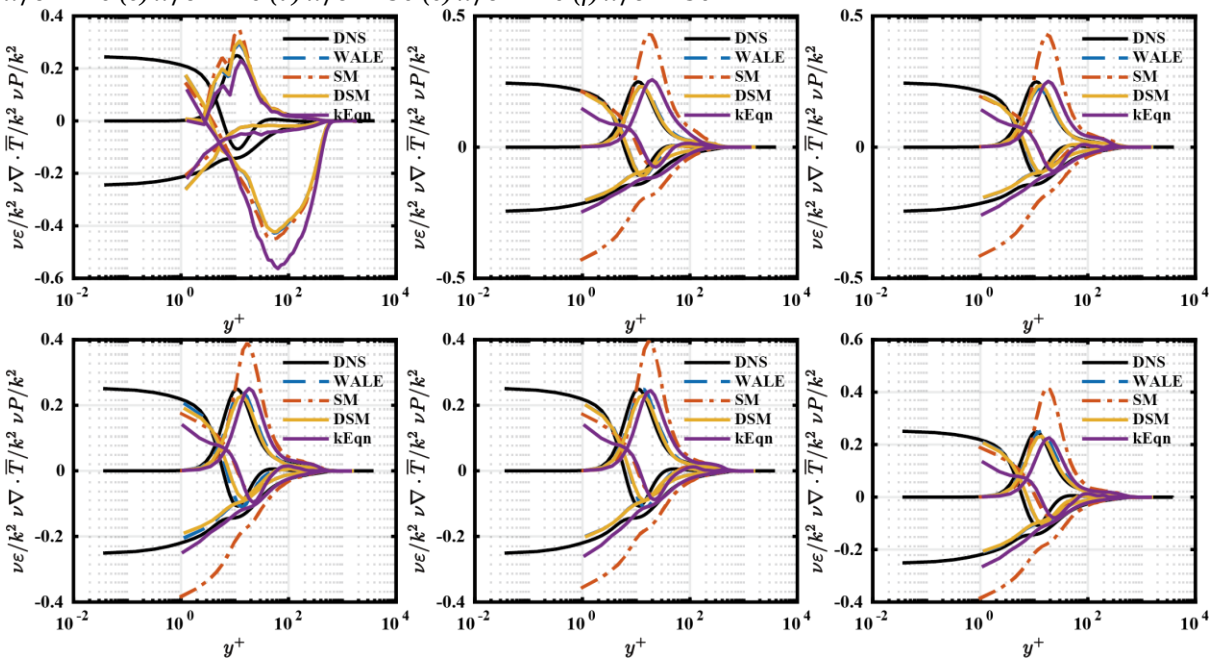


Figure A42. Distribution of the TKE budget terms profiles in simulations based on DFM where the turbulent length scale is 0.6δ with different sub-grid scale models at different positions: (a) at x=inlet (b) at $x/\delta = 10$ (c) $x/\delta = 20$ (d) $x/\delta = 30$ (e) $x/\delta = 40$ (f) $x/\delta = 50$

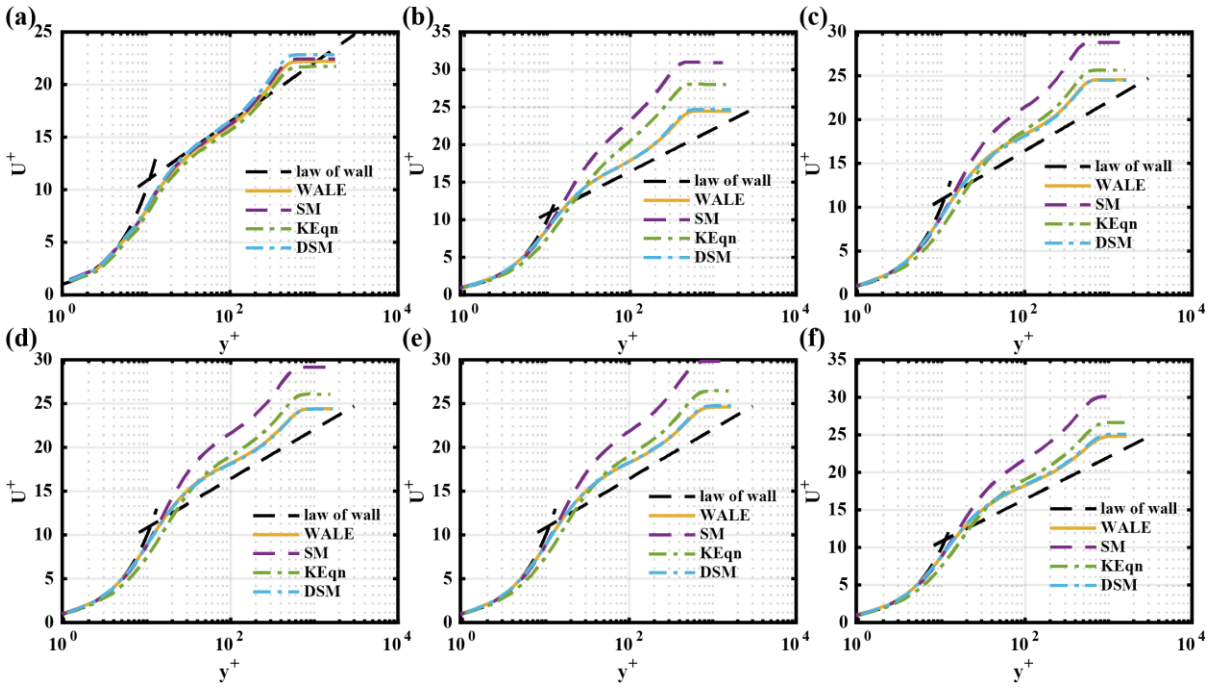


Figure A43. Distribution of the mean velocity profiles of simulations based on DFM where the turbulent length scale is 1.0δ *with different sub-grid scale models at different positions: (a) at x=inlet (b) at* $x/\delta = 10$ *(c)* $x/\delta = 20$ *(d)* $x/\delta = 30$ *(e)* $x/\delta = 40$ *(f)* $x/\delta = 50$

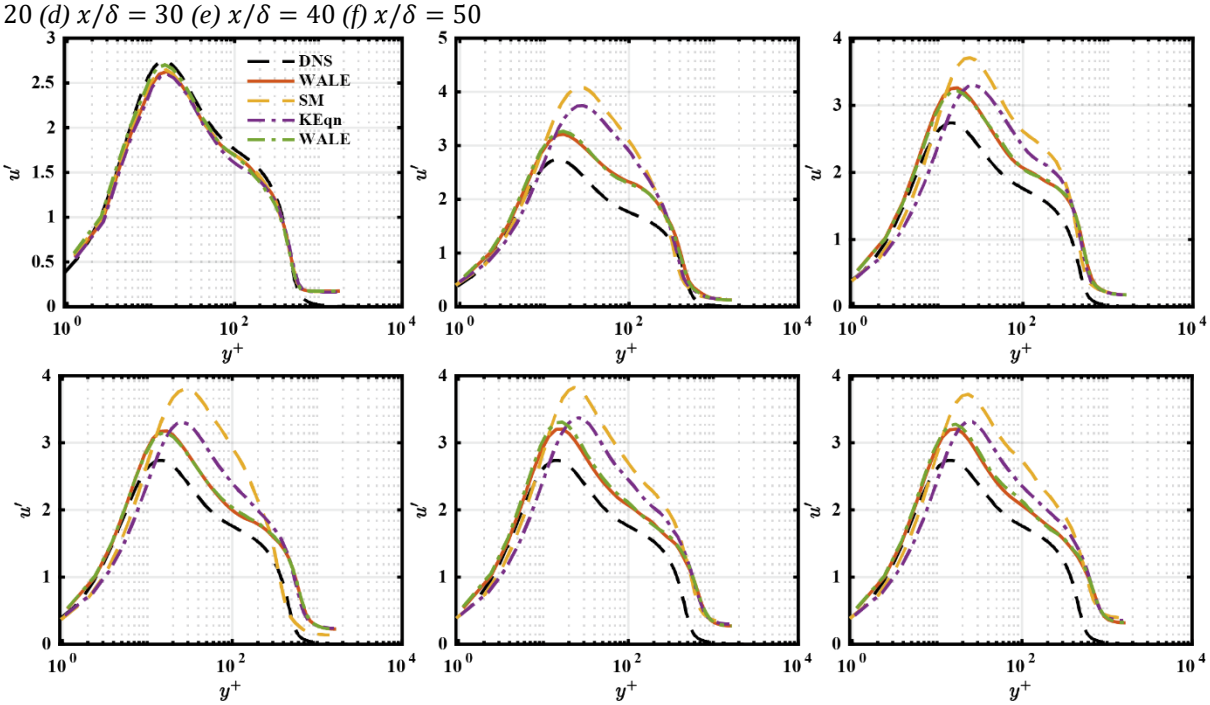


Figure A44. Distribution of the Reynolds stresses component $\overline{u'u'}$ *of simulations based on DFM where the turbulent length scale is* 1.0δ *with different sub-grid scale models at different positions: (a) at x=inlet (b) at* $x/\delta = 10$ *(c)* $x/\delta = 20$ *(d)* $x/\delta = 30$ *(e)* $x/\delta = 40$ *(f)* $x/\delta = 50$

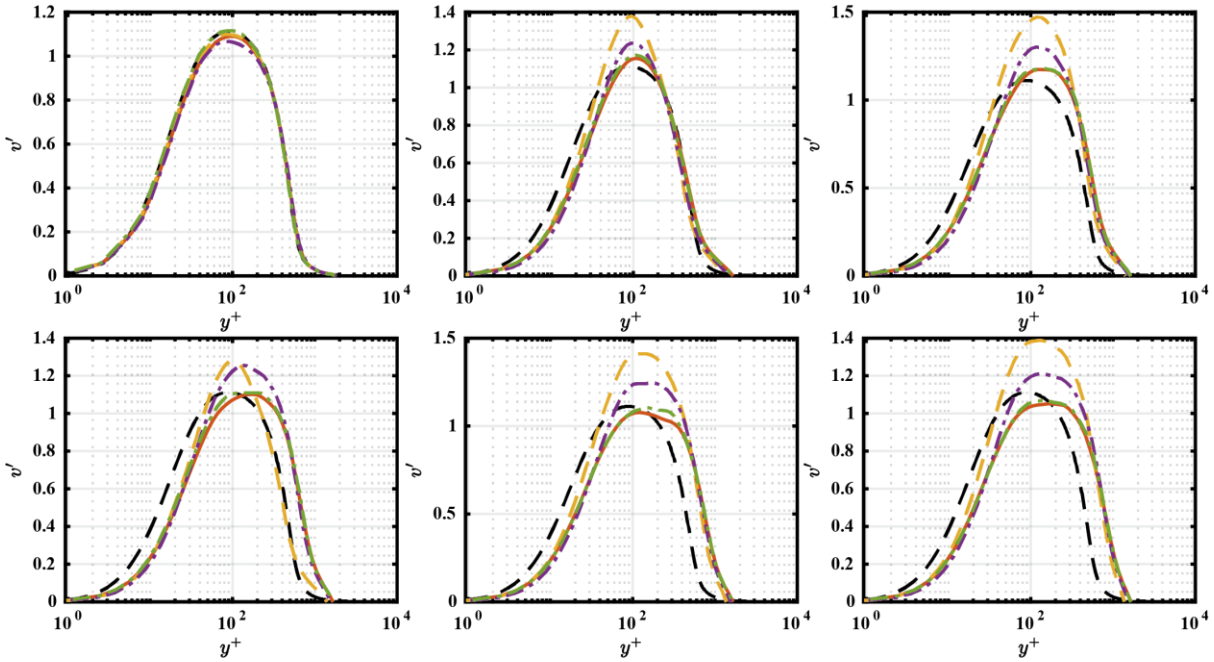


Figure A45. Distribution of the Reynolds stresses component $\overline{v'v'}$ of simulations based on DFM where the turbulent length scale is 1.0δ with different sub-grid scale models at different positions: (a) at x=inlet (b) at $x/\delta = 10$ (c) $x/\delta = 20$ (d) $x/\delta = 30$ (e) $x/\delta = 40$ (f) $x/\delta = 50$

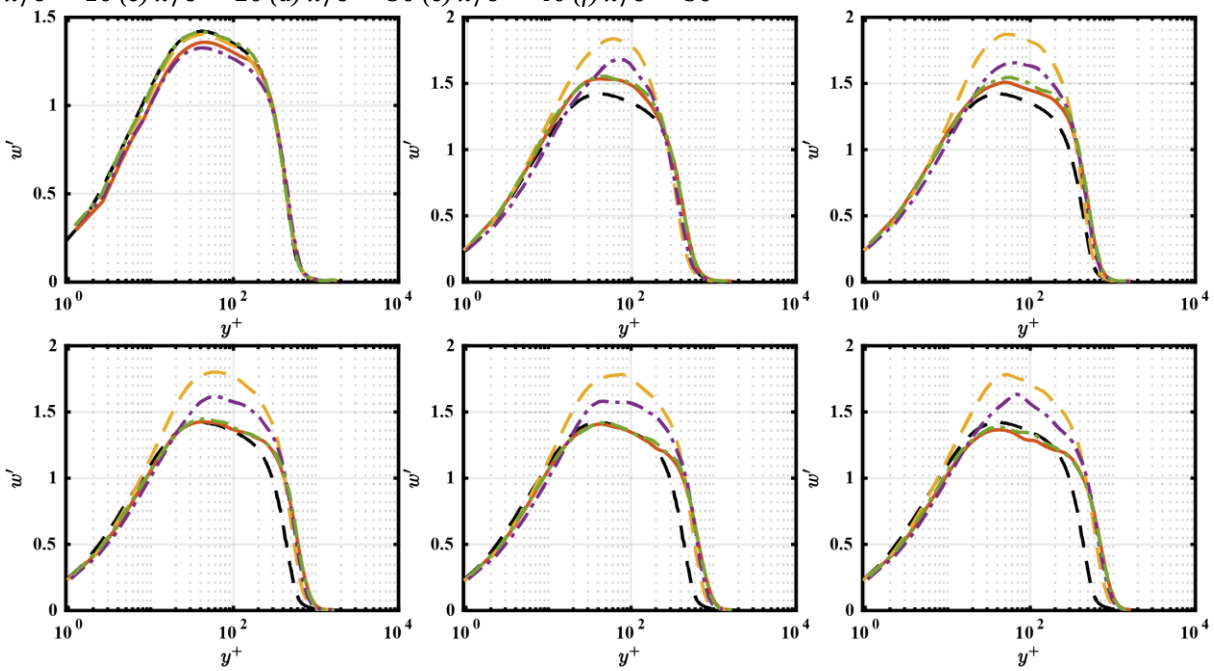


Figure A46. Distribution of the Reynolds stresses component $\overline{w'w'}$ of simulations based on DFM where the turbulent length scale is 1.0δ with different sub-grid scale models at different positions: (a) at x=inlet (b) at $x/\delta = 10$ (c) $x/\delta = 20$ (d) $x/\delta = 30$ (e) $x/\delta = 40$ (f) $x/\delta = 50$

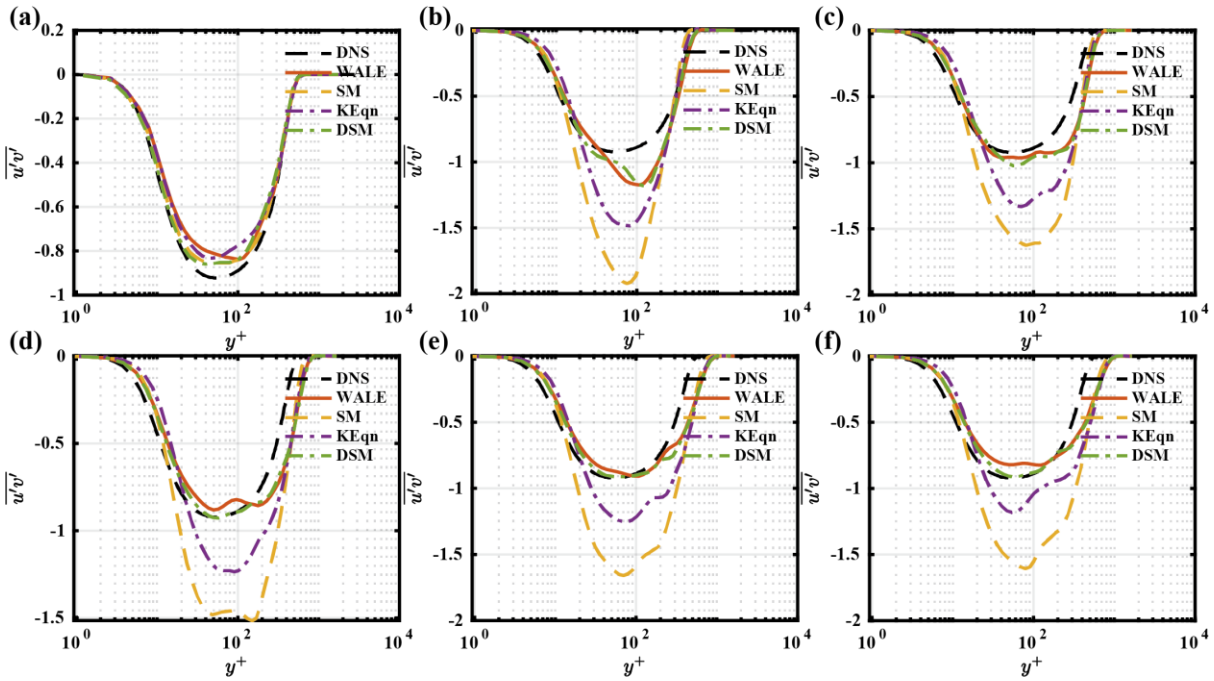


Figure A47. Distribution of the Reynolds stresses component $\overline{u'v'}$ of simulations based on DFM where the turbulent length scale is 1.0δ with different sub-grid scale models at different positions: (a) at x=inlet (b) at $x/\delta = 10$ (c) $x/\delta = 20$ (d) $x/\delta = 30$ (e) $x/\delta = 40$ (f) $x/\delta = 50$

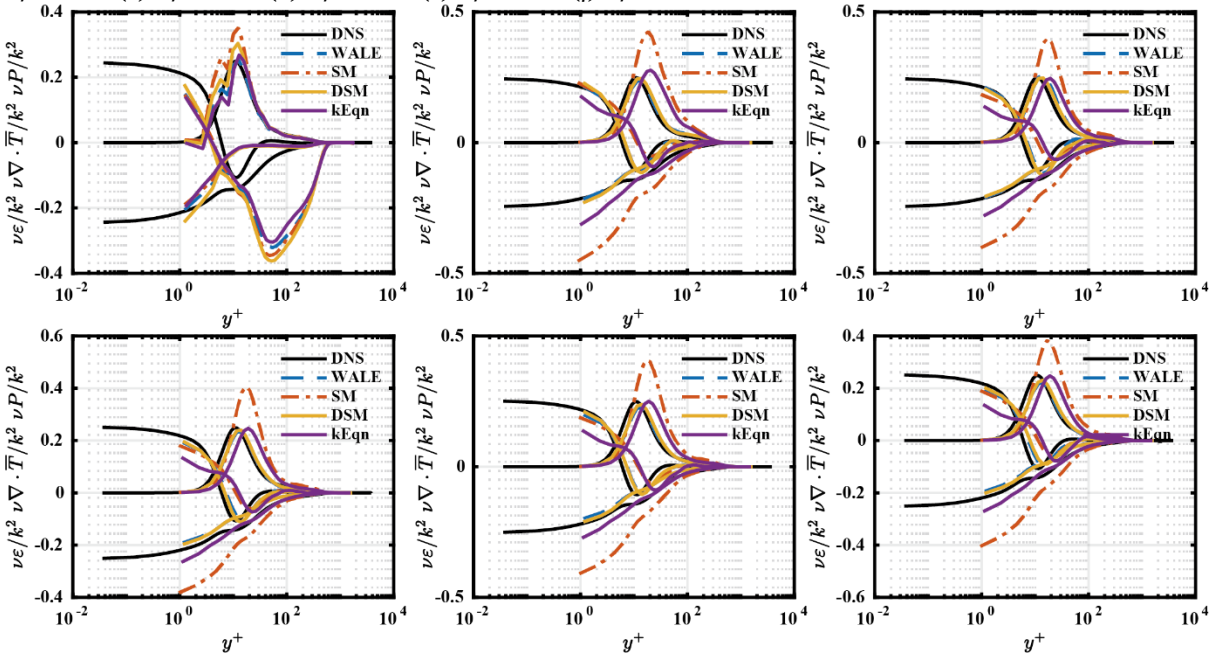


Figure A48. Distribution of the TKE budget terms profiles in simulations based on DFM where the turbulent length scale is 1.0δ with different sub-grid scale models at different positions: (a) at x=inlet (b) at $x/\delta = 10$ (c) $x/\delta = 20$ (d) $x/\delta = 30$ (e) $x/\delta = 40$ (f) $x/\delta = 50$

A5. The post-processing code originally implemented in this work

For the calculation of the turbulent kinetic energy budget terms, there is a file “tkeBudget.H”:

```
if
(
     U.db().foundObject<volVectorField>("UMean")
  && U.db().foundObject<volSymmTensorField>("UPrime2Mean")
)
{

    const objectRegistry& db = U.db();

    const volSymmTensorField G(turbulence->R());

    const volScalarField nu_SGS(turbulence->nut());

    UPrime = (U - db.lookupObject<volVectorField>("UMean"));

    pPrime = (p-db.lookupObject<volScalarField>("pMean"));

    volScalarField kSGS = turbulence->k(); //Instantaneous subgrid-scale
tke

    volScalarField kRes = 0.5*(UPrime & UPrime); //Instantaneous resolved
tke

    B=-2*nu_SGS*symm(fvc::grad(U));

    SGSstrainTensor=symm(fvc::grad(UPrime));

    turbDiff=-0.5*(UPrime*magSqr(UPrime));

    pressDiff=-UPrime & fvc::grad(pPrime);

    viscDiff=-2*nuLam*(UPrime & SGSstrainTensor);

    viscDiss=-2*nuLam*(SGSstrainTensor && SGSstrainTensor);

    SGSDiff=-UPrime & G;

    SGSDiss=B && SGSstrainTensor;

    kTot = kRes + kSGS;

//  volScalarField epsilonSGS = turbulence->epsilon(); //ERROR!!!

    volSymmTensorField SRes = symm(fvc::grad(UPrime)); //Instantaneous
resolved fluctuating rate of strain
    volScalarField epsilonRes=-2*nuLam*(SRes && SRes); //Instantaneous
resolved dissipation rate

    TKEMeanProd = - db.lookupObject<volSymmTensorField>("UPrime2Mean") &&
```

```
fvc::grad(db.lookupObject<volVectorField>("UMean"));

    epsilonTot = mag(viscDiss + SGSDiss);

    LESResIndex = kRes/max(kSmall,kTot); //Instantaneous ratio of resolved
to total (Resolved + SGS) tke

    Info << "ESTIMATED LESResIndex min, max, avg: " <<
min(LESResIndex).value()
                                            << ", " <<
max(LESResIndex).value()
                                            << ", " <<
LESResIndex.weightedAverage(mesh.V()).value()
                                            << endl;
}

else
{
     Warning << "Averaging of velocity U is not active in controlDict." <<
endl
             << "This is necessary to calculate resolved TKE and
dissipation rate." << endl
             << "Add field U to the fieldAverage utility in controlDict."
<< endl;
}
```

The file should be put in the same folder as the file “pimpleFoam”. The name “pimpleFoam” can be substituted by “TKEFoam”, and the code should be modified as listed:

```
 /*---------------------------------------------------------------------------
---*\
  =========                 |
  \\      /  F ield         | OpenFOAM: The Open Source CFD Toolbox
   \\    /   O peration     |
    \\  /    A nd           | www.openfoam.com
     \\/     M anipulation  |
-------------------------------------------------------------------------------
-----
    Copyright (C) 2011-2017 OpenFOAM Foundation
    Copyright (C) 2019 OpenCFD Ltd.
-------------------------------------------------------------------------------
-----
License
    This file is part of OpenFOAM.

    OpenFOAM is free software: you can redistribute it and/or modify it
    under the terms of the GNU General Public License as published by
    the Free Software Foundation, either version 3 of the License, or
    (at your option) any later version.

    OpenFOAM is distributed in the hope that it will be useful, but
WITHOUT
```

```
    ANY WARRANTY; without even the implied warranty of MERCHANTABILITY or
    FITNESS FOR A PARTICULAR PURPOSE.  See the GNU General Public License
    for more details.

    You should have received a copy of the GNU General Public License
    along with OpenFOAM.  If not, see <http://www.gnu.org/licenses/>.

Application
    pimpleFoam.C

Group
    grpIncompressibleSolvers

Description
    Transient solver for incompressible, turbulent flow of Newtonian
fluids
    on a moving mesh.

    \heading Solver details
    The solver uses the PIMPLE (merged PISO-SIMPLE) algorithm to solve the
    continuity equation:

        \f[
            \div \vec{U} = 0
        \f]

    and momentum equation:

        \f[
            \ddt{\vec{U}} + \div \left( \vec{U} \vec{U} \right) - \div
\gvec{R}
          = - \grad p + \vec{S}_U
        \f]

    Where:
    \vartable
        \vec{U} | Velocity
        p       | Pressure
        \vec{R} | Stress tensor
        \vec{S}_U | Momentum source
    \endvartable

    Sub-models include:
    - turbulence modelling, i.e. laminar, RAS or LES
    - run-time selectable MRF and finite volume options, e.g. explicit
porosity

    \heading Required fields
    \plaintable
        U       | Velocity [m/s]
        p       | Kinematic pressure, p/rho [m2/s2]
        \<turbulence fields\> | As required by user selection
    \endplaintable
```

```
Note
   The motion frequency of this solver can be influenced by the presence
   of "updateControl" and "updateInterval" in the dynamicMeshDict.

\*-------------------------------------------------------------------------
---*/

#include "fvCFD.H"
#include "dynamicFvMesh.H"
#include "singlePhaseTransportModel.H"
#include "turbulentTransportModel.H"
#include "pimpleControl.H"
#include "CorrectPhi.H"
#include "fvOptions.H"

// * * * * * * * * * * * * * * * * * * * * * * * * * * * * * * * * * * * * *
* //

int main(int argc, char *argv[])
{
    argList::addNote
    (
        "Transient solver for incompressible, turbulent flow"
        " of Newtonian fluids on a moving mesh."
    );

    #include "postProcess.H"

    #include "addCheckCaseOptions.H"
    #include "setRootCaseLists.H"
    #include "createTime.H"
    #include "createDynamicFvMesh.H"
    #include "initContinuityErrs.H"
    #include "createDyMControls.H"
    #include "createFields.H"
    #include "createUfIfPresent.H"
    #include "CourantNo.H"
    #include "setInitialDeltaT.H"

    turbulence->validate();

    // * * * * * * * * * * * * * * * * * * * * * * * * * * * * * * * * * * * *
* //

    Info<< "\nStarting time loop\n" << endl;

    while (runTime.run())
    {
        #include "readDyMControls.H"
        #include "CourantNo.H"
        #include "setDeltaT.H"

        ++runTime;
```

```
    Info<< "Time = " << runTime.timeName() << nl << endl;

    // --- Pressure-velocity PIMPLE corrector loop
    while (pimple.loop())
    {
        if (pimple.firstIter() || moveMeshOuterCorrectors)
        {
            // Do any mesh changes
            mesh.controlledUpdate();

            if (mesh.changing())
            {
                MRF.update();

                if (correctPhi)
                {
                    // Calculate absolute flux
                    // from the mapped surface velocity
                    phi = mesh.Sf() & Uf();

                    #include "correctPhi.H"

                    // Make the flux relative to the mesh motion
                    fvc::makeRelative(phi, U);
                }

                if (checkMeshCourantNo)
                {
                    #include "meshCourantNo.H"
                }
            }
        }

        #include "UEqn.H"

        // --- Pressure corrector loop
        while (pimple.correct())
        {
            #include "pEqn.H"
        }

        if (pimple.turbCorr())
        {
            laminarTransport.correct();
            turbulence->correct();
        }
    }

    #include "tkeBudget.H"

    runTime.write();

    runTime.printExecutionTime(Info);
}
```

```
    Info<< "End\n" << endl;

    return 0;
}


//
*********************************************************************
//
```